Université de Montréal

Towards the Nanomechanical Actuation and Controlled Assembly of Nanomaterials Using Charge-Transfer Reactions in Electroactive Self-Assembled Monolayers

par

Lana Norman

Département de Chimie
Faculté des Arts et des Sciences

Thèse présentée à la Faculté des Études Supérieures
en vue de l'obtention du grade de
Philosophiæ Doctor (Ph. D.)
en Chimie

Juillet 2009

Université de Montréal
Faculté des etudes supérieures

Towards the Nanomechanical Actuation and Controlled Assembly of Nanomaterials Using Charge-Transfer Reactions in Electroactive Self-Assembled Monolayers

par

Lana Norman

a été évaluée par un jury composé des personnes suivantes

Julian Zhu
président-rapporteur

Antonella Badia
directeur de recherche

Dominic Rochefort
member du jury

Paul Rowntree
examinateur externe

Sjoerd Roorda
représentant du doyen de la FES

ABSTRACT

Surface-functionalized microcantilevers provide an ideal platform for nano- and micro-mechanical actuation and highly sensitive sensing technologies. The basic principle of operation is that a chemical or physical event occurring at the functionalized surface of one side of the cantilever generates a surface stress difference (between the active functionalized and passive non-functionalized sides) that causes the cantilever to bend away from its resting position. However, the factors and phenomena contributing to both the nature and magnitude of the surface stress are not well understood. To this end, the first part of this thesis focused on investigating the potential-controlled actuation and surface stress properties of free-standing gold-coated microcantilevers functionalized with a redox-active self-assembled monolayer (SAM).

A ferrocenylundecanethiolate ($FcC_{11}SAu$) SAM on a gold-coated cantilever was used as a model system to investigate the surface stress generated by faradaic chemistry. The data obtained clearly demonstrates that the electrochemical transformation of a ferrocene moiety in a *monomolecular* organic film can generate a surface stress change of sufficient magnitude to deflect a microcantilever. In fact, depending on the flexibility of the microcantilever, the mechanical deflection resulting from the redox transformation of the surface-tethered ferrocene can range on the order of nanometers to micrometers. The oxidation of the $FcC_{11}SAu$ SAM in perchlorate electrolyte generates a compressive surface stress change. The microcantilever deflection is driven by the lateral tension resulting from molecular reorientation/volume expansion accompanying the charge-transfer and ion-pairing events. To verify this hypothesis, mixed SAM-modified microcantilevers, in which the electroactive ferrocenes are isolated from one another by

an inert *n*-alkylthiolate matrix, were investigated. Under an applied potential, a Faradaic current was measured, but no microcantilever beam deflection was observed. This finding confirms that the cantilever responds to the lateral pressure exerted by an ensemble of re-orienting ferrocenium-bearing alkylthiolates upon each other rather than to individual anion pairing events. Changes in molecular structure and anion type can also be used to modulate the extent of micromechanical motion.

In the next part of the dissertation, electrochemical measurements and surface plasmon resonance spectroscopy were combined to present a description of the adsorption and aggregation of *n*-alkyl sulfates at the $FcC_{11}SAu$/electrolyte interface. At all bulk solution concentrations, the surfactant moieties packed perpendicular to the electrode surface in the form of an interdigitated condensed film. However, the density of the specifically adsorbed film was found to be affected by the organizational state of the surfactants in solution. At low concentrations, where the surfactant molecules are present as solvated monomers, the monomers can readily adapt to the changing ferrocenium concentration with the potential potential scan. However, when the molecules are present as micellar structures in solution, a lower surfactant packing density was found because of the inability to respond effectively to the dynamically generated surface ferroceniums.

This research demonstrates the potential utility of charge-transfer interactions for organizing materials at solid interfaces and effecting micromechanical actuation using an electrifical stimulus.

Key words: surface stress, microcantilever, ferrocene, self-assembled monolayers, electrochemistry, surfactant aggregation, surface plasmon resonance.

RÉSUMÉ

Les microcantileviers fonctionnalisés offrent une plateforme idéale pour la nano- et micro-mécanique et pour le développement de (bio-) capteurs tres sensible. Le principe d'opération consiste dans des évènements physicochimiques qui se passent du côté fonctionnalisé du microcantilevier induisant une différence de stress de surface entre les deux côtés du cantilevier qui cause une déflexion verticale du levier. Par contre, les facteurs et les phénomènes interfacials qui régissent la nature et l'intensité du stress de surface sont encore méconnus. Pour éclaircir ce phénomène, la première partie de cette thèse porte sur l'étude des réactions de microcantileviers qui sont recouverts d'or et fonctionnalisés par une monocouche auto-assemblée (MAA) électroactive.

La formation d'une MAA de ferrocènylundécanethiol ($FcC_{11}SH$) à la surface d'or d'un microcantilevier est le modèle utilisé pour mieux comprendre le stress de surface induit par l'électrochimie. Les résultats obtenus démontrent qu'une transformation rédox de la MAA de $FcC_{11}SH$ crée un stress de surface qui résulte dans une déflexion verticale du microcantilevier. Dépendamment de la flexibilité du microcantilevier, cette déflexion peut varier de quelques nanomètres à quelques micromètres. L'oxydation de cette MAA de $FcC_{11}SH$ dans un environnement d'ions perchlorate génère un changement de stress de surface compressive. Les résultats indiquent que la déflexion du microcantilevier est due à une tension latérale provenant d'une réorientation et d'une expansion moléculaire lors du transfért de charge et de pairage d'anions. Pour vérifier cette hypothèse, les mêmes expériences ont été répéteés avec des microcantileviers qui ont été couverts d'une MAA mixte, où les groupements électroactifs de ferrocène sont isolés par des alkylthiols inactifs. Lorsqu'un potentiel est appliqué, un courant est détecté mais le microcantilevier

ne signale aucune déflexion. Ces résultats confirment que la déflexion du microcantilevier est due à une pression latérale provenant du ferrocènium qui se réorganise et qui crée une pression sur ses pairs avoisinants plutôt que du couplage d'anions. L'amplitude de la déflexion verticale du microcantilevier dépend de la structure moléculaire de la MAA et du le type d'anion utilisés lors de la réaction électrochimique.

Dans la prochaine partie de la thèse, l'électrochimie et la spectroscopie de résonance de plasmon en surface ont été combinées pour arriver à une description de l'adsorption et de l'agrégation des *n*-alkyl sulfates à l'interface $FcC_{11}SAu$/électrolyte. À toutes les concentrations de solution, les molécules d'agent tensio-actif sont empilées perpendiculairement à la surface d'électrode sous forme de monocouche condensé entrecroisé. Cependant, la densité du film spécifiquement adsorbé s'est avérée être affectée par l'état d'organisation des agents tensio-actifs en solution. À faible concentration, où les molécules d'agent tensio-actif sont présentes en tant que monomères solvatés, les monomères peuvent facilement s'adapter à l'évolution de la concentration en surface du ferrocènium lors du balayage du potential. Cependant, lorsque les molécules sont présentes en solution en tant que micelles une densité plus faible d'agent tensio-actif a été trouvée en raison de l'incapacité de répondre effectivement à la surface de ferrocenium générée dynamiquement.

Mots clés: tension de surface, ferrocène, monocouches auto-assemblées, microcantilevier, électrochimie, spectroscopie de résonance de plasmons de surface.

ACKNOWLEDGMENTS

First and foremost, I would like to thank my thesis supervisor, Professor Antonella Badia for her guidance, enthusiasm and encouragement throughout my degree. Her knowledge and passion for research were truly inspiring and I feel fortunate to have been a member of her group.

I have also benefited form the expertise of numerous people in the Department of Chemistry. To Martin Lambert, Jean-François Myre, Louis Beaumont, Yves Teasdale, and Cédric Ginart, I would like to express my sincerest thanks.

I would also like to thank Brian Seivewright for his help with the cantilever experimental setup and Jeff Shepherd for the corresponding computer programming. Other McGill present and past students have provided helpful comments, suggestions and endless encouragement during the entire process of my Ph.D; in particular I would like to mention Andrew O'Donnell and Shane Pawsey.

A special thanks is directed to Piotr Kujawa for his many helpful comments and suggestions and I would also like to thank him for his editorial efforts.

I would also like to thank my labmates for their helpful conversations, AFM acquisitions, as well as the translation of my abstract.

Finally, I would like to say thank you to my entire family and Stephanie Maynard. Their support and encouragement have meant so much to me over the many years of this academic accomplishment.

TABLE OF CONTENTS

Abstract iii

Résumé v

Acknowledgments vii

Table of Contents viii

List of Frequently Used Symbols xii

List of Frequently Used Abbreviations xiii

List of Tables xiv

List of Figures xv

Thesis Overview and Research Objectives xxii

Chapter 1

General Introduction..... 1

1.1 Self-Assembled Monolayers (SAMs) 4

1.2 Electrochemical Characteristics of Monolayers 14

1.3 Surface Plasmon Resonance (SPR) Spectroscopy..... 17

1.4 Microcantilever Actuators..... 24

1.4.1 *Cantilever Modes of Operation*..... 26

1.4.2 *Cantilever Deflection* 28

1.4.3 *Quantifying Surface Stress* 30

1.4.4 *Interpretation of the Measured Surface Stress* 33

1.5 The Present Work 36

1.6 References 36

Chapter 2

Redox Actuation of a Microcantilever Driven by a Self-Assembled Ferrocenylundecanethiolate Monolayer: An Investigation of the Origin of the Micromechanical Motion and Surface Stress 46

2.1 Abstract 46

2.2 Introduction 48

2.3 Experimental Section 53

2.3.1 *Materials and Methods* 53

2.3.2 *Preparation and Characterization of the SAM-Gold Substrates* 54

2.3.3 *Electrochemical and Contact Angle Measurements* 56

2.3.4 *Electrochemical Microcantilever Measurements* 56

2.3.5 *Microcantilever Deflection and Surface Stress* 59

2.4 Results and Discussion 60

2.4.1 *Electrochemical Characterization of the $FcC_{11}SAu$ Microcantilever* 60

2.4.2 *Surface Stress Measurements* 60

2.4.3 *Microcantilever Deflection vs. Quantity of Electrogenerated Ferrocenium* 67

2.4.4 *Influence of the Ferrocene Surface Coverage on the Surface Stress Response* 73

2.4.5 *Origin of the Redox-Induced Surface Stress Change* 77

2.5 Conclusions 82

2.6 Acknowledgments 83

2.7 References 84

Chapter 3

Redox Induced Actuation of a Microcantilever Driven by Ferrocene-Terminated Self-Assembled Monolayers: An Investigation of the Effects of the Alkyl Chain and Anion on the Micromechanical Motion and Surface Stress 93

3.1 Introduction 93

3.2 Experimental 95

3.2.1 *Materials and Methods* 95
3.2.2 *Preparation of Gold-Covered Substrates and SAMs* 96
3.2.3 *Spectroscopic Ellipsometry* 97
3.2.4 *Fourier Transform Infrared Reflection–Absorption Spectroscopy* 98
3.2.5 *Electrochemical Characterization* 98
3.2.6 *Electrochemical Surface Plasmon Resonance Spectroscopy* 98
3.2.7 *Electrochemical Microcantilever Measurements* 101
3.3 Results and Discussion 102
3.3.1 *Characterization of the Ferrocene-Terminated Monolayers* 102
3.3.2 *Influence of the Alkyl Chain on the Surface Stress* 104
3.3.3 *Influence of the Anion on the Surface Stress Change of $FcC_{11}SAu$ Microcantilevers.* 111
3.4 Conclusions 116
3.5 References 117

Chapter 4

Electrochemical Surface Plasmon Resonance Investigation of Dodecyl Sulfate Adsorption to Electroactive Self-Assembled Monolayers via Ion-Pairing Interactions **123**

4.1 Abstract 123
4.2 Introduction 124
4.3 Experimental 131
4.3.1 *Materials* 131
4.3.2 *Preparation of Gold-Covered Substrates and SAMs* 132
4.3.3 *Ellipsometry* 133
4.3.4 *Electrochemistry* 134
4.3.5 *SPR Spectroscopy* 136
4.3.6 *Atomic Force Microscopy* (*AFM*) 139
4.4 Results and Discussion 140
4.4.1 *$FcC_{11}SAu$ SAM Characterization* 140
4.4.2 *Electrochemical Behaviour* 141

4.4.3 *Determination of Redox-Induced $FcC_{11}SAu$ Thickness Change*..148

4.4.4 *Assembly of Dodecyl Sulfate and Hydroxyundecyl Sulfonate to $FcC_{11}SAu$ SAMs* 152

4.5 Conclusions 164

4.6 Acknowledgments..... 165

4.7 References 166

Chapter 5

Electrochemical Surface Plasmon Resonance Investigation of the Directed Interfacial Assembly of Sodium n-Alkyl Sulfates to a Redox-Active Self-Assembled Monolayer via Ion-Pairing Interactions……. 173

5.1 Introduction 173

5.2 Materials and Methods..... 176

5.2.1 *Materials*..... 176

5.2.2 *$FcC_{11}SH$, Electrode, and Monolayer Preparation*..... 177

5.2.3 *Instrumentation and Electrochemical Measurements*..... 177

5.3 Results and Discussion..... 179

5.3.1 *Electrochemical Characterization of $FcC_{11}SAu$ SAMs in Sodium n-Alkyl Sulfate ($C_nH_{2n+1}OSO_3Na$) Electrolytes*..... 179

5.3.2 *Assembly of n-Alkyl Sulfates onto $Fc^+C_{11}SAu$ SAMs* 187

5.4 Conclusion..... 196

5.4 References 197

Chapter 6

General Conclusions, Contributions to Original Knowledge, and Suggestions for Future Work……..201

6.1 General Conclusions and Contributions to Original Knowledge 201

6.2 Suggestions for Future Work..... 206

***Appendix A*.....A1**

LIST OF FREQUENLTY USED SYMBOLS

A	electrode area, in cm^2
Γ	surface coverage
ΔE_p	anodic-to-cathodic peak separation
ΔE_{fwhm}	full width at half maximum
$\Delta\Theta_m$	shift in spr angle
$\Delta\sigma$	surface stress, in $N \cdot m^{-1}$
Δz	cantilever deflection, in nm
$E_{1/2}$	half-wave potential or the average of the main oxidation and reduction peak potentials
E_a	anodic peak potential
F	Faraday constant, 96 485.3 $C \cdot mol^{-1}$
Q	charge
Φ_{Fc^+}	fractional coverage of electrogenerated ferrocenium
χ_{Fc}^{soln}	mole fraction of ferrocenylalkythiolate in solution
χ_{Fc}^{surf}	mole fraction of ferrocenylalkythiolate on the surface
v	scan rate, in $mV \cdot s^{-1}$

LIST OF FREQUENLTY USED ABBREVIATIONS

AFM	Atomic force microscopy
C_nSAu	alkylthiolate SAM on gold, *n* indicates chain length
cmc	critical micelle concentration
CV	cyclic voltammetry
ESPR	electrochemical surface plasmon resonance
EQCM	electrochemical quartz microbalance
FT-IRRAS	fourier-transform infrared reflection absorption spectroscopy
Fc	ferrocene
Fc^+	ferrocenium ion
$FcC_{11}SAu$	ferrocenylundecanethiolate SAM on gold
$FcC_{12}SAu$	ferrocenyldodecanethiolate SAM on gold
FcC_6SAu	ferrocenylhexanethiolate SAM on gold
$FcCOC_{11}SAu$	ferrocenylcarboxy-1-undecanethiolate SAM on gold
FcRSH	ferrocenylalkythiol
SN_cS	Sodium *n*-alkyl sulfate, N_c indicates the alkyl chain length
PSD	position sensitive detector
RSAu	alkylthiolate SAM on gold
RSH	*n*-alkylthiol
SAM	self-assembled monolayer
SPR	Surface plasmon resonance spectroscopy

LIST OF TABLES

Table 1.1	Properties and dimensions of the microcantilevers illustrated in **Figure 1.12**.	32
Table 3.1	Layer Models and Parameters for the Fresnel Calculations Table **(A)** FcC_6SAu, **(B)** $FcC_{12}SAu$, and **(C)** $FcCOC_{11}SAu$.	100
Table 3.2	Ferrocene Surface Coverages, SPR and Film Thickness Changes, FT-IR, and Surface Stress Results of FcRSAu SAMs in Perchlorate Electrolyte.	103
Table 3.3	Surface Stress and Electrochemical Characteristics of $FcC_{11}SAu$-Modified Microcantilevers as Depicted in **Figure 3.3**.	112
Table 4.1	Layer Models and Parameters for the Fresnel Calculations.	138
Table 5.1	Parameters for Determining the Effective Thickness and Surface Coverage of the Potential-Induced Surfactant Adsorption.	178
Table 5.2	Relative Ion Pairing Affinity, Surface Coverages, and Peak Widths, After Deconvolution of the CVs for $FcC_{11}SAu$ in the Sodium *n*-Alkyl Sulfate Electrolyte Solutions.	182

LIST OF FIGURES

Figure 1.1 Schematic illustration of a self-assembled monolayer (SAM) on gold. 5

Figure 1.2 Characteristic morphology of a decanethiolate SAM on Au(111). **(A)** STM topograph, 20 nm × 20 nm, taken after the sample was thermally annealed. The primitive rectangular unit cell (green square) and the c(4 × 2) superlattice (blue rectangle) are indicated in the inset. **(B)** Schematic diagram illustrating the lattice structure (blue rectangle) and unit cell (green rectangle) of an alkanethiolate SAM on Au(111). The Au(111) surface structure is depicted by the black hexagonal square. Data is reproduced from reference 83. 10

Figure 1.3 STM topographs taken after thermal annealing of the sample. **(A)** $Fc(CH_2)_3SAu$**,** **(B)** $Fc(CH_2)_5SAu$, and **(C)** $Fc(CH_2)_{11}SAu$ monolayers formed on Au(111). The unit cell is marked in green as shown in **(A).** The blue lines in **(A)** and **(B)** depict the observed characteristic pattern. In **(C)** stripped monolayer features are marked in white, whereas the green arrows represent a change in monolayer height. Data is reproduced from reference 111. 11

Figure 1.4 Schematic diagrams illustrating the effects of functional groups on the packing density and organization of SAMs. **(A)** Small terminal groups (i.e., $–CH_3$**,** –OH, –CN) do not distort the secondary organization and have no effect on the sulfur arrangement. **(B)** Larger terminal groups (i.e., ferrocene, viologen, ruthenium complexes) impose steric constraints where the resulting monomolecular structures are more disordered and less dense than those formed with types of molecules shown in **(A)**. 13

Figure 1.5 **(A)** An idealized reversible cyclic voltammogram (CV) of a surface-tethered redox couple. See text for symbol descriptions. **(B)** CV of a $FcC_{11}S/HOC_{11}SAu$ mixed SAM in perchlorate solution. **(C)** CV scan of a single-component $FcC_{11}SAu$ SAM. CVs in **(B)** and **(C)** were acquired in perchlorate at 10 $mV \cdot s^{-1}$. The redox centers are represented by ●. 15

Figure 1.6 Schematic representation of the electromagnetic field associated with a surface plasmon propagating along a metal/dielectric interface. 18

Figure 1.7	Illustration of the excitation of surface plasmons in the ATR-Krestchmann geometry.	21
Figure 1.8	Illustration of typical SPR curves.	23
Figure 1.9	Schematic representations of the rectangular- and V-shaped microcantilevers manufactured by **(A)** Veeco Metrology Inc. and **(B)** MikroMasch USA.	25
Figure 1.10	Schematic representations of the rectangular- and V-shaped microcantilevers manufactured by **(A)** Veeco Metrology Inc. and **(B)** MikroMasch USA.	26
Figure 1.11	Illustration of the beam deflection parameters used to determine the microcantilever bending with nanometer accuracy.	29
Figure 1.12	Schematic of the V- and rectangular shaped microcantilevers and dimensional variables..	32
Figure 1.13	Photograph of the electrochemical-microcantilever experimental set-up showing the configuration of the liquid cell and electrodes (microcantilever: working electrode, Ag/AgCl: reference electrode, and Pt wire: auxiliary electrode). The microcantilever is mechanically clamped with a stainless steel clip onto a Teflon holder (as shown in the inset) which is attached to the micropositioner. The optical beam deflection configuration (laser and PSD) is also shown.	35
Figure 2.1	Schematic of the custom-built electrochemical cell (not shown to scale) incorporating the microcantilever chip as the working electrode, an Ag/AgCl reference electrode, and a platinum wire as the counter electrode.	58
Figure 2.2	**(A)** Typical CV traces of $FcC_{11}SAu$ (—) and $C_{11}SAu$ (—) modified microcantilever substrates in 0.1 M $NaClO_4$/0.01 M $HClO_4$. The potential scan rate was 5 $mV \cdot s^{-1}$. **(B)** Corresponding deflection (Δz, left axis) and surface stress ($\Delta\sigma$, right axis) profiles for the $FcC_{11}SAu$ (○) and $C_{11}SAu$ (○) modified V-shaped microcantilevers (k = 0.011 ± 0.002 $N \cdot m^{-1}$) in 0.1 M $NaClO_4$/0.01 M $HClO_4$. **(C)** Zoom-in of the current-time (top) and deflection-time (bottom) traces recorded by cyclic voltammetry for the $C_{11}SAu$ microcantilever.	62
Figure 2.3	**(A)** Typical CV trace of a $FcC_{11}SAu$-modified microcantilever substrate in 0.1 M $NaClO_4$/0.01 M $HClO_4$. The potential was scanned at a rate of 5 mV s^{-1}. **(B)** The PSD response obtained when the laser is focused on the apex of the microcantilever (○, k	63

= 0.011 ± 0.002 N m^{-1}) vs. the immobile chip (—). **(C)** A schematic of the laser positioning (●) at the apex (○) of the microcantilever vs. the immobile chip.

Figure 2.4 Plots of the **(A)** microcantilever deflection (Δz) and **(B)** microcantilever surface stress ($\Delta\sigma$) vs. the spring constant (k) for $FcC_{11}SAu$ modified microcantilevers. In both graphs solid black dots (●) represent SiN_x microcantilevers while the solid green dots (●) represent Si/SiO_x microcantilever measurements. The Δz values reported for each spring constant are the average and standard error measured for at least four different cantilevers of that spring constant. The Si/SiO_x (●) cantilevers are all rectangular in shape, whereas the SiN_x (●) microcantilevers are V-shaped, except for the cantilever with k = 0.0206 (±0.0004) N m^{-1}. 66

Figure 2.5 Plots of the fractional coverage (Φ_{Fc^+}) of ferrocenium (—) and % change in cantilever deflection (%Δz, ○) vs. the applied potential for scan rates: **(A)** 10 mV s^{-1}, **(B)** 5 mV s^{-1}, and **(C)** 1 mV s^{-1}. The left panel of the graphs represent the anodic scan (–0.10 to +0.70 V), whereas the right panel represents the cathodic scan (+0.70 to –0.10 V). Φ_{Fc^+} was determined by integrating incrementally the areas under the anodic and cathodic current-potential curves of the CVs after correcting for the charging current by a baseline approximation. The % change in the cantilever deflection was calculated by assigning the PSD signals at 0 V and +0.70 V to, respectively, the zero and maximum cantilever positions. The arrows indicate the direction of potential cycling for the redox cycle. 68

Figure 2.6 **(A)** Time-dependent surface stress profiles observed for a $FcC_{11}SAu$ microcantilever (k = 0.024 ± 0.002 N m^{-1}) in single-step potential-hold experiments, where the potential was stepped from open circuit potential to potentials corresponding to ferrocenium surface coverages: Φ_{Fc^+} = 0 (0.050 V, ○), 0.34 (0.340 V, ○), 0.64 (0.385 V, ○), 0.82 (0.415 V, ○) and 0.99 (0.550 V, ○). **(B)** Plot of the $\Delta\sigma$ values obtained by potential step-hold (○) and cyclic voltammetry (■) for a given Φ_{Fc^+}. The CVs were acquired at a scan rate of 5 mV s^{-1}. 70

Figure 2.7 **(A)** A plot of the simulated ferrocenium nearest neighbor (> 1) distribution vs. the ferrocenium coverage (Φ_{Fc^+}) for a 36 × 36 grid (1296 molecules). **(B)** Plot of the % change in the cantilever 72

deflection vs. the fractional coverage of ferrocenium (Φ_{Fc^+}) for the anodic (■) and cathodic (□) scans.

Figure 2.8 Typical CV traces (left axis, —) and corresponding Δσ responses (right axis, —) obtained for microcantilevers modified with binary $FcC_{11}S$-/$C_{11}SAu$ SAMs for which the $FcC_{11}S$- concentration is **(A)** ~35% and **(B)** ~14% of that of single-component $FcC_{11}SAu$ modified microcantilever substrates. The green dashed line in **(B)** is the stress response obtained for the $C_{11}SAu$ microcantilever shown in **Figure 1C**. 75

Figure 2.9 Example of the anodic peak deconvolution of a SAM prepared by incubation of a microcantilever for ~12 hours in a 1 mM $FcC_{11}SH/C_{11}SH$ (0.24:0.76) solution. The anodic segment (○) was initially corrected for the charging current and the baseline is shown in grey (—). The solid red line (—) represents the Gaussian-Lorentzian fittings and the dotted green lines (----) represent the individual Gaussian and Lorentzian fittings. The CV was run in 0.1 M $NaClO_4$/0.01 M $HClO_4$ and the potential was scanned at a rate of 5 $mV \cdot s^{-1}$. 76

Figure 2.10 Schematic representation of the redox-induced deflection of $FcC_{11}SAu$ microcantilevers in perchlorate solution. 81

Figure 3.1 Typical CVs (left axis, —) and corresponding differential surface stresses, $\Delta\sigma$, (right axis, —) for **(A)** $FcC_{12}SAu$, **(B)** FcC_6SAu and **(C)** $FcCOC_{11}SAu$ modified microcantilevers in 0.10 M $NaClO_4$/ 0.01 M $HClO_4$. Scan rate = 5 $mV \cdot s^{-1}$. 106

Figure 3.2 Plot of the % change in the cantilever deflection vs. the fractional coverage of the ferrocenium (Φ_{Fc^+}) for the anodic scans of $FcC_{12}SAu$ (□), $FcC_{11}SAu$ (×), FcC_6SAu (Δ) and $FcCOC_{11}SAu$ (○) modified microcantilever substrates. 111

Figure 3.3 Typical CV traces (top panel) and corresponding differential surface stress (bottom panel) of $FcC_{11}SAu$ modified microcantilevers in **(A)** 0.10 M $NaPF_6$ **(B)** 0.10 M $NaBF_4$ **(C)** 0.10 M $NaNO_3$ and **(D)** 0.10 M NaF electrolyte solutions. Scan rate = 5 $mV \cdot s^{-1}$. 113

Scheme 4.1 **(A)** Molecular dimensions of a dodecyl sulfate molecule: (i) extended length $d \approx 1.98$ nm, (ii) cross-sectional area of headgroup ≈ 0.28 nm^2, (iii) cross-sectional area of CH_2 group ≈ 0.21 nm^2. Surface aggregate structures suggested by AFM: **(B)** Cylindrical hemimicelles[4] and **(C)** Interdigitated monolayer. An average molecular area of 0.25 nm^2 per dodecyl sulfate molecule 125

yields a theoretical Γ of 6.6 x 10^{-10} mol cm^{-2} for the interdigitated monolayer configuration.

Figure 4.1 Absorption spectra of ferrocene (black) and ferrocenium (green) in DMF. 134

Figure 4.2 Tapping-mode AFM images (topography) in air of **(A)** bare Au substrate and **(B)** $FcC_{11}SAu$ monolayer assembly. 141

Figure 4.3 $FcC_{11}SAu$ SAM in perchlorate solution (0.01 M $HClO_4$/0.1 M $NaClO_4$). **(A)** CV scan (scan rate = 10 $mV \cdot s^{-1}$) and **(B)** DPV scan (scan rate = 5 $mV \cdot s^{-1}$). 143

Figure 4.4 Example of peak deconvolution of a typical CV scan of $FcC_{11}SAu$ SAM in perchlorate solution. CV taken from **Figure 4.3A**. Peak devolution using a Gaussian and Lorentzian functions. The solid red line is the fitted curve and dashed lines are the deconvoluted peaks. The grey line is the baseline correction. 144

Figure 4.5 $FcC_{11}SAu$ SAM in 100 mM $SN_{12}S$ solution. **(A)** CV scan (scan rate = 10 $mV \cdot s^{-1}$). The inset shows the linear relationship of the peak current vs. scan rate for the first anodic peak at 0.16 V (filled circles) and the second anodic peak at 0.40 V (unfilled circles). **(B)** DPV scan (scan rate = 5 $mV \cdot s^{-1}$). 145

Figure 4.6 $FcC_{11}SAu$ SAM in 50 mM SHS solution: **(A)** CV scan (scan rate = 10 $mV \cdot s^{-1}$) and **(B)** DPV scan (scan rate = 5 $mV \cdot s^{-1}$). 147

Figure 4.7 **(A)** Current vs. time profile obtained during potential cycling between –0.10 V and +0.75 V of a $FcC_{11}SAu$ SAM at a rate of 10 $mV \cdot s^{-1}$ in 0.01 M $HClO_4$/0.1 M $NaClO_4$ solution. **(B)** Corresponding SPR profiles. Maximum $\Delta\Theta_m = 0.0193 \pm 0.0003°$. 149

Figure 4.8 Plot of fractional coverage (Φ) of ferrocenium (—) and % change in SPR response (○) vs. the time for a complete voltammetric cycle. 150

Figure 4.9 Comparison of the adsorption of $SN_{12}S$ (100 mM) to a $FcC_{11}SAu$ SAM (○) and to a $HO(EO)_3C_{11}SAu$ SAM (○) using a scanning angle SPR spectrometer (λ = 633 nm, Resonant Probes GmbH). 153

Figure 4.10 Current vs. time profiles obtained during potential cycling between -0.10 V and +0.75 V of a $FcC_{11}SAu$ SAM at a rate of 10 $mV\ s^{-1}$ and the corresponding SPR profiles in **(A)** 100 mM (12.5 x cmc), **(B)** 32 mM (4 x cmc), **(C)** 8 mM (cmc) and (**D**) 2 mM (0.25 x cmc) $SN_{12}S$ solution. 154

Figure 4.11 **(A)** A plot of the surface coverage (Γ) of dodecyl sulfate vs. the bulk concentration of SN_{12}S for a 100% FcC_{11}SAu SAM. The shaded region indicates data acquired below the cmc in water (8 mM). A surface concentration of ~3.6 x 10^{-10} mole·cm^{-2} corresponds to an effective layer thickness of 1 nm. **(B)** A plot of Q_{Fc^+} versus the [SN_{12}S] for a 100 % FcC_{11}SAu SAM. The error bars represent the standard deviation for at least 4 different experiments. 155

Figure 4.12 CV scans of FcC_{11}SAu and FcC_{11}S/HOC_{11}SAu SAMs in perchlorate solution (scan rate 10 mV·s^{-1}). 160

Figure 4.13 **(A)** A plot of $\Gamma_{\text{dodecyl sulfate}}$ vs. the mole fraction of ferrocene in FcC_{11}SAu/HOC_{11}SAu SAMs: 100 mM (●) and 2 mM (○) SN_{12}S. The solid (100 mM) and dotted (2 mM) lines are guides for the eye. The mole fraction of ferrocene in the mixed SAMs was determined from the anodic voltammetric scans in perchlorate solution. **(B)** A plot of Q_{Fc^+} vs. the mole fraction of ferrocene in mixed SAMs: 100 mM (●) and 2 mM (○) SN_{12}S. The error bars represent the standard deviation for at least 4 different experiments. 161

Figure 5.1 CVs of the FcC_{11}SAu SAM in different sodium *n*-alkyl sulfate solutions. The potential was scanned between –0.10 V to +0.75 V at a constant rate of 10 mV·s^{-1} for all electrolyte solutions. The electrolyte concentration was 100 mM for all the SN_cS solutions, except for SN_{14}S where the concentration was 25 mM. 180

Figure 5.2 Plots of the **(A)** midpoint half-wave potential ($E_{1/2}$) and **(B)** the anodic peak potentials (E_a) of peaks I (■), II (▲), and III (●) for the FcC_{11}SAu SAM as function of the increasing *n*-alkyl chain (N_c) length of the anionic sulfate (N_cS^-). The solid red line is a linear regression of the plotted data having a slope of –0.0123 V per methylene unit. The error bars represent the standard deviation of at least four different experiments. 183

Figure 5.3 **(A)** Plot of the electrogenerated ferrocenium concentration (Γ_{Fc^+}) for the FcC_{11}SAu SAM as a function of the increasing *n*-alkyl chain (N_c) length of the sulfate anions (N_cS^-). **(B)** Plot of the charge density (Q_{Fc^+}) vs. the solution concentration of SN_8S (○), SN_{10}S (□), and SN_{12}S (Δ). The error bars represent the standard deviation of at least four different experiments. 186

Figure 5.4 Current (top panel) vs. time profile obtained during potential cycling between –0.10 V and +0.75 V of the $FcC_{11}SAu$ SAM at a rate of 10 mV s^{-1} and the corresponding SPR profiles (bottom panel) in **(A)** 0.10 M SN_{10}S, **(B)** 0.10 M SN_8S and **(C)** 0.03 M SN_6S solutions. 189

Figure 5.5 Plot of maximum $\Delta\Theta_m$ for the oxidation of the $FcC_{11}SAu$ SAM vs. the *n*-alkyl chain (N_c) length of the investigated anionic sulfates (N_cS^-) below the cmc (●), at the (▲) and above the cmc (■). The error bars represent the standard deviation of at least four different experiments. 190

Figure 5.6 Plot of the surface coverage (Γ_{SPR}) of N_8S^-, $N_{10}S^-$ and $N_{12}S^-$; where □ < cmc, ■ = cmc, and ■ > cmc for all investigated surfactants. The error bars represent the standard deviation of at least four different experiments. 193

THESIS OVERVIEW AND RESEARCH OBJECTIVES

The first chapter provides a general introduction to self-assembled monolayers of alkanethiolates on metal surfaces. In the same chapter, an overview of the electrochemical techniques, surface plasmon resonance spectroscopy, and microcantilever actuation methods used to carry out the research presented in the thesis is provided. The introduction of each subsequent chapter specifically addresses the topics covered in that part of the dissertation.

The electrochemical actuation of gold-coated mircocantilevers functionalized with a model redox-active ferrocenylundecanethiolate monolayer is investigated in Chapter 2. The results presented demonstrate that the redox transformation of the ferrocene moieties in a *monomolecular* organic film can generate a surface stress change of sufficient magnitude to deflect a micron-size lever. The molecular origin of the electrogenerated surface stress change is discussed.

Chapter 3 investigates the effects of the ferrocenylalkylthiolate molecular structure and the nature of the electrolyte anion on the microcantilever bending response. It is shown here that these two chemical variables have an important effect on the magnitude of the measured surface stress.

Chapters 4 and 5 describe the potential-induced adsorption/desorption of a series of amphiphilic *n*-alkyl sulfates to the surface-confined ferrocenylalkanethiolate. *In-situ*

surface plasmon resonance spectroscopy is used to investigate the surface aggregation of the anionic surfactants at the redox monolayer/liquid interface.

Finally, Chapter 6 provides the general conclusions drawn from the work presented in the Thesis. The significant contributions made to the original knowledge are noted and suggestions for future work are proposed.

Chapter 1

General Introduction

Nanostructured materials are those having structural components where at least one dimension is on the order of 1 to 100 nanometers. The field of engineered nanostructured surfaces has undergone tremendous growth over the last decade during which a significant body of the research has focused on self-assembled monolayers (SAMs). SAMs are *monomolecular* thick films formed by the spontaneous adsorption of alkanethiolates at noble metal surfaces. The intrinsic chemical stability of SAMs, particularly those formed by ω-alkanethiolates on gold, makes it possible to fabricate well-defined organic interfaces with significant control over the material properties. In fact, tailored SAM surfaces have served as model systems for studying many interfacial phenomena, such as wettability, friction, adhesion, and charge-transfer processes, that occur in natural heterogeneous materials. In these systems, a simple surface tether, self-assembling hydrocarbons, and a small functional group (i.e., $-CH_3$, –COOH, –OH, –F) are often adequate to provide the desired surface chemistry. More recently, increasing attention has been placed on the development of SAMs that can respond to an external stimulus in a specific manner, thereby enabling dynamic control over macroscopic phenomena. The external triggers that can be used to switch the surface properties include changes in temperature, light, and chemical or electrochemical energy. These characteristic surfaces, or so-called "switching surfaces", are of growing interest in areas as diverse as cell culture, microfluidics, organic electronics, and coatings.

The present work focuses on electroactive SAMs featuring redox-active molecules which can be converted between discrete states with the introduction of an electric field. Two distinct advantages of electrochemically switchable systems include the ability to address the entire sample rapidly by an electrochemical perturbation and the ability to precisely control the redox state of "individual" molecules by the magnitude of the potential applied. The original motivation for immobilizing electroactive molecules onto metal surfaces was to investigate interfacial electron transfer phenomena.[1] The robust nature of SAMs chemisorbed to metal surfaces allows them to retain their structural integrity when the electrode potential is kept within a certain potential window, making electrochemical measurements possible, particularly in aqueous electrolytes. The monolayer is also generally impermeable toward both solvent and electrolyte ions since the hydrocarbon SAM spacer acts as a barrier to prevent free diffusion to the underlying electrode. Moreover, anchoring the redox-active moiety to the electrode has the added advantage that pinholes and defects do not affect the charge-transfer rate as much as they do in blocking experiments where the electroactive species is found freely diffusing in the solution. Furthermore, the surface concentration of the reactant is easily measured and mass transport is not a rate-limiting factor. An excellent review by Finklea covers early experiments and theoretical developments using SAM-modified electrodes to study the kinetics and thermodynamics of charge-transfer across thin organic films.[1]

Electrochemistry not only provides important information about the charge-transfer process occurring at the interface but is also an attractive means of dynamically controlling the interfacial properties. In fact, several groups have developed strategies to effect macroscopic phenomena using redox transformations of SAMs. For example, Willner et al. reported the redox-controlled bending over of viologen terminated

monolayers on gold surfaces.[2] In their study, the monolayers were loosely packed (~4.2 $\times 10^{-11}$ moles cm^{-2}) to ensure sufficient steric space for conformational transitions of the redox-active units based on the nature of the applied potential. The different configurations of the thiol chains were reflected in the hydrophobic/hydrophilic properties of the surface. Various electroactive SAMs have also been used to modulate biomolecular activity, protein immobilisation, and cell adhesion and migration at the liquid-solid interface.[3-12] For instance, Mrkisch and coworkers[3-7] have demonstrated the site-selective generation of bioactive surfaces based on the hydroquinone-quinone redox couple.[3-7] The electroactive monolayers were able to directly switch peptide ligand activities on and off, and subsequently influence the behaviour of attached cells. Surface-tethered ferrocenes have been used for years to probe the electrochemical properties of interfaces and have only recently been explored for switching interfacial properties. A notable example is the potential-dependent wetting changes caused by the oxidation of surface-confined ferrocenes to ferroceniums.[13-15] Other examples of phenomena that can be electrochemically driven via the oxidation of surface-bound ferrocenes include changes in the orientation of thermotropic liquid crystals[16] and the serial deposition of charged nanoparticles[17].

Ferrocene-terminated monolayers, which are an integral part of this dissertation, are probably the most studied electroactive SAMs. This is in part due to the fact they are synthetically accessible, which readily permits the construction of organic surfaces whose composition, structure, and properties can be varied in a rational manner. Moreover, the ferrocene/ferrocenium couple exhibits straightforward electrochemistry, where under appropriate experimental conditions, the redox-active couple undergoes a reversible one-

electron oxidation/reduction reaction. The redox reaction can be expressed as an (1) electron transfer reaction

$$Fc^0 \rightleftharpoons Fc^+ + 1e^- \quad (1.1)$$

and (2) a charge compensating ion-pair formation

$$Fc^+ + X^- \rightleftharpoons Fc^+X^- \quad (1.2).$$

It should be noted that the ion-pairing event is not ubiquitous. Ion-pairing interactions between the redox-generated ferrocenium species and counter ions are not simply driven by pure electrostatics. Certain anions pair more effectively than others with the ferrocenium.[18-26] The consistent trend observed is that more "hydrophobic" anions, such as PF_6^-, ClO_4^-, and BF_4^-, ion pair more effectively than "hydrophilic" anions, such as NO_3^- and F^-.[18,20,22,25-27] This is attributed to the ability of the counter ion to stabilize the preferred microenvironment of the hydrophobic ferrocene/ferrocenium couple.[22,28-30] The ion-pairing strength with the terminal ferrocenium is also known to effect different structural changes in the oxidized monolayer (with respect to the reduced state).[26,31] The research presented herein exploits the anion pairing interactions and monolayer structural changes which accompany the oxidation of ferrocene to ferrocenium for the assembly of anionic surfactants at the liquid/SAM interface and for micromechanical actuation. The sections that follow will outline the relevant SAM, electrochemistry, surface plasmon resonance spectroscopy and microcantilever concepts.

1.1 Self-Assembled Monolayers (SAMs)

SAMs are monomolecular assemblies that are formed by the spontaneous adsorption of organic constituents onto the surface of a solid. The self-assembly process

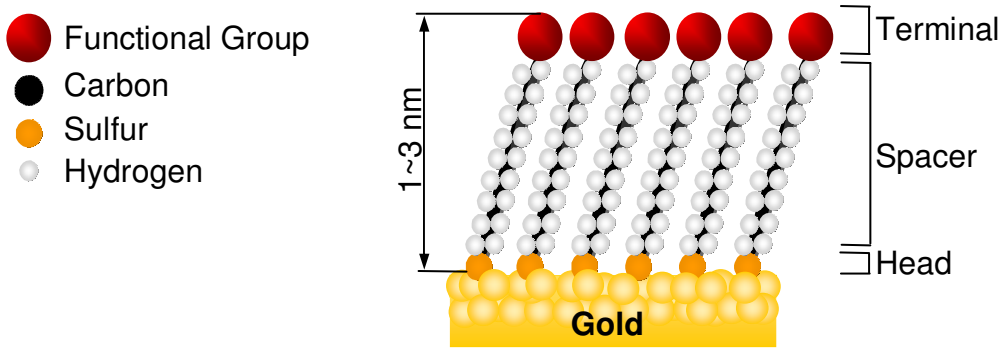

Figure 1.1 Schematic illustration of a self-assembled monolayer (SAMs) on gold.

is predominantly driven by molecule-substrate interactions and intermolecular forces. The concept of SAM formation was introduced as early as 1946 by Zisman and coworkers, who reported on the preparation of a monomolecular layer by the adsorption of a surfactant to a platinum substrate.[32] Many SAM systems have since been identified, including organosilanes on glass and silicon oxide,[33] acid-functionalized alkanes on metal oxides,[33] and organosulfurs on noble metals[33-35]. All components that comprise the SAM play an integral role in determining its propensity to form, molecular packing density, and functional reactivity. The self-organizing molecules have a similar structure (Figure 1.1): (i) chemical functionality or "head-group" that has a specific affinity for the solid surface, (ii) a spacer group that defines the monolayer thickness and molecular organization, and (iii) a terminal group that characterizes the monolayer functionality. The SAM packing density and intermolecular separation depends on the density or crystallography of the surface binding sites, as well as the relative molecular areas of the spacer and end groups.

The spacer and end groups promote molecular order and orientation through favourable dispersion interactions (i.e., van der Waals, electrostatic, hydrogen bonding). The terminal or end group dictates the interfacial properties, such as hydrophobicity/ hydrophilicity and chemical reactivity. By incorporating the appropriate end and spacer groups, it is possible to generate well-defined organic surfaces that present a wide range of functionalities (i.e., hydrophobic/hydrophilic, charged, electroactive, biologically active).

To date, by far the most studied SAMs are derived from the chemisorption of alkanethiols (RSH) or alkyldisulfides (RSSR) to gold, silver, copper, palladium, platinum, or mercury surfaces.[34] Of the noble metals, gold remains the most extensively employed substrate for film formation, which is evidenced by a number of comprehensive literature reviews.[33-38] The ability of thiols to spontaneously chemisorb on gold to form SAMs of well-defined thickness and packing characteristics was first demonstrated in 1983 by Nuzzo and Allara.[39] Since then, these films have become the most studied monolayers worldwide. There are several reasons for the popularity of thin film or colloidal gold substrates. The most significant characteristic is that thiols bind to gold with high affinity forming a Au-S bond of bond strength of ~40–50 kcal·mol^{-1}.[10] RSAu films can endure strong acidic or basic conditions, rendering them ideal surfaces that can be chemically modified following SAM formation. Gold is relatively inert and it is not readily contaminated by the spontaneous formation of an oxide layer, thereby facilitating the manipulation of samples under atmospheric conditions.[36] Thin films of gold can be readily prepared by physical vapor deposition, sputtering or electrodeposition, and single crystals are commercially available. These substrates are commonly used for a number of existing optical spectroscopies and analytical techniques, including surface plasmon

resonance (SPR) spectroscopy, reflection absorption infrared spectroscopy (RAIRS), ellipsometry, quartz crystal microbalance (QCM), scanning probe microscopy (SPM) and electrochemistry.

Planar gold substrates prepared by thermal evaporation predominantly display the lowest surface energy (111) face and are the most widely used. Chemisorption of RSHs or RSSRs on clean Au(111) give indistinguishable monolayers,[40] and the spontaneous adsorption of these organosulfur compounds from either the gas or solution phases onto a gold surface results in film formation. In both cases, a subtle interplay of the energetics of the gold-sulfur bond and non-covalent lateral interactions among the alkyl chains determines the kinetics and thermodynamics of SAM formation. Although still being investigated, the proposed reaction is an oxidative addition of the S-H or S-S bond to gold producing a surface gold thiolate species:[33]

$$\begin{array}{l} R-SH+Au_n^0 \xrightarrow{-H_2?\ -H_2O?\ -H_2O_2?} R-S^{\delta^-}Au_n^{\delta^+}\cdot Au_{n-1}^0 \\ RS-SR+Au_n^0 \end{array} \qquad (1.3).$$

While there is no direct evidence for the proposed reactions 1.3, the absence of S-H (~2600 cm^{-1}) and S-S (~520 cm^{-1}) stretching vibrations in both the infrared[41-43] and Raman[44,45] spectra after SAM formation, as well as a 20 cm^{-1} shift to lower frequency observed for the *gauche* and *trans* C-S stretching[44,45] bands, suggests the cleavage of the S-H and S-S bonds. Moreover, X-ray photoelectron spectroscopy (XPS) data indicates that the sulfur is in a reduced state, with a charge per S of ca. –0.2e, and the gold is partially oxidized so that the S-Au bond has a largely covalent character.[46] The fate of the hydrogen atom of the S-H group however is still debated in the literature.[47-50] In vacuum it seems probable that the adsorption leads to the reductive elimination of H_2

from the Au(111), since the reaction proceeds in the complete absence of oxygen. In solution however, the thiol hydrogen is not necessarily lost in the form of H_2, but might also experience an oxidative conversion to water.

The kinetics of *n*-alkanethiolate monolayer film formation from the gas phase is a relatively well-understood phenomenon and has been reviewed in detail by Schreiber et al.[38] However, the most common protocol for preparing RSAu SAMs involves the immersion of a clean gold substrate into a dilute thiol solution (~1 mM). This is the preferred method of film preparation largely due to its cost effectiveness, convenience and flexibility (i.e., not all thiols are volatile). While the involvement of the solvent molecules complicates the kinetics of film formation, the alkylthiol assembly process can be *qualitatively* approximated by a Langmuir adsorption model which assumes that the rate of deposition is proportional to the available free space.[34,38,51] This was initially supported by an investigation by Bain and coworkers of the ellipsometric thicknesses and contact angles of SAMs removed at different times from the incubation solution.[52-55] Their study revealed that at least 2 time scales are involved in the mechanism of film formation.[52-55] The first step involves the formation of the S-Au bond, where dense coverages of adsorbate (~80–90%) are observed on the order of milliseconds to minutes. Next, a slow reorganization process, occurring on the order of hours, proceeds until the optimal monolayer configuration is obtained. This process has been described as a surface crystallization, where the alkyl chains reorganize with respect to each other in order to minimize the free energy of the system. The final result is a densely packed, well-ordered, two-dimensional nanostructured assembly. Numerous studies on the kinetics of SAM film formation, including second-harmonic generation (SHG),[56,57] XPS,[57] *in-situ* SPR,[58,59] *in-situ* QCM,[60-62] atomic force microscopy (AFM),[63] scanning

tunneling microscopy (STM),[64] and near edge x-ray absorption fine structure (NEXAFS),[65] have confirmed a multi-step process. It should also be underlined that a number of experimental parameters have been found to affect both the rate of formation and the resulting structure of the SAM. These include solvent,[52,59,61,66-68] temperature,[69,70] immersion time,[52,71] as well as the thiol adsorbate purity, structure, and solution concentration[52]. However, most experimental conditions for the preparation of SAMs reproducibly yield organic interfaces with the desired functional behavior.

The structure of the alkylthiolate-gold adlayer has been elucidated using various techniques, including spectroscopy, diffraction, and microscopy.[72-80] Among these investigations, STM have been integral in extending the current understanding of both the SAM structural organization and assembly process since this technique provides a visual picture at the atomic and molecular level.[35,81-83] Figure 1.2A presents an STM topograph illustrating the well-known morphology of a typical *n*-alkanethiolate SAM on Au(111).[83] A schematic representation of the geometric arrangement of the sulfur headgroups on the Au surface is given in Figure 1.2B. The surface structure is generally accepted to be based on a $(\sqrt{3}\times\sqrt{3})R30°$ (R = rotated) hexagonal lattice, where the sulfur groups are positioned in the 3-fold hollow sites formed by the gold atoms.[35,47] This hollow site state has been established by STM studies and is consistent with the most stable binding site.[35,47] For well-ordered, densely packed saturated *n*-alkanethiolates on gold, the maximum surface density is 7.5×10^{-10} moles·cm^{-2} (4.5 molecules·nm^{-2}).[73,84] This corresponds to an average spacing of ~5 Å between adjacent sulfur atoms and an area per molecule of 21.6 Å^2.[36-38,64] The chain-chain interactions contribute ~1.5 to 2 kcal·mol^{-1} of

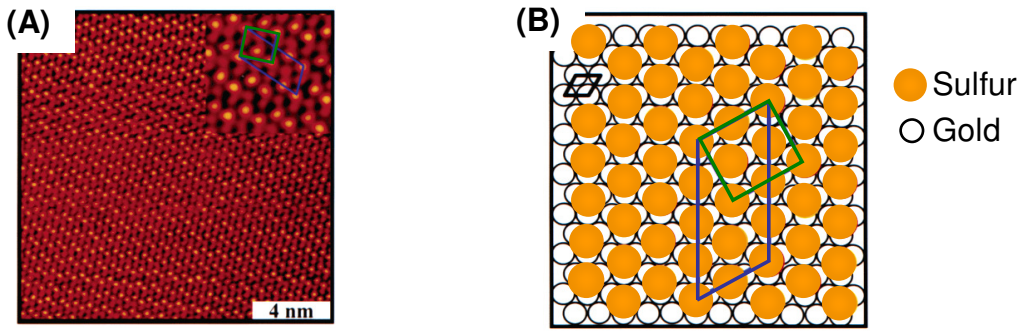

Figure 1.2 Characteristic morphology of a decanethiolate SAM on Au(111). **(A)** STM topograph, 20 nm × 20 nm, taken after the sample was thermally annealed. The primitive rectangular unit cell (green square) and the c(4 × 2) superlattice (blue rectangle) are indicated in the inset. **(B)** Schematic diagram illustrating the lattice structure (blue rectangle) and unit cell (green rectangle) of an alkanethiolate SAM on Au(111). The Au(111) surface structure is depicted by the black hexagonal square. Data is reproduced from reference 83.

stabilization per CH_2 unit to the SAM.[85] In order to maximize lateral van der Waals interactions[86] (and in some cases hydrogen bonds[87-94]), the parallel alkane chains have been shown to tilt ~30º from the surface normal towards their nearest neighbor.[35,36,74,95] This tilt angle is independent of the terminal group provided that its size is not larger than the spacing between the alkane chains, which has been determined to be 4.97 Å[10] by low-energy electron diffraction (LEED).[72] This arrangement yields a secondary level of monolayer organization corresponding to a c(4 × 2) superlattice.[76,96-101] The orientation of the alkyl chains was previously elucidated from data obtained by ellipsometry,[43] infrared (IR) spectroscopy,[42,102] and NEXAFS[103].

For SAMs formed from ω-alkylthiols containing a large terminal group (i.e., ferrocene, viologen, ruthenium complexes), the steric bulk of the functional group hinders the formation of a densely-packed monolayer and introduces disorder in the system. For

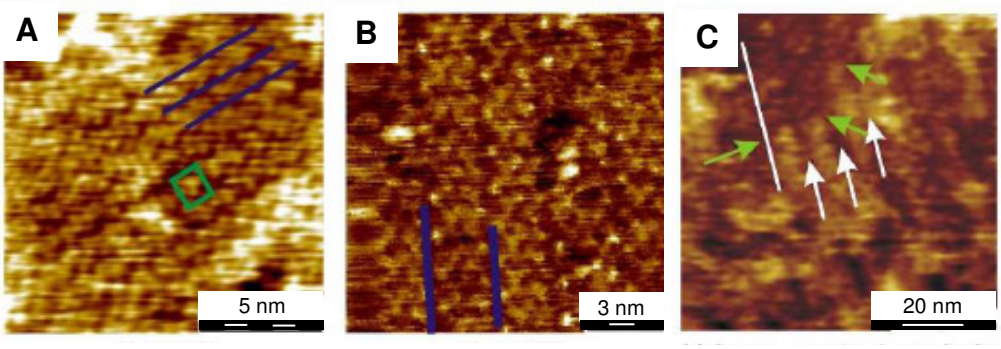

Figure 1.3 STM topographs taken after thermal annealing of the sample. **(A)** $Fc(CH_2)_3SAu$**, (B)** $Fc(CH_2)_5SAu$, and **(C)** $Fc(CH_2)_{11}SAu$ monolayers formed on Au(111). The unit cell is marked in green as shown in **(A).** The blue lines in **(A)** and **(B)** depict the observed characteristic pattern. In **(C)** stripped monolayer features are marked in white, whereas the green arrows represent a change in monolayer height. Data is reproduced from reference 111.

example, the molecular packing density of single-component ferrocenylalkanethiolate monolayers has been found to be 4.5×10^{-10} moles·cm^{-2} (2.5 molecules·nm^{-2}).[21,104-109] This packing density is consistent with the theoretical coverage based on the 0.66 nm spherical diameter of the terminal ferrocene[105] and is only ~0.6 × that found of the methyl terminated analogue[73,84]. Furthermore, when ordered domains of adsorbate do form, the structural arrangement differs from that for SAMs of *n*-alkanethiolates. While there is limited experimental information available pertaining to functionalised alkylthiolates, a recent STM study of a homologous series of mercaptoalkyl-ferrocenes with different alkyl spacer lengths (i.e., $Fc(CH_2)_nSH$ where n = 3, 5, and 11) demonstrated that these have a tendency to form a loose hexagonal lattice structure.[110-112] Representative STM topographs of the $Fc(CH_2)_nSAu$ monolayers are provided in Figure 1.3.[111,112] Contrary to

n-alkanethiolates, the short alkyl spacers (n = 3 or 5) resulted in significantly more ordered surface structures compared to the longer alkyl spacer $Fc(CH_2)_{11}SAu$ SAMs. Again, the spatial hindrance of the bulky ferrocene moiety and the weak interactions between the ferrocenes impede the formation of an ordered SAM (Figure 1.4). The conformation and orientation of the hydrocarbon chains within ω-alkylthiols monolayers have been characterized using surface IR spectroscopy. For the ferrocene-terminated monolayers in question, IR spectroscopic results consistently demonstrate antisymmetric (υ_a), 2924 – 2925 cm^{-1}, and symmetric (υ_s), 2850 – 2854 cm^{-1}, $-CH_2-$ stretching vibrations that more closely resemble that of the bulk disordered or liquid state.[106,113-117] By comparison, crystalline-like hydrocarbon chains exhibit $\upsilon_a(CH_2)$ and $\upsilon_s(CH_2)$ at 2920 cm^{-1} and 2850 cm^{-1}, respectively, whereas the peak positions are shifted to 2928 cm^{-1} (υ_a) and 2856 cm^{-1} (υ_s) in the liquid-like state.[43]

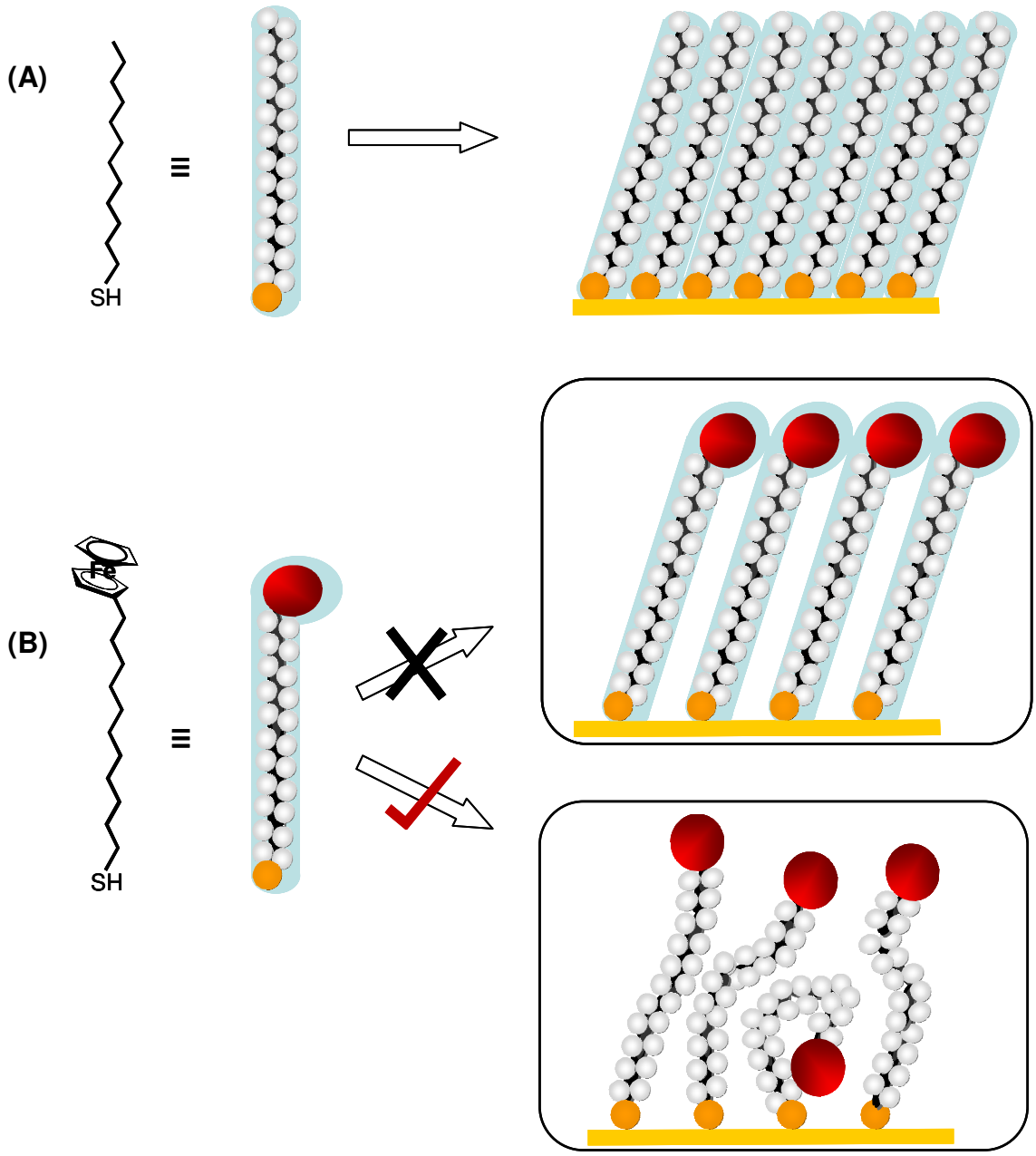

Figure 1.4 Schematic diagrams illustrating the effects of functional groups on the packing density and organization of SAMs. **(A)** Small terminal groups (i.e., $-CH_3$, –OH, –CN) do not distort the secondary organization and have no effect on the sulfur arrangement. **(B)** Larger terminal groups (i.e., ferrocene, viologen, ruthenium complexes) impose steric constraints where the resulting structures are more disordered and less dense than those formed with types of molecules in **(A)**.

1.2 Electrochemical Characteristics of Monolayers

Cyclic voltammetry is a popular electrochemical technique for the mechanistic study of redox systems. In this technique, the electrode potential is scanned by sweeping the voltage between two potentials at a fixed linear rate, and the current at the working electrode is plotted against the voltage. A schematic representation of a typical cyclic voltammogram (CV), with the relevant parameters of peak current (i_a and i_c), peak position (E_a and E_c), and peak area, for a surface-immobilized electroactive species is shown in Figure 1.5A. In this analysis, it is assumed that the electroactive component is not present in solution. Immobilization of the electroactive species at the electrode leads to changes in the shape of the CV when compared to that of the solution–phase reactant since the redox-active material does not have to diffuse to or from the electrode surface.[118] For an ideally responding surface-confined reactant, the peak current i_p, is given by:

$$i_p = \frac{n^2 F^2 \Gamma A \nu}{4RT} = \frac{nFQ\nu}{4RT} \tag{1.4}$$

where n is the number of electrons, F is the Faraday constant, v is the scan rate, R is the gas constant, T is the absolute temperature, A is the electrode area and Γ is the surface coverage or concentration of the redox active moiety (in mol cm^{-2}).[118] Characteristic for a surface-confined redox species, the anodic (oxidation) or cathodic (reduction) peak current (i_a or i_c) is linearly proportional to the scan rate v.[118] Conversely, a diffusible redox couple exhibits a $v^{1/2}$ dependence.[118] The charge Q associated with reduction/oxidation is obtained by integrating the area under either the anodic or cathodic peak after correcting for the charging current. A surface coverage Γ of the electroactive species can readily be obtained from Q by:[118]

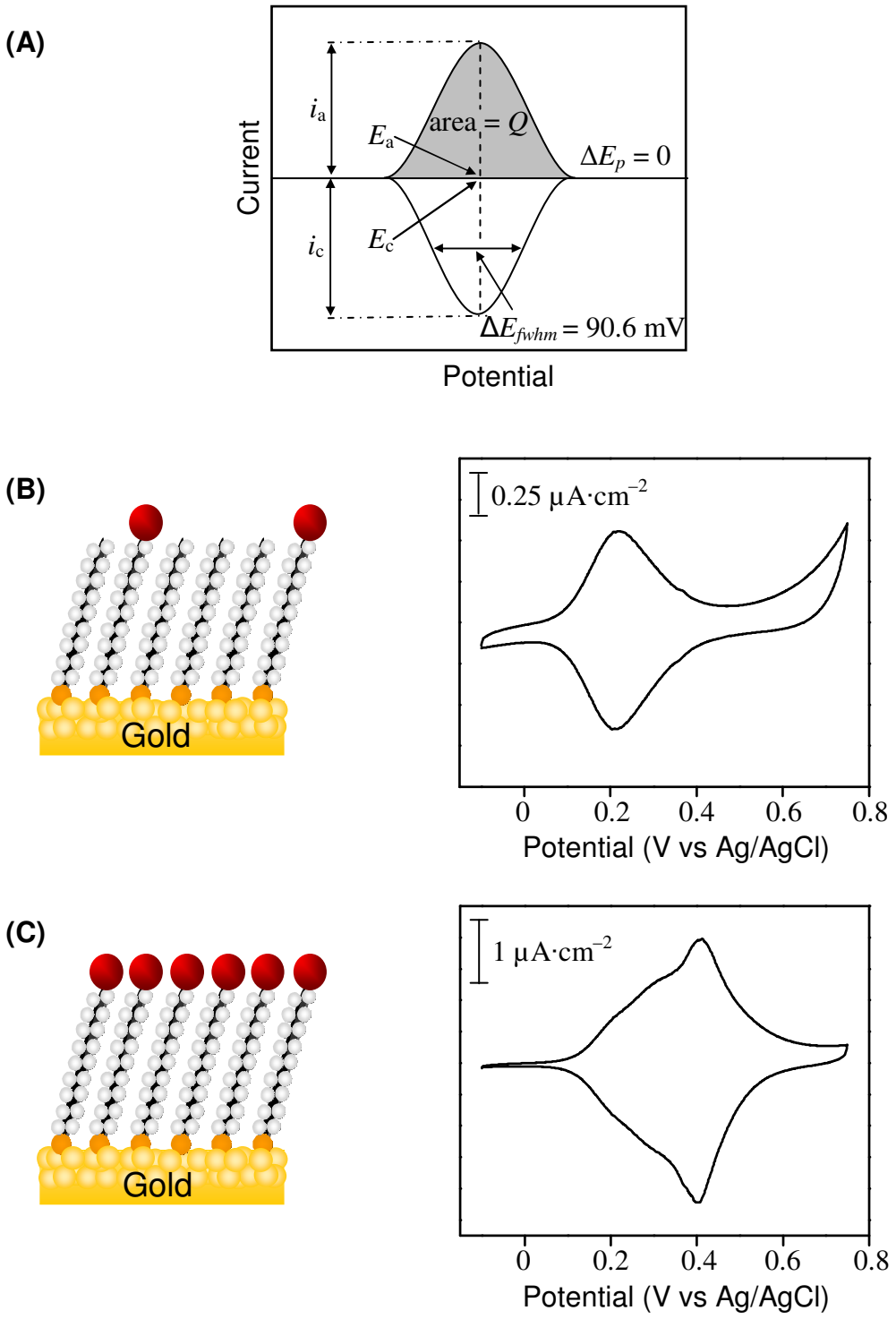

Figure 1.5 **(A)** An idealized reversible cyclic voltammogram (CV) of a surface-tethered redox couple. See text for symbol descriptions. **(B)** CV of a $FcC_{11}S/HOC_{11}SAu$ mixed SAM in perchlorate solution. **(C)** CV scan of a single-component $FcC_{11}SAu$ SAM. CVs in **(B)** and **(C)** were acquired in perchlorate at 10 mV·s^{-1}. The redox centers are represented by ● .

$$\Gamma = \frac{Q}{nFA} \quad (1.5).$$

For an ideal Nerstian reaction, a surface confined species will follow the general relationship:

$$\Delta E_{fwhm} = 3.53RT / nF = 90.6 / n \quad \text{mV at } 25°\text{C} \quad (1.6)$$

where ΔE_{fwhm} is the *full-width at half-maximum* of either the cathodic or anodic wave. The difference between the anodic (E_a) and cathodic (E_c) peak potentials gives the peak splitting (ΔE_p), which should ideally be equal to 0. Nearly ideal voltammetric responses are observed when the ferrocene moieties are sufficiently diluted or spaced apart with an electro-inactive thiol (i.e. *n*-alkanethiols), as illustrated in Figure 1.5B.

In the case where the formal potential ($E^{0'}$) for the surface-confined species is unknown, the average of the main oxidation and reduction peaks potential (half-wave potential, $E_{1/2}$) is used. The $E_{1/2}$ of the main oxidation/reduction peaks indicates the ease of oxidation. In other words, a shift to more negative values is indicative of a more favorable redox process, whereas a positive shift would indicate a less favorable redox reaction requiring more energy to oxidize the surface-bound terminal moiety. $E_{1/2}$ also shifts to more positive values when the redox moiety is buried within the hydrocarbon microenvironment of an alkylthiolate SAM.[24] The direction of the shift is consistent with destabilization of the more highly charged oxidation state.

It is rare that ideal behavior is observed for a redox species tethered to a hydrocarbon SAM, and deviations are readily apparent in the CV (Figure 1.5C). In general, voltammetric peaks that are broader or narrower than theoretically predicted, $E_{1/2}$ values that shift with changes in the surface coverage of the redox species, and peak

currents that do not depend directly on the scan rate, are typically associated with laterally interacting redox moieties.[1] The presence of multiple voltammetric waves, which are often observed for single component ferrocenylalkylthiolate SAMs (Figure 1.5C), are attributable to the existence of electrochemically distinct microenvironments of the redox moiety.[108,109,119-123] Finally, a $\Delta E_p \neq 0$ value may indicate either strong interactions between the redox groups or that switching the redox composition triggers a structural change within the SAM[124] (i.e., adsorbate reorientation or monolayer volume expansion to enable ion-pair formation).

1.3 Surface Plasmon Resonance (SPR) Spectroscopy

Surface plasmon resonance (SPR) spectroscopy is a highly sensitive, label-free optical technique used to observe in real-time molecular events occurring at a metal/dielectric interface. The detection principle relies on the resonant excitation of freely oscillating electrons (plasmons) at the metal/dielectric interface by *p*-polarized light, resulting in an associated surface-bound evanescent electromagnetic wave of optical frequency (Figure 1.6). The conditions required for resonant excitation are extremely sensitive to changes in the refractive index of the medium directly adjacent to the metal. This property makes the technique ideal for accurately monitoring molecular processes occurring at the interface, such as the adsorption or desorption of molecules and changes in molecular orientation. These changes are typically monitored as variations in the reflected light intensity from the metal/dielectric/analyte interface. In turn, a quantitative description of the molecular layer properties is investigated through Fresnel multilayer analysis. The phenomenon of SPR has been reviewed extensively in the literature[125-129] and will only be described briefly here.

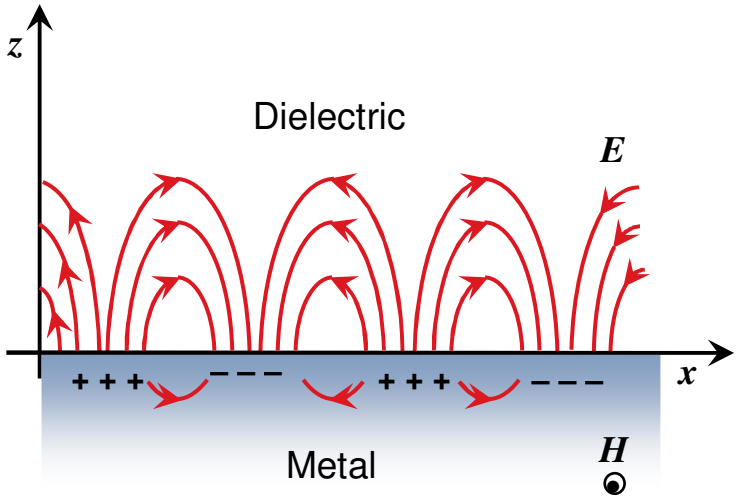

Figure 1.6 Schematic representation of the electromagnetic field associated with a surface plasmon propagating along a metal/dielectric interface.

SPR is a quantum phenomenon; however, it can readily be described with classical Maxwell's wave equations for electromagnetic modes. In the classical model, a semi-infinite media with frequency-dependent dielectric functions $\varepsilon_i(\omega)$ separated by a planar interface at $z = 0$ is considered. Choosing the x-axis as the direction of propagation, there exists a set of Maxwell's solutions called "surface waves" at the boundary between the two media which take the form

$$\boldsymbol{E}_i = (E_{xi}, 0, E_{zi}) \exp^{i(k_{xi}x + k_{zi}z - \omega t)} \tag{1.7}$$

$$\boldsymbol{H}_i = (0, H_{yi}, 0) \exp^{i(k_{xi}x + k_{zi}z - \omega t)} \tag{1.8}$$

where E and H are the electric and magnetic fields, respectively, k_i represents the magnitude of a wave vector, and the index i denotes the media: $i = m$ for the metal and $i =$

d for the dielectric medium. While any linearly polarized radiation can be represented as a superposition of *p*- and *s*-polarization, it is only *p*-polarization modes (transversal magnetic TM) that result in a charge density oscillation in the *z*-direction at an interface. A schematic representation of the electromagnetic field associated with a surface plasmon propagating along a metal-dielectric interface is shown in Figure 1.6.

The interfacial boundary conditions stipulate that the tangential components of the *E* and *H* fields should be continuous at the interface, which leads to a nontrivial solution:

$$\frac{k_{z1}}{k_{z2}} = -\frac{\varepsilon_1}{\varepsilon_2} \tag{1.9}.$$

Equation (1.9) indicates that surface plasmon modes can only be excited at interfaces between two media with dielectric constants of opposite sign, which is the case when one material is a dielectric ($\varepsilon_d > 0$) and the second material is a metal ($\varepsilon_m < 0$). From the boundary conditions also follows the continuity of the 2-dimensional wave vector, i.e. $k_{xm} = k_{xd} = k_x$. For any electromagnetic mode, the wave vector is given by

$$k_{zi} = \sqrt{\varepsilon_i (\omega/c)^2 - k_x^2} \quad \text{or} \quad k_x^2 + k_{zi}^2 = \varepsilon_i \cdot (\omega/c)^2 \tag{1.10}.$$

Equations (1.9) and (1.10) lead to the dispersion relation (i.e., the energy momentum relation) of surface plasmons at a metal/dielectric interface:

$$k_x = k_{sp} = \frac{\omega}{c}\sqrt{\frac{\varepsilon_m \cdot \varepsilon_d}{(\varepsilon_m + \varepsilon_d)}} \tag{1.11}.$$

It is important to note that both the dielectric functions and wave vectors are taken as complex, i.e, $k_x = k_x^{'} + ik_x^{''}$. The real part of k_x describes the finite surface plasmon propagation, while the imaginary part corresponds to the dampening of the surface plasmon in the metal and dielectric media. Since the refractive index of a material is

defined by the square root of its dielectric constant ($n = \sqrt{\varepsilon}$), the surface plasmon resonance can also be said to depend on *n*.

The coupling and subsequent excitation of the surface plasmons require that the incident photon must be matched in both angular frequency and momentum with that of the surface plasmon. This requirement is met when the wave vector for the photon and the surface plasmon are equal in both magnitude and direction for the same frequency of the waves. The momentum of a free photon propagating in a dielectric medium is given by

$$k_{ph} = \frac{\omega}{c_d}\sqrt{\varepsilon_d} \tag{1.12}$$

where the dispersion of the photons is described by the light line, $\omega = c_d k$. Since the wave vector of the plasmon mode is bound to the planar metal/dielectric interface, it is only the wave vector in the parallel direction that is the relevant parameter:

$$k_{ph}^{x} = \frac{\omega}{c_d}\sin\Theta\sqrt{\varepsilon_d} \tag{1.13}.$$

The wave vector of the light k_{ph}^{x} can be tuned to equate to the surface plasmon mode k_{sp} by varying the angle of incidence, Θ. However, by comparing equations (1.11) and (1.13), it is evident that there is no angle of incidence on the metal surface for which the horizontal component of light matches the surface plasmon for any value of ω and Θ. In other words, the momentum of the photon k_{ph}^{x} propagating in a dielectric medium is always smaller than the momentum of a surface plasmon mode k_{sp} propagating along an interface between that same medium and the metal.

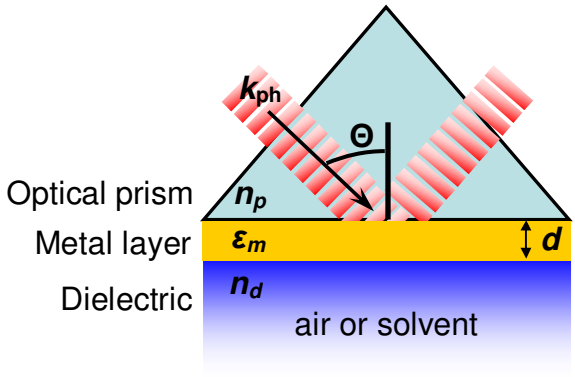

Figure 1.7 Illustration of the excitation of surface plasmons in the ATR-Krestchmann geometry.

Nevertheless, there are mechanisms that permit the external radiation to be coupled to surface plasmons, such as attenuated total reflection (ATR).[130,131] There are two configurations of the ATR method: the Kretschmann geometry[130] and the Otto geometry[131]. In the Kretschmann geometry, a high refractive index prism with refractive index, n_p, is interfaced with a metal-dielectric waveguide consisting of a thin metal film of permittivity, ε_m, and thickness, d_m, and a semi-infinite dielectric with a refractive index, n_d (where $n_d < n_p$), Figure 1.7. The effect of the more optically dense medium is to modify the wave vector of the incident light by increasing the momentum of the photons. The new dispersion relation for the light yields

$$k_{ph} = \left(\frac{\omega}{c_d}\right)\sin\Theta\sqrt{\varepsilon_p} \qquad (1.14).$$

From the above equation k_{ph} can now be modified simply by increasing the refractive index of the prism.

The Kretschmann configuration[131,132] is one of many waveguided optical techniques that relies on the well-known phenomenon of the total internal reflection (TIR) of light at a boundary between two media. For an incident light beam propagating through the optically dense prism (n_p), Snell's law[133] stipulates that at an angle of incidence (Θ_i) exceeding a critical value (Θ_c) all the light will be totally internally reflected. This can readily be observed by monitoring the reflected light intensity as function of Θ_i (at a constant wavelength of the incident light). As Θ_i approaches Θ_c, more and more energy from the incident light appears in the reflected beam and the reflectivity (i.e., the ratio between the reflected light and incoming intensity) reaches unity. Although the incident light is totally internally reflected, a component of this light (the evanescent wave or field) penetrates into the adjacent lower refractive index medium. The amplitude of this evanescent field wave decreases exponentially with increasing distance from the interface, decaying over a distance of about one light wavelength from the surface. When the surface opposite of the high refractive index substrate is coated with a thin metal film of an appropriate thickness (d_m) with permittivity (ε_m), the electric field of the evanescent wave can overlap with that of the surface plasmon and energy transfer between the two waves is possible. The angle at which this phenomenon occurs is referred to as the surface plasmon resonance angle, Θ_{spr}.

When the reflectivity is monitored as a function of Θ_i, there exists a minimum in the reflectance that corresponds to the resonant coupling of photon energy by the surface plasmon (Θ_{spr}). A schematic representation of an SPR curve is shown in Figure 1.8, based on the known parameters ε_p, ε_d, and for $\varepsilon_m = \varepsilon_m^{'} + i\varepsilon_m^{''}$ and the metal thickness (d) (black curve). As previously mentioned, the resonant conditions are extremely sensitive

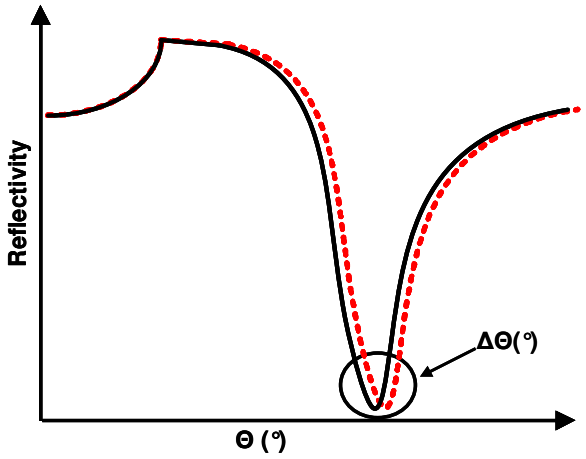

Figure 1.8 Illustration of typical SPR curves.

to the dielectric properties of the region within ~200 nm directly adjacent to the metal interface and any changes (i.e., molecular adsorption or surface reactions) will result in a change in Θ_{spr} (red curve). Notably, layer thickness changes of 1–2 Å or nanograms of adsorbed mass are readily measured. It should also be noted that surface-bound and bulk material are distinguished in the SPR profile which allows their acquisition in turbid or opaque samples. The observed reflectivity vs. Θ profiles are generally analyzed using a multilayer Fresnel analysis to obtain information about the optical and structural properties at the interface. This involves numerical calculations where it is assumed that each phase is homogenous and parallel. Furthermore, the analysis requires knowledge of the wavelength dependent complex index of refraction of each phase. Experimentally, silver, gold, copper, and aluminum have been shown to exhibit free electronic behaviour and thus are suitable metal choices for SPR. However, given the inherent stability of gold

to oxidation and because silver provides a sharp peak these metals are used most often. The metal surface may also act as a surface for chemisorption, physisorption or electrochemistry. It is the combination of the ability to coat a metal surface (particularly gold) with organic films tailored to have a specific chemical functionality and the fundamental sensitivity of plasmons which has given rise to the wide range of SPR-based applications reported in the literature.

1.4 Microcantilever Actuators

The nanometer scale mechanical bending of surface-functionalized microcantilevers provides an ideal platform for sensing and actuating technologies.[134-137] The growth in microcantilever-based technologies parallels advances made in micromachining methodologies. Cantilevers are generally fabricated from silicon or silicon nitride by top-down micromachining methods and can be produced efficiently and affordably. The resulting cantilever is a free-standing rectangular- or V-shaped structure that is supported only at one end (Figure 1.9). Although the cantilevers have micrometer dimensions, their nanometer-scale deflection or vertical bending response lends itself to their reference as nanomechanical transducers. A compelling feature of microcantilevers is that they can be operated in several modes within vacuum, air, or liquid. In general, when a force is applied to the end of a free standing cantilever a vertical bending will result. As described by Hooke's Law ($F = -k_{spring}\Delta z$), the bending or deflection (Δz) of the cantilever is directly proportional to the applied force F, and the cantilever spring constant k_{spring} is the proportionality factor. The cantilever spring constant dictates the

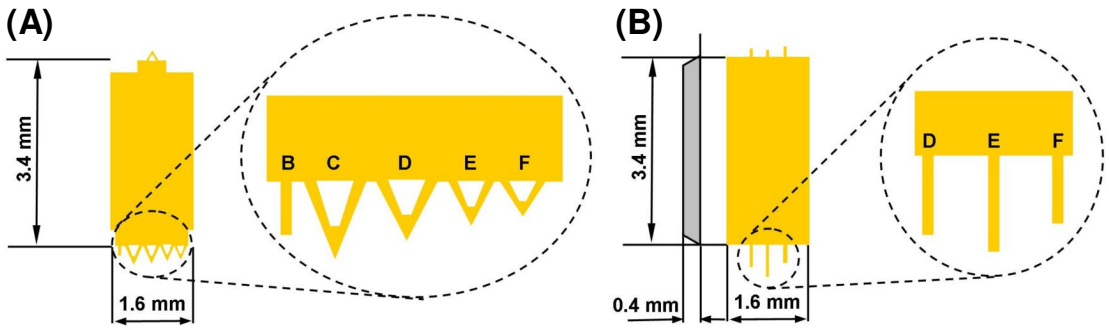

Figure 1.9 Schematic representations of the rectangular- and V-shaped microcantilevers manufactured by **(A)** Veeco Metrology Inc. and **(B)** MikroMasch USA.

flexibility and sensitivity of the cantilever and is defined by its dimensions and material constants. For a rectangular-shaped cantilever, k_{spring}, is given by[138]

$$k_{spring} = \frac{Ewt^3}{4l^3} \tag{1.15}$$

where E is the elasticity or Young's Modulus, w is the cantilever width, t its thickness, and l its length. If the cantilever is set to oscillate, its resonance frequency f_{res} is related to k_{spring} by[135]

$$f_{res} = \frac{1}{2\pi}\sqrt{\frac{k_{spring}}{m^*}} \tag{1.16}$$

where m^* an effective mass which takes into account the cantilever geometry and mass distribution along the cantilever.

1.4.1 Cantilever Modes of Operation

Illustrated in Figure 1.10 are the three basic modes of operation for microcantilever based systems: dynamic (resonant) mode, heat (bimetallic) mode, and static (surface stress) mode.[134-137] In all cases, only one face of the microcantilever is rendered environmentally or stimuli responsive. Conversely, each mode differs from the other in terms of the principle of transduction, functionalisation, and detection mechanisms. In this Chapter, a brief introduction to the major modes of operation will be provided, while highlighting in more detail the static or surface stress mode used in the studies presented in this thesis.

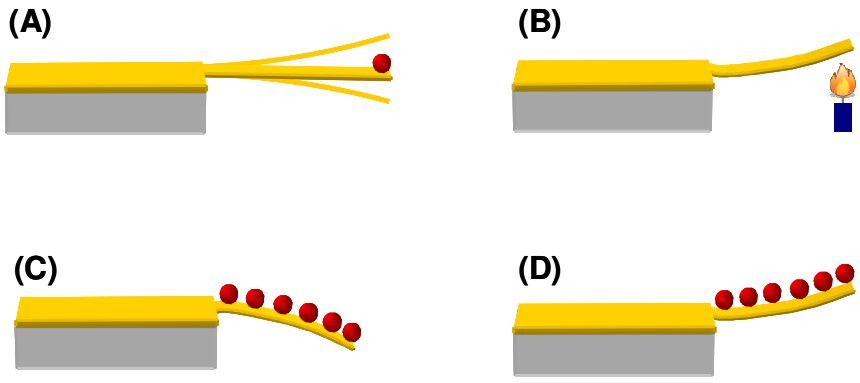

Figure 1.10 Cantilever modes of operation: **(A)** Dynamic mode detects mass changes on the cantilever via changes in the resonance frequency; **(B)** Bimetallic mode detects temperature changes by a static bending due to the different thermal expansion coefficients of the metal layer and silicon cantilever; and **(C,D)** Surface stress mode, where asymmetric physical or chemical events occurring at the cantilever's functionalized surface leads to an overall cantilever bending. For example, adsorption on the top surface can either cause a compressive stress **(C)**, resulting in a bending of the cantilever downwards, or a tensile stress **(D)**, which results in a bending of the cantilever upwards.

In the dynamic or resonance mode (Figure 1.10A), cantilevers are excited close to their resonance frequency, which is typically on the order of hundreds of Hz to a few GHz. The resonance frequency changes when an additional mass is adsorbed to the oscillating cantilever. For a rectangular cantilever, the change in mass (Δm) can be calculated from the frequency shift using

$$\Delta m = \frac{k_{spring}}{4\pi^2}\left(\frac{1}{f_1^2} - \frac{1}{f_0^2}\right) \tag{1.17}$$

where the resonance frequency before and during the experiment are f_o and f_1, respectively.[139] With optimized cantilever geometries and under ultra-high vacuum, it is possible to measure mass changes down to the single molecule level in the resonant mode.[140] Unfortunately, the detection of molecules in solution is hindered by the inherent dampening of the cantilever oscillation in a liquid environment, which decreases the mass resolution and requires a more sophisticated setup.[136] Recently, Burg and coworkers developed an innovative way to avoid viscous dampening by placing the liquid sample inside a hollow cantilever rather than oscillating the cantilever in a liquid environment.[141] This method eliminates viscous damping while at the same time preserving the mass resolution of the nanomechanical resonator.[141]

In another mode of operation, referred to as the heat or bimetal mode, the cantilever is coated with a metal layer so that differences in the thermal expansitivity of the cantilever and coating (i.e., silicon-gold composite) will influence the cantilever bending as a function of temperature (see Figure 1.10B). Heat changes can result from an external influence (changes in temperature), occur directly on the surface by exothermal reactions (catalysis), or are due to the material properties of a sample attached to the apex of the cantilever (micromechanical calorimetry). In comparison to traditional

calorimetric methods performed on milligram samples, the sensitivity of the cantilever heat mode is orders of magnitudes higher, requiring only nanogram amounts of sample with which sensitivities in the range of nanojoules to femtojoules have been achieved.[142-144]

By far the most commonly employed cantilever mode of operation is known as the static or surface stress mode (Figure 1.10C and D). The basic principle arises from a chemical or physical event occurring on one face of the microcantilever generating a surface stress change that is manifested as a nanometer-scale bending away from the equilibrium position. The transduction mechanism can be monitored in real-time with considerable sensitivity via an optical beam reflected from the free end of the microcantilever. The deflection is directly proportional to the surface stress through a modified form of the Stoney's equation.[145] By definition, a *compressive stress* corresponds to an expansion of the microcantilever, whereas a *tensile stress* corresponds to a contraction.[146-149] In accordance with common sign convention, a compressive stress is generally expressed with a negative value, while a tensile stress is expressed with a positive one.[150]

1.4.2 Cantilever Deflection

The optical beam deflection technique is the most frequently employed approach to monitor cantilever displacements as a result of asymmetrical changes in the surface stress. In this configuration, a laser beam is focused on the apex of the microcantilever and the reflected beam is monitored with a position sensitive detector (PSD). The measurement scheme used to correlate the cantilever deflection, Δz, to the change in signal, ΔS, observed at the PSD is depicted in Figure 1.11. It can be assumed that the

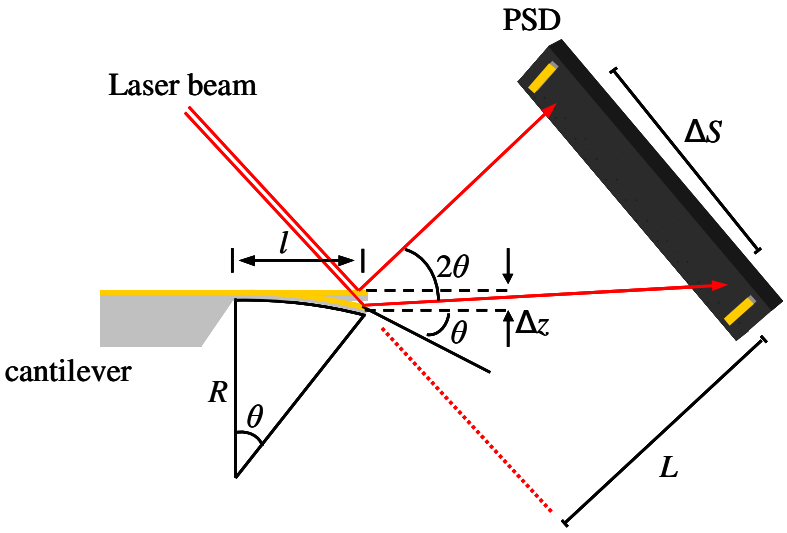

Figure 1.11 Illustration of the beam deflection parameters used to determine the microcantilever bending with nanometer accuracy.

bending angle of the deflected laser beam is equal to twice that of the cantilever bending angle since all the angles are very small. The cantilever deflection Δz is calculated from the microcantilever bending angle θ[147-149]

$$\theta = \frac{\Delta S}{L} \tag{1.18}$$

and the cantilever length l by

$$\Delta z = \frac{\theta}{4} l \tag{1.19}$$

where L is the distance between the PSD and the cantilever and for small deflections $L \approx L \pm \Delta z$, since $L \gg \Delta z$. The combination of equations (1.18) and (1.19) relates the actual microcantilever deflection to the PSD signal:[147-149,151]

$$\Delta z = \frac{l}{4L}\Delta S \qquad (1.20).$$

Equation (1.20) is valid for laser beam deflection measurements carried out in air. If the cantilever is immersed in a liquid, then the reflected laser path is modified according to Snell's law. In order to correct for the change in angle resulting from the reflected laser beam passing through an aqueous electrolyte solution, the following relationship is used:[149]

$$\Delta S = \frac{\Delta S'}{n_{liquid}} \frac{1}{\left(1 - \frac{d}{L} + \frac{d}{n_{liquid} L}\right)} \qquad (1.21)$$

where n_{liquid} is the index of refraction of the solution and d is the distance between the optical window and the cantilever. For the optical beam configuration used herein and using the index of refraction of water ($n_{589\text{nm}}^{20°\text{C}}$=1.33), we obtain:

$$\Delta S = \frac{\Delta S'}{1.33} \qquad (1.22).$$

1.4.3 Quantifying Surface Stress

It is common practice to report surface stress values instead of absolute deflections so that the results of cantilever experiments with different geometries or materials can be directly compared. In many cases, the physically- or chemically-induced deformations of microcantilevers have been assessed with the classic formula derived by Stoney,[145] which simply relates the induced radius of curvature, R (see Figure 1.11), of the microcantilever to the change in surface stress, $\Delta\sigma$:

$$\Delta\sigma = \frac{Et^2}{6R(1-v)} \tag{1.23}$$

where E is Young's modulus, t is the thickness of the cantilever, and v is the Poisson's ratio. However, there has been much debate in the recent literature as to the application of Stoney's equation to *micro*cantilevers.[152-162] This not only arises from an inconsistency between the experimental and modeled systems, but also from large discrepancies in the reported experimental parameters. For example, it was established by Grütter and coworkers[147,149] that a considerable uncertainty is introduced when using Stoney's formula due to the large range of values reported for the Young's modulus of silicon nitride ($E \approx$ 130–385 GPa)[161,163,164]. To compensate, they derived a formula starting with Hooke's law that relates the energy stored in a deflected microcantilever to its spring constant. This calculation eliminates the need to know the elastic modulus and requires only knowledge of the geometry, spring constant, and Poisson's ratio of the microcantilever. The formulas for the differential surface stress derived in their work[147-149] for a rectangular microcantilever

$$\Delta\sigma = \frac{4}{3(1-v)}\frac{l}{Wt}k_{rect}\Delta z \tag{1.24}$$

and for a triangular microcantilever

$$\Delta\sigma = \frac{4}{3(1-v)}\frac{l^2}{\left[Wtl_1 + \frac{tb}{4l}(l-l_1)^2\right]}k_{\Delta}\Delta z \tag{1.25}$$

are used in the work presented herein. The numerical constants in the above formulas account for the microcantilever beam curvature resulting from a uniform surface stress, as opposed to a concentrated load applied to the tip. The rectangular and V-shaped cantilever geometric parameters W, l, l_1, t, and b are illustrated in Figure 1.12 and their

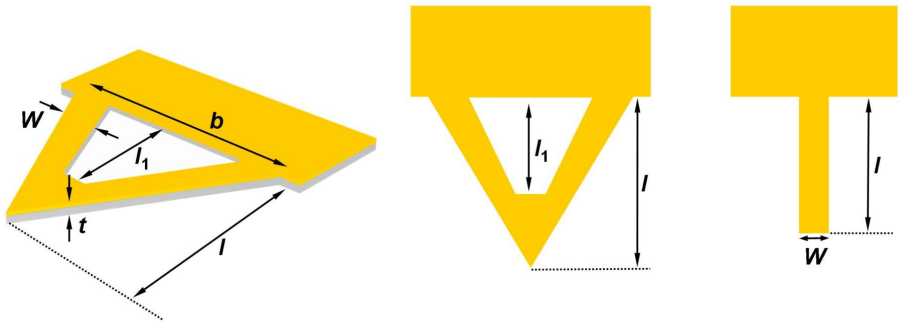

Figure 1.12 Schematic of the V- and rectangular shaped microcantilevers and dimensional variables.

Table 1.1 Properties and dimensions of the microcantilevers as illustrated in **Figure 1.12**.

Property (Variable)	*Veeco cantilevers*			*MikroMasch cantilevers*		
	B	**C**	**E**	**D**	**E**	**F**
Length (l)	200 µm	320 µm	140 µm	300 µm	350 µm	250 µm
Thickness (t)	0.6 µm	0.6 µm	0.6 µm	1.0 µm	1.0 µm	1.0 µm
Width (w)	20 µm	22 µm	18 µm	35 µm	35 µm	35 µm
Intermediate Length (l_1)		230 µm	85 µm			
Base Width (b)		221 µm	141µm			
Spring Constant (k)	0.02 $N \cdot m^{-1}$	0.01 $N \cdot m^{-1}$	0.1 $N \cdot m^{-1}$	0.05 $N \cdot m^{-1}$	0.03 $N \cdot m^{-1}$	0.08 $N \cdot m^{-1}$

numerical values are listed in Table 1.1. The dimensions are those given by the manufacturer or determined by M. Godin.[165] Poisson's ratio, v, was taken to be 0.25 for the silicon nitride microcantilevers[155] and 0.064 for the silicon/silicon oxide microcantilevers[166,167]. An independent assessment of k_{rect} and k_{Δ} was undertaken as described in section 2.3.5.

1.4.4 Interpretation of the Measured Surface Stress

In microcantilever experiments, the interpretation of the origin of the surface stress is not trivial. It is known that the absolute bending signal is a convolution of specific and non-specific adsorption events and the corresponding surface stress change may not necessarily correlate with the amount of adsorbed material. Microcantilevers are also highly susceptible to vertical deflections that may be caused by extraneous interactions, particularly when operating in liquids. Thermal drift, non-specific physisorption of molecules from the surrounding liquid or changes in the index of refraction near the sensing surface can contribute to the drift.[168-173] To circumvent this problem and extract the surface stress changes arising from specific physico-chemical reactions, the simultaneous measurements of reference cantilevers aligned in the same array as the responsive cantilevers are often employed. To obtain reliable data under these circumstances, not only do the microcantilever properties have to be independently characterised but the reference interface must be truly inert.[169-172,174]

The parallel optical detection and surface functionalisation of multiple cantilevers in an array format are not always easily realized. When single cantilever experiments are employed, the combination of the surface stress measurement with a complementary technique can enable the interpretation of the measured surface stress. Electrochemical

techniques are particularly attractive since they offer the ability to address the entire sample rapidly by an electrochemical perturbation or control the redox state of "individual" molecules by an applied potential scan. A distinct drawback of electrochemistry arises when the underlying gold substrate is exposed to anions giving rise to the well-known charge-induced surface stress addressed by both Haiss[146] and Ibach[175]. To this end, electroactive SAMs, where the dense molecular packing restricts ion penetration and solvent interactions to the outermost layer, are excellent candidates to probe specific molecular events on the nanoscale. The integrated aspect of the combined electrochemical microcantilever instrument provides the surface and interfacial characterization capabilities required for the interpretation of the vertical deflection response. A photograph of the experimental set-up employed herein is provided in Figure 1.13.

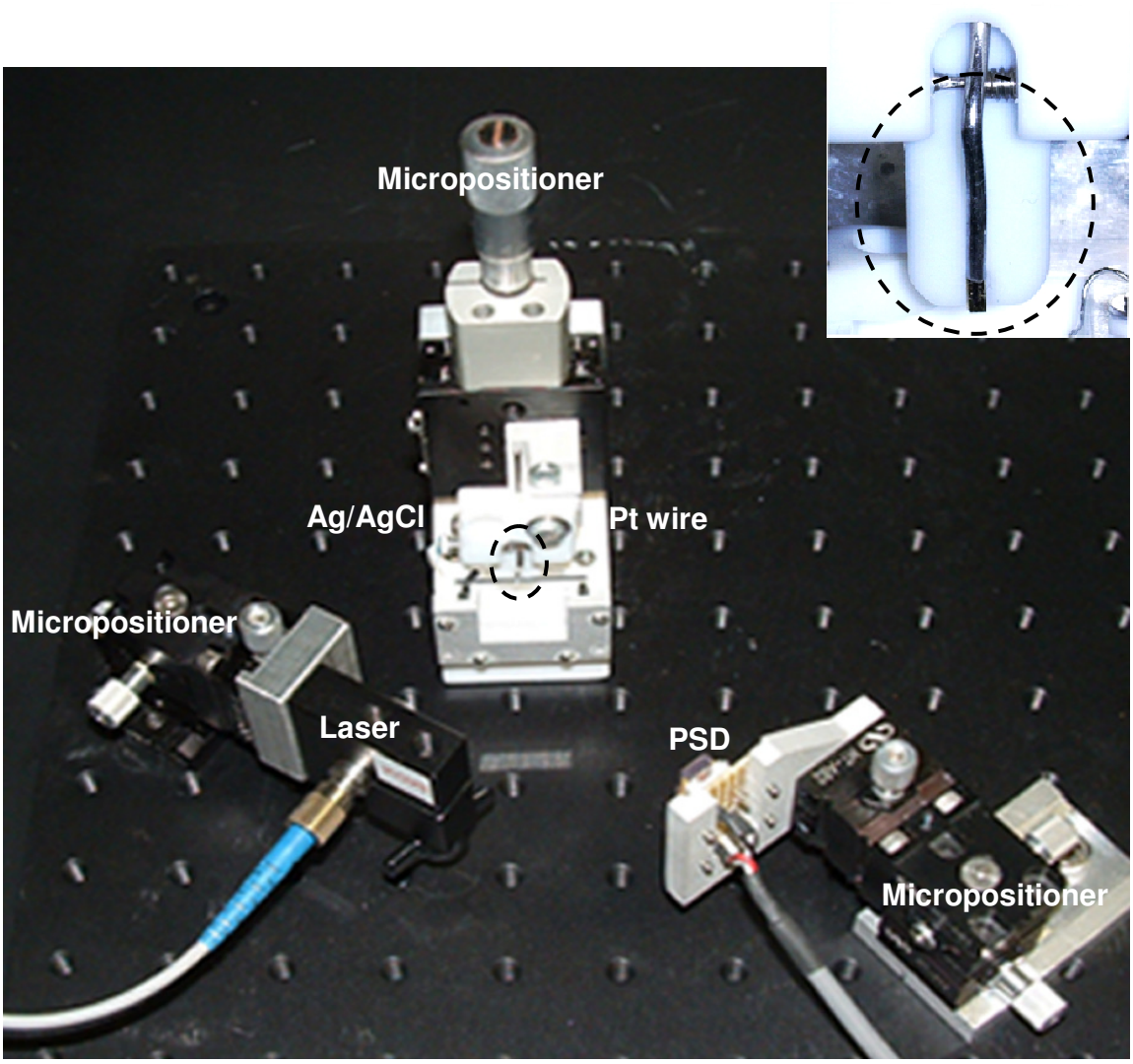

Figure 1.13 Photograph of the electrochemical-microcantilever experimental set-up showing the configuration of the liquid cell and electrodes (microcantilever: working electrode, Ag/AgCl: reference electrode, and Pt wire: auxiliary electrode). The microcantilever is mechanically clamped with a stainless steel clip onto a Teflon holder (as shown in the inset) which is attached to the micropositioner. The optical beam deflection configuration (laser and PSD) is also shown.

1.5 The Present Work

In this dissertation, the electrochemical switching capabilities of ferrocene-terminated alkylthiol monolayers (FcRSAu) are exploited for two distinct purposes: (1) the redox-induced actuation of micromechanical structures under an applied potential and (2) interfacial assembly of anionic surfactants by ion-pairing interactions with the electrogenerated ferrocenium. The dynamically controlled actuation and surface stress properties of gold-coated microcantilevers functionalised with a model redox-active FcRS- SAM are investigated. In an effort to implement control over the magnitude and direction of the actuation, the molecular structure of the ferrocenylalkylthiolate and the anion electrolyte are varied. Next, the potential-induced adsorption/desorption of a series of amphiphilic *n*-alkyl sulfates to the surface-confined ferrocenylalkanethiolates are investigated by *in-situ* SPR spectroscopy. It is demonstrated that the surface association and dissociation of these molecules can be triggered by an applied potential.

1.6 References

(1) Finklea, H. O. In *Electroanalytical Chemistry*; Bard, A. J., Rubinstein, I., Eds.; Marcel Dekker: New York, 1996; Vol. 19, p 109–335 and references therein.

(2) Wang, X.; Kharitonov, A. B.; Katz, E.; Willner, I. *Chem. Comm.* **2003**, 542–1543.

(3) Yousaf, M. N.; Houseman, B. T.; Mrksich, M. *Angew. Chem. Int. Ed.* **2001**, *40*, 1093–1096.

(4) Yeo, W.-S.; Hodneland, C. D.; Mrksich, M. *ChemBioChem.* **2001**, 590–594

(5) Yousaf, M. N.; Houseman, B. T.; Mrksich, M. *PNAS* **2001**, *98*, 5992–5996.

(6) Yeo, W.-S.; Yousaf, M. N.; Mrksich, M. *J. Am. Chem. Soc.* **2003**, *125*, 14994–14995.

(7) Yeo, W.-S.; Mrksich, M. *Langmuir* **2006**, *22*, 10816–10820.

(8) Chan, E. W. L.; Yousaf, M. N. *J. Am. Chem. Soc.* **2006**, *128*, 15542–15546.

(9) Lee, C.-S.; Baker, S. E.; Marcus, M. S.; Yang, W.; Eriksson, M. A.; Hamers, R. J. *Nano Lett.* **2004**, *4*, 1713–1716.

(10) Curreli, M.; Li, C.; Sun, Y.; Lei, B.; Gunderson, M. A.; Thompson, M. E.; Zhou, C. *J. Am. Chem. Soc.* **2005**, *127*, 6922–6923.

(11) Yang, W.; Baker, S. E.; Butler, J. E.; Lee, C.-S.; Russell, J. N., Jr.; Shang, L.; Sun, B.; Hamers, R. J. *Chem. Mater.* **2005**, *17*, 938–940.

(12) Mendes, P. M.; Christman, K. L.; Parthasarathy, P.; Schopf, E.; Ouyang, J.; Yang, Y.; Preece, J. A.; Maynard, H. D.; Chen, Y.; Stoddard, J. F. *Bioconjugate Chem.* **2007**, *18*, 1919–1923.

(13) Abbott, N. L.; Whitesides, G. M. *Langmuir* **1994**, *10*, 1493–1497.

(14) Sondag-Huethorst, J. A. M.; Fokkink, L. G. J. *Langmuir* **1994**, *10*, 4380–4387.

(15) Abbott, N. L.; Folkers, J. P.; Whitesides, G. M. *Science* **1992**, *257*, 1380–1382.

(16) Luk, Y.-Y.; Abbott, N. L. *Science* **2003**, *301*, 623–626.

(17) Ivanisevic, A.; Im, J.-H.; Lee, K.-B.; Park, S.-J.; Demers, L. M.; Watson, K. J.; Mirkin, C. A. *J. Am. Chem. Soc.* **2001**, *123*, 12424–12425.

(18) Kondo, T.; Okamura, M.; Uosaki, K. *J. Organomet. Chem.* **2001**, *637–639*, 841–844.

(19) Kazakevičienė, B.; Valincius, G.; Niaura, G.; Talaikytė, Z.; Kažemėkaitė, M.; Razumas, V. *J. Phys. Chem. B* **2003**, *1007*, 6661–6663.

(20) Rowe, G. K.; Creager, S. E. *J. Phys. Chem.* **1994**, *98*, 5500–5507.

(21) Chidsey, C. D. E. *Science* **1991**, *251*, 919–922.

(22) Rowe, G. K.; Creager, S. E. *Langmuir* **1991**, *7*, 2307–2312.

(23) Finklea, H. O. In *Electroanalytical Chemistry*; Bard, A. J., Rubinstein, I., Eds.; Marcel Dekker: New York, 1996; Vol. 19, p 109–335.

(24) Sumner, J. J.; Creager, S. E. *J. Phys. Chem. B* **2001**, *105*, 8739–8745.

(25) Ju, H.; Leech, D. *Phys. Chem. Chem. Phys.* **1999**, *1*, 1549–1554.

(26) Valincius, G.; Niaura, G.; Kazakevičienė, B.; Talaikytė, Z.; Kažemėkaitė, M.; Butkus, E.; Razumas, V. *Langmuir* **2004**, *20*, 6631–6638.

(27) Conway, B. E. *Ionic Hydration in Chemistyr and Biophysics*; Elsevier Scientific Publishing Company: New York, 1981; Vol. 12.

(28) Rowe, G. K.; Creager, S. E. *Langmuir* **1994**, *10*, 1186–1192.

(29) Creager, S. E.; Rowe, G. K. *Anal. Chim. Acta* **1991**, *246*, 233–239.

(30) Cruañes, M. T.; Drickamer, H. G.; Faulkner, L. R. *Langmuir* **1995**, *11*, 4089–4097.

(31) Kazakevičienė, B.; Valincius, G.; Niaura, G.; Talaikytė, Z.; Kažemėkaitė, M.; Razumas, V.; Plaušinaitis, D.; Teišerskienė, A.; Lisauskas, V. *Langmuir* **2007**, *23*, 4965–4971.

(32) Bigelow, W. C.; Pickett, D. L.; Zisman, W. A. *J. Colloid Interface Sci.* **1946**, *1*, 513–538.

(33) Ulman, A. *Chem. Rev.* **1996**, *96*, 1533–1554.

(34) Love, J. C.; Estroff, L. A.; Kriebel, J. K.; Nuzzo, R. G.; Whitesides, G. M. *Chem. Rev.* **2005**, *105*, 1103–1169.

(35) Poirier, G. E. *Chem. Rev.* **1997**, *97*, 1117–1128.

(36) Dubois, L. H.; Nuzzo, R. G. *Annu. Rev. Phys. Chem.* **1992**, *43*, 437–463.

(37) Schwartz, D. K. *Annu. Rev. Phys. Chem.* **2001**, *52*, 107–137.

(38) Schreiber, F. *Prog. Surf. Sci.* **2000**, *65*, 151–257.

(39) Nuzzo, R. G.; Allara, D. L. *J. Am. Chem. Soc.* **1983**, *105*, 4481–4483.

(40) Biebuyck, H. A.; Bain, C. D.; Whitesides, G. M. *Langmuir* **1994**, *10*, 1825–1831.

(41) Nuzzo, R. G.; Fusco, F. A.; Allara, D. L. *J. Am. Chem. Soc.* **1987**, *109*, 2358–2368.

(42) Nuzzo, R. G.; Dubois, L. H.; Allara, D. L. *J. Am. Chem. Soc.* **1990**, *112*, 558–569.

(43) Porter, M. D.; Bright, T. B.; Allara, D. L.; Chidsey, C. E. D. *J. Am. Chem. Soc.* **1987**, *109*, 3559–3568.

(44) Garrell, R. L.; Chadwick, J. E.; Severance, D. L.; McDonald, N. A.; Myles, D. C. *J. Am. Chem. Soc.* **1995**, *117*, 11563–11571.

(45) Bryant, M. A.; Pemberton, J. E. *J. Am. Chem. Soc.* **1991**, *113*, 8284–8293.

(46) Bourg, M.-C.; Badia, A.; Lennox, R. B. *J. Phys. Chem. B* **2000**, *104*, 6562–6567.

(47) Widrig, C. A.; Chung, C.; Porter, M. D. *J. Electroanal. Chem.* **1991**, *310*, 335–359.

(48) Zhong, C.-J.; Woods, N. T.; Dawson, G. B.; Porter, M. D. *Electrochem. Comm.* **1999**, *1*, 17–21.

(49) Hasan, M.; Bethell, D.; Brust, M. *J. Am. Chem. Soc.* **2002**, *124*, 1132–1133.

(50) Lee, J.-G.; Lee, J.; Yates, J. T. J. *J. Am. Chem. Soc.* **2004**, *126*, 440–441.

(51) Gupta, V. K.; Abbott, N. L. *Langmuir* **1996**, *12*, 2587–2593.

(52) Bain, C. D.; Troughton, E. B.; Tao, Y. T.; Evall, J.; Whitesides, G. M.; Nuzzo, R. G. *J. Am. Chem. Soc.* **1989**, *111*, 321–335.

(53) Bain, C. D.; Whitesides, G. M. *Langmuir* **1989**, *5*, 1370–1378.

(54) Bain, C. D.; Whitesides, G. M. *J. Am. Chem. Soc.* **1988**, *110*, 3665–3666.

(55) Bain, C. D.; Evall, J.; Whitesides, G. M. *J. Am. Chem. Soc.* **1989**, *111*, 7155–7164.

(56) Buck, M.; Eisert, F.; Grunze, M.; Traeger, F. *Berichte der Bunsen-Gelleschaft* **1993**, *97*, 399–401.

(57) Buck, M.; Eisert, F.; Fischer, J.; Grunze, M.; Träger, F. *Appl. Phys. A* **1991**, *53*, 552–556.

(58) Debono, R. F.; Loucks, G. D.; Della Manna, D.; Krull, U. J. *Can. J. Chem.* **1996**, *74*, 677–688.

(59) Peterlinz, K. A.; Georgiadis, R. *Langmuir* **1996**, *12*, 4731–4740.

(60) Fruböse, C.; Doblhofer, K. *J. Chem. Soc. Faraday Trans.* **1995**, *91*, 1949–1953.

(61) Schneider, T. W.; Buttry, D. A. *J. Am. Chem. Soc.* **1993**, *115*, 12391–12397.

(62) Shimazu, K.; Yagi, I.; Sato, Y.; Uosaki, K. *Langmuir* **1992**, *8*, 1385–1387.

(63) Xu, S.; Cruchon-Dupeyrat, S. J. N.; Garno, J. C.; Liu, G.-Y.; Jennings, G. K.; Yong, T.-H.; Laibinis, P. E. *J. Chem. Phys.* **1998**, *108*, 5002–5012.

(64) Kim, Y. T.; Bard, A. J. *Langmuir* **1992**, *8*, 1096–1102.

(65) Haehner, G.; Woell, C.; Buck, M.; Grunze, M. *Langmuir* **1993**, *9*, 1955–1958.

(66) Yamada, R.; Sakai, H.; Uosaki, K. *Chem. Lett.* **1999**, *28*, 667–668.

(67) Dannenberger, O.; Wolff, J. J.; Buck, M. *Langmuir* **1998**, *14*, 4679–4682.

(68) Ishida, T.; Mizutani, W.; Azehara, H.; Sato, F.; Choi, N.; Akiba, U.; Fujihira, M.; Tokumoto, H. *Langmuir* **2001**, *17*, 7459–7463.

(69) Kawasaki, M.; Sato, T.; Tanaka, T.; Takao, K. *Langmuir* **2000**, *16*, 1719–1728.

(70) Yamada, R.; Wano, H.; Uosaki, K. *Langmuir* **2000**, *16*, 5523–5525.

(71) Bensebaa, F.; Voicu, R.; Huron, L.; Ellis, T. H. *Langmuir* **1997**, *13*, 5335–5340.

(72) Strong, L.; Whitesides, G. M. *Langmuir* **1988**, *4*, 546–558.

(73) Camillone, N., III; Chidsey, C. D. E.; Liu, G.-Y.; Putvinski, T. M.; Scoles, G. *J. Chem. Phys.* **1991**, *94*, 8493–8502.

(74) Chidsey, C. D. E.; Liu, G.-Y.; Rowntree, P.; Scoles, G. J. *J. Chem. Phys.* **1989**, *91*, 4421–4423.

(75) Fenter, P.; Eisenberger, P.; Liang, K. S. *Phys. Rev. Lett.* **1993**, *70*, 2447–2450.

(76) Poirier, G. E.; Tarlov, M. J. *Langmuir* **1994**, *10*, 2853–2856.

(77) Poirier, G. E.; Tarlov, M. J.; Rushmeier, H. E. *Langmuir* **1994**, *10*, 3383–3386.

(78) Poirier, G. E.; Pylant, E. D. *Science* **1996**, *272*, 1145–1148.

(79) Delamarche, E.; Michel, B.; Gerber, C.; Anselmetti, D.; Güntherodt, H.-J.; Wolf, H.; Ringsdorf, H. *Langmuir* **1994**, *10*, 2869–2871.

(80) Schöenenberger, C.; Sondag-Huethorst, J. A. M.; Jorritsma, J.; Fokkink, L. G. J. *Langmuir* **1994**, *10*, 611–614.

(81) Chiang, S. *Chem. Rev.* **1997**, *97*, 1083–1096.

(82) Delamarche, E.; Michel, B.; Biebuyck, H. A.; Gerber, C. *Adv. Mater.* **1996**, *8*, 719–729.

(83) Yang, G.; Lui, G.-Y. *J. Phys. Chem. B* **2003**, *107*, 8746–8759.

(84) Schlenoff, J. B.; Li, M.; Ly, H. *J. Am. Chem. Soc.* **1995**, *117*, 12528–12536.

(85) Ulman, A. *An Introduction to Ultrathin Organic Films: From Langmuir-Blodgett to Self-Assembly*; Academic Press: Boston, 1991.

(86) Bareman, J. P.; Klein, C. A. *J. Phys. Chem.* **1990**, *94*, 5202–5205.

(87) Barrena, E.; Palacios-Lidón, E.; Munuera, C.; Torrelles, X.; Ferrer, S.; Jonas, U.; Salmeron, M.; Ocal, C. *J. Am. Chem. Soc.* **2004**, *126*, 385–395.

(88) Boal, A. K.; Rotello, V. M. *Langmuir* **2000**, *16*, 9527–9532.

(89) Ferguson, M. K.; Lohr, J. R.; Day, B. S.; Morris, J. R. *Phys. Rev. Lett.* **2004**, *92*, 073201.

(90) Ferguson, M. K.; Low, E. R.; Morris, J. R. *Langmuir* **2004**, *20*, 3319–3323.

(91) Gurau, M. C.; Kim, G.; Lim, S. M.; Albertorio, F.; Fleisher, H. C.; Cremer, P. S. *Chemphyschem* **2003**, *4*, 1231–1233.

(92) Kim, J. H.; Shin, H. S.; Kim, S. B.; Hasegawa, T. *Langmuir* **2004**, *20*, 1674–1679.

(93) Lewis, P. A.; Smith, R. K.; Kelly, K. F.; Bumm, L. A.; Reed, S. M.; Clegg, R. S.; Gunderson, J. D.; Hutchison, J. E.; Weiss, P. S. *J. Phys. Chem. B* **2001**, *105*, 10630–10636.

(94) Valiokas, R.; Östblom, M.; Svedhem, S.; Svensson, S. C. T.; Liedberg, B. *J. Phys. Chem. B* **2002**, *106*, 10401–10409.

(95) Dubois, L. H.; Zegarski, B. R.; Nuzzo, R. G. *J. Chem. Phys.* **1993**, *98*, 678–688.

(96) Camillone, N., III; Chidsey, C. D. E.; Liu, G.-Y.; Scoles, G. *J. Chem. Phys.* **1993**, *98*, 3503–3511.

(97) Jiang, S. *Mol. Phys.* **2002**, *100*, 2261–2275.

(98) Poirier, G. E. *Langmuir* **1997**, *13*, 2019–2026.

(99) Paradis, E.; Rowntree, P. *J. Electroanal. Chem.* **2003**, *550–551*, 175–185.

(100) Zhang, L.; Goddard, W. A., III; Jiang, S. *J. Chem. Phys.* **2002**, *117*, 7342–7349.

(101) Hayashi, T.; Kodama, C.; Nozoye, H. *Appl. Surf. Sci.* **2001**, *169–170*, 100–103.

(102) Dubois, L. H.; Zegarski, B. R.; Nuzzo, R. G. *J. Electron Spectrosc. Relat. Phenom.* **1990**, *54–55*, 1143–1152.

(103) Hähner, G.; Kinzler, M.; Thümmler, C.; Wöll, C.; Grunze, M. *J. Vac. Sci. Technol., A* **1992**, *10*, 2758–2763.

(104) Norman, L. L.; Badia, A. *J. Am. Chem. Soc.* **2008**, *131*, 2328–2337.

(105) Chidsey, C. E. D.; Bertozzi, C. R.; Putvinski, T. M.; Mujsce, A. M. *J. Am. Chem. Soc.* **1990**, *112*, 4301–4306.

(106) Popenoe, D. D.; Deinhammer, R. S.; Porter, M. D. *Langmuir* **1992**, *8*, 2521–2530.

(107) De Long, H. C.; Donohue, J. J.; Buttry, D. A. *Langmuir* **1991**, *7*, 2196–2202.

(108) Uosaki, K.; Sato, Y.; Kita, H. *Langmuir* **1991**, *7*, 1510–1514.

(109) Creager, S. E.; Rowe, G. K. *J. Electroanal. Chem.* **1997**, *420*, 291–299.

(110) Müller-Meskamp, L.; Lüssem, B.; Karthäuser, S.; Prikhodovski, S.; Homberger, M. *Phys. Stat. Sol.* **2006**, *203*, 1448–1452.

(111) Müller-Meskamp, L. *Ferrocenes as Potential Building Blocks for Molecular Electronics Self-Assembly and Tunneling Spectroscopy*; Forschungszentrum Jülich, Zentralbibliothek, Verlag: Jülich, 2008.

(112) Müller-Meskamp, L.; Karthäuser, S.; Waser, R.; Homberger, M.; Wang, Y.; Englert, U.; Simon, U. *Surf. Sci.* **2009**, *603*, 716–722.

(113) Sato, Y.; Frey, B. L.; Corn, R. M.; Uosaki, K. *Bull. Chem. Soc. Jpn.* **1994**, *67*, 21–25.

(114) Lee, M.; Chung, C. *Bull. Korean Chem. Soc.* **1999**, *20*, 1–3.

(115) Ye, S.; Sato, Y.; Uosaki, K. *Langmuir* **1997**, *13*, 3157–3161.

(116) Ye, S.; Haba, T.; Sato, Y.; Shimazu, K.; Uosaki, K. *Phys. Chem. Chem. Phys.* **1999**, *1*, 3653–3659.

(117) Viana, A. S.; Abrantes, L. M.; Jin, G.; Floate, S.; Nichols, R. J.; Kalaji, M. *Phys. Chem. Chem. Phys.* **2001**, *3*, 3411–3419.

(118) Bard, A. J.; Faulkner, L. R. *Electrochemical Methods Fundamentals and Applications*; 2nd. ed.; J. Wiley & Sons: New York, 2001.

(119) Fujii, S.; Kurokawa, S.; Murase, K.; Lee, K.-H.; Sakai, A.; Sugimura, H. *Electrochim. Acta* **2007**, *52*, 4436–4442.

(120) Chidsey, C. E. D.; Bertozzi, C. R.; Putvinski, T. M.; Mujsce, A. M. *J. Am. Chem. Soc.* **1990**, *112*, 4301–4306.

(121) Walczak, M. M.; Popenoe, D. D.; Deinhammer, R. S.; Lamp, B. D.; Chung, C.; Porter, M. D. *Langmuir* **1991**, *7*, 2687–2693.

(122) Calvente, J. J.; Andreu, R.; Molero, M.; López-Pérez, G.; Domínguez, M. *J. Phys. Chem. B* **2001**, *105*, 9557–9568.

(123) Smith, C. P.; White, H. S. *Anal. Chem.* **1992**, *64*, 2398–2405.

(124) Vos, J. G.; Forster, R. J.; Keyes, T. E. *Interfacial Supramolecular Assemblies*; John Wiley & Sons Ltd.: West Susex, 2003.

(125) Pitarke, J. M.; Silkin, V. M.; Chulkov, E. V.; Echenique, P. M. *Rep. Prog. Phys.* **2007**, *70*, 1–87.

(126) Knoll, W. *Annu. Rev. Phys. Chem.* **1998**, *49*, 569–638.

(127) Raether, H. *Surface Plasmons on Smooth and Rough Surfaces and on Gratings*; Springer-Verlag: Berlin, 1985.

(128) *Surface Plasmon Resonance Based Sensors*; Homola, J., Ed.; Springer-Verlag: Berlin, 2006.

(129) Davies, J. *Nanobiology* **1994**, *3*, 5–16.

(130) Kretschmann, E.; Raether, H. *Z. Naturf. A* **1968**, *23*, 2135.

(131) Otto, A. *Z. Phys.* **1968**, *216*, 398–410.

(132) Kretschmann, E. *Z. Phys.* **1971**, *241*, 313–324.

(133) Hecht, E.; Zajac, A. *Optics*; Addison-Wesley, 1974.

(134) Goeders, K. M.; Colton, J. S.; Bottomley, L. A. *Chem. Rev.* **2008**, *108*, 522–542.

(135) Fritz, J. *Analyst* **2008**, *133*, 855–863.

(136) Ziegler, C. *Anal. Bioanal. Chem.* **2004**, *379*, 946–959.

(137) Baller, M. K.; Fritz, J. In *Protein Microarray Technology*; Kambhampati, D., Ed.; Wiley-VCH Verlag GmBH & Co. KGaA: Weinheim, 2004, p 195–213.

(138) Sader, J. E. In *Encyclopedia of Surface and Collid Science*; Hubbard, A., Ed.; Marcel Dekker: New York, USA, 2002, p 846–856.

(139) Thundat, T.; Warmack, R. J.; Chen, G. Y.; Allison, D. P. *Appl. Phys. Lett.* **1994**, *64*, 2894–2896.

(140) Sepaniak, M.; Datskos, P.; Lavrik, N. V.; Tipple, C. *Anal. Chem. A* **2002**, *74*, 568A–575A.

(141) Burg, T. P.; Godin, M.; Knudsen, S. M.; Shen, W.; Carlson, G.; Foster, J. S.; Babcock, K.; Manalis, S. R. *Nature* **2007**, *446*, 1066–1069.

(142) Berger, R.; Lang, H. P.; Gerber, C.; Gimzewski, J. K.; Fabian, J. H.; Scandella, L.; Meyer, E.; Güntherodt, H.-J. *Chem. Phys. Lett.* **1998**, *294*, 363–369.

(143) Barnes, J. R.; Stephenson, R. J.; Woodburn, C. N.; O'Shea, S. J.; Welland, M. E.; Rayment, T.; Gimzewski, J. K.; Gerber, C. *Rev. Sci. Instrum.* **1994**, *65*, 3793–3798.

(144) Bachels, T.; Tiefenbacher, F.; Schäfer, R. *J. Chem. Phys.* **1999**, *110*, 10008–10015.

(145) Stoney, G. G. *Proc. R. Soc. London, Ser. A* **1909**, *82*, 172–175.

(146) Haiss, W. *Rep. Prog. Phys.* **2001**, *64*, 591–648.

(147) Godin, M.; Tabard-Cossa, V.; Grütter, P.; Williams, P. *Appl. Phys. Lett.* **2001**, *79*, 551–553.

(148) Tabard-Cossa, V.; Godin, M.; Beaulieu, L. Y.; Grütter, P. *Sens. Actuators, B* **2005**, *107*, 233–241.

(149) Tabard-Cossa, V.; Godin, M.; Beaulieu, L. Y.; Grütter, P. *Sens. Actuators, B* **2006**, *119*, 352–354.

(150) Ibach, H. *Surf. Sci. Rep.* **1997**, *29*, 195–263.

(151) Lang, H. P.; Gerber, C. In *STM and AFM Studies on (Bio)molecular Systems: Unravelling the Nanoworld*; Samori, P., Ed.; Springer Verlag: Heidelberg, 2008; Vol. 285, p 1–27.

(152) Butt, H.-J. *J. Colloid Interface Sci.* **1996**, *180*, 251–260.

(153) Evans, D. R.; Craig, V. S. J. *J. Phys. Chem. B* **2006**, *110*, 5450–5461.

(154) Freund, L. B.; Floro, J. A.; Chason, E. *Appl. Phys. Lett.* **1999**, *74*, 1987–1989.

(155) Godin, M.; Tabard-Cossa, V.; Grütter, P. *Appl. Phys. Lett.* **2001**, *79*, 551–553.

(156) Jeon, S.; Thundat, T. *Appl. Phys. Lett.* **2004**, *85*, 1083–1084.

(157) Klein, C. A. *J. Appl. Phys.* **2000**, *88*, 5487–5490.

(158) Mertens, J.; Álvarez, M.; Tamayo, J. *Appl. Phys. Lett.* **2005**, *87*, 234102–3.

(159) Rasmussen, P. A.; Hansen, O.; Boisen, A. *Appl. Phys. Lett.* **2005**, *86*, 203502–3.

(160) Sader, J. E. *J. Appl. Phys.* **2001**, *89*, 2911–2921.

(161) Sader, J. E.; Larson, I.; Mulvaney, P.; White, L. R. *Rev. Sci. Instrum.* **1995**, *66*, 3789–3798.

(162) Zhang, Y.; Ren, Q.; Zhoa, Y.-p. *J. Phys. D: Appl. Phys.* **2004**, *37*, 2140–2145.

(163) Miyatani, T.; Fujihira, M. *J. Appl. Phys.* **1997**, *80*, 7099–7115.

(164) Khan, A.; Philip, J.; Hess, P. *J. Appl. Phys.* **2004**, *95*, 1667–1672.

165) Godin, M., McGill Univeristy, 2004.

(166) Tabard-Cossa, V.; Godin, M.; Beaulie, L. Y.; Grütter, P. *Sens. Actuators B* **2005**, *107*, 233–241.

(167) Brantley, W. A. *J. Appl. Phys.* **1973**, *44*, 534–535.

(168) Fritz, J.; Baller, M. K.; Lang, H. P.; Rothuizen, H.; Vettiger, P.; Meyer, E.; Güntherodt, H.-J.; Gerber, C.; Gimzewski, J. K. *Science* **2000**, *288*, 316–318.

(169) McKendry, R. A.; Zhang, J.; Arntz, Y.; Strunz, T.; Hegner, M.; Lang, H. P.; Baller, M. K.; Certa, U.; Meyer, E.; Güntherodt, H.-J.; Gerber, C. *PNAS* **2002**, *99*, 9783–9788.

(170) Shu, W.; Liu, D.; Watari, M.; Riener, C. K.; Strunz, T.; Welland, M. E.; Balasubramanian, S.; McKendry, R. A. *J. Am. Chem. Soc.* **2005**, *127*, 17054–17060.

(171) Watari, M.; Galbraith, J.; Lang, H.-P.; Sousa, M.; Hegner, M.; Gerber, C.; Horton, M. A.; McKendry, R. A. *J. Am. Chem. Soc.* **2007**, *129*, 601–609.

(172) Backmann, N.; Zahnd, C.; Huber, F.; Bietsch, A.; Plückthun, A.; Lang, H.-P.; Güntherodt, H.-J.; Hegner, M.; Gerber, C. *PNAS* **2005**, *102*, 14587–14592.

(173) Zhang, J.; Lang, H. P.; Huber, F.; Bietsch, A.; Grange, W.; Certa, U.; McKendry, R. A.; Güntherodt, H.-J.; Hegner, M.; Gerber, C. *Nature Nanotech.* **2006**, *1*, 214–220.

(174) Ndieyira, J. W.; Watari, M.; Barrera, A. D.; Zhou, D.; Vögtli, M.; Batchelor, M.; Cooper, M. A.; Strunz, T.; Horton, M. A.; Abell, C.; Rayment, T.; Aeppli, G.; McKendry, R. A. *Nat. Nanotechnol.* **2008**, 691–696.

(175) Ibach, H. *Surf. Sci. Rep.* **1997**, *29*, 193–263.

Chapter 2

Redox Actuation of a Microcantilever Driven by a Self-Assembled Ferrocenylundecanethiolate Monolayer: An Investigation of the Origin of the Micromechanical Motion and Surface Stress*

2.1 Abstract

The electrochemically-induced motion of free-standing microcantilevers is attracting interest as micro-/nano-actuators and robotic devices. The development and implementation of these cantilever-based actuating technologies requires a molecular-level understanding of the origin of the surface stress that causes the cantilever to bend. Here, we report a detailed study of the electroactuation dynamics of gold-coated microcantilevers modified with a model, redox-active ferrocenylundecanethiolate self-assembled monolayer ($FcC_{11}SAu$ SAM). The microcantilever transducer enabled the observation of the redox transformation of the surface-confined ferrocene. Oxidation of the $FcC_{11}SAu$ SAM in perchlorate electrolyte generated a compressive surface stress

---

* This chapter is a reproduced copy almost verbatim of the text of the paper *J. Am. Chem. Soc.* **2009**, *131*, 2328–2337. Copyright 2009, American Chemical Society. It is co-authored by Antonella Badia.

change of –0.20 ± 0.04 $N \cdot m^{-1}$, and cantilever deflections ranging from 0.8 μm to 60 nm for spring constants between ~0.01 and ~0.8 $N \cdot m^{-1}$. A comparison of the charge normalized surface stress of the $FcC_{11}SAu$ cantilever with values published for the electrochemical oxidation of polyaniline- and polypyrrole-coated cantilevers reveals a striking 10- to 100-fold greater stress for the monomolecular $FcC_{11}SAu$ system compared to the conducting polymer multilayers used for electroactuation. The larger stress change observed for the $FcC_{11}SAu$ microcantilever is attributable to steric constraints in the close-packed $FcC_{11}SAu$ SAM and an efficient coupling between the chemisorbed $FcC_{11}S$-monolayer and the Au-coated microcantilever transducer (vs. physisorbed conducting polymers). The microcantilever deflection vs. quantity of electrogenerated ferrocenium obtained in cyclic voltammetry and potential step/hold experiments, as well as the surface stress changes obtained for mixed $FcC_{11}S$-/$C_{11}SAu$ SAMs containing different populations of clustered vs. isolated ferrocenes, have permitted us to establish the molecular basis of stress generation. Our results strongly suggest that the redox-induced deflection of a $FcC_{11}SAu$ microcantilever is caused by a monolayer volume expansion resulting from collective re-orientational motions induced by the complexation of perchlorate ions to the surface-immobilized ferroceniums. The cantilever responds to the lateral pressure exerted by an ensemble of re-orienting ferrocenium-bearing alkylthiolates upon each other rather than individual anion pairing events. This finding has general implications for using SAM-modified microcantilevers as (bio-)sensors because it indicates that the cantilever responds to collective in-plane molecular interactions rather than reporting individual (bio-)chemical events.

2.2 Introduction

This chapter reports the reversible potential-controlled actuation and surface stress properties of free-standing gold-coated microcantilevers functionalized with a redox-active SAM. Our results show that the electrochemical transformation of a redox (ferrocene) moiety confined to the surface of a chemisorbed organic film can induce a vertical bending or deflection approaching the micrometer scale for a very flexible microcantilever. The surface stress change per charge density for the *monomolecular* redox-active SAM is ~10- to 100-fold greater in magnitude than that of conducting macromolecular systems used for electroactuation. The work reported herein expands the types of organic coatings than can be used for mechanical actuation and provides fundamental insights into the response mechanism of microcantilever-based sensing and actuating technologies.

The deflection of micromechanical cantilevers used as imaging probes and picoNewton force sensors in Atomic Force Microscopy (AFM) is generating growing interest for label-free (bio-)chemical sensing and mechanical actuation.[1-11] To date, a variety of biomolecular interactions and chemical reactions have been translated into a nanoscale deflection of the cantilever: DNA hybridization,[12-21] ligand-receptor binding,[12,22-24] protein-protein recognition,[12,17,25,26] cell adhesion,[27,28] alkanethiol self-assembly,[29-34] protonation/deprotonation of acid/base groups,[35-39] metal ion complexation,[40-43] underpotential metal deposition,[44-48] doping/dedoping of conducting polymers,[49,50] and the swelling/collapse of polyelectrolyte brushes[51-55]. The basic principle is that a chemical or physical event occurring at the functionalized surface of one side of the cantilever generates a surface stress difference (between the active functionalized and passive non-functionalized sides) that causes the cantilever to bend away from its resting position. To activate one side of the silicon or silicon nitride cantilever, its surface is usually coated with

a thin metal film and/or modified with a (bio)-organic layer. The cantilever deflection can be monitored in real-time with Ångstrom sensitivity via a laser beam reflected from the free end of the microcantilever onto a position-sensitive detector (PSD).[56] The deflection can be converted to a differential surface stress through a modified form of Stoney's equation.[57-60] It is well known that for isotropic materials, a compressive surface stress change yields an increase in the surface area, while a tensile stress leads to a decrease in area. In the case of microcantilevers, the compressive stress arises from repulsive, in-plane molecular interactions and results in a deflection away from the active surface, whereas a tensile stress represents attractive interactions and the microcantilever bends towards the functionalized side.

Key to the development and implementation of cantilever-based sensing and actuating technologies is the ability to precisely control the direction and amplitude of the cantilever movement. This level of control requires a comprehensive understanding of the origin of the surface stress generated in the (bio-)chemical system under investigation. Nonetheless, the factors and phenomena contributing to both the nature (compressive/tensile) and magnitude of the surface stress in microcantilever experiments are often difficult to identify, especially those involving inherently complex biomolecular interactions. For example, DNA hybridization at oligonucleotide-modified cantilevers has received a lot of attention.[12,13,15-18] Steric and electrostatic repulsions, configuration entropy, hydration forces, conformational changes, and changes in osmotic pressure have all been proposed to contribute to the resulting surface stress. Furthermore, these contributions may compete with each other rendering nontrivial the interpretation of the surface stress arising from multiple interactions at the cantilever interface. This is supported by ongoing debates in the literature.[12,16,17,19-21,35]

Studies have also demonstrated that the selectivity and sensitivity of microcantilever systems rely heavily on the reproducible formation of a functional layer on one surface of the cantilever.[29,32,33,61-65] In this regard, chemically well-defined SAMs formed by ω-functionalized alkanethiols on noble metal surfaces can provide a model system with tailorable and reproducible interfacial chemistry, enabling one to probe specific molecular events. For example, investigations of the evolution of the surface stress during the chemisorption of *n*-alkanethiols onto gold-coated cantilevers have provided some much needed insight into the experimental factors and chemical interactions that drive the self-assembly process and determine the predominant structural phase adopted by the alkanethiolates.[29-34] Other work involving the pH titration of microcantilevers functionalized with carboxylic acid-terminated alkanethiolate SAMs has demonstrated that the in-plane surface forces which dictate the magnitude and nature of the surface stress associated with protonation/deprotonation reactions are sensitive to the solution pH, ionic strength, solution ion composition[12,35], as well as the alkyl chain length[39]. These findings with acidic SAMs are of broader relevance to understanding the molecular origins of surface stress at charged solid interfaces and in biological interactions. The studies cited above demonstrate that, in fact, micromechanical cantilevers can be very valuable tools for the investigation and characterization of SAMs.

In the study reported here, we used a ferrocenylundecanethiolate SAM on a gold-coated cantilever ($FcC_{11}SAu$) as a model system to investigate the origin of the surface stress generated by faradaic electrochemistry. We have extended a preliminary investigation[66] to (i) quantify the cantilever deflection/surface stress changes and (ii) probe the dynamics of the system. These investigations enable an assessment of the actuation properties of the ferrocenyl-modified surface and the identification of the molecular

phenomena giving rise to the redox-induced deflection. Ferrocenylalkanethiolate SAMs are probably the most studied electroactive SAMs and the electrochemistry of single-component systems as well as of mixed monolayers consisting of ferrocenylalkanethiolates and inert alkanethiolates is extensively documented in the literature.[67-78] Ferrocene-terminated alkanethiolate SAMs exhibit relatively straightforward electrochemistry, meaning that every surface-tethered ferrocene can undergo a reversible one-electron redox reaction. Oxidation of the neutral ferrocene to the ferrocenium cation involves coupled electron-transfer and anion-pairing reactions.[67] Studies have also shown that the oxidation of the ferrocene to ferrocenium leads to changes in the water contact angle[79,80] and a molecular re-orientation[69,70,76,81-84]. These redox-induced changes in surface wettability and monolayer organization can drive macroscopic phenomena at ferrocenyl monolayer interfaces, such as the flow of aqueous solutions[80] and the orientation of liquid crystals[85], and have been taken into account in our interpretation of the surface stress results. In our $FcC_{11}SAu$ microcantilever investigations, the environmental parameters remain unaltered (i.e., solvent, electrolyte concentration, temperature, and pH), and an electrical potential is used as an external stimulus to trigger specific molecular orientational changes by the electrochemical generation of ferrocenium. To determine the mechanism of the microcantilever response, the number and distribution of the immobilized ferrocenium cations were varied with time by linearly scanning the potential across the oxidation region or a specific number of ferroceniums was instantaneously created by the application of a fixed potential. The cantilever deflection of mixed $FcC_{11}S–/C_{11}SAu$ SAMs containing different populations of "clustered" vs. "isolated" ferrocenes was also compared with that of pure $FcC_{11}SAu$ monolayers to determine the effect of ferrocenium alkanethiolate interactions on the surface stress.

Systems that are capable of converting electrical energy into mechanical motion are needed for a wide range of applications, e.g. robotics, artificial muscles, optical displays, and microfluidic devices. Conducting polymers have received a lot of attention as electro-actuators, and the redox-induced deflection of polyanaline-[49] and polypyrrole-coated[50] cantilevers has been investigated. These conducting polymer-coated cantilever systems are only superficially akin to the $FcC_{11}SAu$ cantilevers used in the present study. The quantity of charge per area generated during oxidation of the polyaniline and polypyrrole multilayer films is *ca*. 300-[86,87] to 2000-[88]times greater than that electrogenerated at the $FcC_{11}SAu$ cantilever. Moreover, in the macromolecular systems, stress changes result from the combined effects of physical swelling of the charged polymer matrix (due to the incorporation of counterions and solvent)[49,50] and the interaction of the supporting electrolyte ions with the underlying metal surface[50] (referred to as charge-induced surface stress) in areas where the polymer film does not properly adhere to the microcantilever as well as through defects in the polymer matrix. The contribution from charge-induced ion adsorption to the surface stress complicates the quantification of the redox-induced surface stress in conducting polymer actuators. By contrast, the stress changes in the SAM system are more straightforwardly attributable to redox-induced phenomena since solvent[73,81,89] and ion (perchlorate)[69,70,73,81,89] penetration into a full-coverage, close-packed $FcC_{11}SAu$ monolayer film is significantly inhibited.

Finally, it is important to note that a number of investigations employing gold-coated microcantilevers modified with functionalized SAMs have attributed the observed micromechanical deflection to *collective* in-plane molecular interactions.[12,16,17,90,91] For example, Stoddart and coworkers tethered to gold-coated microcantilevers linear molecular muscles based on bistable [3]rotaxanes consisting of a pair of mechanically

mobile rings encircling a single dumbbell. The redox-controlled collective movement of the rings along the dumbbell induced a contractile strain on the surface of the microcantilever which caused it to bend.[90,91] The micromechanical motion arising from the hybridization of complementary oligonucleotides has also been attributed to collective phenomena within the biomolecular layer.[12,14-17] While these experiments claim collective interactions, there is limited evidence to support the mechanism of the microcantilever response. In the case of our $FcC_{11}SAu$ microcantilevers, electrochemistry provides an independent measure or count of the surface activated species, thereby allowing us to establish that the microcantilever responds to collective molecular re-orientations rather than to single electron transfer/anion pairing events. This finding has important consequences for employing SAM-functionalized cantilever microdevices for quantification in (bio)analytical chemistry.

2.3 Experimental Section

2.3.1 Materials and Methods.

The following compounds were purchased and used without further purification: 1-undecanethiol ($C_{11}SH$, 98%, Sigma-Aldrich), 11-bromoundecanoic acid (≥98%, Fluka), perchloric acid (70%, Fluka), ferrocene (≥98%, Fluka), and sodium perchlorate (98%, Sigma-Aldrich). 11-Ferrocenyl-1-undecanethiol ($FcC_{11}SH$) was prepared starting from ferrocene and 11-bromoundecanoic acid according to the procedure of Creager and Rowe.[92] The purity and identity of the product was verified by thin layer chromatography (silica gel, hexanes/ethyl acetate 99:1 v/v) and ^1H NMR (400 MHz, $CDCl_3$), and are consistent with those previously reported.

The perchlorate electrolyte solution consisted of 0.01 M $HClO_4$/0.1M $NaClO_4$ (pH 3.1, $n_{589nm}^{20°C}$ = 1.33) and was prepared with deionized-distilled water obtained by purification of distilled water with a Milli-Q Gradient system (Millipore, Bedford, MA). The resistivity of the purified water was 18.2 MΩ·cm, and its surface tension, measured at 24 °C, was 72 $mN \cdot m^{-1}$. The perchlorate electrolyte solution was purged with nitrogen for at least 20 min prior to running electrochemical measurements.

2.3.2 Preparation and Characterization of the SAM-Gold Substrates.

V- and rectangular-shaped silicon nitride microcantilevers were purchased from Veeco (MLCT-NOHW, Santa Barbara, CA). Six microcantilevers of different geometric dimensions and spring constants are mounted on a single chip substrate. The experiments described in the present study predominantly used the V-shaped microcantilevers with spring constants (k) of 0.01 and 0.13 $N \cdot m^{-1}$, as well as the rectangular-shaped microcantilever of k = 0.02 N m^{-1}. We also used rectangular silicon/silicon oxide microcantilevers obtained from MikroMasch USA (CSC12/tipless/without Al, Wilsonville, OR). The V- and rectangular-shaped microcantilevers had dimensions in the range of 85–350 μm length, 18–35 μm width, and 0.6–1.0 μm thickness. The typical dimensions provided by the manufacturer and the experimentally determined spring constants for the microcantilevers used in our experiments are listed in Table 1.1.

Prior to metal deposition, the original reflective gold coating was stripped off the Veeco microcantilevers and chip support by immersion in a dilute aqua regia (3:1:6 $HCl/HNO_3/H_2O$) solution for ~5 min, followed by a thorough rinse with deionized-distilled water. To remove any residual grease, both the Veeco and MikroMasch microcantilever chip substrates were immersed for ~3 min in a piranha solution (3:1 H_2SO_4 and 30% H_2O_2-

CAUTION: Piranha solution is extremely hazardous and should be handled cautiously). Directly after the piranha cleanse, the microcantilever chip substrates were rinsed extensively with both deionized-distilled water and absolute ethanol and dried with nitrogen. One face of the clean microcantilevers was rendered electrically conductive by the deposition of an adhesion layer of 5 nm Ti (99.99 %, Alfa Aesar, USA) followed by an 85 nm film of Au (99.999%, Plasma Materials, USA) at rates of 0.04 nm s^{-1} and 0.14 nm s^{-1}, respectively. The evaporation was initiated once a base pressure of ~3×10^{-7} Torr was reached in a VE-90 thermal evaporator equipped with a quartz crystal deposition monitor (Thermionics Vacuum Products, Port Townsend, WA). At the end of the metal deposition, the evaporation chamber reached a temperature of 135 ± 15 °C. The surface morphology of the bare gold-coated microcantilevers was imaged using tapping mode AFM under ambient conditions. The gold surface was found to have an average grain size of ~100 nm with a RMS of 0.6–0.7 nm over areas of 1–25 μm^2.

Immediately following the evaporation process, the gold-coated microcantilevers were functionalized via passive self-assembly by immersing the chip substrates into a 1 mM solution of $FcC_{11}SH$ in 80:20 absolute ethanol/THF or a 1 mM $C_{11}SH$/ethanol solution for ~12 hours. Upon removal from the incubation solution, the thiol-modified microcantilevers were rinsed copiously with absolute ethanol and dried with nitrogen. Preferential chemisorption (>100:1) of *n*-alkanethiols and ferrocenylalkanethiols to the Au-coated side of a substrate compared to physisorption of the molecules to the silicon nitride was demonstrated by Whitesides and co-workers.[93,94]

Macroscopic B270 glass slides (Esco Products, Inc., Oak Ridge, NJ) were used in place of the microcantilever chip substrates to determine the surface concentration of ferrocene, as well as to investigate the potential-dependent wetting of the $FcC_{11}SAu$ SAM.

Both procedures are outlined below. The glass slides required only a piranha cleanse prior to metal deposition and thiol-modification, both of which were carried out using the same procedures detailed above for the microcantilever substrates.

2.3.3 Electrochemical and Contact Angle Measurements.

The Γ_{Fc} in the $FcC_{11}SAu$ SAMs was determined electrochemically using the SAMs formed on the gold-coated B270 substrates prepared in the same manner as the gold-coated microcantilevers according to equation 1.5. The use of a macroscopic substrate was necessary because in our microcantilever experimental set-up the electrode area immersed in electrolyte solution is not accurately defined.

$FcC_{11}SAu$-modified glass slides were also used for contact angle measurements where the substrate served as the working electrode. In our set up, a drop (~5 μL) of the perchlorate solution was placed on the $FcC_{11}SAu$ substrate using a glass syringe. An Ag wire (99.99%, Alfa Aesar, USA) quasi-reference electrode (QRE) and a platinum wire (99.99%, Alfa Aesar, USA) counter electrode were immersed in the drop to allow the application of an electrochemical potential. The potential was scanned from –0.1 V to +0.85 V at a rate of 5 mV s^{-1} using an Epsilon potentiostat (Bioanalytical Systems, Inc. West Lafayette, IN). Images of the drop shape acquired with a digital camera at open circuit and potentials greater than +0.65 V were analyzed with Adobe Photoshop software.

2.3.4 Electrochemical Microcantilever Measurements.

A custom-built, reflecting laser beam deflection set-up connected to an Epsilon potentiostat (Bioanalytical Systems, Inc. West Lafayette, IN) was used to monitor the

static deflection of the $FcC_{11}SAu$ microcantilever as a function of the applied potential. The modified gold-coated microcantilever chip (1.6 mm × 3.4 mm) serves as both the working electrode and the reflective platform of the optical set-up. In this method, the functionalized microcantilever is clamped and immersed into the electrochemical cell filled with the perchlorate electrolyte as depicted in Figure 2.1. The counter electrode was a platinum wire (99.99%, Alfa Aesar, USA) and all potentials are measured with respect to an Ag/AgCl aqueous reference electrode (3 M NaCl, Bioanalytical Systems). The CVs were acquired at a potential scan rate of 5 $mV \cdot s^{-1}$, unless otherwise indicated. In the single-step potential amperometry experiments, the potential applied to the $FcC_{11}SAu$ microcantilever electrode was stepped from open circuit to potentials of 0.050, 0.340, 0.385, 0.415 and 0.550 V, corresponding to fractional coverages of electrogenerated ferrocenium (Φ_{Fc^+}) of 0, 0.34, 0.64, 0.82 and 0.99, respectively. The applied potential was held for 50 s, with a sampling interval of 0.5 s. Concurrent to the application of a potential, a reflected laser beam is used to monitor the deflection of the microcantilever. In this method, a low powered (1 mW, 635 nm) laser diode is focused at the apex of the thiol-modified face of the microcantilever, and the vertical cantilever bending or deflection is measured by monitoring the position of the laser spot reflected from the functionalized surface onto a linear position sensitive detector (PSD IL10, ON-TRAK Photonics, Inc.). The laser is equipped with a commercial focuser having a working distance of 50 mm and a diameter of 30 μm. Both the laser and the PSD are mounted on

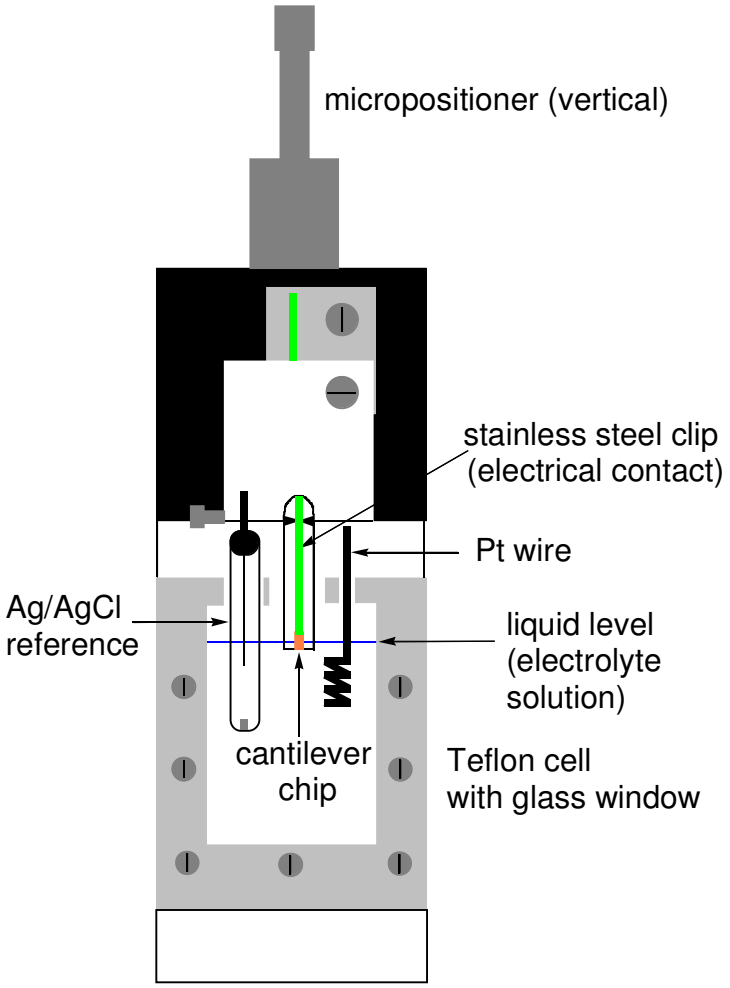

Figure 2.1 Schematic of the custom-built electrochemical cell (not shown to scale) incorporating the microcantilever chip as the working electrode, an Ag/AgCl reference electrode, and a platinum wire as the counter electrode.

micropositioners in order to position the focused laser beam on the apex of the microcantilever. The PSD is positioned at a distance of ~30 mm away from the microcantilever. The detector measures beam displacement on a 1-D axis and generates normalized displacement signals ranging from –10 V to +10 V, which are independent of the beam size and intensity. The PSD output voltage was digitized using a 16-bit analog-to-digital converter card (PCI-MIO-16XE-10, National Instruments) and continuously monitored at a sampling rate of 1 s and stored onto a PC using Labview (National Instruments). The displacement of the reflected laser spot on the PSD, which is linearly proportional to the microcantilever deflection, can be directly converted to a surface stress change, as outlined below.[58-60]

2.3.5 Microcantilever Deflection and Surface Stress

In static mode, the vertical displacement of the microcantilever, Δz, can be obtained from the output of the PSD using the equation 1.20, which is an approximation that accounts for the curvature of the microcantilever beam.[58-60] Here ΔS was corrected for the change in angle resulting from the reflected laser beam passing through the solution ($n_{589\text{nm}}^{20°\text{C}}$=1.33)/air ($n_{589\text{nm}}^{20°\text{C}}$=1.00) boundary (Snell's Law).[59] The formulas derived by Grütter and co-workers for the differential surface stress used in this investigation are given by equations 1.24 and 1.25 for a rectangular and triangular microcantilever, respectively.[58-60] k_{rect} (equation 1.24) and k_{Δ} (equation 1.25) are the experimentally determined spring constants for rectangular and triangular $FcC_{11}SAu$-modified cantilevers, respectively. The spring constants were determined by one of the following two methods: (i) using a Molecular Force Probe (Asylum Research, USA), spring constants of several microcantilevers from a number of different chips taken from the same wafer were

calibrated by pressing the modified microcantilevers against a very stiff surface and then against a reference spring of known and lesser compliance[95] or (ii) using a Nanoscope V scanning probe microscope (Veeco, USA), the spring constants of individual microcantilevers were calibrated via the spectral analysis of free-oscillations in the ambient, which are assumed to result from thermal excitation.[96]

2.4 Results and Discussion

2.4.1 Electrochemical Characterization of the $FcC_{11}SAu$ Microcantilevers.

The CVs obtained for the oxidation/reduction in 0.10 M $NaClO_4$/0.01 M $HClO_4$ of $FcC_{11}SAu$ monolayers formed on the AFM microcantilevers resemble those previously published for 100% $FcC_{11}SAu$[81,83,97] and $FcC_{12}SAu$[66,72] SAMs on macroscopic polycrystalline Au electrodes, and will be only briefly described here. Ferrocene oxidation and ferrocenium reduction peaks are observed at 0.39 V and 0.38 V (vs. Ag/AgCl), respectively. Shoulders are also present on the negative potential side of the main redox peaks. The presence of multiple voltammetric waves is attributable to the existence of electrochemically distinct ferrocene microenvironments.[72,75,98-10095] The ferrocene surface coverage of 4.7 (±0.3) × 10^{-10} mol·cm^{-2} (Q_{Fc^+} = 45 (±3) μC·cm^{-2}), determined experimentally on macroscopic Au-coated slides prepared and functionalized in the same manner as the microcantilevers, is close to the theoretical value (4.5 × 10^{-10} mol·cm^{-2}) expected from the close packing of ferrocene spheres of 6.6 Å diameter.[101]

2.4.2 Surface Stress Measurements.

For the electrochemical microcantilever experiments presented in this chapter, the measured electrochemical current arises mainly from the chip substrate, given the relative $FcC_{11}SAu$-covered surface areas of the cantilevers, ~10^{-5}–10^{-4} cm^2, and chip, ~0.02–0.03 cm^2, immersed in the electrolyte solution. However, the measured PSD signal is associated with the free end of the V- or rectangular-shaped microcantilever, as verified below. A previous ToF-SIMS analysis of the $FcC_{12}SAu$-coated side of AFM probes revealed a homogeneous distribution of the ferrocene across the microcantilever and chip surfaces.[66] We can therefore correlate the microcantilever deflection with the electrochemistry data collected.

Shown in Figure 2.2 are the typical current (Figure 2.2A) and deflection (Figure 2.2B) responses obtained for successive CV scans of a $FcC_{11}SAu$-coated microcantilever in perchlorate solution. The PSD output voltage was converted to a cantilever beam deflection, Δz (Figure 2.2B, left y-axis), which was then used to calculate the difference in surface stress, $\Delta\sigma$ (Figure 2.2B, right y-axis), between the $FcC_{11}SAu$-modified and unmodified (silicon/silicon oxide or silicon nitride) sides of the microcantilever, as outlined in the Chapter 1. In this work, microcantilever deflections that result in a positive increase in the PSD voltage indicate a bending of the cantilever away from the gold-coated face due to a compressive surface stress, which we express as a negative value, in accordance with common sign convention.[102]

A number of control experiments were initially completed to ensure that the microcantilever deflection and associated surface stress changes arise *primarily* from the ferrocene/ferrocenium redox reaction. To start, the corresponding PSD signals measured at the apex of the microcantilever beam vs. a region of the support chip during potential cycling are presented in Figure 2.3. As expected, no significant change in the PSD voltage

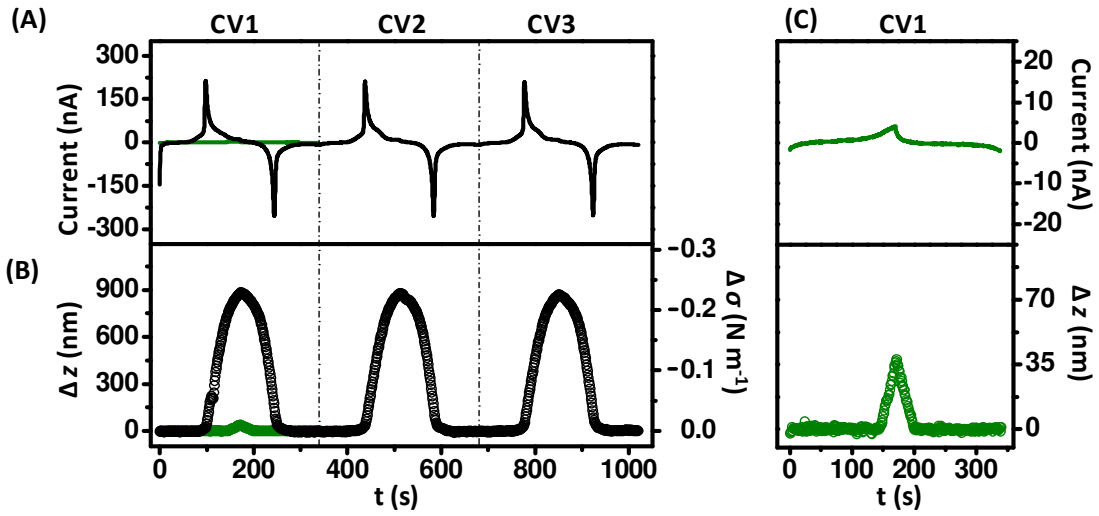

Figure 2.2 **(A)** Typical CV traces of $FcC_{11}SAu$ (—) and $C_{11}SAu$ (—) modified microcantilever substrates in 0.1 M $NaClO_4$/0.01 M $HClO_4$. The potential scan rate was 5 mV s^{-1}. **(B)** Corresponding deflection (Δz, left axis) and surface stress ($\Delta\sigma$, right axis) profiles for the $FcC_{11}SAu$ (○) and $C_{11}SAu$ (○) modified V-shaped microcantilevers (k = 0.011 ± 0.002 N m^{-1}) in 0.1 M $NaClO_4$/0.01 M $HClO_4$. **(C)** Zoom-in of the current-time (top) and deflection-time (bottom) traces recorded by cyclic voltammetry for the $C_{11}SAu$ microcantilever.

is observed when the laser is focused on the immobile chip. We can therefore affirm that the PSD response tracks the deflection of the mobile and flexible microcantilever and rule out a contribution from potential-induced changes in the reflectivity of the monolayer-coated gold surface.[103-105] The microcantilever is deflected to a higher PSD voltage upon oxidation of the ferrocene (neutral form) to ferrocenium (cationic form) and returns to nearly its initial position when the ferrocenium is reduced back to ferrocene, although a continuous drift in either the positive or negative direction is usually observed with time (Figure 2.3B). Single microcantilever experiments in solution are susceptible to spurious deflections that may be caused by temperature fluctuations, the

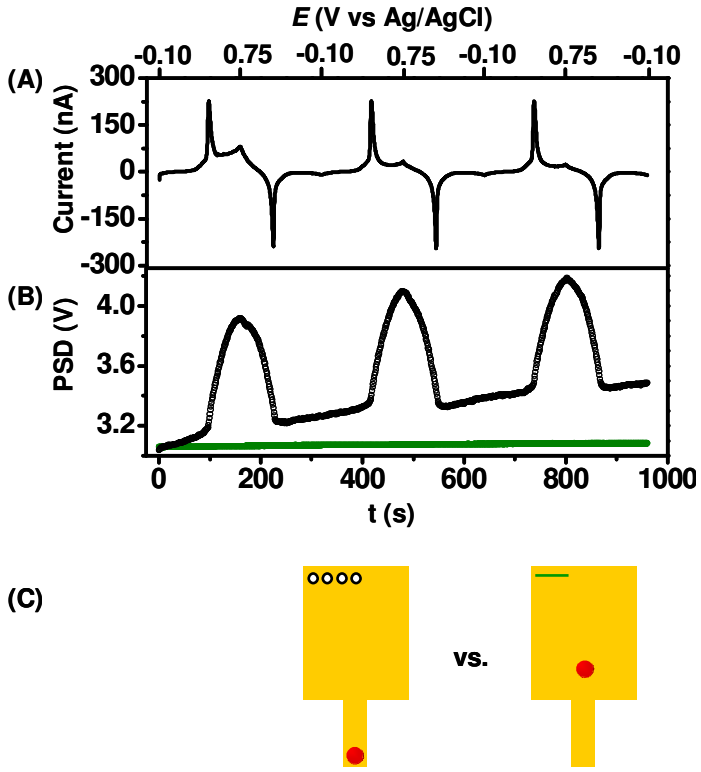

Figure 2.3 (A) Typical CV trace of a $FcC_{11}SAu$-modified microcantilever substrate in 0.1 M $NaClO_4$/0.01 M $HClO_4$. The potential was scanned at a rate of 5 mV s^{-1}. **(B)** The PSD response obtained when the laser is focused on the apex of the microcantilever (○, k = 0.011 ± 0.002 N m^{-1}) vs. the immobile chip (—). **(C)** A schematic of the laser positioning (●) at the apex (○) of the microcantilever vs. the immobile chip.

release of stress accumulated during the gold evaporation process or the slow rearrangement of the molecules in the SAM.[56] This background drift can be easily corrected for mathematically and does not affect the magnitude of the maximum deflection observed in a given oxidation/reduction cycle (results not shown here).

Next, inert $C_{11}SAu$-coated cantilevers were used as non-ferrocenylated analogues to verify that the potential-induced deflection of the $FcC_{11}SAu$-modified cantilevers reported herein is not dominated by charge-induced ion adsorption to the underlying gold

surface. Such verification is pertinent because investigations of the potential-induced surface stress response of organic (ultra)thin film-modified metal-coated microcantilevers have reported deflections resulting from ion penetration and adsorption to the metal surface.[50] In the absence of free redox species in solution, SAMs of *n*-alkanethiols of chain length ≥ 10 carbons are relatively impermeable to various electrolyte ions in aqueous medium within the potential range of ~–0.2 V to ~+0.5 V (vs. Ag/AgCl), provided that the monolayers are sufficiently defect-free.[106] In the present investigation, monolayer capacitances of 1.4 (±0.1) $\mu F \cdot cm^{-2}$ and 1.8 (±0.2) $\mu F \cdot cm^{-2}$, were found for the $C_{11}SAu$ and $FcC_{11}SAu$ SAMs, respectively, in perchlorate solution.[107] These results are in good agreement with previously reported capacitances of 1.5 $\mu F \cdot cm^{-2}$ for $C_{11}SAu$[108] and 1.5 to 2.0 $\mu F \cdot cm^{-2}$ for $FcC_{11}SAu$[109] and $FcCO_2C_{11}SAu$[79] SAMs. Even though the molecular packing density of the $FcC_{11}SAu$ SAM (2.5 molecules$\cdot nm^{-2}$) is ~0.6 × that of the $C_{11}SAu$ SAM (4.7 molecules$\cdot nm^{-2}$)[110] due to the bulky terminal ferrocene, their capacitances are comparable. The $C_{11}SAu$ system should therefore provide a reasonable estimate of the contribution of ion permeation to the surface stress. As expected, no faradaic current was observed (Figure 2.2C, top panel) upon cycling the potential of a $C_{11}SAu$ microcantilever from –0.10 to +0.75 V (vs. Ag/AgCl) in 0.10 M $NaClO_4$/0.01 M $HClO_4$ solution. A deflection of the microcantilever was however detected (Figure 2.2C, bottom panel) at potentials >+0.60 V. The magnitude of the resulting surface stress change is ~–0.01 $N \cdot m^{-1}$, which corresponds to $\lesssim 5\%$ of the response observed for the $FcC_{11}SAu$ microcantilever over the same potential scan range (Figure 2.2B). We therefore attribute the potential-induced deflection/surface stress change of a $FcC_{11}SAu$ microcantilever principally to the oxidation/reduction of the surface-bound ferrocene/ferrocenium species.

The data obtained for 43 different $FcC_{11}SAu$-modified probe chips shows that the

SAM and magnitude of the cantilever deflection are stable over three successive redox cycles run at a potential scan rate of 5 $mV \cdot s^{-1}$ between –0.10 to +0.75 V in 0.10 M $NaClO_4$/0.01 M $HClO_4$ solution (Figure 2.2). Between the first and third CV scan, there is an average variation of 1% in Q_{Fc^+} and a change of 7% in the peak deflection amplitude, although 20% of the microcantilevers exhibited a peak amplitude change of $\lesssim 2\%$.

A systematic investigation of the effect of the microcantilever spring constant (k) on the measured deflection and surface stress change was undertaken. Such an effect has not usually been investigated in microcantilever experiments, but can be important to understanding the magnitude of the observed stress.[23] Figure 2.4 summarizes the results obtained for $FcC_{11}Au$-modified microcantilevers ranging from a low k of 0.011 (±0.002) $N \cdot m^{-1}$ to a considerably stiffer k of 0.791 (±0.004) $N \cdot m^{-1}$. The values reported are the maximum deflections measured at the switching potential of +0.75 V, where all of the ferrocene has been oxidized to ferrocenium. As expected, the largest Δz was recorded for the floppiest microcantilever (k = 0.01 $N \cdot m^{-1}$) and the magnitude of the deflection decreases *pseudo*-exponentially from ~0.8 μm to ~60 nm as k increases from ~0.01 to ~0.8 $N \cdot m^{-1}$ (Figure 2.4A). The $\Delta\sigma$ values calculated from the microcantilever deflections are however very similar, i.e. –0.17 to –0.23 $N \cdot m^{-1}$, for *k's* ranging between ~0.01 to ~0.13 $N \cdot m^{-1}$ (Figure 2.4B). This range encompasses the microcantilever spring constants typically employed in microcantilever experiments. Furthermore, the $\Delta\sigma$ measured for the electrochemical oxidation/reduction of $FcC_{11}SAu$ SAMs does not depend on the characteristics of the microcantilever, such as shape (triangular or rectangular) or material (silicon/silicon oxide or silicon nitride), as shown in Figure 2.4.

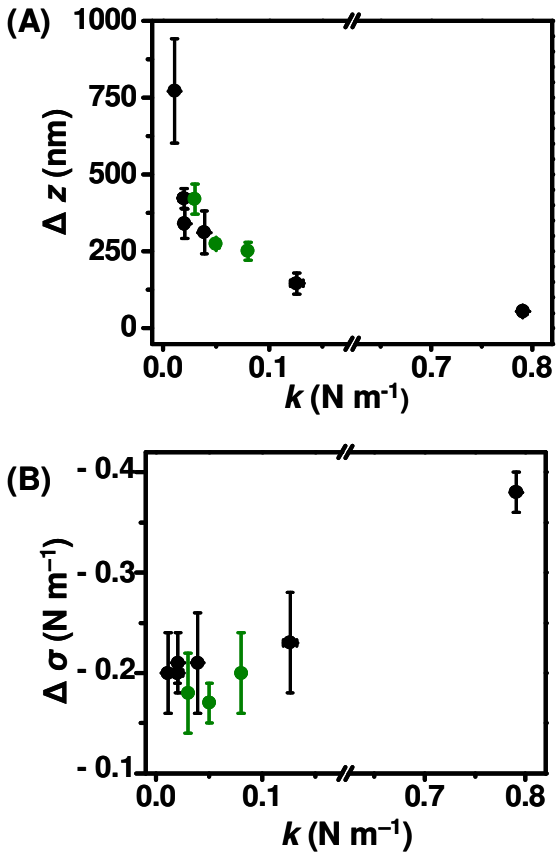

Figure 2.4 Plots of the **(A)** microcantilever deflection (Δz) and **(B)** microcantilever surface stress ($\Delta\sigma$) vs. the spring constant (k) for $FcC_{11}SAu$ modified microcantilevers. In both graphs solid black dots (●) represent SiN_x microcantilevers while the solid green dots (●) represent Si/SiO_x microcantilever measurements. The Δz values reported for each spring constant are the average and standard error measured for at least four different cantilevers of that spring constant. The Si/SiO_x (●) cantilevers are all rectangular in shape, whereas the SiN_x (●) microcantilevers are V-shaped, except for the cantilever with k = 0.0206 (± 0.0004) N m^{-1}.

2.4.3 Microcantilever Deflection vs. Quantity of Electrogenerated Ferrocenium.

To rationalize the electrochemically-induced deflection of the $FcC_{11}SAu$-modified microcantilever, we compare the % microcantilever deflection-potential profile with that of the Φ_{Fc^+} electrogenerated at potential scan rates of 10, 5, and 1 $mV \cdot s^{-1}$ (Figure 2.5). The following significant observations can be made from such a comparison. First, both curves exhibit a sigmoidal shape. The % change in microcantilever deflection ($\%\Delta z$) attains a limiting value (defined as 100%) when all of the ferrocene has been converted to ferrocenium in the anodic scan (i.e., $\Phi_{Fc^+} = 1$), and a constant value of 0% as Φ_{Fc^+} approaches 0 in the cathodic scan. This observation is consistent with the $FcC_{11}SAu$ microcantilever deflection resulting principally from a redox transformation of the ferrocenyl group. Interestingly, bending of the microcantilever is detectable only after ~15–20% conversion of the ferrocene to ferrocenium, i.e., $\Phi_{Fc^+} \approx 0.2$ (at the usual scan rate of 5 $mV \cdot s^{-1}$). In other words, the microcantilever deflection is triggered by the electrogeneration of ~5.8×10^9 Fc^+s per cm^2 ($\Phi_{Fc^+} \approx 0.2$). On the reverse scan, the microcantilever has already returned to within 15–30% of its original resting position after 50% of the ferrocenium is reduced back to ferrocene ($\Phi_{Fc^+} \approx 0.5$). The appreciable offset of the microcantilever deflection–potential response from the Φ_{Fc^+} (i.e., integrated current–potential curve could not be diminished by using a more flexible microcantilever (0.01 $N \cdot m^{-1}$ vs. 0.10 $N \cdot m^{-1}$) or a slower potential scan rate (1 $mV \cdot s^{-1}$ vs. 10 $mV \cdot s^{-1}$).

Φ_{Fc^+} is directly related to electron transfer across the SAM–electrode interface. On the other hand, the cantilever deflection may arise from the accumulation of charge on the cantilever surface, causing there to be a time offset between the deflection and current

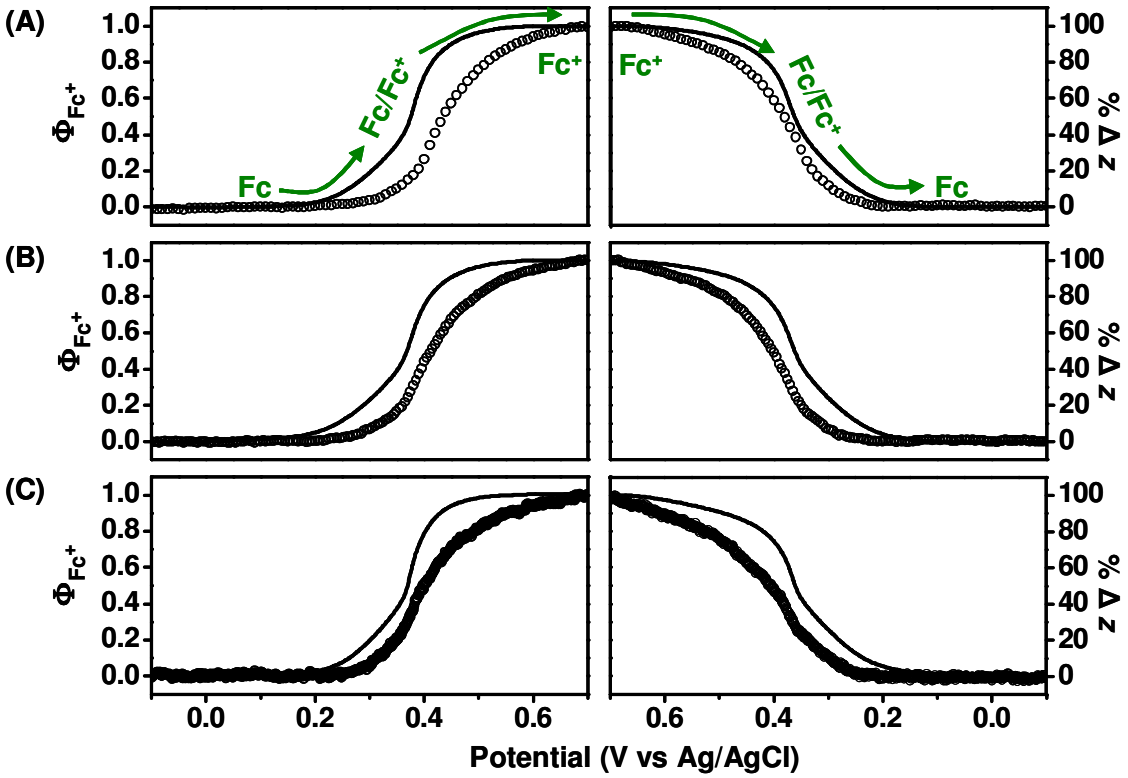

Figure 2.5 Plots of the fractional coverage (Φ_{Fc^+}) of ferrocenium (—) and % change in cantilever deflection (%Δz, ○) vs. the applied potential for scan rates: **(A)** 10 mV s^{-1}, **(B)** 5 mV s^{-1}, and **(C)** 1 mV s^{-1}. The left panel of the graphs represent the anodic scan (–0.10 to +0.70 V), whereas the right panel represents the cathodic scan (+0.70 to –0.10 V). Φ_{Fc^+} was determined by integrating incrementally the areas under the anodic and cathodic current-potential curves of the CVs after correcting for the charging current by a baseline approximation. The % change in the cantilever deflection was calculated by assigning the PSD signals at 0 V and +0.70 V to, respectively, the zero and maximum cantilever positions. The arrows indicate the direction of potential cycling for the redox cycle.

responses. To investigate the cause of this offset, potential step-hold experiments were performed, where the applied potential was stepped from open circuit to potentials corresponding to $\Phi_{Fc^+} = 0$ (0.050 V), 0.34 (0.340 V), 0.64 (0.385 V), 0.82 (0.415 V), and 0.99 (0.550 V). The potential holds were kept within the potential range where no deflection of the $C_{11}SAu$ microcantilever was observed (Figure 2.2C). The $\Delta\sigma$–time profiles (Figure 2.6A) demonstrate that the maximum $FcC_{11}SAu$ microcantilever deflections are obtained within ~3 s of the potential step (i.e., 3 × microcantilever sampling time) and the deflections remain relatively constant during the potential hold interval of 50 s. A decrease of ~10% was observed in the case of $\Phi_{Fc^+} = 0.99$, probably due to some decomposition of the ferrocenium cations with time at the higher oxidizing potential (0.550 V).[82,111] The microcantilevers returned to their original positions within ~3 s of the applied potential being stepped back to open circuit. The potential step-hold experiments indicate that the offset between the deflection–potential and integrated current–potential curves obtained in the CV experiments (Figure 2.6) is not due to the microcantilever having a longer response time due to charge accumulation. This is certainly true for the 1 mVs^{-1} cycles (slowest scan rate used), in which the applied potential changes by only ~3 mV within the ~3 s that it takes the microcantilever to reach its steady-state position at each point of the potential scan. More importantly, the $\Delta\sigma$ values obtained at different Φ_{Fc^+} values for ferrocene oxidation by CV are very close to those acquired in the potential step and hold experiments (Figure 2.6B). This observation supports the notion that the deflections recorded during CV scans are not limited by the microcantilever response time but by collective events occurring at the microcantilever interface.

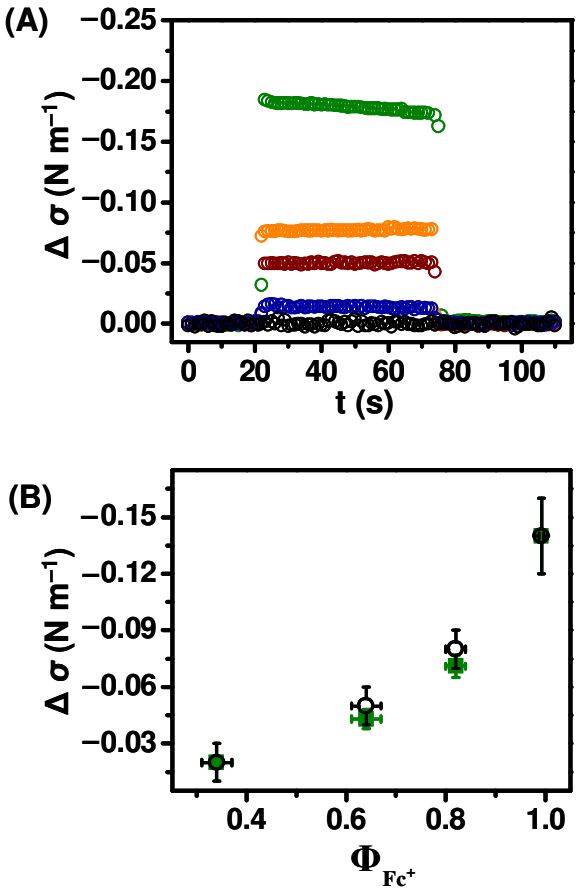

Figure 2.6 **(A)** Time-dependent surface stress profiles observed for a $FcC_{11}SAu$ microcantilever (k = 0.024 ± 0.002 N m^{-1}) in single-step potential-hold experiments, where the potential was stepped from open circuit potential to potentials corresponding to ferrocenium surface coverages: Φ_{Fc^+} = 0 (0.050 V, ○), 0.34 (0.340 V, ○), 0.64 (0.385 V, ○), 0.82 (0.415 V, ○) and 0.99 (0.550 V, ○). **(B)** Plot of the Δσ values obtained by potential step-hold (○) and cyclic voltammetry (■) for a given Φ_{Fc^+}. The CVs were acquired at a scan rate of 5 mV s^{-1}.

We propose that the delayed bending response of the $FcC_{11}SAu$ microcantilever under an applied potential is due to the *measured current* reporting *individual redox events*, whereas the *microcantilever beam deflection* reflects an *ensemble of in-plane molecular interactions*. Collective interactions are possible if there is a sufficient number of neighboring ferroceniums. Interactions between ferroceniums (vs. isolated non-interacting ferroceniums) are detected electrochemically in binary SAMs when the surface mole fraction of ferrocene is $\gtrsim 0.2$, due to the presence of domains or clusters of ferrocene alkanethiolates.[72,75] In single-component FcRSAu, the oxidation of a ferrocene next to an already oxidized ferrocenium cation is unfavorable due to electrostatic or Coulombic repulsion between the charged moieties, so that a critical number of electrogenerated ferroceniums may be needed for neighboring interactions.[99,100] A simulation of the ferrocenium distribution as a function of Φ_{Fc^+} provides an approximate idea of the extent of neighboring ferrocenium interactions with the applied potential (Figure 2.7A), which we have used to rationalize the % deflection vs. Φ_{Fc^+} behavior obtained experimentally (Figure 2.7B). Our crude modeling exercise consisted of placing ferroceniums in single fashion at random in a 36×36 grid (1296 molecules) and, for a given Φ_{Fc^+}, counting the number of ferroceniums which have more than one nearest neighbor.[112113-115] A more accurate model would account for the actual ferrocene domain size (unknown parameter), loose hexagonal lattice structure,[116] and the number of nearest and next-nearest ferrocenium neighbors for a given Φ_{Fc^+}. Such an exercise is outside the scope of our modeling capabilities. The results of our simplified simulation (Figure 2.7A) are nevertheless informative as these reveal that the number of electrogenerated ferroceniums that are surrounded by more than one neighboring ferrocenium becomes significant

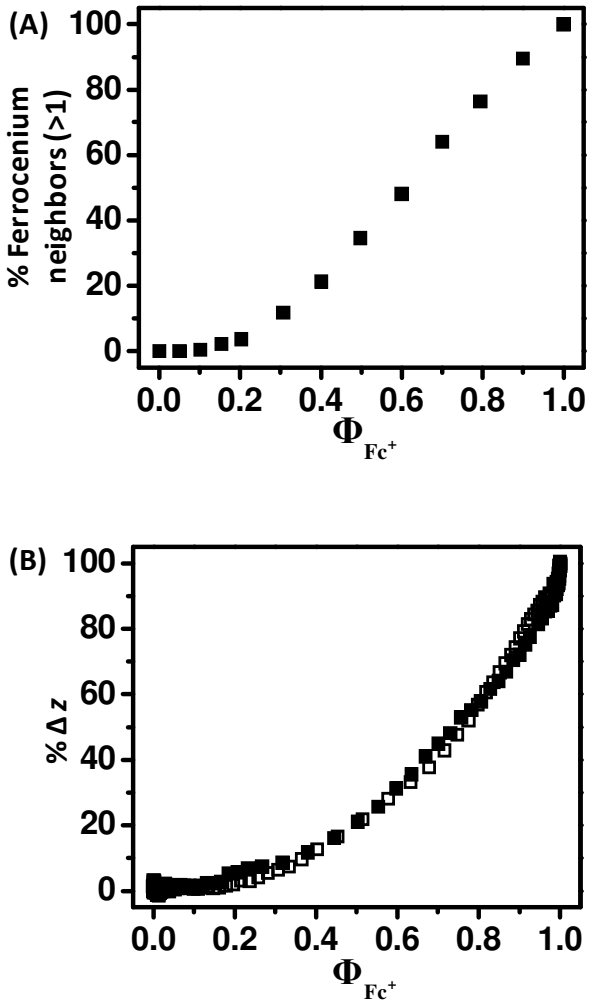

Figure 2.7 (A) A plot of the simulated ferrocenium nearest neighbor (> 1) distribution vs. the ferrocenium coverage (Φ_{Fc^+}) for a 36 × 36 grid (1296 molecules). **(B)** Plot of the % change in the cantilever deflection vs. the fractional coverage of ferrocenium (Φ_{Fc^+}) for the anodic (■) and cathodic (□) scans.

starting at $\Phi_{Fc^+} \approx 0.15–0.20$ and the number increases non-linearly as Φ_{Fc^+} increases. This calculated Φ_{Fc^+} onset is consistent with the minimum surface concentration required for electrochemically interacting ferrocenes in mixed SAMs.[72,75,99] More importantly, it coincides with the experimentally observed Φ_{Fc^+} range in which the onset of microcantilever deflection occurs (Figure 2.7B), suggesting that there is a correlation between the extent of the microcantilever deflection or bending and the number of neighboring ferroceniums.

2.4.4 Influence of the Ferrocene Surface Coverage on the Surface Stress Response.

To verify our hypothesis that the observed microcantilever deflection arises from combined lateral interactions between ferrocenium-bearing alkylthiolates, we investigated mixed SAM-modified microcantilevers in which the electroactive ferrocenes are isolated from one another by an inert *n*-alkylthiolate matrix. The voltammetric parameters are of interest here as we investigate the consequence of the phase state ("isolated" vs. "clustered") of the surface-confined ferrocenes on the microcantilever response. Typical CVs and corresponding $\Delta\sigma$ responses obtained for microcantilevers modified with binary $FcC_{11}S–/C_{11}SAu$ SAMs for which the $FcC_{11}S–$ concentration corresponds to ~35% and ~14% of the surface coverage (Γ_{Fc}) of a single-component $FcC_{11}SAu$ SAM (4.7 (±0.3) × 10^{-10} mol·cm^{-2}) are depicted in Figure 2.8. The different surface concentrations were obtained by varying the relative concentrations of $FcC_{11}SH$ and $C_{11}SH$ in the incubation solution. The resulting phase state of the mixed SAM depends on the relative concentrations and solubilities of the two thiols in the incubation solution.[72,117] The two-peak nature of the CV for $\Gamma_{Fc} \approx 35\%$ (Figure 2.8A) is consistent with a phase-separated

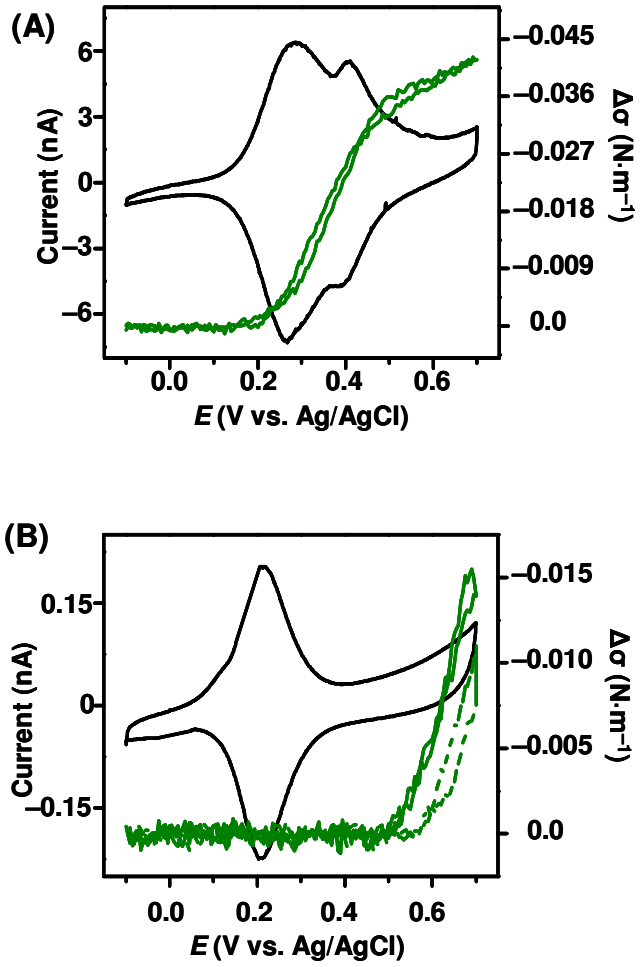

Figure 2.8 Typical CV traces (left axis, —) and corresponding Δσ responses (right axis, —) obtained for microcantilevers modified with binary $FcC_{11}S$-/$C_{11}SAu$ SAMs for which the surface $FcC_{11}S$- concentration is **(A)** ~35% and **(B)** ~14% of that of single-component $FcC_{11}SAu$ modified microcantilever substrates. The green dashed line in **(B)** is the stress response obtained for the $C_{11}SAu$ microcantilever shown in **Figure 2.2C**.

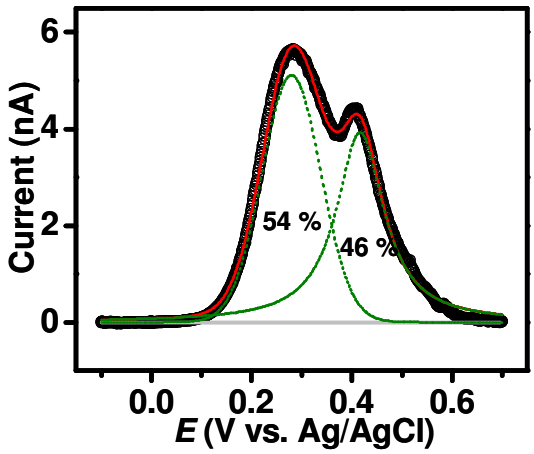

Figure 2.9 Example of the anodic peak deconvolution of a SAM prepared by incubation of a microcantilever for ~12 hours in a 1 mM $FcC_{11}SH/C_{11}SH$ (0.24:0.76) solution. The anodic segment (○) was initially corrected for the charging current and the baseline is shown in grey (—). The solid red line (—) represents the Gaussian-Lorentzian fittings and the dotted green lines (----) represent the individual Gaussian and Lorentzian fittings. The CV was run in 0.1 M $NaClO_4$/0.01 M $HClO_4$ and the potential was scanned at a rate of 5 $mV \cdot s^{-1}$.

monolayer where the $FcC_{11}S$– are either isolated from one another (peak I, $E_{1/2}$ = 0.30 ± 0.03 V) or clustered together inside domains (peak II, $E_{1/2}$ = 0.41 ± 0.01 V).[72,75] A positive shift in $E_{1/2}$ for the clustered domains (peak II) results because electrostatic repulsion between ferrocenium cations renders the oxidation of neighboring ferrocenes less favorable,[72,75] as already mentioned. Using a redox peak deconvolution method described elsewhere,[72] the relative surface proportions of the isolated and clustered ferrocene species were estimated. Briefly, peak I was fit to a Gaussian distribution and peak II was fit to a Lorentzian function.[118] A Gaussian fit is consistent with the bell-shaped symmetric CV expected for a surface-adsorbed redox species.[119] A Lorentzian fit is not model specific,

however, it provides good fits over many voltammograms. Both peaks were fit using three free fitting parameters: peak position, peak width, and peak area. The deconvolution of the CVs obtained for the binary $FcC_{11}S$-/$C_{11}SAu$ ($\Gamma_{Fc} \approx 35\%$) substrates reveals that the "isolated" ferrocene moieties constitute ~62% (1.01×10^{-10} mol·cm^{-2}) of the total surface-confined ferrocene, whereas ~38% (6.18×10^{-11} mol·cm^{-2}) of the ferrocenes are found within close proximity to each other. An example of a deconvoluted anodic CV is given in Figure 2.9. For the $\Gamma_{Fc} \approx 14\%$ SAM (Figure 2.8B), the single symmetrical redox peak observed indicates that the $FcC_{11}SAu$ molecules are

predominantly dispersed throughout the inert $C_{11}SAu$ matrix.[72,75] We expect that "isolated" ferrocenium moieties, which are not surrounded by other ferrocenium neighbors, but by inert $C_{11}S$–, will not contribute to the measured $\Delta\sigma$. Consistent with this hypothesis, the surface stress response of the 14% $FcC_{11}S$–/$C_{11}SAu$ SAM, –0.011 ± 0.007 N·m^{-1}, is of essentially the same magnitude (within experimental variability) as the inert $C_{11}SAu$ SAM (Figure 2.8B). On the other hand, "clustered" ferroceniums experience environmental and steric constraints that cause the monolayer reorganization

giving rise to the microcantilever deflection (*vide infra*). The size and shape of the domains formed by the aggregated $FcC_{11}S$– are unknown, so that the observed $\Delta\sigma$ of –0.037 ± 0.006 N·m^{-1} for the 35% $FcC_{11}S$–/$C_{11}SAu$ SAM cantilevers is a weighted average of all the in-plane interactions for a range of cluster sizes. The aggregated $FcC_{11}S$– population comprising this binary SAM was determined to be 6.18×10^{-11} mol cm^{-2}, which corresponds to ~14% of the surface coverage of a full-coverage single-component analogue. The $\Delta\sigma$ measured for the 35% $FcC_{11}S$-/$C_{11}SAu$ cantilevers is ~18% of that observed for the single-component $FcC_{11}SAu$ ($\Delta\sigma = -0.20 \pm 0.04$ N m^{-1}). This

proportional decrease in $\Delta\sigma$ is consistent with the microcantilever response arising from lateral interactions between aggregated ferroceniums.

2.4.5 Origin of the Redox-Induced Surface Stress Change

The measured $\Delta\sigma$ of –0.20 ± 0.04 N m^{-1} indicates that the electrochemical oxidation of the $FcC_{11}SAu$ SAM generates an average *in-plane* repulsive force of 132 pN per $Fc^{+}C_{11}S$- molecule (calculated using a ferrocene diameter of 0.66 nm) and an internal film pressure of *ca*. 0.1 GPa ($=\Delta\sigma \times d^{-1}$,[30] where the thickness, *d*, of the $FcC_{11}SAu$ monolayer is 1.8 nm[105]). What are the repulsive lateral interactions that could generate such a force and cause the $Fc^{+}C_{11}SAu$ microcantilever to bend? To answer this question, we have considered the ion pair formation,[89,120-122] changes in interfacial properties,[79,80,111] and the molecular re-orientation that have been identified by various *in-situ* electrochemical surface analytical methods to accompany electron transfer[69,70,77,82-84]. Both contact angle[79,80] and AFM-adhesion force[111] measurements have reported that the oxidation of the surface-confined ferrocene adjacent to a polar carboxylate ($FcCO_2C_{11}SAu$) or carbonyl ($FcCOC_{15}SAu$) group results in a notably more hydrophilic interface. We also found a decrease in the static perchlorate solution contact angle, from 77 (±5)º to 65 (±4)º, upon oxidation of the terminal ferrocene to ferrocenium for the $FcC_{11}SAu$ SAM. This increased hydrophilicity results in a decrease in the interfacial (monolayer/water) surface tension so that one would intuitively expect to observe a *tensile* surface stress, corresponding to bending of the microcantilever toward the film-coated Au side, upon oxidation of the ferrocene to ferrocenium in aqueous perchlorate solution. Although a redox-induced change in the macroscopic wettability of the $FcC_{11}SAu$ surface may contribute to the overall surface stress measured, it clearly is not the source of the net

compressive stress reported herein.

CV[101,121,122] and EQCM[84,89] experiments have established that the hydrophobic perchlorate anions complex strongly with the terminal ferrocenium cations to form 1:1 ion pairs at the monolayer/solution interface. Ion pairing with a perchlorate anion facilitates the oxidation of the ferrocene by stabilizing the ferrocenium cation. This 1:1 ion pair formation should reduce the Coulombic repulsion between neighboring ferroceniums as well as between the positively charged Au surface and the terminal ferrocenium cations by the neutralization of the excess positive charge on the ferroceniums. Therefore, it is unlikely that repulsive Coulombic forces cause significant bending of the microcantilever.[123] Repulsive dipolar interactions between ferrocenium-bearing alkanethiolates ($Au^{\delta+} - S^{\delta-} - R^{\delta+} - Fc^{+} - ClO_4^{-}$) are expected to be even weaker.[124-125,126] The relative magnitudes of the adhesion forces between neutral and oxidized polyvinylferrocene films in aqueous perchlorate solution have been measured by Hudson and Abruña.[127] No comparison can however be made between these adhesion force measurements and our surface stress measurements with regards to $Fc^{+} - ClO_4^{-}$ ion pair interactions since (i) AFM force spectroscopy probes *out-of-plane* adhesive forces between two surfaces in contact,[111] whereas the microcantilever measurements reflect *in-plane* forces acting at an interface and (ii) adhesion forces measured in liquid reflect the surface free energies of solvated functional groups rather than bare molecular interactions.[128]

A high-pressure electrochemical investigation of $FcC_{11}SAu$ SAMs by Cruañes et al. suggests that the complexation of the perchlorate to the ferrocenium requires a reorganization of the monolayer due to steric constraints.[109] CVs run at hydrostatic

pressures ranging from 1 atm (ambient pressure) to 6000 atm show that the oxidation of the monolayer-confined ferrocene is thermodynamically and kinetically more difficult at high pressures, whereas the same reaction for ferrocene in solution is not. The reduction of ferrocenium back to ferrocene was found to be affected to a lesser degree by pressure. Positive volumes of reaction and activation, indicative of a volume expansion, were found to be associated with the oxidation of ferrocene in the SAM. This volume increase, on the order of 10–20 $cm^3 \cdot mol^{-1}$, is attributable to the surface confinement of the ferrocene moiety which requires a reorganization of the $Fc^+C_{11}SAu$ SAM to allow for the complexation of perchlorate counterions.[109] Such a volume expansion would produce an internal film pressure of *ca*. 0.1–0.2 GPa[129] and result in bending of the $FcC_{11}SAu$ microcantilever away from the Au-coated face, as observed in our experiments.

Surface spectroscopic investigations of FcRSAu SAMs support the notion of a ferrocene-oxidation-induced monolayer reorganization. Recent ellipsometry[77,97,130] and SPR[105,131] investigations of FcRSAu SAMs report a thickening of the monolayer film (Δd) by 0.1–0.3 nm upon oxidation of the terminal ferrocene moieties. Such an increase in film thickness translates into a volume change ($= \Delta d \times 4.5 \times 10^{-10}$ $mol \cdot cm^{-2}$), ~20–70 $cm^3 \cdot mol^{-1}$, that is of similar magnitude to that reported by Cruañes et al. (i.e., 10–20 $cm^3 \cdot mol^{-1}$)[109]. Cruañes et al. originally proposed a stretching of the surface-tethered ferrocenylalkylthiolate alkyl chains to facilitate the association of the ferrocenium cations with perchlorate counterions.[109] Fourier transform infrared reflection absorption spectroscopy (FT-IRRAS) indicates that the observed changes in film thickness arise from a molecular orientational change in the SAM, resulting in either the alkyl chains[83,84] or cyclopentadiene rings[77,82] adopting a more perpendicular orientation with respect to the surface normal. A more recent *in situ* Fourier transform surface-enhanced Raman

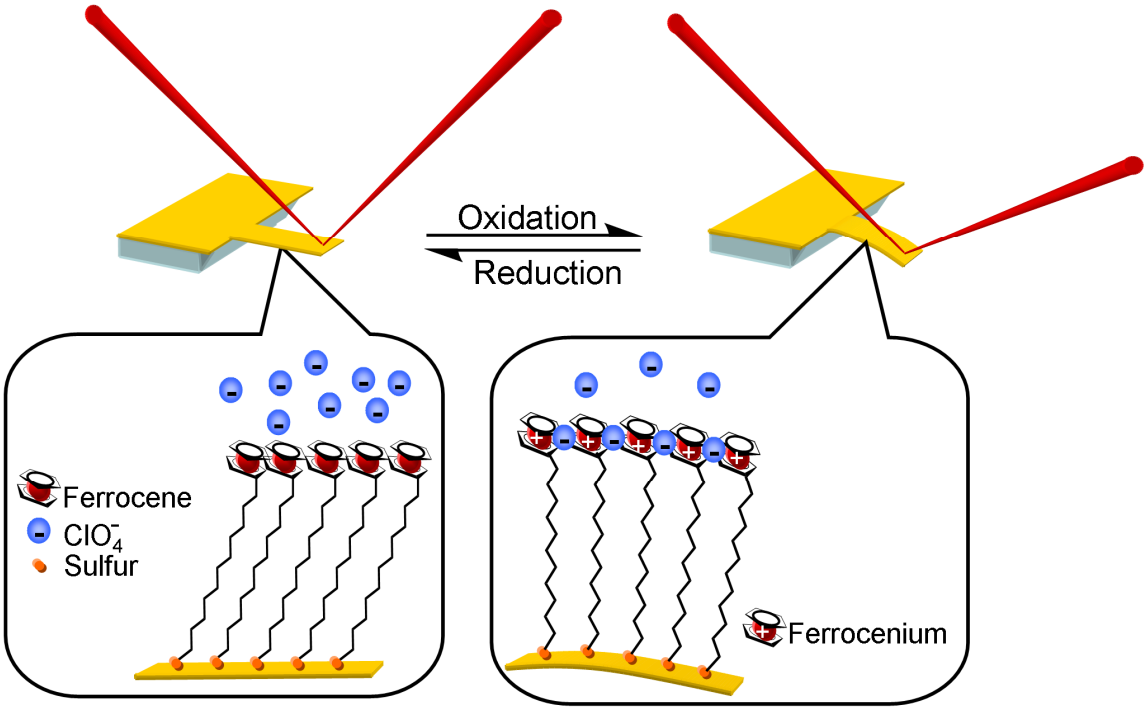

Figure 2.10 Schematic representation of the redox-induced deflection of $FcC_{11}SAu$ microcantilevers in perchlorate solution.

spectroscopy (FT-SERS) study of FcC_4COOC_nSAu SAMs, suggests that ferrocene oxidation causes the alkyl chains to adopt a more perpendicular orientation with respect to the electrode surface.[70] The ferrocenium-bearing alkyl chains and ferrocenium cyclopentadiene rings can change their orientation, to allow for the complexation of perchlorate counterions (Figure 2.10).[69,70,76,82-84,132-134] More importantly, the proposed molecular re-orientation could only occur in a concerted (as opposed to isolated) movement. The molecular re-orientation/monolayer volume expansion would result in an expanding lateral tension that could drive the microcantilever deflection reported herein.

As mentioned in section 2.2, mechanical actuation based on redox-induced volume changes is a well-known phenomenon in conducting polymer film systems. We therefore attribute a redox-induced SAM volume expansion, brought about by collective molecular re-orientations, as the most likely source of the surface stress changes measured for the $FcC_{11}SAu$ cantilevers. A comparison of the results reported for polyaniline-[49] and polypyrrole-[50]coated microcantilevers with those obtained for the $FcC_{11}SAu$-modified microcantilevers reveals that the surface stress change per charge density generated by the monomolecular (1.8 nm thick)[105] $FcC_{11}SAu$ (4500 N m^{-1}/C cm^{-2}) is significantly greater than the stresses of the thicker multilayer polymer films: ~300 $N \cdot m^{-1}/C \cdot cm^{-2}$ (polyaniline; 190 nm thick)[86,87] and ~20 $N \cdot m^{-1}$/ $C \cdot cm^{-2}$ (polypyrrole; 300 nm thick).[88] The larger stress change observed for the $FcC_{11}SAu$ microcantilever is probably due to the greater steric constraints in the closer-packed $FcC_{11}SAu$ SAM compared to the conducting polymer films and an efficient coupling between the chemisorbed $FcC_{11}S–$ monolayer and the Au-coated microcantilever transducer vs. the physisorbed polyaniline and polypyrrole. Although larger deflections are theoretically obtainable by building thicker films of conducting polymers (i.e., increase the number of redox sites per square area), the charge-normalized surface stress of the $FcC_{11}SAu$ SAM demonstrates that other system properties can be tailored to produce a larger actuation. Finally, our results point to ferrocenylalkanethiolate SAMs as potentially promising electroactuating coatings in such applications as nanomechanics, nanotweezers, and micromechanical elements, where there is a strong preference for actuation in a constant chemical environment.

2.5 Conclusions

We demonstrate that the surface stress changes associated with the oxidation and subsequent reduction of an electroactive moiety confined at an organic monolayer/solution interface can induce a reversible micromechanical motion. While SAM-modified microcantilevers often exhibit small nanometer-scale deflections, the electrochemical oxidation of $FcC_{11}SAu$ generates maximum deflections that approach the micrometer scale for cantilevers with low spring constant (0.01 $N \cdot m^{-1}$). The significance of this work is that it demonstrates that electroactive SAM films of well-defined structure can be used for micromechanical actuation.

Our results are consistent with the redox-induced deflection of a $FcC_{11}SAu$ microcantilever being predominantly driven by a monolayer volume expansion resulting from collective re-orientational motions caused by the complexation of perchlorate ions to the surface-immobilized ferroceniums. The cantilever responds to the lateral pressure exerted by an ensemble of re-orienting ferrocenium-bearing alkylthiolates upon each other rather than to individual anion pairing events, resulting in a complex non-linear dependence of the cantilever deflection on the quantity of electrogenerated ferrocenium (i.e., Figure 2.5B). Our work suggests that steric constraints and/or the ability of the complexing ion to induce organizational changes within the monolayer film play an important role in the magnitude of the observed cantilever bending in redox-induced actuation. We believe that this finding is not limited to ferrocene-terminated monolayers, and that SAM-modified cantilevers generally respond to collective in-plane molecular interactions rather than reacting to single (bio-)chemical events. This notion is based on literature examples of other types of interfacial reactions at SAMs being affected by steric crowding of the terminal functional groups (e.g. pK_a/pK_b of acid-base groups[135], binding capacity of proteins[136], and DNA-drug binding affinity[137]). The steric crowding of the reactive termini

is imposed by the packing density of the ω-functionalized alkanethiolates and is present to various extents in all SAMs, so that a molecular rearrangement of the alkanethiolates within the SAM is expected for the (bio-)chemical reaction to proceed.

In an effort to further understand the fundamental mechanisms of surface stress in ferrocenylalkanethiolate SAMs, we will continue to investigate the response of modified microcantilevers as a function of chemical structure and molecular order as well as anion-pairing strength. These experimental variables should provide further dynamic control over both the magnitude and direction of microcantilever deflection. In view of potential applications, an evaluation of the mechanical actuation performance of ferrocenylalkanethiolate-modified cantilevers upon continuous redox cycling and under prolonged potential holds will be undertaken by our laboratory.

2.6 Acknowledgments

This work was supported by NSERC (Canada), CFI (Canada), FQRNT (Québec), the Canada Research Chairs program, and the Université de Montréal. L.N. gratefully acknowledges fellowship support from the Groupe de recherche en technologie des couches minces of the Regroupement québécois sur les matériaux de pointe. We thank Mr. Jean-François Myre and Mr. Louis Beaumont (Chemistry Mechanics and Electronics Shop, Université de Montréal) for their contributions to the microcantilever optical deflection setup. We would also like to thank Brian Seivewright (McGill University) and

Jeff Shepherd (Laurentian University) for their help with the software programming used for data collection.

2.7 References

(1) Lang, H. P.; Hegner, M.; Gerber, C. *Mater. Today* **2005**, *8*, 30–36.

(2) Raiteri, R.; Grattarola, M.; Butt, H.-J.; Skádal, P. *Sens. Actuators B* **2001**, *79*, 115–126.

(3) Sepaniak, M.; Datskos, P.; Lavrik, N.; Tipple, C. *Anal. Chem.* **2002**, *74*, 568A–575A.

(4) Hansen, K. M.; Thundat, T. *Methods* **2005**, *37*, 57–64.

(5) Lang, H. P.; Baller, M. K.; Berger, R.; Gerber, C.; Gimzewski, J. K.; Battiston, F. M.; Fornaro, P.; Ramseyer, J. P.; Meyer, E.; Güntherodt, H. J. *Anal. Chim. Acta* **1999**, *393*, 59–65.

(6) Ziegler, C. *Anal. Bioanal. Chem.* **2004**, *379*, 946–959.

(7) Lavrik, N. V.; Sepaniak, M. J.; Datskos, P. G. *Rev. Sci. Instrum.* **2004**, *75*, 2229–2253.

(8) Goeders, K. M.; Colton, J. S.; Bottomley, L. A. *Chem. Rev.* **2008**, *108*, 522–542.

(9) Raiteri, R.; Grattarola, M.; Berger, R. *Mater. Today* **2002**, *5*, 22–29.

(10) Waggoner, P. S.; Craighead, H. G. *Lab Chip* **2007**, *7*, 1238–1255.

(11) Singamaneni, S.; LeMieux, M. C.; Lang, H.-P.; Gerber, C.; Jiang, H.; Naik, R. R.; Bunning, J. J.; Tsukruk, V. V. *Adv. Mater.* **2008**, *20*, 653–680.

(12) Fritz, J.; Baller, M. K.; Lang, H. P.; Rothuizen, H.; Vettiger, P.; Meyer, E.; Güntherodt, H.-J.; Gerber, C.; Gimzewski, J. K. *Science* **2000**, *288*, 316–318.

(13) Fritz, J.; Cooper, E. B.; Gaudet, S.; Sorger, P. K.; Manalis, S. R. *PNAS* **2002**, *99*, 14142–14146.

(14) Mukhopadhyay, R.; Lorentzen, M.; Kjems, J.; Besenbacher, F. *Langmuir* **2005**, *21*, 8400–8408.

(15) Shu, W.; Liu, D.; Watari, M.; Riener, C. K.; Strunz, T.; Welland, M. E.; Balasubramanian, S.; McKendry, R. A. *J. Am. Chem. Soc.* **2005**, *127*, 17054–17060.

(16) McKendry, R. A.; Zhang, J.; Arntz, Y.; Strunz, T.; Hegner, M.; Lang, H. P.; Baller, M. K.; Certa, U.; Meyer, E.; Güntherodt, H.-J.; Gerber, C. *PNAS* **2002**, *99*, 9783–9788.

(17) Wu, G.; Ji, H.; Hansen, K.; Thundat, T.; Datar, R.; Cote, R.; Hagan, M. F.; Chakraborty, A. K.; Majumdar, A. *PNAS* **2001**, *98*, 1560–1564.

(18) Stachowiak, J. C.; Yue, M.; Castelino, K.; Chakraborty, A.; Majumdar, A. *Langmuir* **2006**, *22*, 263–268.

(19) Álvarez, M.; Carrascosa, L. G.; Moreno, M.; Calle, A.; Zaballos, Á.; Lechuga, L. M.; Martínez-A, C.; Tamayo, J. *Langmuir* **2004**, *20*, 9663–9668.

(20) Khaled, A.-R. A.; Vafia, K.; Yang, M.; Zhang, X.; Ozkan, C. S. *Sens. Actuat. B* **2003**, *94*, 103–115.

(21) Hagan, M. F.; Majumdar, A.; Chakraborty, A. K. *J. Phys. Chem. B* **2002**, *106*, 10163–10173.

(22) Yue, M.; Stachowick, J. C.; Lin, H.; Datar, R.; Cote, R.; Majumdar, A. *Nano Lett.* **2008**, *8*, 520–524.

(23) Wu, G.; Datar, R.; Hansen, K. M.; Thundat, T.; Cote, R. J.; Majumdar, A. *Nat. Biotechnology* **2001**, *19*, 856–860.

(24) Ndieyira, J. W.; Watari, M.; Barrera, A. D.; Zhou, D.; Vögtli, M.; Batchelor, M.; Cooper, M. A.; Strunz, T.; Horton, M. A.; Abell, C.; Rayment, T.; Aeppli, G.; McKendry, R. A. *Nat. Nanotechnol.* **2008**, *3*, 691–696.

(25) Backmann, N.; Zahnd, C.; Huber, F.; Bietsch, A.; Plückthun, A.; Lang, H.-P.; Güntherodt, H.-J.; Hegner, M.; Gerber, C. *PNAS* **2005**, *102*, 14587–14592.

(26) Savran, C. A.; Knudsen, S. M.; Ellington, A. D.; Manalis, S. R. *Anal. Chem.* **2004**, *76*, 3194–3198.

(27) Park, J.; Ryu, J.; Choi, S. K.; Seo, E.; Cha, J. M.; Ryu, S.; Kim, J.; Kim, B.; Lee, S. H. *Anal. Chem.*, *77*, 6571–6580.

(28) ILic, B.; Yang, Y.; Craighead, H. G. *Appl. Phys. Lett.* **2004**, *85*, 2604–2606.

(29) Godin, M.; Williams, P. J.; Tabard-Cossa, V.; Laroche, O.; Beaulie, L. Y.; Lennox, R. B.; Grütter, P. *Langmuir* **2004**, *20*, 7090–7096.

(30) Berger, R.; Delamarche, E.; Lang, H.-P.; Gerber, C.; Gimzewski, J. K.; Meyer, E.; Güntherodt, H.-J. *Science* **1997**, *276*, 2021–2024.

(31) Berger, R.; Delamarche, E.; Lang, H. P.; Gerber, C.; Gimzewski, J. K.; Meyer, E.; Güntherodt, H.-J. *Appl. Phys. A* **1998**, *66*, S55–S59.

(32) Kohale, S.; Molina, S. M.; Weeks, B. L.; Kare, R.; Hope-Weeks, L. J. *Langmuir* **2007**, *23*, 1258–1263.

(33) Desikan, R.; Lee, I.; Thundat, T. *Ultramicroscopy* **2006**, *106*, 795–799.

(34) Desikan, R.; Armel, S.; Meyer III, H. M.; Thundat, T. *Nanotechnology* **2007**, *18*, 424028.

(35) Watari, M.; Galbraith, J.; Lang, H.-P.; Sousa, M.; Hegner, M.; Gerber, C.; Horton, M. A.; McKendry, R. A. *J. Am. Chem. Soc.* **2007**, *129*, 601–609.

(36) Ji, H.-F.; Hansen, K. M.; Hu, Z.; Thundat, T. *Sens. Actuators B* **2001**, *72*, 233–238.

(37) Fritz, J.; Baller, M. K.; Lang, H. P.; Strunz, T.; Meyer, E.; Güntherodt, H.-J.; Delamarche, E.; Gerber, C.; Gimzewski, J. K. *Langmuir* **2000**, *16*, 9694–9696.

(38) Raiteri, R.; Butt, H.-J.; Grattarola, M. *Electrochim. Acta* **2000**, *46*, 157–163.

(39) Sushko, M. L.; Harding, J. H.; Shluger, A. L.; McKendry, R. A.; Watari, M. *Adv. Mater.* **2008**, *20*, 3848–3853.

(40) Ji, H.-P.; Zhang, J.; Purushotham, V. V.; Kondu, S.; Ramachandran, B.; Thundat, T.; Haynie, D. T. *Analyst* **2005**, *130*, 1577–1579.

(41) Ji, H.-F.; Finot, E.; Dabestani, R.; Thundat, T.; Brown, G. M.; Britt, P. F. *Chem. Comm.* **2000**, 457–458.

(42) Ji, H.-F.; Thundat, T. *Biosens. Bioelectron.* **2002**, *17*, 337–343.

(43) Ji, H.-F.; Thundat, T.; Debastani, R.; Brown, G. M.; Britt, P. F.; Bonnesen, P. V. *Anal. Chem.* **2001**, *73*, 1572–1576.

(44) Brunt, T. A.; Chabala, E. D.; Rayment, T.; O'Shea, S. J.; Welland, M. E. *J. Chem. Soc. Faraday Trans.* **1996**, *92*, 3807–3812.

(45) Brunt, T. A.; Rayment, T.; O'Shea, S. J.; Welland, M. E. *Langmuir* **1996**, *12*, 5942–5946.

(46) Haiss, W. *Rep. Prog. Phys.* **2001**, *64*, 591–648.

(47) Tian, F.; Pei, J. H.; Hedden, D. L.; Brown, G. M.; Thundat, T. *Ultramicroscopy* **2004**, *100*, 217–233.

(48) Ibach, H.; Bach, C. E.; Giesen, M.; Grossmann, A. *Surf. Sci.* **1997**, *375*, 107–119.

(49) Lahav, M.; Durkan, C.; Gabai, R.; Katz, E.; Willner, I.; Welland, M. E. *Angwe. Chem. Int. Ed.* **2001**, *40*, 4095–4097.

(50) Tabard-Cossa, V.; Godin, M.; Grütter, P.; Burgress, I.; Lennox, R. B. *J. Phys. Chem. B* **2005**, *109*, 17531–17537.

(51) Bumbu, G.-G.; Kircher, G.; Wolkenhauer, M.; Berger, R.; Gutmann, J. S. *Macromol. Chem. Phys.* **2004**, *205*, 1713–1720.

(52) Bumbu, G.-G.; Wolkenhauer, M.; Kircher, G.; Gutmann, J. S.; Berger, R. *Langmuir* **2007**, *23*, 2203–2207.

(53) Zhou, F.; Shu, W.; Welland, M. E.; Huck, W. T. S. *J. Am. Chem. Soc.* **2006**, *128*, 5326–5327.

(54) Zhou, F.; Biesheuvel, P. M.; Choi, E.-Y.; Shu, W.; Poetes, R.; Steiner, U.; Huck, W. T. S. *Nano Lett.* **2008**, *8*, 725–730.

(55) Valiaev, A.; Abu-Lail, N. I.; Lim, D. W.; Chilkoti, A.; Zauscher, S. *Langmuir* **2007**, *33*, 339–344.

(56) Baller, M. K.; Fritz, J. In *Protein Microarray Technology*; Kambhampati, D., Ed.; Wiley-VCH Verlag GmBH & Co. KGaA: Weinheim, 2004, p 195–213.

(57) Stoney, G. G. *Proc. R. Soc. London, Ser. A* **1909**, *82*, 172.

(58) Godin, M.; Tabard-Cossa, V.; Grütter, P. *Appl. Phys. Lett.* **2001**, *79*, 551–553.

(59) Tabard-Cossa, V.; Godin, M.; Beaulie, L. Y.; Grütter, P. *Sens. Actuators B* **2006**, *119*, 352–354.

(60) Tabard-Cossa, V.; Godin, M.; Beaulie, L. Y.; Grütter, P. *Sens. Actuators B* **2005**, *107*, 233–241.

(61) Tabard-Cossa, V.; Godin, M.; Burgress, I. J.; Monga, T.; Lennox, R. B.; Grütter, P. *Anal. Chem.* **2007**, *79*, 8136–8143.

(62) Headrick, J. J.; Sepaniak, M. J.; Lavrik, N. V.; Datskos, P. G. *Ultramicroscopy* **2003**, *97*, 417–424.

(63) Lavrik, N. V.; Tipple, C. A.; Sepaniak, M. J.; Datskos, P. G. *Chem. Phys. Lett.* **2001**, *336*, 371–376.

(64) Hansen, A. G.; Martensen, M. W.; Anderson, J. E. T.; Ulstrup, J.; Kuhlue, A.; Garnaes, J.; Boisen, A. *Probe Microsco.* **2001**, *2*, 139–150.

(65) Mertens, J.; Calleja, M.; Tarýn, A.; Tamayo, J. *J. Appl. Phys.* **2007**, *101*, 034904–1–8.

(66) Quist, F.; Tabard-Cossa, V.; Badia, A. *J. Phys. Chem. B* **2003**, *107*, 10691–10695.

(67) Finklea, H. O. In *Electroanalytical Chemistry*; Bard, A. J., Rubinstein, I., Eds.; Marcel Dekker: New York, 1996; Vol. 19, p 109–335 and references therein.

(68) Weber, K. S.; Creager, S. E. *J. Electroanal. Chem.* **1998**, *458*, 17–22.

(69) Valincius, G.; Niaura, G.; Kazakevičienė, B.; Talaikytė, Z.; Kažemėkaitė, M.; Butkus, E.; Razumas, V. *Langmuir* **2004**, *20*, 6631–6638.

(70) Kazakevičienė, B.; Valincius, G.; Niaura, G.; Talaikytė, Z.; Kažemėkaitė, M.; Razumas, V.; Plaušinaitis, D.; Teišerskienė, A.; Lisauskas, V. *Langmuir* **2007**, *23*, 4965–4971.

(71) Ju, H.; Leech, D. *Phys. Chem. Chem. Phys.* **1999**, *1*, 1549–1554.

(72) Lee, L. Y. S.; Sutherland, T. C.; Rucareanu, S.; Lennox, R. B. *Langmuir* **2006**, *22*, 4438–4444.

(73) Sato, Y.; Mizutani, F.; Shimazu, K.; Ye, S.; Uosaki, K. *J. Electroanal. Chem.* **1999**, *474*, 94–99.

(74) Kondo, T.; Okamura, M.; Uosaki, K. *J. Organomet. Chem.* **2001**, *637–639*, 841–844.

(75) Auletta, T.; van Veggel, F. C. J. M.; Reinhoudt, D. N. *Langmuir* **2002**, *18*, 1288–1293.

(76) Kazakevičienė, B.; Valincius, G.; Niaura, G.; Talaikytė, Z.; Kažemėkaitė, M.; Razumas, V. *J. Phys. Chem. B* **2003**, *1007*, 6661–6663.

(77) Viana, A. S.; Jones, A. H.; Abrantes, L. M.; Kalaji, M. *J. Electroanal. Chem.* **2001**, *500*, 290–298.

(78) Weber, K. S.; Hockett, L. A.; Creager, S. E. *J. Phys. Chem. B* **1997**, *101*, 8286–8291.

(79) Sondag-Huethorst, J. A. M.; Fokkink, L. G. J. *Langmuir* **1994**, *10*, 4380–4387.

(80) Abbott, N. L.; Whitesides, G. M. *Langmuir* **1994**, *10*, 1493–1497.

(81) Uosaki, K.; Sato, Y.; Kita, H. *Langmuir* **1991**, *7*, 1510–1514.

(82) Popenoe, D. D.; Deinhammer, R. S.; Porter, M. D. *Langmuir* **1992**, *10*, 2521–2530.

(83) Ye, S.; Sato, Y.; Uosaki, K. *Langmuir* **1997**, *13*, 3157–3161.

(84) Ye, S.; Haba, T.; Sato, Y.; Shimuza, K.; Uosaki, K. *Phys. Chem. Chem. Phys.* **1999**, *1*, 3653–3659.

(85) Luk, Y.-Y.; Abbott, N. L. *Science* **2003**, *301*, 623–626.

(86) The quantity of charge per cm^2 was estimated using the polyaniline film thickness of 190 nm reported by Lahav et al. (see reference 49) and the relation between the anodic charge density and the electropolymerized film thickness (see reference 87, equation 3).

(87) Guiseppi-Elie, A.; Pradhan, S. R. *Chem. Mater.* **1993**, *5*, 1474–1480.

(88) The charge per area was estimated from the reported polypyrrole film thicknesses (t (nm)) using the equation t (nm) = 2.8Q (mC cm^{-2}) given in reference 50.

(89) Shimazu, K.; Yagi, I.; Sato, Y.; Uosaki, K. *J. Electroanal. Chem.* **1994**, *372*, 117–124.

(90) Huang, T. J.; Brough, B.; Ho, C.-M.; Liu, Y.; Flood, A. H.; Bonvallet, P. A.; Tseng, H.-R.; Stoddard, J. F.; Baller, M.; Magonova, S. *Appl. Phys. Lett.* **2004**, *85*, 5391–5393.

(91) Liu, Y.; Flood, A. H.; Bonvallet, P. A.; Vignon, S. A.; Northrop, B. H.; Tseng, H.-R.; Jeppesen, J. O.; Huang, T. J.; Brough, B.; Baller, M.; Magonova, S.; Solares, S. D.; Goddard, W. A.; Ho, C.-M.; Stoddard, J. F. *J. Am. Chem. Soc.* **2005**, *127*, 9745–9759.

(92) Creager, S. E.; Rowe, G. K. *J. Electroanal. Chem.* **1994**, *370*, 203–211.

(93) Laibinis, P. E.; Hickman, J. J.; Wrighton, M. S.; Whitesides, G. M. *Science* **1989**, *245*, 845–847.

(94) Hickman, J. J.; Ofer, D.; Zou, C.; Wrighton, M. S.; Laibinis, P. E.; Whitesides, G. M. *J. Am. Chem. Soc.* **1991**, *113*, 1128–1132.

(95) Torrii, A.; Sasaki, M.; Hane, K.; Okuma, S. *Meas. Sci. Technol.* **1996**, *7*, 179–184.

(96) Hutter, J. L.; Bechhoefoer, J. *Rev. Sci. Instrum.* **1993**, *64*, 1868–1873.

(97) Ohtsuka, T.; Sato, K.; Uosaki, K. *Langmuir* **1994**, *10*, 3658–3662.

(98) Fujii, S.; Kurokawa, S.; Murase, K.; Lee, K.-H.; Sakai, A.; Sugimura, H. *Electrochim. Acta* **2007**, *52*, 4443–4448.

(99) Calvente, J. J.; Andreu, R.; Molero, M.; Lopez-Perez, G.; Domínguez, M. *J. Phys. Chem. B* **2001**, *105*, 9557–9568.

(100) Smith, C. P.; White, H. S. *Anal. Chem.* **1992**, *64*, 2398–2405.

(101) Chidsey, C. E. D.; Bertozzi, C. R.; Putvinski, T. M.; Mujsce, A. M. *J. Am. Chem. Soc.* **1990**, *112*, 4301–4306.

(102) Ibach, H. *Surf. Sci. Rep.* **1997**, *29*, 193–263.

(103) Badia, A.; Arnold, S.; Scheumann, V.; Zizlsperger, M.; Mack, J.; Jung, G.; Knoll, W. *Sens. Actuators B* **1999**, *54*, 145–165.

(104) Heaton, R. J.; Peterson, A. W.; Gerogiadis, R. M. *PNAS* **2001**, *98*, 3701–3704.

(105) Norman, L. L.; Badia, A. *Langmuir* **2007**, *23*, 10198–10208.

(106) Boubour, E.; Lennox, R. B. *J. Phys. Chem. B* **2000**, *104*, 9004–9010.

(107) The capacitance was measured by CV on macroscopic gold film electrodes in perchlorate solution at –0.050 V (potential at which there is no ferrocene oxidation). The potential range of –0.150 V to +0.050 V (vs. Ag/AgCl) was scanned at a rate of 100 mV/s.

(108) Porter, M. D.; Bright, T. B.; Allara, D. L.; Chidsey, C. E. D. *J. Am. Chem. Soc.* **1987**, *109*, 3559–3568.

(109) Cruañes, M. T.; Drickamer, H. G.; Faulkner, L. R. *Langmuir* **1995**, *11*, 4089–4097.

(110) Sigal, G. B.; Mrksich, M.; Whitesides, G. M. *J. Am. Chem. Soc.* **1998**, *120*, 3464–3473.

(111) Green, J.-B. D.; McDermott, M. T.; Porter, M. D. *J. Phys. Chem.* **1996**, *100*, 13342–13345.

(112) Alkylthiol domain sizes typically range from 10 to 100 nm and contain between 350 to 38 000 alkylthiol molecules (see references 113 and 114). For ferrocenylundecanethiol assembled on gold, the same size domains would contain 225 to 22 500 molecules. A Monte Carlo simulation showed that a 224-molecule system size is large enough to produce well-differentiated domains (see reference 115).

(113) Nelles, G.; Schönherr, H.; Jaschke, M.; Wolf, H.; Schaub, M.; Küther, J.; Tremel, W.; Bamberg, E.; Ringsdorf, H.; Butt, H.-J. *Langmuir* **1998**, *14*, 808–815.

(114) Fenter, P.; Eisenberger, P.; Liang, K. S. *Phys. Rev. Lett.* **1993**, *70*, 2447–2450.

(115) Siepmann, J. I.; McDonald, I. R. *Langmuir* **1993**, *9*, 2351–2355.

(116) Müller-Meskamp, L.; Lüssem, B.; Karthäuser, S.; Prikhodovski, S.; Homberger, M. *Phys. Stat. Sol.* **2006**, *203*, 1448–1452.

(117) Bain, C. D.; Evall, J.; Whitesides, G. M. *J. Am. Chem. Soc.* **1989**, *111*, 7155–7164.

(118) Creager, S. E.; Hockett, L. A.; Rowe, G. K. *Langmuir* **1992**, *8*, 854–861.

(119) Bard, A. J.; Faulkner, L. R. *Electrochemical Methods Fundamentals and Applications*; 2nd. ed.; J. Wiley & Sons: New York, 2001.

(120) Chidsey, C. D. E. *Science* **1991**, *251*, 919–922.

(121) Creager, S. E.; Rowe, G. K. *Anal. Chim. Acta* **1991**, *246*, 233–239.

(122) Rowe, G. K.; Creager, S. E. *Langmuir* **1991**, *7*, 2307–2312.

(123) The average Coulombic force contribution of each individual ferrocenium–ferrocenium interaction (for unpaired ferroceniums) to the deflection of the cantilever, calculated using Coulomb's law, is only ~3 pN (for an x-vector along the length of the cantilever). The calculation is shown in Appendix A.

(124) The apparent dipole moment of an alkanethiolate-Au monolayer is composed of contributions from $Au^{\delta+}$-$S^{\delta-}$ and from $S^{\delta-}$-$R^{\delta+}$ (see reference 125), where the partial charge on the S determined by X-ray photoelectron spectroscopy is ~–0.2e (see reference 126). Formation of the ion pair will increase the apparent molecular dipole moment and the magnitude of the associated repulsive dipolar forces between the alkanethiolate molecules. Such dipolar repulsive forces have already been identified as being the source of the compressive surface stress changes observed during the self-assembly of *n*-alkanethiols on gold-coated microcantilevers (see reference 30).

(125) Evans, S. D.; Ulman, A. *Chem. Phys. Lett.* **1990**, *105*, 462–466.

(126) Bourg, M.-C.; Badia, A.; Lennox, R. B. *J. Phys. Chem. B* **2000**, *104*, 6562–6567.

(127) Hudson, J. E.; Abruña, H. D. *J. Am. Chem. Soc.* **1996**, *118*, 6303–6304.

(128) Noy, A.; Vezenov, D. V.; Lieber, C. M. *Annu. Rev. Mater. Sci.* **1997**, *27*, 381–421.

(129) These values were obtained through a rough calculation using the ideal gas law with a molar volume change of 10-20 cm^3 mol^{-1} and T = 295 K.

(130) Abrantes, L. M.; Kalaji, M.; Viana, A. S. *Russ. J. Electrochem.* **2002**, *38*, 39–43.

(131) Yao, X.; Wang, J.; Zhou, F.; Wang, J.; Tao, N. *J. Phys. Chem. B* **2004**, *108*, 7206–7212.

(132) The packing density of the ferrocenylundecanethiolates restricts the redox-induced folding of the ferrocene-terminated alkanethiolates, so that direct interaction of the ferrocenes with the underlying Au surface is unlikely, except at grain boundaries and defect sites (see references 133 and 134).

(133) Wang, X.; Kharitonov, A. B.; Katz, E.; Willner, I. *Chem. Comm.* **2003**, 1542–1543.

(134) Lahann, J.; Mitragotri, S.; Tran, T.-N.; Kaido, H.; Sundaram, J.; Choi, I. S.; Hoffer, S.; Somorjai, G. A.; Langer, R. *Science* **2003**, *299*, 371–374.

(135) Fears, K. P.; Creager, S. E.; Latour, R. A. *Langmuir* **2008**, *24*, 837–843.

(136) Spinke, J.; Liley, M.; Schmitt, F. J.; Guder, H. J.; Angermaier, L.; Knoll, W. *J. Chem. Phys.* **1993**, *99*, 7012–7019.

(137) Wolf, L. K.; Gao, Y.; Georgiadis, R. M. *J. Am. Chem. Soc.* **2007**, *129*, 10503–10511.

Chapter 3

Redox Induced Actuation of a Microcantilever Driven by Ferrocene-Terminated Self-Assembled Monolayers: An Investigation of the Effects of the Alkyl Chain and Anion on the Micromechanical Motion and Surface Stress

3.1 Introduction

A detailed study of the electroactuation dynamics of gold-coated microcantilevers modified with a model, redox-active $FcC_{11}SAu$ SAM was reported in the previous chapter. The microcantilever transducer enabled the observation of the redox transformation of the surface-confined ferrocene. Oxidation of the $FcC_{11}SAu$ SAM in perchlorate electrolyte generated a compressive surface stress change of -0.20 ± 0.04 $N \cdot m^{-1}$, and cantilever deflections ranging from 0.8 μm to 60 nm for spring constants between ~0.01 and ~0.8 $N \cdot m^{-1}$. The microcantilever deflection vs. quantity of electrogenerated ferrocenium obtained in cyclic voltammetry and potential step/hold experiments, as well as the surface stress changes obtained for mixed $FcC_{11}S-/C_{11}SAu$ SAMs containing different populations of clustered vs. isolated ferrocenes, permitted us to establish the molecular basis of the stress generation. Our results are consistent with the redox-induced deflection of a $FcC_{11}SAu$ microcantilever being predominantly driven by a monolayer volume expansion resulting from collective re-orientational motions

caused by the complexation of the perchlorate ions to the surface-immobilized ferroceniums.

In their high-pressure electrochemical study, Cruañes et al attributed the monolayer volume expansion to a structural transformation required for the complexation of the counter ion with the oxidized ferrocenium in the sterically constrained SAM.[1] *In-situ* spectroelectrochemical investigations of ferrocene-terminated SAMs have played an integral role in elucidating the structural transformations accompanying the redox reaction.[2-14] A recent *in-situ* Fourier transform surface-enhanced Raman spectroscopy (FT-SERS) study of FcC_4COOC_nSAu SAMs (where n = 3, 6, 9, and 11) suggested that ferrocene oxidation in perchlorate electrolyte causes the alkyl chains to adopt a more perpendicular orientation with respect to the electrode surface.[6] Likewise, Fourier-transform infrared reflection adsorption spectroscopy (FT-IRRAS) of a $Fc(CH_2)_{11}$SAu monolayer also indicated a more perpendicular orientation of the alkyl chains with ferrocene oxidation.[4,5,14] However, FT-IRRAS also showed that the simple substitution of the methylene group immediately adjacent to the ferrocene for an electron withdrawing group, resulted in only the cyclopentadiene rings changing their orientation to allow for anion complexation. This was independently observed for $FcCOO(CH_2)_{11}$SAu[2] and $FcCO(CH_2)_n$SAu[3] (where $n \leq 9$) SAMs. The spectroelectrochemical studies cited above were carried out in perchlorate. However, the nature of the electrolyte has been shown to have strong effects on the redox-induced structural transformation. In an FT-SERS study, Valincius et al. demonstrated that strong ion paring of the counter ion with the oxidized ferrocenium in a FcC_4COOC_9SAu monolayer resulted in a rigid two-dimensional ionic layer, whereas weaker ion pairing gave a structurally less ordered assembly and rendered the SAM susceptible to ion/solvent penetration.[8]

To this end, chemically well-defined ferrocene-terminated SAMs provide a relatively simple and versatile system, enabling one to systematically investigate the role of molecular order, intermolecular interactions, and anion effects on the magnitude and reversibility of the potential-induced bending of ferrocenylalkanethiolate functionalized gold-coated cantilevers. The present work considers the following ferrocene-terminated monolayers: $FcCO(CH_2)_{11}SH$, $Fc(CH_2)_{12}SH$, and $Fc(CH_2)_6SH$, which are respectively denoted $FcCOC_{11}SH$, $FcC_{12}SH$, and FcC_6SH. We also investigate the dynamically controlled actuation and surface stress properties of a $FcC_{11}SAu$ modified microcantilever in the presence of different anions.

3.2 Experimental

3.2.1 Materials and Methods

The following compounds were used without any further purification: 12-bromododecanoic acid (≥98%, Fluka), 11-bromoundecanoic acid (≥98%, Fluka), 6-bromohexanoic acid (≥97%, Fluka), ferrocene (Fc, ≥98%, Fluka), perchloric acid ($HClO_4$, 70%, Fluka), sodium perchlorate ($NaClO_4$, 98%, Sigma-Aldrich), sodium fluoride (NF, 99+%, Sigma Aldrich), sodium nitrate (99.0%, Sigma Aldrich), sodium tetrafluoroborate (Alfa Inorganics, MA, $NaBF_4$), and sodium hexafluorophosphate (99%, Strem Chemicals, MA, $NaPF_6$).

The ferrocenylalkylthiolates $Fc(CO)(CH_2)_{11}SAu$, $Fc(CH_2)_{12}SAu$, $Fc(CH_2)_{11}SAu$, and $Fc(CH_2)_6SAu$ were prepared according to the procedure of Creager and Rowe,[15] starting from ferrocene and either 12-bromododecanoic acid, 11-bromoundecanoic acid (≥98%, Fluka) or 6-bromohexanoic acid. The identity and purity of the product was

verified by thin layer chromatography (silica gel, hexanes/ethyl acetate 99:1 v/v) and ^{1}H NMR (400 MHz, $CDCl_3$) and are consistent with those previously reported.

All aqueous electrolyte solutions were prepared with deionized-distilled water obtained by further purification of distilled water with a Milli-Q Gradient system (Millipore, Bedford, MA). The resistivity of the purified water was 18.2 MΩ·cm, and its surface tension, measured at 24 °C, was 72 $mN \cdot m^{-1}$. The perchlorate electrolyte solution contained 0.01 M $HClO_4$/0.10 M $NaClO_4$ (pH 3.1), whereas the 0.10 M $NaPF_6$ (pH 2.3), 0.10 M $NaBF_4$ (pH 3.0), 0.10 M $NaNO_3$ (pH 5.4), and 0.10 M NaF (pH 7.1) electrolyte solutions contained no added acid. A refractive index of 1.33 measured at 20 ºC and 589 nm with an AR200 Digital Handheld Refractometer (Reichert Analytical Instruments, USA) was obtained for all the electrolyte solutions. Prior to the electrochemical measurements, the electrolyte solutions were purged with nitrogen for at least 20 minutes.

3.2.2 Preparation of Gold-Covered Substrates and SAMs

V- and rectangular-shaped silicon nitride microcantilevers were purchased from Veeco (MLCT-NOHW, Santa Barbara, CA). A single chip substrate has six microcantilevers of different geometric dimensions and spring constants (Figure 1.9). The experiments described in the present study use the V-shaped microcantilevers with k of 0.01 and 0.13 $N \cdot m^{-1}$, as well as the rectangular-shaped microcantilever of k = 0.02 $N \cdot m^{-1}$. An independent assessment of the microcantilever k was performed when the magnitude of the deflection was markedly different as described in Chapter 2 (section 2.3.5). The typical dimensions of the microcantilevers are provided by the manufacturer and the experimentally determined spring constants for the microcantilevers are listed in Table 1.1. When the dimensions of the microcantilevers were limited for a given

analytical method, the microcantilevers were substituted with macroscopic B270 glass slides purchased from Esco Products, Inc. (Oak Ridge, NJ).

The Veeco microcantilever/chip supports and B270 glass slides cleansing procedure and metal deposition is outlined in the previous chapter. Following the metal deposition, the gold-coated substrates were subsequently functionalized by immersing the samples for ~12 hours into one of the following 1 mM thiol solutions: $FcC_{12}SH$ and FcC_6SH (80:20 absolute EtOH/THF) or $FcCOC_{11}SH$ (95 % EtOH). Immediately prior to the electrochemical experiments, the thiol-modified substrates were rinsed copiously with absolute ethanol and dried with nitrogen. As already mentioned, Whitesides and co-workers have demonstrated the preferential chemisorption (>100:1) of *n*-alkanethiols and ferrocenylalkanethiols to the Au-coated side of a substrate compared to physisorption of the material to the silicon nitride side.[16,17]

3.2.3 Spectroscopic Ellipsometry

The ellipsometric thicknesses of the ferrocene-terminated SAMs and the optical constants (*n* and *k*) of the supporting gold layer were determined using a multiwavelength ellipsometer equipped with a QTH lamp and rotating compensator (Model M-2000V, J.A. Woollam Co, Inc., Lincoln, NE). All measurements were performed in air at an incident angle of 70° and a wavelength range of 370 nm to 1000 nm. Five to six different spots on each substrate surface were analyzed and the results averaged. The complex refractive index ($\hat{n} = n - ki$) of the freshly-evaporated gold films was first calculated from a three-layer model: glass (0.92 mm)/Ti (1.2 nm)/Au (48 nm). The plots of Ψ and Δ vs. wavelength (λ) obtained for the bare gold were fit using the Levenberg-Marquardt non-

linear optimization algorithm of the vendor's WVASE32® software. The titanium and gold film thicknesses were fixed to those measured by the calibrated quartz crystal monitor during thermal evaporation. The $n(\lambda)$ and $k(\lambda)$ values provided in the vendor's materials database for polycrystalline titanium and BK7 glass were used in the fitting process. The complex refractive index of the evaporated gold was thus determined to be 0.18 - 4.86i at the surface plasmon excitation λ of 780 nm. This $\hat{n}$ value is very close to the literature value for bulk gold, 0.174 - 4.86i.[18]

3.2.4 Fourier Transform Infrared Reflection–Absorption Spectroscopy

The FT-IRRAS measurements on FcRSAu-coated glass slides were collected using a Bio Rad FTS-6000 Fourier transform infrared spectrometer. The measurement was carried out with a resolution of 2 cm^{-1} and each spectrum was composed of 10 co-added scans. The optical path was purged with dry nitrogen before and during the measurement and liquid nitrogen cooled the mercury-cadmium-telluride detector.

3.2.5 Electrochemical Characterization

All CV experiments were carried out using an Epsilon potentiostat (Bioanalytical Systems, Inc., West Lafayette, IN). A custom-built, one-compartment three-electrode cell was employed, where the FcRSAu substrate served as the working electrode, the counter electrode was a platinum wire (99.9%, Alfa Aesar), and all potentials are reported with respect to an aqueous Ag/AgCl reference electrode (3 M NaCl, Bioanalytical Systems).

3.2.6 Electrochemical SPR Spectroscopy

Redox-induced thickness changes were investigated with a SR7000 SPR instrument (Reichert, Inc., Depew, NY) where a custom-built electrochemical cell, fitted with the reference and counter electrodes, was mounted onto the SAM functionalized side of the gold-coated slide (working electrode). For the SPR spectroscopy measurements, 1.2 nm of titanium and 48 nm of gold were evaporated on the macroscopic B270 glass slides. The CVs were acquired at a scan rate of 10 $mV \cdot s^{-1}$ in an aqueous solution of 0.10 M $NaClO_4$/0.01 M $HClO_4$. The SR7000 SPR instrument employs the Kretschmann-type attenuated total reflection configuration[19,20], where surface plasmons are excited with TM-polarized incident light from a 15 mW GaAlAs emitter (peak emission λ = 780 nm) which is focused through a sapphire prism onto the underside of the gold-coated glass. The glass slide was optically coupled to the base of the sapphire prism using immersion oil (Cargille Type A liquid, $n_{589\,nm}^{20°C}$ = 1.515). All experiments were carried out at 25 ºC and the temperature at the gold/solution interface is controlled to within ± 0.015°C by a Peltier device. The total internally reflected light from the gold/solution interface is detected with a 3696-pixel CCD linear array and the optical pixel signals are digitized with a 14-bit analogue-to-digital converter. A National Instruments Labview interface (SR7000 Alpha Instrument version 2.24) is used for data acquisition and transfer. The change in minimum pixel was monitored with a time resolution of 2 to 3 s as function of the applied potential which was externally controlled using an Epsilon potentiostat (Bioanalytical systems, Inc., West Lafayette, IN). The minimum pixel shifts recorded during potential cycling were converted to resonance angle changes ($\Delta\Theta_m$) using a pixel-to-incident angle relation, i.e. 1 pixel = 0.00502°, established through calibration of the SR7000 instrument.[10] Film thickness changes (Δd) were derived from the resulting $\Delta\Theta_m$

Table 3.1 Layer Models and Parameters for the Fresnel Calculations Table **(A)** FcC_6SAu, **(B)** $FcC_{12}SAu$, and **(C)** $FcCOC_{11}SAu$.

$AuSC_nFc/\ Fc^+\text{-}ClO_4^-$				
	Layer	*d* (nm)	*n*	*k*
	Prism	∞	1.761[a]	0
	Glass slide	∞	1.515[b]	0
	Ti	1.2	2.768[c]	3.307[c]
	Au	48.0	0.181	4.856
(A)	$-SC_6Fc$	1.1	1.48	0
	$-SC_6Fc^+\text{-}ClO_4^-$	1.45		
(B)	$-SC_{12}Fc$	2.1	1.464	0
	$-SC_{12}Fc^+\text{-}ClO_4^-$	2.35		
(C)	$-SC_{11}OCFc$	2.6	1.464	0
	$-SC_{11}OCFc^+\text{-}ClO_4^-$	2.8		
	$NaClO_{4\ (aq)}$	∞	1.328[d]	0

[a]Value at 780 nm and 24°C from *American Institute of Physics Handbook*; Gray, D.E. Ed; 3rd ed., McGraw-Hill, Inc.: New York, **1972**.
[b] Value at 780 nm provided by Reichert Analytical, Inc.
[c] Value at 780 nm from *Handbook of Optical Constants of Solids III*; Palik, E. D.; Academic Press: New York, **1985**.
[d] The refractive index of the perchlorate solution, measured at 589 nm, was found to be the same as that of water. Water value, relative to air, at 780 nm and 25°C from *J. Phys. Chem. Ref. Data* **1998**, *27*, 761–774.

using Fresnel multilayer modeling (Winspall software version 2.20, MPI-P, Mainz, Germany). Listed in Table 3.1 are the parameters used in a multilayer Fresnel analysis to account for the orientational changes occurring within the electroactive film. In the Fresnel multilayer analysis, the $n(\lambda)$ and $k(\lambda)$ values for polycrystalline titanium and glass slides used in the fitting process were provided in the vendor's materials database. The

$n(\lambda)$ and $k(\lambda)$ of the evaporated gold were previously determined to be 0.18 – 4.86i at the surface plasmon excitation wavelength of 780 nm.[10] Based on previous ellipsometric studies, an n of 1.48[12] for FcC_6S– and 1.46[12,14] for both $FcC_{12}S$– and $FcCOC_{11}S$– are taken as fixed values.

3.2.7 Electrochemical Microcantilever Measurements

The static mode of operation was employed to monitor the deflection of the ferrocenylalkanethiolate-coated microcantilever as a function of an applied potential (scan rate of 5 $mV \cdot s^{-1}$). The custom-built, reflecting beam deflection set-up integrating a standard AFM microcantilever with a potentiostat has been described in Chapter 2 (section 2.3.4).[21,22] In brief, the functionalized microcantilever is clamped and immersed into the three-probe electrochemical set-up. The modified gold-coated microcantilever (1.6 mm × 3.4 mm) serves as both the working electrode and the reflective platform. All potentials are reported with respect to an Ag/AgCl aqueous electrode (3 M NaCl, Bioanalytical Systems) and a platinum wire (99.99%, Alfa Aesar, USA) was used as the counter electrode. A low powered (1 mW, 635 nm) laser is focused at the apex of the microcantilever where the bending is monitored by following the position of the reflected laser beam on a position sensitive detector (PSD IL10, ON-TRAK Photonics, Inc.). The PSD signal (ΔS), converted from volts to a length scale, has been corrected for the change in angle resulting from the reflected laser beam passing through the solution/air ($n_{589nm}^{20°C}=1.33/n_{589nm}^{20°C}=1.00$) boundary (Snell's Law).[23,24] Nanometer-scale microcantilever deflections, Δz (equation 1.20), is directly proportional to the induced surface stress .[23,25,26] Equations 1.24 (rectangular cantilever) and 1.25 (V-shaped cantilever) for the

differential surface stress derived by Grütter and co-works[23,25,26] are given in Chapter 1. It is important to recognize that although the electrochemical microcantilever experiments reported here were done on different microcantilevers, the same response behavior was consistently observed. Furthermore, in the previous chapter it was established that the magnitude of the observed $\Delta\sigma$ (–0.17 to –0.23 $N \cdot m^{-1}$) is independent of k (~0.01 to ~0.13 $N \cdot m^{-1}$) and all values reported herein are an average of at least 15 independent microcantilever experiments with varying k.

3.3 Results and Discussion

3.3.1 Characterization of the Ferrocene-Terminated Monolayers

The ferrocene surface coverages, molecular order, film thicknesses, and redox-induced change in the monolayer thicknesses were investigated for FcC_6SAu, $FcC_{12}SAu$ and $FcCOC_{11}SAu$ SAMs formed on macroscopic gold-coated glass slides prepared in the same manner as the microcantilevers. From the anodic scan of CVs obtained in 0.10 M $NaClO_4$/0.01 M $HClO_4$, an average surface coverage of 4.7 (±0.4) × 10^{-10} $mol \cdot cm^{-2}$, corresponding to a molecular packing density of 2.9 (±0.2) $molecules \cdot nm^{-2}$ (or ~0.35 nm^2 per molecule) was found for all the FcRSAu SAMs investigated (Table 3.2, column 1). This value is in good agreement with that expected for a loosely hexagonal close-packed assembly (i.e., 4.5 × 10^{-10} $mol \cdot cm^{-2}$), based on the 0.66 nm spherical diameter of the terminal ferrocene.[27,28] Ellipsometric film thicknesses of 1.1 ± 0.1 nm, 2.1 ± 0.2 nm and 2.6 ± 0.1 nm were obtained in air for FcC_6SAu, $FcC_{12}SAu$, and $FcCOC_{11}SAu$, respectively, and correspond well with previously published results for similar ferrocene-

Table 3.2 Ferrocene Surface Coverages, SPR and Film Thickness Changes, FT-IR, and Surface Stress Results of FcRSAu SAMs in Perchlorate Electrolyte.

FcRAu SAM	Γ_{Fc} ($\times 10^{-10}$ mol·cm^{-2})	$\Delta\Theta_m$ (°)	Δd (nm)	$\nu_s(CH_2)$ cm^{-1}	$\nu_a(CH_2)$ cm^{-1}	$\Delta\sigma$ (N·m^{-1})
FcC_6SAu	4.9 ± 0.4	0.020 ± 0.001	0.25			–0.11 ± 0.04
$FcC_{12}SAu$	4.6 ± 0.3	0.021 ± 0.002	0.26	2853	2925	–0.21 ± 0.05
$FcCOC_{11}SAu$	4.8 ± 0.3	0.020 ± 0.002	0.24	2853	2924	–0.17 ± 0.02

terminated monolayers.[10,22] The ferrocene surface coverages and film thicknesses are consistent with a full monolayer coverage.

The monolayer structure is influenced by several factors such as the chain length and composition as well as the terminal functional group.[29] It has been demonstrated by several groups that the bulky size of the ferrocene group leads to a more fluid-like monolayer structure compared to the *n*-alkanethiol analogue.[2,4,5,9,12,13,30-32] *Ex-situ* FT-IRRAS was used to evaluate the chain contributions to the monolayer structural order. The CH_2 symmetric ($\nu_s(CH_2)$) and asymmetric ($\nu_{as}(CH_2)$) vibration modes observed at 2853 cm^{-1} and 2925 cm^{-1}, respectively, for the $FcC_{12}SAu$ and $FcCOC_{11}SAu$ suggest a similar disordered, liquid-like environment for all the SAMs (Table 3.2, columns 3 and 4).[30] The band positions for the FcC_6SAu monolayer could not be accurately resolved because of the low signal-to-noise ratio.[30] Our results agree well with previously

published FT-IR investigations of various ferrocene-terminated alkylthiol monolayers.[2,4,9,30,31]

In-situ ESPR was used to investigate the change in film thickness (Δd) as a result of redox-induced structural transformations. Surprisingly, a shift in the SPR resonance angle ($\Delta\Theta_m$) of 0.020 ± 0.002° was measured at 0.7 V (vs. Ag/AgCl) in perchlorate electrolyte for all the FcRSAu SAMs investigated (Table 3.2, column 2). We have interpreted the measured $\Delta\Theta_m$ as resulting from a change in the orientation of the Fc^+–bearing alkylthiolate chains with respect to the gold electrode surface to facilitate complexation with the ClO_4^-. From a multilayer Fresnel analysis (Winspall software version 2.20, MPI-P, Mainz, Germany) an average Δd value of 0.25 ± 0.01 nm was derived from $\Delta\Theta_m$ for all the FcRSAu SAMs (Table 3.2, column 2). Our thickness changes are within the range of 0.1–0.3 nm reported in previous SPR[10,11] and ellipsometry[3,12-14] investigations for the oxidation of ferrocene-terminated SAMs in perchlorate electrolyte. However, it is not expected that ferrocene-terminated monolayers possessing differing degrees of ordering and redox site interactions would give rise to equivalent Δd values. Unfortunately, SPR does not permit a definitive comment on the nature of the structural orientation of the electroactive film.

3.3.2 Influence of the Alkyl Chain on the Surface Stress

The importance of the alkyl chain length and chemical structure on the packing density, intermolecular environment and geometry of monomolecular assemblies has been well established.[29] Consequently, by varying these parameters, one can examine the effect of structural organization on the redox-elicited microcantilever response. Typical

voltammetric and corresponding $\Delta\sigma$ responses obtained for the oxidation/reduction in 0.10 M $NaClO_4$/0.01 M $HClO_4$ of $FcC_{12}SAu$, FcC_6SAu and $FcCOC_{11}SAu$ monolayers formed on AFM microcantilevers are shown in Figure 3.1. The CVs resemble those usually observed for single-component ferrocenylalkylthiolate monolayers on macroscopic polycrystalline Au electrodes,[2,22,33-38] and the electrochemical parameters for the FcRSAu monolayers in perchlorate are discussed in brief below. All the FcRSAu monolayers exhibited asymmetric peaks with non-zero values for the ΔE_p, which may indicate intermolecular interactions between the redox centers or that the SAM structure changes with the oxidation state of the redox center.[39,40] $E_{1/2}$ (vs. Ag/AgCl) values were found to be 0.38 V and 0.34 V for the $FcC_{12}SAu$ and FcC_6SAu modified microcantilevers, respectively. A significant positive shift in $E_{1/2}$ to 0.63 V is observed with the introduction of the electron-withdrawing carbonyl group (C=O) adjacent to the ferrocene moiety for the $FcCOC_{11}SAu$-microcantilevers. The ΔE_{fwhm}, determined after deconvolution of the main anodic peak,[33] provide a qualitative measure of the extent of interaction between the surface tethered ferrocene groups. For the $FcCOC_{11}SAu$-microcantilevers, a ΔE_{fwhm} of 0.089 V for the anodic peak is close to the ideal value of 90.6 mV[41], indicating that the ferrocene groups have similar microenvironments with minimal interactions between the redox centers. Whereas, narrower values for the ΔE_{fwhm} of the main oxidation peaks for $FcC_{12}SAu$ (0.055 V) and FcC_6SAu (0.073 V) modified microcantilevers were found. The presence of electrochemically distinct ferrocene microenvironments is evidenced by shoulder peaks found on the negative side of the main oxidation peaks of the FcC_6SAu and $FcC_{12}SAu$ SAMs.[28,30,33,38,42-45] Distinct molecular

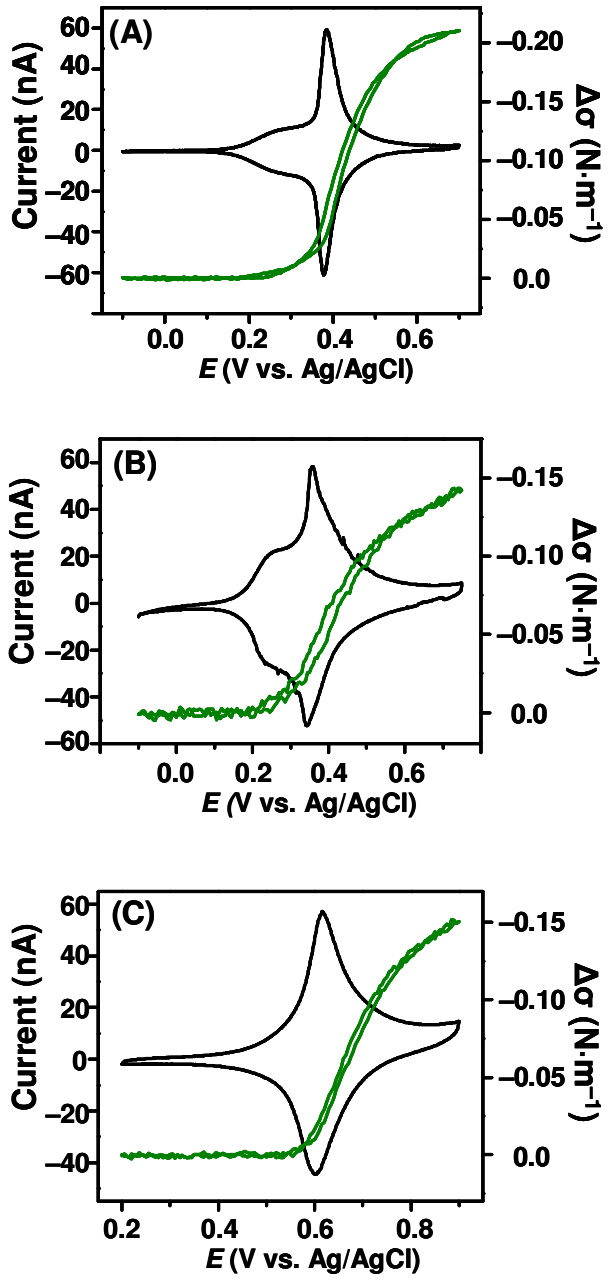

Figure 3.1 Typical CVs (left axis, —) and corresponding differential surface stress, $\Delta\sigma$, (right axis, —) responses for **(A)** $FcC_{12}SAu$, **(B)** FcC_6SAu and **(C)** $FcCOC_{11}SAu$ modified microcantilever substrates in 0.10 M $NaClO_4$/0.01 M $HClO_4$. Scan rate = 5 $mV \cdot s^{-1}$.

environments are possible in single-component monolayers because the ferrocene alkyl chains found at grain boundaries or defect sites are postulated to be less constrained than the surrounding matrix, having greater conformational mobility as well as increased accessibility to the surrounding electrolyte solution.[1,37,46,47]

Figure 3.1 shows the effect of the chain length on the potential-induced response of microcantilevers modified with either $FcC_{12}SAu$ (Figure 3.1A) or FcC_6SAu SAMs (Figure 3.1B). While the length of the thiolate-to-ferrocene alkyl spacer had little effect on the electrochemical properties, a marked difference is observed in the vertical deflection. A compressive surface stress of -0.21 ± 0.05 $N \cdot m^{-1}$ was observed for the $FcC_{12}SAu$-modified microcantilevers. This result is in good agreement with the previously investigated $FcC_{11}SAu$-modified microcantilever (-0.20 ± 0.04 $N \cdot m^{-1}$), where the observed $\Delta\sigma$ was attributed predominantly to a monolayer volume expansion induced by changes in the ferrocenylalkanethiolate orientation accompanying the $Fc^+ - ClO_4^-$ complexation at the monolayer/solution interface.[21] When the alkyl spacer chain length is reduced from 12 to 6 CH_2s (i.e., FcC_6SAu SAM), a decrease in $\Delta\sigma$ of ~50% to -0.11 ± 0.04 $N \cdot m^{-1}$ is observed. This proportional decrease concurs with the linear relation of additive chain-chain interactions which contribute ~1.0 $kcal \cdot mol^{-1}$ of stabilization to the SAM for each methylene group in the chain.[48] A linear chain-length dependence of $\Delta\sigma$ has been previously observed for the self-assembly and organization of *n*-alkanethiols on gold-coated microcantilevers.[49] More recently, a pH titration of carboxylic acid modified gold-coated microcantilevers also showed a chain-length dependence on the direction and amplitude of the cantilever response.[50]

The magnitude of the maximum deflection remained relatively constant for the FcC_6SAu-modified microcantilevers, although variability in cantilever profile appearance was observed. A monolayer capacitance of 2.0 (±0.1) $\mu F \cdot cm^{-2}$ was found for the FcC_6SAu SAMs in perchlorate solution.[51] This value is close to the capacitance measured for the $FcC_{11}SAu$[1] SAM of 1.8 (±0.2) $\mu F \cdot cm^{-2}$, as well as other published results for $FcC_{11}SAu$[1] and $FcCO_2C_{11}SAu$[52] SAMs of 1.5 to 2.0 $\mu F \cdot cm^{-2}$. The FcC_6SAu SAM should therefore be reasonably impermeable to ions. It is commonly known that shorter chain alkanethiols promote a loss of film organization, which results in a more fluid-like packing density and poorer coupling between the alkyl chains.[29] The microcantilever is critically sensitive to the uniformity and robustness of the SAM layer and small changes will generate a different surface stress behavior due to differences in the lateral interactions which give rise to the surface force at the modified cantilever.[53-62] We therefore attribute the irregularity of the cantilever response to an inconsistent film formation arising from the inherent disorder imparted by the short alkyl chain.

The effect of polarity on the redox-induced microcantilever bending was investigated by replacing the methylene adjacent to the ferrocene molecule with a carbonyl group (C=O). The $FcCOC_{11}SAu$-modified microcantilever exhibits a reversible deflection upon potential cycling in 0.10 M $NaClO_4$/0.01 M $HClO_4$ (Figure 3.1C), with a maximum compressive surface stress of –0.17 ± 0.02 $N \cdot m^{-1}$. There are several competing intermolecular forces at the monolayer/solution interface that are likely to contribute to the overall surface stress for the $FcCOC_{11}SAu$-modified microcantilever. The introduction of a dipole moment is expected to affect the molecular organization of the electroactive SAM. Spectroscopic studies have shown that the dipole will align itself

in order to maximize both interchain hydrogen bonding and non-covalent interactions with the aqueous environment.[2,30,32] However, given that the $\nu_s(CH_2)$ and $\nu_a(CH_2)$ vibration modes and the molecular packing density found for the $FcCOC_{11}SAM$ (3.0 ± 0.1 molecules·nm^{-2}) are comparable to both the $FcC_{11}SAu$ (2.9 ± 0.2 molecules·nm^{-2}) and $FcC_{12}SAu$ (2.8 ± 0.2 molecules·nm^{-2}) SAMs, it is anticipated that the extent of the alkyl chain ordering is similar. It is unlikely that the perturbation experienced by the molecular packing of the aliphatic chains is a major component contributing to the decrease in the observed surface stress. The electron withdrawing nature of the C=O adjacent to the ferrocene moiety contributes to an inefficiency of the ClO_4^- anions to effectively neutralize and screen the charge between neighboring oxidized ferrocenium cations.[63] Therefore, Coulomb repulsion between the ferrocenium moieties would be expected to increase the observed compressive surface stress, with respect to $FcC_{11}SAu$ and $FcC_{12}SAu$, and this is not the case.

In order to account for the decrease in the compressive stress, we considered the fact that the introduction of the C=O is not only known to perturb the molecular packing density, but it has also been shown to significantly alter the interfacial properties upon oxidation of the ferrocene to ferrocenium. Both contact angle[52,64] and AFM-adhesion force[65] measurements have reported that the oxidation of the surface-confined ferrocene adjacent to a polar carboxylate ($FcCO_2C_{11}SAu$) or carbonyl ($FcCOC_{15}SAu$) group results in a notably more hydrophilic interface. For example, Abbott and Whitesides showed a significant contact angle change from 71° to 43° upon oxidation of the $FcCOC_{15}SAu$.[64] In the previous chapter, we reported a markedly smaller change in the static contact angle from 77° to 65° for the oxidation of the $FcC_{11}SAu$ SAM in perchlorate solution.[21]

Therefore, we anticipate the increased hydrophilicity for the $FcCOC_{11}SAu$ SAM will contribute to a greater decrease in the interfacial (monolayer/water) surface tension so that a *tensile* stress would be of greater consequence to the overall surface stress change compared to the all-methylene analogue. Moreover, the high-pressure electrochemical investigation of a surface-confined ferrocene SAM in perchlorate by Cruañes et al. demonstrated that redox-active SAMs exhibiting different voltammetric responses impose different volume constraints on the oxidation process.[1] The oxidation/reduction of the $FcCOC_{11}SAu$ SAM (Figure 3.1C) showed markedly different electrochemical properties compared to the $FcC_{12}SAu$ (Figure 3.1A) and FcC_6SAu (Figure 3.1B) SAMs. As mentioned in Section 3.1, FT-IRRAS also suggests that it is only the cyclopentadiene rings that change their orientation with respect to the electrode surface. The decrease in the compressive stress is most likely a result of the variation in the volume constraints imposed on the charge-transfer and ion paring event for the $FcCOC_{11}SAu$ SAM. It is anticipated that the difference in lateral tension arising from such a molecular reorientation/volume expansion would be reflected in the microcantilever response.

A comparison of the $\%\Delta z$ and Φ_{Fc^+} for the anodic scans of FcC_6SAu–, $FcC_{11}SAu$–,[21] $FcC_{12}SAu$–, and $FcCOC_{11}S$–Au modified microcantilevers is shown in Figure 3.2. Independent of the chain structure and consistent with the number of interacting ferroceniums,[33,44,66] cantilever bending is detectable only after ~15–20% conversion of the ferrocene to ferrocenium. This behavior continues to support our original hypothesis that the cantilever responds to collective in-plane interactions rather than individual ion pairing as outlined in Chapter 2.[21]

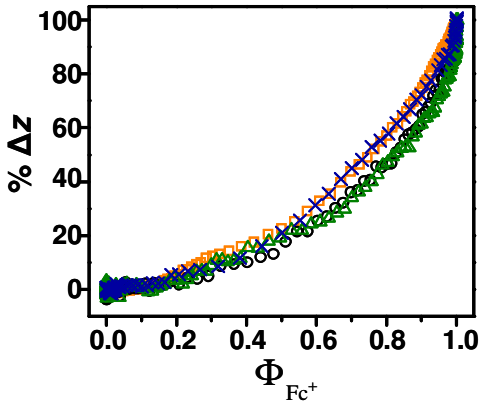

Figure 3.2 Plot of the % change in the cantilever deflection vs. the fractional coverage of the ferrocenium (Φ_{Fc^+}) for the anodic scans of $FcC_{12}SAu$ (□), $FcC_{11}SAu$ (×), FcC_6SAu (Δ) and $FcCOC_{11}SAu$ (○) modified microcantilever substrates.

3.3.3 Influence of the Anion on the Surface Stress Change of $FcC_{11}SAu$ Microcantilevers

Summarized in Table 3.3 are the $\Delta\sigma$ and electrochemical characteristics observed for the $FcC_{11}SAu$ modified microcantilevers in $NaPF_6$, $NaClO_4$, $NaBF_4$, $NaNO_3$, and NaF solutions. Several groups employing different ferrocene terminated alkanethiols have investigated the relative ion pairing strength of different anions with the surface-bound ferrocenium.[8,27,36,67,68] Our results are consistent with the observed trend that larger, poorly solvated anions, such as PF_6^-, ion pair more readily than hydrated, smaller anions

Table 3.3 Surface Stress and Electrochemical Characteristics of $FcC_{11}SAu$-Modified Microcantilevers as Depicted in **Figure 3.3**.

Anion	$\Delta\sigma$ (N m^{-1})	$E_{1/2}$ (mV)	ΔE_{fwhm} (mV)	ΔE_p (mV)	Γ_{Fc^+} [b] ($\times 10^{-10}$ moles·cm^{-2})
PF_6^-	–0.21 ± 0.05	320 ± 11	46 ± 12	10 ± 4	4.8 ± 0.2
ClO_4^- [a]	–0.20 ± 0.04	385 ± 6	42 ± 12	7 ± 2	4.7 ± 0.3
BF_4^-	–0.13 ± 0.04	444 ± 4	47 ± 10	7 ± 1	4.3 ± 0.3
NO_3^-	–0.11 ± 0.03	510 ± 3	114 ± 13	10 ± 3	3.6 ± 0.1
F^-	–0.06 ± 0.03	585 ± 14	181 ± 37	88 ± 14	2.2 ± 0.3

[a] These values are taken from Chapter 2 for comparison of all studied electrolytes.
[b] The electrogenerated concentration of surface-confined ferrocene (Γ_{Fc^+}) was determined from voltammetric scans obtained in the appropriate electrolyte for $FcC_{11}SAMs$ formed on gold-coated macroscopic B270 glass slides prepared in the same manner as the microcantilevers.

such as F^-. The relative strength of the ion pair is evidenced by asymmetry of the redox peaks, the electrogenerated ferrocenium concentration (Γ_{Fc^+}, Table 3.3, column 5) and a positive shift in the $E_{1/2}$ (vs. Ag/AgCl) values (Table 3.3, column 2). The positive shift in $E_{1/2}$ is also an indirect measure of the increasing difficulty for the anions to release their associated water molecules so that they can ion pair with the monolayer-bound ferrocenium.[8,36,67,68] A high-pressure electrochemical investigation of $FcC_{11}SAu$ SAMs in ClO_4^- and NO_3^- showed that each electrolyte imposed different volume constraints on the charge transfer reaction.[1] As mentioned in section 3.1, the FT-SERS study of Valincius et al. also found different structural rearrangements for the surface-confined ferrocene SAM depending on the anion identity.[8] To this end, we investigate how ion

pairing with different anions affects the magnitude and reproducibility of the $\Delta\sigma$ for a $FcC_{11}SAu$-modified microcantilever.

Shown in Figure 3.3 are the typical current and $\Delta\sigma$ responses obtained for successive CV scans of a $FcC_{11}SAu$-modified microcantilever in the different electrolyte solutions. The potential was scanned between –0.10 V to +0.70 V at a constant rate of 5

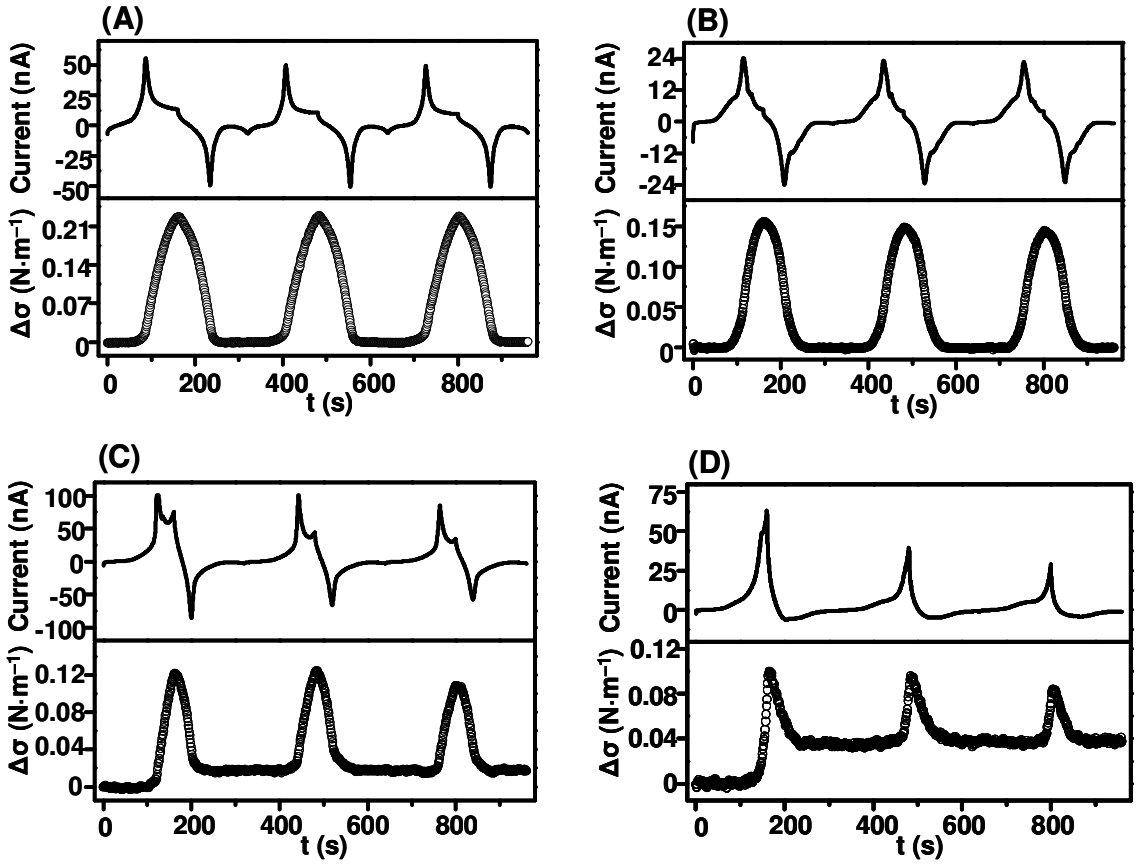

Figure 3.3 Typical CV traces (top panel) and corresponding differential surface stress (bottom panel) responses of $FcC_{11}SAu$ modified microcantilever substrates in **(A)** 0.10 M $NaPF_6$ **(B)** 0.10 M $NaBF_4$ **(C)** 0.10 M $NaNO_3$ and **(D)** 0.10 M NaF electrolyte solutions.

$mV \cdot s^{-1}$ and a maximum deflection was observed at the switching potential of +0.70 V. The deflection/surface stress of the $FcC_{11}SAu$ microcantilever and the quantity of electrogenerated ferrocenium is strongly dependent on the nature of the electrolyte (Figure 3.3). While the ClO_4^- (Chapter 2, Figure 2.2), PF_6^- (Figure 3.3A), and BF_4^- (Figure 3.3B) anions gives rise to reversible and stable microcantilever deflections, NO_3^- (Figure 3.3C) and F^- (Figure 3.3D) anions produce an obvious irreversible deformation in the microcantilever actuation. The likely source of deformation will be addressed below.

The PF_6^- anion (Figure 3.3A) has a similar ionic size and solvation free energy relative to the ClO_4^-, and is known to form a strong ion pair with the oxidized Fc^+.[8,35,67,68] A Γ_{Fc^+} of 4.8 (±0.2) × 10^{-10} $mol \cdot cm^{-2}$ for the $Fc^+ - PF_6^-$ ion pair concurs with the theoretical maximum coverage of ferrocene calculated from the close-packing of ferrocene spheres (i.e. 4.5×10^{-10} $mol \cdot cm^{-2}$), indicating a 1:1 ion pair formation.[28,69] Not surprisingly, the $\Delta\sigma$ of –0.21 (±0.05) $N \cdot m^{-1}$ for the $Fc^+ - PF_6^-$ ion pair is in good agreement with our previously reported value of –0.20 (±0.04) $N \cdot m^{-1}$ for the $Fc^+ - ClO_4^-$ system.[21] The small increase in compressive stress could be a result of slight differences in environmental or steric constraints involved in the ion pair complexation forcing the alkyl chains farther apart.[1] Similar to PF_6^-, BF_4^- anions also form ion pairs with the electrochemically-generated ferroceniums, as evidenced in the stability and reproducibility of both the microcantilever deflection and CV results (Figure 3.3B). However, a weaker association of the BF_4^- anion with the oxidized $Fc^+C_{11}SAu$ monolayer

is reflected in a slight decrease of ~6% in Γ_{Fc^+} for the $Fc^+ - BF_4^-$ ion pair and a positive shift of ~125 mV in $E_{1/2}$. There is a notable decrease in the $\Delta\sigma$ value to –0.13 (±0.03) $N \cdot m^{-1}$. This suggests that the weaker association of the BF_4^- anions with the $Fc^+C_{11}SAu$ monolayer is not able to disrupt the monolayer organization to the same extent as the ClO_4^- and PF_6^- anions which form a rigid 2-dimensional ionic layer.[70,71] Orlwoski et al. have recently investigated the reorganization energy of ferrocene-peptide monolayers in the presence of PF_6^- and BF_4^- anions.[72] Their study showed an increase in reorganization energy for the $Fc^+ - BF_4^-$ ion pair, which was attributed to the weaker association of the BF_4^- anion with the ferrocenium cation, and possibly a perturbation of the monolayer structural integrity due to anion penetration.[72]

A clear difference in the $FcC_{11}SAu$-modified microcantilever response is evident with increasing hydrophilicity of the anion. The inability to ion pair effectively is readily reflected in a significant decrease in Γ_{Fc^+} by ~25% and ~54% for the $Fc^+ - NO_3^-$ and $Fc^+ - F^-$, respectively. Considering the microcantilever profiles obtained during the second CV scan for $Fc^+ - NO_3^-$ and $Fc^+ - F^-$, the resulting $\Delta\sigma$ was found to be –0.11 (±0.03) $N \cdot m^{-1}$ and –0.06 (±0.03) $N \cdot m^{-1}$, respectively. It should be pointed out that there is a non-linear correlation between Γ_{Fc^+} and $\Delta\sigma$ measured for the series of anions. For $Fc^+ - NO_3^-$ and $Fc^+ - F^-$ interactions, deducing the origin of the surface stress becomes more complicated. When ion pairing occurs less effectively, it is expected that Coulomb repulsions between the neighboring ferrocenium moieties will be of greater consequence for the lateral in-plane forces giving rise to the observed $\Delta\sigma$. Furthermore, a decrease in the peak current and a deformation in the microcantilever response are observed with

potential cycling for both NO_3^- (Figure 3.3C) and F^- (Figure 3.3D). It has been shown that the anion solvation directly influences the stability of the ferrocene-terminated monolayer.[8,27,36] More hydrophilic anions, such as NO_3^- and F^-, are transported with large amounts of water, inhibiting the extent of anion interaction with the ferrocenium cation.[8,27,36] Consequently, the ferrocene cation is subject to nucleophilic attack involving the demetallization of the ferrocene resulting in a loss of electroactivity.[2] The demetallization of the terminal ferrocene observed between the initial and subsequent oxidation and reduction cycles (Figure 3.3) is a probable source of the current decrease and the microcantilever deformation. Moreover, the inability of the anion to form contact ion pairs has been shown to result in electrolyte ions penetrating into the SAM.[8,36,68,73] This renders the underlying gold electrode surface susceptible to anion interactions under an applied potential, which would also contribute to the overall compressive microcantilever response.[74-78] Potential-induced surface stress changes have been investigated on free standing gold-functionalized microcantilevers where the adsorption of negative ions induced a compressive stress stress.[77,78] However, a monolayer volume expansion resulting from anion pairing with the surface-confined ferrocenium is still expected to occur but to a lesser extent than for ClO_4^- and PF_6^- to the overall surface and remains a contributor to the overall surface stress.

3.4 Conclusions

Chemically well-defined ferrocene-terminated SAMs provide a relatively simple and versatile system where the amplification of conformational transformations to

macroscopically measured deflection can readily be tuned. In the current study, it is demonstrated that the alkyl chain and anion play a crucial role in the magnitude and reversibility of the observed microcantilever bending. Investigating the affinity of the anion for the oxidized $Fc^{+}C_{11}SAu$ modified microcantilever made it possible to further substantiate the hypothesis that the magnitude of the observed microcantilever surface stress reflects the extent of the redox-induced perturbation of the structural organization of the monolayer. This work suggests that steric constraints and/or the ability of the complexing ion to induce organizational changes within the monolayer film play an important role in the magnitude of the observed cantilever bending in redox-induced actuation by SAMs. The results also demonstrate that the in-plane intermolecular forces associated with the molecular re-orientations vary depending on the chain length and dipole-dipole interactions introduced to the SAM-modified microcantilever. Finally, this study continues to demonstrate that the surface stress changes associated with the oxidation and subsequent reduction of an electroactive moiety confined at an organic monolayer/solution interface can induce a reversible micromechanical motion with controlled magnitude and direction which demonstrates that electroactive self-assembled monolayer films of well-defined structure can be used for electroactuating systems.

3.5 References

(1) Cruañes, M. T.; Drickamer, H. G.; Faulkner, L. R. *Langmuir* **1995**, *11*, 4089–4097.

(2) Popenoe, D. D.; Deinhammer, R. S.; Porter, M. D. *Langmuir* **1992**, *10*, 2521–2530.

(3) Viana, A. S.; Jones, A. H.; Abrantes, L. M.; Kalaji, M. *J. Electroanal. Chem.* **2001**, *500*, 290–298.

(4) Ye, S.; Sato, Y.; Uosaki, K. *Langmuir* **1997**, *13*, 3157–3161.

(5) Ye, S.; Haba, T.; Sato, Y.; Shimuza, K.; Uosaki, K. *Phys. Chem. Chem. Phys.* **1999**, *1*, 3653–3659.

(6) Kazakevičienė, B.; Valincius, G.; Niaura, G.; Talaikytė, Z.; Kažemėkaitė, M.; Razumas, V.; Plaušinaitis, D.; Teišerskienė, A.; Lisauskas, V. *Langmuir* **2007**, *23*, 4965–4971.

(7) Kazakevičienė, B.; Valincius, G.; Niaura, G.; Talaikytė, Z.; Kažemėkaitė, M.; Razumas, V. *J. Phys. Chem. B* **2003**, *1007*, 6661–6663.

(8) Valincius, G.; Niaura, G.; Kazakevičienė, B.; Talaikytė, Z.; Kažemėkaitė, M.; Butkus, E.; Razumas, V. *Langmuir* **2004**, *20*, 6631–6638.

(9) Shimazu, K.; Ye, S.; Sato, Y.; Uosaki, K. *J. Electroanal. Chem.* **1994**, *375*, 409–413.

(10) Norman, L. L.; Badia, A. *Langmuir* **2007**, *23*, 10198–10208 and references therein.

(11) Yao, X.; Wang, J.; Zhou, F.; Wang, J.; Tao, N. *J. Phys. Chem. B* **2004**, *108*, 7206–7212.

(12) Abrantes, L. M.; Kalaji, M.; Viana, A. S. *Russ. J. Electrochem.* **2002**, *38*, 39–43.

(13) Viana, A. S.; Abrantes, L. M.; Jin, G.; Floate, S.; Nichols, R. J.; Kalaji, M. *Phys. Chem. Chem. Phys.* **2001**, *3*, 3411–3419.

(14) Ohtsuka, T.; Sato, K.; Uosaki, K. *Langmuir* **1994**, *10*, 3658–3662.

(15) Creager, S. E.; Rowe, G. K. *J. Electroanal. Chem.* **1994**, *370*, 203–211.

(16) Laibinis, P. E.; Hickman, J. J.; Wrighton, M. S.; Whitesides, G. M. *Science* **1989**, *245*, 845–847.

(17) Hickman, J. J.; Ofer, D.; Zou, C.; Wrighton, M. S.; Laibinis, P. E.; Whitesides, G. M. *J. Am. Chem. Soc.* **1991**, *113*, 1128–1132.

(18) *Handbook of Optical Constants of Solids III*; Academic Press, Inc.: New York, 1985.

(19) Davies, J.; Faulkner, I. In *Surface Analytical Techniques for Probing Biomaterial Processes*; Davies, J., Ed.; CRC Press: Boca Raton, 1996, p 67–87 and references therein.

(20) Knoll, W. *Annu. Rev. Phys. Chem.* **1998**, *49*, 569–638.

(21) Norman, L. L.; Badia, A. *J. Am. Chem. Soc.* **2009**, *131*, 2328–2337.

(22) Quist, F.; Tabard-Cossa, V.; Badia, A. *J. Phys. Chem. B* **2003**, *107*, 10691–10695.

(23) Tabard-Cossa, V.; Godin, M.; Beaulie, L. Y.; Grütter, P. *Sens. Actuators B* **2006**, *119*, 352–354.

(24) Rokob, T. A.; Láng, G. G. *Electrochim. Acta* **2005**, *51*, 93–97.

(25) Godin, M.; Tabard-Cossa, V.; Grütter, P. *Appl. Phys. Lett.* **2001**, *79*, 551–553.

(26) Tabard-Cossa, V.; Godin, M.; Beaulie, L. Y.; Grütter, P. *Sens. Actuators B* **2005**, *107*, 233–241.

(27) Rowe, G. K.; Creager, S. E. *Langmuir* **1991**, *7*, 2307–2312.

(28) Chidsey, C. E. D.; Bertozzi, C. R.; Putvinski, T. M.; Mujsce, A. M. *J. Am. Chem. Soc.* **1990**, *112*, 4301–4306.

(29) Ulman, A. *Chem. Rev.* **1996**, *96*, 1533–1554.

(30) Walczak, M. M.; Popenoe, D. D.; Deinhammer, R. S.; Lamp, B. D.; Chung, C.; Porter, M. D. *Langmuir* **1991**, *7*, 2687–2693.

(31) Sato, Y.; Frey, B. L.; Uosaki, K.; Corn, R. M. *Bull. Chem. Soc. Jpn.* **1994**, *67*, 21.

(32) Lee, M.; Chung, C. *Bull. Korean Chem. Soc.* **1999**, *20*, 1–3.

(33) Lee, L. Y. S.; Sutherland, T. C.; Rucareanu, S.; Lennox, R. B. *Langmuir* **2006**, *22*, 4438–4444.

(34) Yao, X.; Yang, M.; Wang, Y.; Hu, Z. *Sens. Actuators B* **2007**, *122*, 351–356.

(35) Rowe, G. K.; Creager, S. E. *Langmuir* **1994**, *10*, 1186–1192.

(36) Ju, H.; Leech, D. *Phys. Chem. Chem. Phys.* **1999**, *1*, 1549–1554.

(37) Collard, D. M.; Fox, M. A. *Langmuir* **1991**, *7*, 1192–1197.

(38) Uosaki, K.; Sato, Y.; Kita, H. *Langmuir* **1991**, *7*, 1510–1514.

(39) Vos, J. G.; Forster, R. J.; Keyes, T. E. *Interfacial Supramolecular Assemblies*; John Wiley & Sons Ltd.: West Susex, 2003.

(40) Finklea, H. O. In *Electroanalytical Chemistry*; Bard, A. J., Rubinstein, I., Eds.; Marcel Dekker: New York, 1996; Vol. 19, p 109–335.

(41) Bard, A. J.; Faulkner, L. R. *Electrochemical Methods Fundamentals and Applications*; 2nd. ed.; J. Wiley & Sons: New York, 2001.

(42) Fujii, S.; Kurokawa, S.; Murase, K.; Lee, K.-H.; Sakai, A.; Sugimura, H. *Electrochim. Acta* **2007**, *52*, 4443–4448.

(43) Creager, S. E.; Rowe, G. K. *J. Electroanal. Chem.* **1997**, *420*, 291–299.

(44) Calvente, J. J.; Andreu, R.; Molero, M.; Lopez-Perez, G.; Domínguez, M. *J. Phys. Chem. B* **2001**, *105*, 9557–9568.

(45) Smith, C. P.; White, H. S. *Anal. Chem.* **1992**, *64*, 2398–2405.

(46) Poirier, G. E. *Chem. Rev.* **1997**, *97*, 1117–1127.

(47) Lee, L. Y. S.; Lennox, R. B. *Langmuir* **2007**, *23*, 292–296.

(48) Dubois, L. H.; Nuzzo, R. G. *Annu. Rev. Phys. Chem.* **1992**, *43*, 437–463.

(49) Berger, R.; Delamarche, E.; Lang, H.-P.; Gerber, C.; Gimzewski, J. K.; Meyer, E.; Güntherodt, H.-J. *Science* **1997**, *276*, 2021–2024.

(50) Sushko, M. L.; Harding, J. H.; Shluger, A. L.; McKendry, R. A.; Watari, M. *Adv. Mater.* **2008**, *20*, 3848–3853.

(51) The capacitance was measured by CV on macroscopic gold film electrodes in perchlorate solution at –0.050 V (potential at which there is no ferrocene oxidation). The potential range of –0.150 V to +0.050 V (vs. Ag/AgCl) was scanned at a rate of 100 mV/s.

(52) Sondag-Huethorst, J. A. M.; Fokkink, L. G. J. *Langmuir* **1994**, *10*, 4380–4387.

(53) Ji, H.-F.; Gao, H.; Buchapudi, K. R.; Yang, X.; Schulte, M. K. *Analyst* **2008**, *133*, 434–443.

(54) Raiteri, R.; Grattarola, M.; Berger, R. *Mater. Today* **2002**, *5*, 22–29.

(55) Desikan, R.; Armel, S.; Meyer III, H. M.; Thundat, T. *Nanotechnology* **2007**, *18*, 424028.

(56) Tabard-Cossa, V.; Godin, M.; Burgress, I. J.; Monga, T.; Lennox, R. B.; Grütter, P. *Anal. Chem.* **2007**, *79*, 8136–8143.

(57) Godin, M.; Williams, P. J.; Tabard-Cossa, V.; Laroche, O.; Beaulie, L. Y.; Lennox, R. B.; Grütter, P. *Langmuir* **2004**, *20*, 7090–7096.

(58) Headrick, J. J.; Sepaniak, M. J.; Lavrik, N. V.; Datskos, P. G. *Ultramicroscopy* **2003**, *97*, 417–424.

(59) Lavrik, N. V.; Tipple, C. A.; Sepaniak, M. J.; Datskos, P. G. *Chem. Phys. Lett.* **2001**, *336*, 371–376.

(60) Hansen, A. G.; Martensen, M. W.; Anderson, J. E. T.; Ulstrup, J.; Kuhlue, A.; Garnaes, J.; Boisen, A. *Probe Microsco.* **2001**, *2*, 139–150.

(61) Desikan, R.; Lee, I.; Thundat, T. *Ultramicroscopy* **2006**, *106*, 795–799.

(62) Mertens, J.; Calleja, M.; Tarýn, A.; Tamayo, J. *J. Appl. Phys.* **2007**, *101*, 034904–1–8.

(63) Kondo, T.; Takechi, M.; Sato, Y.; Uosaki, K. *J. Electroanal. Chem.* **1995**, *381*, 203–209.

(64) Abbott, N. L.; Whitesides, G. M. *Langmuir* **1994**, *10*, 1493–1497.

(65) Green, J.-B. D.; McDermott, M. T.; Porter, M. D. *J. Phys. Chem.* **1996**, *100*, 13342–13345.

(66) Auletta, T.; van Veggel, F. C. J. M.; Reinhoudt, D. N. *Langmuir* **2002**, *18*, 1288–1293.

(67) Kondo, T.; Okamura, M.; Uosaki, K. *J. Organomet. Chem.* **2001**, *637–639*, 841–844.

(68) Rowe, G. K.; Creager, S. E. *J. Phys. Chem.* **1994**, *98*, 5500–5507.

(69) Chidsey, C. D. E. *Science* **1991**, *251*, 919–922.

(70) Shimazu, K.; Yagi, I.; Sato, Y.; Uosaki, K. *J. Electroanal. Chem.* **1994**, *372*, 117–124.

(71) Sato, Y.; Mizutani, F.; Shimazu, K.; Ye, S.; Uosaki, K. *J. Electroanal. Chem.* **1999**, *474*, 94–99.

(72) Orlowski, G. A.; Chowdhury, S.; Kraatz, H.-Z. *Langmuir* **2007**, *23*, 12675–12770.

(73) De Long, H. C.; Donohue, J. J.; Buttry, D. A. *Langmuir* **1991**, *7*, 2196–2202.

(74) Tabard-Cossa, V.; Godin, M.; Grütter, P.; Burgress, I.; Lennox, R. B. *J. Phys. Chem. B* **2005**, *109*, 17531–17537.

(75) Bay, L.; Jacobsen, T.; Skaarup, S. *J. Phys. chem. B* **2001**, *105*, 8492–8497.

(76) Lee, D.; Thundat, T.; Jeon, S. *Sens. Actuators B* **2007**, *124*, 143–146.

(77) Heaton, T.; Friesen, C. *J. Phys. Chem. C* **2007**, *111*, 14433–14439.

(78) Tian, F.; Pei, J. H.; Hedden, D. L.; Brown, G. M.; Thundat, T. *Ultramicroscopy* **2004**, *100*, 217–233.

Chapter 4

Electrochemical Surface Plasmon Resonance Investigation of Dodecyl Sulfate Adsorption to Electroactive Self-Assembled Monolayers via Ion-Pairing Interactions*

4.1 Abstract

The redox-induced assembly of amphiphilic molecules and macromolecules at electrode surfaces is a potentially attractive means of electrochemically modulating the organization of materials and nanostructures on solid substrates via ion-pairing interactions or charge-transfer complexation. In this regard, we have investigated the potential-induced adsorption and aggregation of dodecyl sulfate, a common anionic surfactant, at a ferrocenylundecanethiolate SAM/aqueous solution interface by electrochemical surface plasmon resonance spectroscopy. The surfactant anions adsorb onto the electroactive SAM by specific ion-pairing interactions with the oxidized ferrocenium species. The ferrocenium charge density obtained by cyclic voltammetry and surface coverage measured by surface plasmon resonance indicate that the dodecyl

---

*This chapter is a reproduced copy almost verbatim of the text of the paper *Langmuir* **2007**, 2*3*, 10198–10208. Copyright 2007, American Chemical Society. It is co-authored by Antonella Badia.

sulfate forms an interdigitated monolayer, where half of the surfactant molecules have their sulfate headgroups paired to the surface and half have their headgroups exposed to the aqueous solution. The surface coverage of dodecyl sulfate was found to depend on both the ferrocenium surface concentration and the surfactant aggregation state in solution. A maximum coverage of dodecyl sulfate on the ferrocenium surface is obtained below the critical micelle concentration, in contrast to dodecyl sulfate adsorption to SAM surfaces of static positive charge. This marked difference in adsorption behavior is attributed to the dynamic generation of the ferrocenium by potential cycling and the specific nature of the ion-pairing interactions versus pure electrostatic ones. The results presented point to a new way for organizing molecules via electrical stimulus.

4.2 Introduction

Interactions between surfactants, many of which are charged, and solid surfaces are the essence of a variety of applied physicochemical processes. In surface and materials science, the focus of this work, applications of surfactants include ore flotation, lubrication, detergency, waterproofing, ion-pair chromatography, templating, electroplating, and the stabilization of colloidal suspensions.[1] Knowledge of the adsorbate layer structure and coverage is important for understanding and controlling the surface activity in a given application. Considerable efforts have therefore been made to investigate the details of the adsorption and aggregation of surfactants at solid/liquid

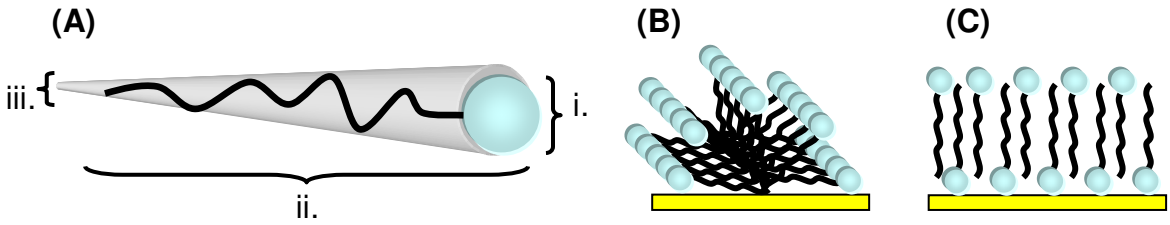

Scheme 4.1 **(A)** Molecular dimensions of a dodecyl sulfate molecule: (i) extended length $d \approx 1.98$ nm,[3] (ii) cross-sectional area of headgroup ≈ 0.28 nm^2,[18] (iii) cross-sectional area of CH_2 group ≈ 0.21 nm^2.[18] Surface aggregate structures suggested by AFM: **(B)** Cylindrical hemimicelles[4] and **(C)** Interdigitated monolayer. An average molecular area of 0.25 nm^2 per dodecyl sulfate molecule yields a theoretical Γ of 6.6×10^{-10} mol cm^{-2} for the interdigitated monolayer configuration.[3,4]

interfaces.[2-25] In this regard, many studies have focused on the adsorption of ionic surfactants onto oppositely-charged surfaces in aqueous solution through electrostatic interactions between the surfactant headgroups and the substrate.[2-4,7,9-14,17,23-25] Herein, we report the redox-induced assembly of dodecyl sulfate (Scheme 4.1A), a common anionic surfactant, at an electroactive organic monolayer film/aqueous solution interface via *ion-pairing* interactions of the sulfate headgroups with surface-bound oxidized cations. We demonstrate that a redox reaction can provide an effective means to electrochemically direct the interfacial adsorption and desorption of surfactant.

The recent application of surface sensitive techniques to probe the adsorption of surfactants onto solid surfaces has provided a clearer picture of how the physicochemical properties of the substrate, the surfactant geometry, the bulk surfactant concentration (cf. critical micelle concentration), and co- or counter-ions affect the adsorption kinetics,

adsorption isotherm, surface coverage, and molecular organization.[3,4,16,18,19,23,26-31] More specifically, AFM imaging[26,27] provided the first direct evidence that surfactant ions can aggregate to form discrete surface micelles (e.g., cylinders, hemicylinders, spheres and hemispheres) analogous to the micellar structures and lyotropic liquid crystal phases formed in bulk solution.[32] The aggregate shape, size, and spacing are dictated by the energetics of competing surfactant–substrate, surfactant–surfactant, and surfactant–aqueous phase interactions. The aggregate morphologies observed by AFM for alkyltrimethylammonium halides and sodium dodecyl sulfate ($SN_{12}S$) on different substrates and solution conditions have demonstrated that, in general, hydrophobic surfaces interact primarily with the surfactant alkyl tails, causing the first monomers to physisorb flat on the solid surface. These flat-lying monomers then orient incoming surfactant ions into half-cylinders for alkyl chains of more than 10 carbons.[2,5,26,27] By contrast, oppositely charged hydrophilic surfaces interact primarily with the surfactant ion headgroups, thereby producing aggregates whose structure depends on the density of the electrostatically bound headgroups.[2,5,26,27]

$SN_{12}S$ forms spherical micelles consisting of ~64 monomers in dilute aqueous solutions above the critical micelle concentration (cmc) of 8.1 mM in water at 25 °C.[33-35] Of particular relevance to the study presented in this report are the results of investigations of $SN_{12}S$ adsorption and aggregation at (i) an electrified gold/aqueous solution interface[3,4] and (ii) on positively charged SAMs of alkanethiolates on gold (RSAu).[23,24]

Using a combination of electrochemistry, neutron reflectivity, and high-resolution AFM imaging, Burgess et al. determined the effect of the absolute surface charge density

on the coverage and aggregate structure of dodecyl sulfate adsorbed to a bare Au(111) electrode under potential control.[3,4] At small or moderate charge densities (σ = –10 to +7 μC·cm^{-2}), the total surface coverage of surfactant, Γ = 4.4 (±0.5) x 10^{-10} mol·cm^{-2},[36] is considerably less than would be expected for a tightly-packed monolayer (Γ = 5.9 x 10^{-10} mol·cm^{-2}), based on the cross-sectional area of the sulfate headgroup (0.28 nm^2).[18] The dodecyl sulfate is adsorbed as parallel hemicylindrical micelles, consisting of a unit cell of five dodecyl sulfate monomers: two flat-lying molecules and three molecules with sulfate headgroups orientated towards the aqueous solution (Scheme 4.1B).[28,37] In this particular morphology, the flat-lying dodecyl sulfate molecules are stabilized by hydrogen-bonded water molecules that bridge sulfate groups in adjacent hemimicelle cylinders. The stripe-like nanostructures can be electrochemically reorganized to a condensed interdigitated monolayer film, with double the surface concentration of surfactant anions (Γ = 7.6 (±0.6) x 10^{-10} mol·cm^{-2}), by increasing the amount of positive charge on the metal surface.[3] The transformation to an interdigitated monolayer configuration in which half of the surfactant molecules are oriented with their sulfate headgroups to the metal and half with their headgroups to the aqueous interface (Scheme 4.1C) is complete at an applied voltage where the charge density on the metal (+33 μC·cm^{-2}) is equal to roughly half of the negative charge on the interdigitated dodecyl sulfates.[3,28] In this system, the cylindrical hemimicelle versus interdigitated monolayer configuration depends only on the surface charge density on the metal electrode and not on the aggregation state of the SN_{12}S in solution. Burgess et al. clearly demonstrated that electrochemistry provides an excellent opportunity to study the effect of surface charge on the adsorption behaviour of surfactant ions.[3,4]

Gold is not only a popular electrode material but it is also the substrate of choice for the self-assembly of *n*-alkanethiols and terminally functionalized alkanethiols to form well-defined single-component and mixed monolayer films with controllable surface properties, such as hydrophobicity/hydrophilicity, charge density, and redox activity.[38,39] Because of the tailorable surface chemistry of alkanethiolate monolayers on gold, compared to the substrates used in earlier studies (i.e. metals,[3-5,7] metal oxides,[8-10,27,40-44] graphite,[6,11,14,26,45,46] alumina,[13,47] mica,[2,25] silica,[2,6,25] organosilanes,[8,15,42] and polystryrene[20-22,48]), the adsorption of surfactants at solid/aqueous solution interfaces has been recently revisited by several research groups using these SAMs.[15-19,23,49] In particular, Stroeve et al. characterized the adsorption/desorption of dodecyl sulfate on neutral hydrophobic (CH_3–terminated) and charge-regulated (NH_3^+–terminated) SAMs using both SPR spectroscopy and AFM.[23] For both types of SAMs, the surface coverage of dodecyl sulfate increased with the bulk SN_{12}S concentration and attained a maximum value at concentrations ≥ cmc. The authors used AFM to visualize the surface aggregate structure as a function of the bulk SN_{12}S concentration. At SN_{12}S concentrations well below the cmc, dodecyl sulfate formed distorted structures that were randomly distributed across the methylated SAM surface. As the bulk SN_{12}S concentration was increased above the cmc, surface aggregates filled in the surface and eventually arranged themselves to form the parallel, hemicyclindrical micelle stripes expected for the case of physisorption to hydrophobic surfaces.[27] However, for the positively charged amino-terminated surface, they were not able to observe any distinguishable aggregate structures. Recognizing the difficulty of controlling the position and quantity of charge on surfaces containing dissociable groups (e.g., amino-terminated SAMs and silanols on

silica), as a result of the regulation of charge by the adsorption and desorption of surfactant ions and other added ions, Tulpar et al. investigated the adsorption of dodecyl sulfate from aqueous solution (no added salt) to $N(CH_3)_3^+$-terminated SAMs of *fixed* positive charge.[24] A two-step adsorption process was observed in which the amount of adsorbed surfactant was found to increase with the solution SN_{12}S concentration to a maximum value at the cmc per the CH_3– and NH_3^+–terminated SAMs but contrary to the bulk concentration-independent behaviour reported for an electrified, bare gold surface by Burgess et al.[3,4,24] However, as in the case of the electrified bare gold, the surface coverage of dodecyl sulfate was found to depend on the surface concentration of positive charge (i.e., the amount of surface-bound $-N(CH_3)_3^+$). For 100% $N(CH_3)_3^+$–SAMs where the surface-bound charge is fixed at ~38 $\mu C \cdot cm^{-2}$, the maximum coverage of adsorbed dodecyl sulfate, $\Gamma \approx 7 \times 10^{-10}$ mol·cm^{-2}, is close to the value measured on bare gold by Burgess et al.[3] at metal charge densities of 30–40 $\mu C \cdot cm^{-2}$ that yield a condensed interdigitated surfactant film. The AFM images obtained for mixed SAMs of different $-N(CH_3)_3^+$ densities at SN_{12}S solution concentrations above the cmc showed no distinguishable surface micelles, leading the authors to conclude that on surfaces where the charge is fixed and uniformly distributed, a homogeneous distribution of surfactant is energetically favoured over the formation of surface micelles in the absence of other available counterions.[24] The above-mentioned studies reaffirm the important roles that *both* the magnitude and distribution of charge play in determining the type of surface aggregate structure formed.

In this chapter, we use electrochemical SPR (ESPR) to investigate the adsorption of dodecyl sulfate and a non-amphiphilic analogue, 11-hydroxyundecane-1-sulfonate,

onto a ferrocenylalkanethiolate SAM by one-to-one ion-pairing interactions between the alkyl sulfate or sulfonate headgroups and ferrocenium cations generated by the potential-induced oxidation of the neutral ferrocenes. This work was motivated by reports of different interfacial phenomena that can be electrochemically driven via the oxidation of surface-bound ferrocene to ferrocenium (i.e., wetting and flow of aqueous solutions,[50] changes in the orientation of thermotropic liquid crystals,[51] and the serial deposition of charged nanoparticles[52,53]).

The oxidation of the ferrocene groups in RSAu SAMs involves coupled electron-transfer and anion-pairing reactions.[54] Sumner and Creager previously demonstrated the oxidation of ferrocenylalkanethiolate SAMs by concomitant ion-pairing with *p*-toluene sulfonate and poly-(4-styrene sulfonate).[54] These results suggest that alkyl sulfates and sulfonates should also be capable of associating with the electrogenerated ferroceniums. The alkyl sulfate or sulfonate acts as both the adsorbate and supporting electrolyte (no added salt).

In the ferrocenylalkanethiolate SAM system, the number and distribution of the immobilized ferrocenium cations can be varied with time by linearly scanning the potential across the oxidation region. This aspect allows for a dynamic control over the surfactant adsorption process. Moreover, ion-pairing interactions between the redox-generated ferrocenium species and counter-ions are not simply driven by pure electrostatics; certain anions pair more effectively than others with the ferrocenium.[55-57] These differences in ion-pairing ability introduce a certain degree of specificity to the adsorption of surfactant. We show that the dynamically created cationic ferrocenium surface leads to a different adsorption profile for the dodecyl sulfate compared to that for

a static cationic surface.[24] The work described herein constitutes a beginning in the interfacial assembly of soft materials using a surface-confined redox reaction.

4.3 Experimental

4.3.1 Materials

Sodium dodecyl sulfate ($[CH_3(CH_2)_{11}OSO_3^-Na^+]$, S$N_{12}$S, 99+%, Sigma-Aldrich Canada Ltd.) was recrystallized three times from absolute ethanol before use. The absence of hydrolyzed product (i.e., dodecanol) was verified by ^{1}H NMR spectroscopy (400 MHz, d_6-DMSO). The following compounds were used without any further purification: 11-mercapto-1-undecanol ($HOC_{11}SH$, 97%, Sigma-Aldrich), (1-mercaptoundec-11-yl)tri(ethylene glycol) ($HO(EO)_3C_{11}SH$, SensoPath Technologies, Inc., Bozeman, MT), 11-bromo-1-undecanol (98%, Sigma-Aldrich), 11-bromoundecanoic acid (99%, Sigma-Aldrich), perchloric acid (99.999%, Fluka), sodium perchlorate (98%, Sigma-Aldrich), and sodium sulfite (A&C Chemicals Ltd.). Gold granules (99.99%) were purchased from Plasmaterials, Inc. (Livermore, CA) and the titanium (99.99%) was from Alfa Aesar (Ward Hill, MA).

Sodium 11-hydroxyundecane-1-sulfonate (SHS) was synthesized by Dr. Ximin Chen (Université de Montréal) as follows. Solutions of 11-bromo-1-undecanol, 7.53 g (30 mmol) in 540 mL of ethanol, and sodium sulfite, 9.45 g (75 mmol) in 330 mL of deionized-distilled water, were combined and refluxed for 48 hours. After cooling to room temperature, the reaction mixture was concentrated under reduced pressure and washed three times with ethyl acetate and chloroform, respectively. The crude product

was then recrystallized from methanol. The purity of the desired product (7.00 g, 85 % yield) was verified by ^{1}H NMR spectroscopy (400 MHz, D_2O, δ): 1.10-1.25 (m, 12H, CH_2), 1.31 (m, 2H, CH_2), 1.42 (m, 2H, $CH_2CH_2SO_3^-Na^+$), 1.62 (m, 2H, $HOCH_2CH_2$), 2.79 (t, 2H, $CH_2SO_3^-Na^+$), 3.57 (m, 2H, CH_2OH). 11-Ferrocenyl-1-undecanethiol ($FcC_{11}SH$) was synthesized from 11-bromoundecanoic acid according to the procedure of Creager and Rowe.[58] The identity and purity of the product was verified by thin layer chromatography (silica gel, hexanes/ethyl acetate 99:1 v/v) and ^{1}H NMR (400 MHz, $CDCl_3$).

All aqueous solutions were prepared with deionized distilled water obtained by further purification of distilled water with a Milli-Q Gradient system (Millipore, Bedford, MA). The resistivity of the purified water was 18.2 MΩ·cm, and its surface tension, measured at 24 °C, was 72 mN·m^{-1}.

4.3.2 Preparation of Gold-Covered Substrates and Self-Assembled Monolayers

Prior to metal deposition, B270 glass slides (Esco Products, Inc., Oak Ridge, NJ) were cleaned by sonication at 45 ºC for 15 minutes each in: (i) hot ethanol/chloroform (1:1 v/v) mixture, (ii) 2% (v/v) Hellmanex® II aqueous solution (Hellma Canada Ltd., Concord, ON), (iii) deionized distilled water, and (iv) absolute ethanol. The clean glass slides were coated with titanium and gold using a VE-90 thermal evaporator equipped with a quartz crystal deposition monitor (Thermionics Vacuum Products, Port Townsend, WA). Once a base pressure of ~3 x 10^{-7} Torr was reached, a 1.2 nm titanium adhesion layer was first deposited at a rate of ~0.01 nm·s^{-1}. Gold was then deposited at a rate of ~0.1 nm·s^{-1} to a final thickness of 48 nm. Immediately following metal deposition, the

gold-coated slides were incubated in the appropriate thiol solutions for at least 12 hours. Ferrocenylundecanethiolate monolayers were assembled from 1 mM solutions of $FcC_{11}SH$ in 4:1 v/v absolute ethanol/THF. Mixed monolayers of different $FcC_{11}SH/HOC_{11}SH$ molar ratios were prepared by immersing the gold-coated glass slides in 4:1 ethanol/THF solutions containing the two thiols of interest at a total thiol concentration of 1.0 mM. Upon removal from the incubation solutions, the thiol-modified slides were rinsed copiously with absolute ethanol and dried with nitrogen. $HO(EO)_3C_{11}S$- monolayers were assembled from 1 mM solutions in absolute ethanol.

4.3.3 Ellipsometry

The optical constants (n and k) of the SPR-supporting gold layer and the $FcC_{11}SAu$ monolayer thickness were determined using a multiwavelength ellipsometer equipped with a QTH lamp and rotating compensator (Model M-2000V, J.A. Woollam Co, Inc., Lincoln, NE). All measurements were performed in air at an incident angle of 70° and a wavelength range of 370 nm to 1000 nm. Five to six different spots on each substrate surface were analyzed and the results averaged.

The complex refractive index ($\hat{n} = n - k\mathrm{i}$) of the freshly-evaporated gold films was first calculated from a three-layer model: glass (0.92 mm)/Ti (1.2 nm)/Au (48 nm). The plots of Ψ and Δ vs. wavelength (λ) obtained for the bare gold were fit using the Levenberg-Marquardt non-linear optimization algorithm of the vendor's WVASE32 software. The titanium and gold film thicknesses were fixed to those measured by the calibrated quartz crystal monitor during thermal evaporation. The $n(\lambda)$ and $k(\lambda)$ values provided in the vendor's materials database for polycrystalline titanium and BK7 glass

were used in the fitting process. The complex refractive index of the evaporated gold was thus determined to be 0.18 – 4.86i at the surface plasmon excitation λ of 780 nm. This $\hat{n}$ value is very close to the literature value for bulk gold, 0.174 – 4.86i.[59]

The thickness of the $FcC_{11}SAu$ monolayer was determined at 780 nm, wavelength where ferrocene does not absorb (Figure 4.1), using the optical parameters determined for the bare gold reference, a n of 1.464,[60] and a k of 0 for the chemisorbed ferrocenylalkanethiolate layer.

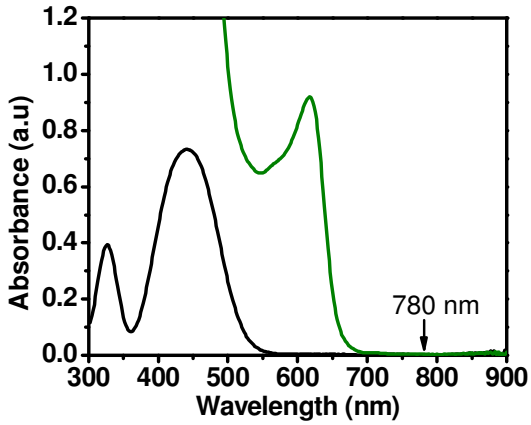

Figure 4.1 Absorption spectra of ferrocene (black) and ferrocenium (green) in DMF.

4.3.4 Electrochemistry

All CV and differential pulse voltammetry (DPV) experiments were performed using a custom-built, one-compartment, three-electrode cell (Delrin) and an Epsilon potentiostat (Bioanalytical Systems, Inc., West Lafayette, IN). The $FcC_{11}SAu$ substrate

served as the working electrode, the counter electrode was a platinum wire (Alfa Aesar), and an Ag/AgCl aqueous electrode (3 M NaCl, Bioanalytical Systems) was used as the reference. All potentials are reported with respect to the Ag/AgCl reference electrode. The aqueous surfactant and perchlorate solutions used as the electrolyte were purged with nitrogen prior to the electrochemical measurements. The CVs were acquired at a potential scan rate of 10 $mV \cdot s^{-1}$. The DPV scans were acquired using a potential scan rate of 5 $mV \cdot s^{-1}$, step potential of 1 mV, pulse width of 50 ms, pulse period of 200 ms, and a pulse amplitude of 50 mV. The perchlorate electrolyte solution contained 0.01 M $HClO_4$/0.1 M $NaClO_4$ (pH = 2.2). The aqueous solutions of $SN_{12}S$ and SHS contained no added salt. The $SN_{12}S$ concentration was varied from 2 to 100 mM (pH = 5.6), whereas experiments were performed using aqueous solutions containing either 10 or 50 mM SHS (pH = 5.5).

The quantity of electrogenerated ferrocenium (Γ_{Fc^+}) was determined using the following equation[61]

$$\Gamma_{Fc^+} = Q_{Fc^+} / nFA \tag{4.3}$$

where Q_{Fc^+} is the charge associated with the ferrocene oxidation determined through integration of the voltammetric anodic peak corrected for the charging current, n is the number of electrons involved in the electron-transfer process (n = 1 for the ferrocene/ferrocenium couple), F is the Faraday constant, and A is the geometric surface area of the exposed $FcC_{11}SAu$ substrate electrode. Depending on the anion affinity for the oxidized ferrocenium $\Gamma_{Fc^+} \leq \Gamma_{Fc}$.

4.3.5 SPR Spectroscopy

In-situ SPR Measurements. SPR measurements were carried out with a computer-controlled SR7000 SPR instrument (Reichert, Inc., Depew, NY). A brief description of the mode of operation of the SPR instrument follows.[62] Surface plasmons are excited in the Kretschmann-type attentuated total reflection configuration using light from a 15 mW GaAlAs emitter (peak emission λ = 780 nm) that is passed through a 10 nm bandpass filter, collimated, and polarized.[63-65] The TM-polarized incident light is then focused through a sapphire prism onto the underside of the gold-coated glass slide with an angle distribution of ~21°. The irradiated gold surface area is ~1 mm x 1.5 mm. Light total internally reflected from the gold/solution interface is detected with a 3696-pixel CCD linear array for which the optical pixel signals are digitized with a 14-bit analogue-to-digital converter. The SPR minimum pixel is tracked with time via a centroid algorithm using the signal from a few pixels on either side of the pixel of lowest intensity.[66] A National Instruments Labview interface (SR7000 Alpha Instrument version 2.24) is used for data acquisition and transfer. A Peltier device allows the temperature at the gold/solution interface to be controlled to within ±0.015 °C between 10 and 90 °C. All experiments were carried out at 25 °C.

To carry out electrochemical SPR (ESPR) measurements, the custom-made electrochemical cell, fitted with the reference and counter electrodes, was mounted onto the $FcC_{11}SAu$ slide (working electrode), which was optically coupled to the base of the sapphire prism using immersion oil (Cargille Type A liquid, $n_{589\,nm}^{20\,°C}$ = 1.515). Liquid introduction and exchange in the electrochemical cell was effected via a syringe pump. A baseline was first run in pure water. The $SN_{12}S$ or SHS solution was then introduced into

the cell. The change in minimum pixel was recorded under stationary conditions, with a time resolution of 2 s, as a function of the applied potential, which was varied at a scan rate of 10 $mV \cdot s^{-1}$. The start and end of each potential cycle were manually noted with respect to the SPR time profile.

Adsorbed Layer Thickness Calculations. The shifts in the minimum pixel recorded during potential cycling were converted to resonance angle changes ($\Delta\Theta_m$) using the pixel-to-incident angle relation (i.e., 1 pixel = 0.00513°) established through calibration of the SR7000 instrument across the refractive index range of ~1.33 to ~1.38 with pure water and aqueous solutions of ~4 to ~50 mass% ethylene glycol. The refractive index of the solutions was measured with a Reichert AR200 digital refractometer (λ = 589 nm) and the values verified against published data.[67]

Adsorbed layer thicknesses were determined from the $\Delta\Theta_m$ values using Fresnel multilayer modeling (Winspall software version 2.20, MPI-P, Mainz, Germany). Table 4.1 lists the layer models and parameters used to calculate the expected resonance angle shift for the formation of the $AuSC_{11}Fc^+ - ClO_4^-$ pair (Table 4.1, columns 1 and 2) and the variation of Θ_m with the dodecyl sulfate ($N_{12}S^-$) or hydroxyundecyl sulfonate (HS^-) layer thickness (*d*) (Table 4.1, column 3). Refractive indices of 1.46 and 1.45 were used in the Fresnel calculations for the self-assembled $FcC_{11}S$– monolayer[60] and the adsorbed layers of $N_{12}S^-$ and HS^-,[18,19] respectively. These are typical *n* values used in ellipsometric or SPR measurements of ultrathin films of aliphatic hydrocarbons (e.g., alkanethiolates, alkylsulfates, and dialkyl phospholipids) in the wavelength region of 544–633 nm.[18,19,23,68-71] The refractive indices of aliphatic hydrocarbons vary weakly with the wavelength of light[72,73] so that values reported at 589 nm or 633 nm can be used

Table 4.1 Layer Models and Parameters for the Fresnel Calculations.

	$AuSC_{11}Fc$				$AuSC_{11}Fc^+$-ClO_4^-				$AuSC_{11}Fc^+$-DS^- or $AuSC_{11}Fc^+$-HS^-			
Layer	*d* (nm)	*n*	*k*		*d* (nm)	*n*	*k*		*d* (nm)	*n*	*k*	
Prism	∞	1.761[a]	0		∞	1.761[a]	0		∞	1.761[a]	0	
Glass slide	∞	1.515[b]	0		∞	1.515[b]	0		∞	1.515[b]	0	
Ti	1.2	2.768[c]	3.307[c]		1.2	2.768[c]	3.307[c]		1.2	2.763[c]	3.307[c]	
Au	48.0	0.181	4.856		48.0	0.181	4.856		48.0	0.181	4.856	
$-SC_{11}Fc$	1.84	1.464	0		2.13	1.464	0		2.13	1.464	0	
-	-	-	-	ClO_4^-	0.472	1.38[d]	0	$N_{12}S^-$ or HS^-	varied[f]	1.45	0	
$NaClO_4$ (aq)	∞	1.328[d]	0	$NaClO_{4(aq)}$	∞	1.328[e]	0	$SN_{12}S$ or SHS	∞	1.328-1.331[g]	0	

[a] Value at 780 nm and 24°C from *American Institute of Physics Handbook*; Gray, D.E. Ed; 3rd ed., McGraw-Hill, Inc.: New York, **1972**.

[b] Value at 780 nm provided by Reichert Analytical, Inc.

[c] Value at 780 nm from *Handbook of Optical Constants of Solids III*; Palik, E. D.; Academic Press: New York, **1985**.

[d] Value taken from *CRC Handbook of Chemistry and Physics*; Lide, D. R., Ed.; 87th ed., CRC Press: Boca Raton, FL, **2006**.

[e] The refractive index of the perchlorate solution, measured at 589 nm, was found to be the same as that of water. Water value, relative to air, at 780 nm and 25°C from *J. Phys. Chem. Ref. Data* **1998**, *27*, 761–774.

[f] Value was varied to determine $\partial\Theta/\partial d$.

[g] Values measured for each solution by refractometry at 589 nm were corrected to 780 nm and 25°C using proprietary software (Michael Reimer, Reichert, Inc.) based on wavelength and temperature-dependent dispersion formulae for aqueous sucrose solutions provided in document "ICUMSA Specification and Standard SPS-3 (1998) Refractometry and Tables – Official".

at 780 nm without a significant error.[74] $\partial\Theta_m/\partial d$ varies slightly with the SN_{12}S or SHS concentration: 0.0405°/nm for 2 mM SN_{12}S, 0.0401°/nm for 100 mM SN_{12}S, 0.0405°/nm for 10 mM SHS, and 0.0400°/nm for 50 mM SHS. The effective thickness of the adsorbed layer can be determined using the reciprocal of the concentration-specific $\partial\Theta_m/\partial d$ by[18,19,24]

$$d = \Delta\Theta_m \frac{\partial d}{\partial \Theta_m} \tag{4.2}$$

where $\Delta\Theta_m$ is the maximum change in resonance angle recorded for the adsorption of $N_{12}S^-$ or HS^- at the ferrocenium alkanethiolate/water interface. The amount of $N_{12}S^-$ or HS^- adsorbed to the surface (Γ), which unlike d and $n_{adsorbate}$, does not depend on the assumption of layer uniformity, can then be obtained as follows[75]

$$\Gamma = d\Delta n \frac{1}{\partial n/\partial c} \tag{4.3}$$

where d is the effective thickness of the adsorbed layer, Δn is the difference in the refractive indices of the adsorbed film ($n_{adsorbate}$ = 1.45) [18,19,24,69,76,77] and pure solvent (n_{water} = 1.328 at 780 nm and 25 °C).[78] The incremental change of refractive index with increasing SN_{12}S[18,24] or SHS concentration, $\partial n/\partial c$, measured by refractometry (λ = 589 nm), are 3.42 (±0.03) x 10^{-5} mM^{-1} for SN_{12}S and 4.14 (±0.04) x 10^{-5} mM^{-1} for SHS at 25 °C. The refractive index increments obtained for SN_{12}S and SHS at 589 nm are expected to be close to those at 780 nm, the experimental SPR wavelength, since our SN_{12}S value is within 8–10% of $\partial n/\partial c$ values reported at 760 nm[18] and 840 nm[79].

4.3.6 AFM

Bare Au and $FcC_{11}S$-modified Au substrates used for ESPR were imaged under ambient conditions using an extended Dimension 3100 scanning probe microscope and Nanoscope IIIa controller (Digital Instruments/Veeco, Santa Barbara, CA). Height images were acquired in intermittent-contact (tapping) mode with silicon probes (Nanosensors type NCHR) of nominal spring constant of 42 $N \cdot m^{-1}$, resonant frequency of 330 kHz, and tip radius <10 nm. All images were captured at a scan rate of 1 Hz and resolution of 512 × 512 pixels.

4.4 Results and Discussion

4.4.1 $FcC_{11}SAu$ SAM Characterization

Prior to the ESPR investigations, the $FcC_{11}SAu$ SAMs were characterized by AFM, spectroscopic ellipsometry, and electrochemistry. The AFM image presented in Figure 4.2A shows that the as-prepared polycrystalline Au surface consists of flat grains, ~100 nm in size, and is characterized by a root-mean-square (rms) roughness of 0.6–0.7 nm over areas of 1 to 25 μm^2. After incubation in $FcC_{11}SH$ solution (Figure 4.2B), the Au surface appears to be homogeneously covered with ferrocenylalkanethiolate (rms roughness of ~0.7 nm for an area of 1 μm^2), although some structural heterogeneity is clearly evident. An effective film thickness of 1.84 ± 0.12 nm was measured in air. This thickness is close to the value expected from the thickness of a $CH_3(CH_2)_{10}SAu$ monolayer (1.2 nm)[80-82] and the diameter of a ferrocene group (0.66 nm).[83] The quantity of surface-immobilized ferrocene, Γ_{Fc}, in the $FcC_{11}SAu$ and mixed $FcC_{11}SAu/HOC_{11}SAu$

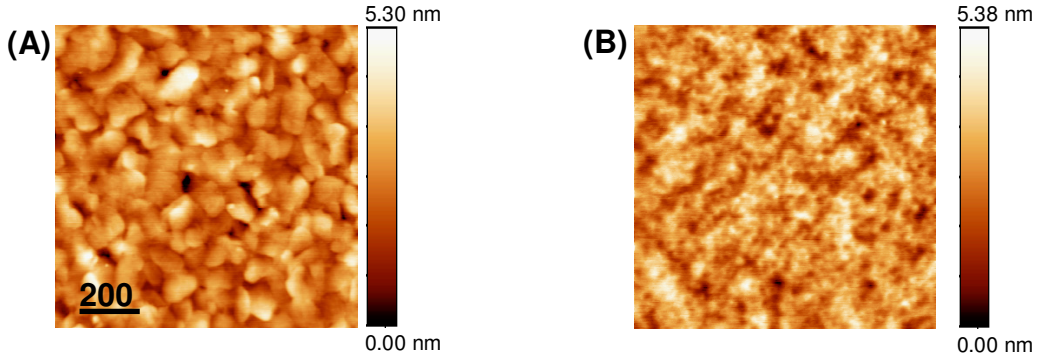

Figure 4.2 Tapping-mode AFM images (topography) in air of **(A)** bare Au substrate and **(B)** $FcC_{11}SAu$ monolayer assembly.

monolayers was determined from cyclic voltammograms acquired in perchlorate solution. A mean Γ_{Fc} of 4.8 (±0.4) x 10^{-10}mole·cm^{-2} was obtained for the $FcC_{11}SAu$ monolayer from the anodic peak area ($Q_{Fc^+} = 46 \pm 4\ \mu C \cdot cm^{-2}$). The measured Γ_{Fc} concurs with the theoretical coverage of ferrocene calculated from close-packing of ferrocene spheres.[83-90] The measured film thickness and Γ_{Fc} are thus consistent with a full-coverage $FcC_{11}SAu$ monolayer. It is worth noting that the density of oxidizable ferrocene moieties (2.9 molecules·nm^{-2}) is comparable to that of the single-component $^{+}(CH_3)_3NC_{11}SAu$ SAMs prepared by Tulpar et al. (2.4 molecules·nm^{-2}).[24]

4.4.2 Electrochemical Behaviour

Ferrocenylalkanethiolate SAMs are probably the most studied electroactive SAMs and their Faradaic electrochemistry is extensively documented in the literature. The

redox potential and shape of the voltammetric waves recorded for ferrocene-terminated SAMs depend on a number of factors, which include the length of the alkanethiol chain, alkyl chain–ferrocene linker functionality, presence of diluent molecules in the monolayer, and the nature and concentration of electrolytes.[55,57,83,89,91-96] Perchloric acid and perchlorate salts are commonly used as the supporting electrolyte in electrochemical investigations as the perchlorate anions form 1:1 contact ion pairs with the electrochemically generated ferroceniums that stabilize the oxidized cations.[55,57,83,92,95] Cyclic and differential pulse voltammograms were therefore recorded for the $FcC_{11}SAu$ monolayer in perchloric acid/perchlorate solution (Figure 4.3) to characterize this SAM and compare the perchlorate ion electrochemistry with that observed in the presence of alkyl sulfate ($N_{12}S^-$) and hydroxyalkyl sulfonate (HS^-) anions.[60,89,94,97-100] The CV resembles those previously published (Figure 4.3A). Peaks centered at 0.41 V (half-wave potential, $E_{1/2}$) are observed for the oxidation and reduction of the ferrocene moiety, with a peak separation of 13 mV. As is often the reported situation in SAMs where the mole fraction of ferrocene (χ_{Fc}^{surf}) = 1, the peaks are asymmetric.[89,94,97,101,102] Shoulders are present on the negative potential side of each peak in both the CV and DPV. These low-potential shoulders can be mathematically deconvoluted into more than one peak (Figure 4.4).[94] The ΔE_{fwhm} of the main oxidation peak at 0.41 V in the CV, after deconvolution, is 118 mV (see Figure 4.4), which is greater than the value of 90.6 mV at 25 °C expected for the ideal case where all the surface-confined ferrocene centers have equivalent environments and there is minimal interactions between them.[61] The peak broadening and asymmetry or multiplicity has been attributed in previous reports to an inhomogeneous spatial distribution of ferrocenes in the SAM,[83,89,90,94,95,103] which is

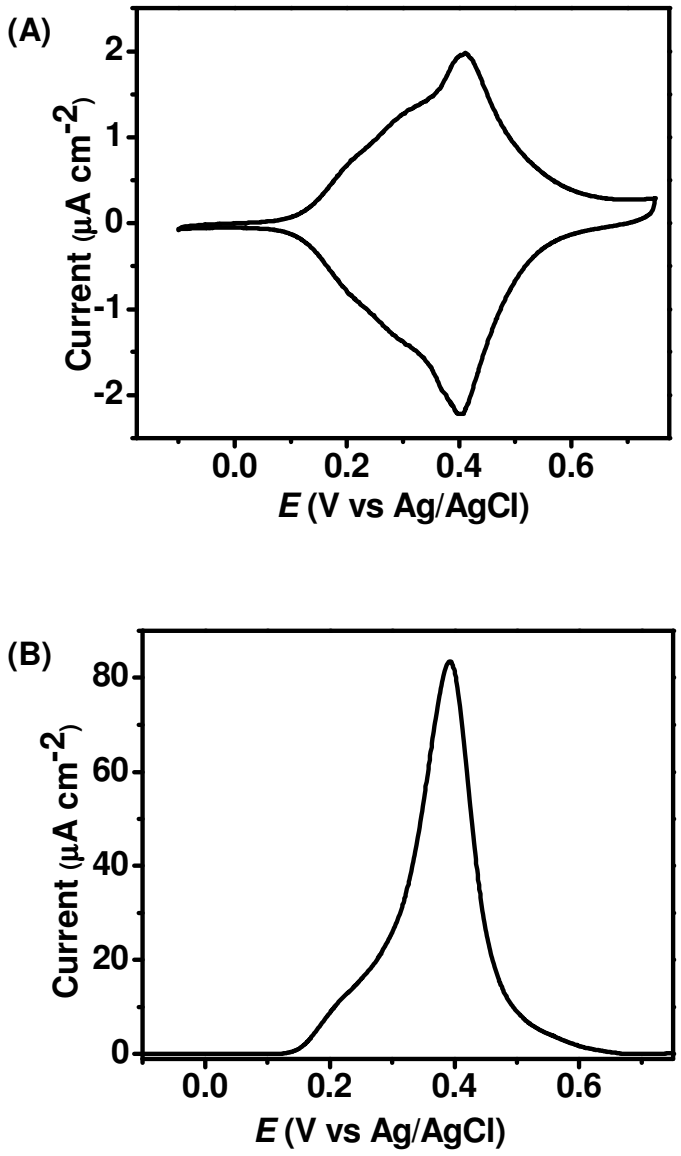

Figure 4.3 $FcC_{11}SAu$ SAM in perchlorate solution (0.01 M $HClO_4$/0.1 M $NaClO_4$). **(A)** CV scan (scan rate = 10 $mV \cdot s^{-1}$) and **(B)** DPV scan (scan rate = 5 $mV \cdot s^{-1}$).

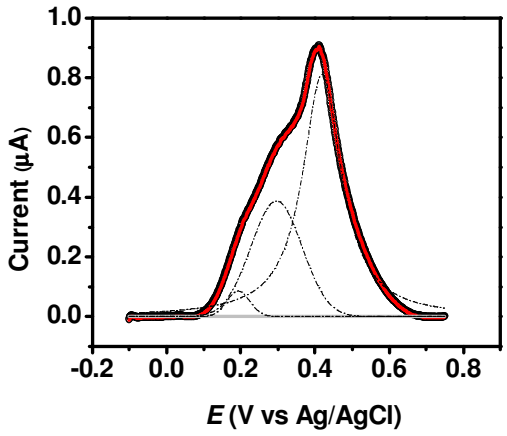

Figure 4.4 Example of peak deconvolution of a typical CV scan of $FcC_{11}SAu$ SAM in perchlorate solution. CV taken from **Figure 4.3A**. Peak devolution using a Gaussian and Lorentzian functions. The solid red line is the fitted curve and dashed lines are the deconvoluted peaks. The grey line is the baseline correction.

consistent with the heterogeneous film structure that we have observed by AFM (Figure 4.2B).

A typical CV for the $FcC_{11}SAu$ monolayer in $SN_{12}S$ electrolyte solution ([$SN_{12}S$] = 100 mM = 12.5 × cmc) is shown in Figure 4.5A. Well-defined reversible redox waves are observed. As in the ClO_4^- case, there is more than one anodic and cathodic peak associated with the oxidation and reduction of ferrocene, respectively. The $E_{1/2}$ of the main redox peaks is 0.38 V, with a peak separation of 22 mV. Peaks of much lower current intensity are also observed on the negative potential side ($E_{1/2}$ = 0.16 V) of the main redox peaks. The lower-potential anodic peak is more clearly evident in the DPV (Figure 4.5B), where the capacitive or charging current component is largely eliminated and the major component of the measured difference current is the faradaic current.[61,104]

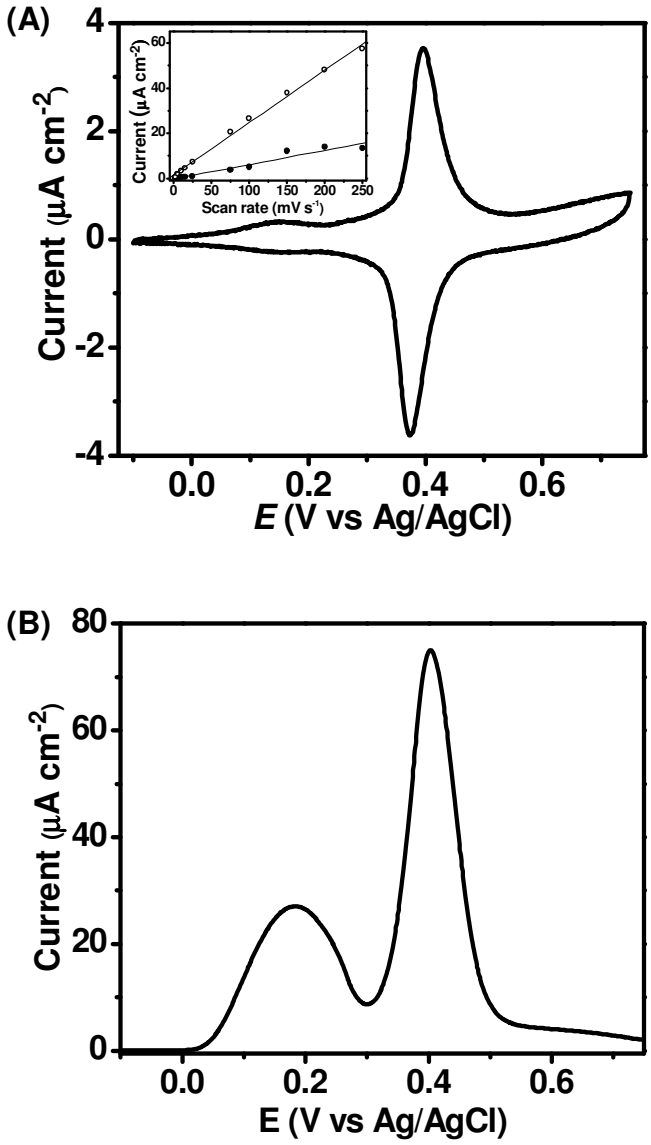

Figure 4.5 $FcC_{11}SAu$ SAM in 100 mM $SN_{12}S$ solution. **(A)** CV scan (scan rate = 10 $mV \cdot s^{-1}$). The inset shows the linear relationship of the peak current vs. scan rate for the first anodic peak at 0.16 V (filled circles) and the second anodic peak at 0.40 V (unfilled circles). **(B)** DPV scan (scan rate = 5 $mV \cdot s^{-1}$).

The DPV peak positions (0.19 V and 0.41 V) compare well with those of the anodic segment of the CV (0.16 V and 0.40 V). The linear relationship between the anodic peak currents measured by CV and the scan rate (Figure 4.5A inset) indicates that both peaks are due to the oxidation of surface-bound ferrocenes.[61] It appears that the different ferrocene microenvironments (i.e., sites of different packing density/order) in the SAM are better resolved by ion pairing to the dodecyl sulfate (isolated peaks, Figure 4.5) than to ClO_4^- (overlapping peaks, Figure 4.3). Moreover, the ΔE_{fwhm} of 57 mV of the main anodic peak, which is less than the theoretical 90.6 mV, may reflect a strong interaction between some of the ferrocene sites as well a structural reorganization of the SAM upon oxidation of the ferrocenes.[89,105] Integration of the anodic peak areas (Q_{Fc^+} = 29 ± 5 $\mu C \cdot cm^{-2}$) reveals that only ~63% of the available ferrocenes are oxidized to ferrocenium in the presence of dodecyl sulfate. We will return to this point later on in the discussion.

We also investigated the redox behaviour of the ferrocenylundecanethiolate SAM in SHS, a non-amphiphilic analog of SN_{12}S. The resulting CV and DPV, shown in Figure 4.6, exhibit anodic peaks at ~0.28 V and ~0.51 V. Integration of the anodic peak areas (Q_{Fc^+} = 34 ± 4 $\mu C \cdot cm^{-2}$) shows that ~74% of the available ferrocenes are oxidized to ferrocenium in the presence of hydroxyundecyl sulfonate.[106] In summary, cyclic and differential pulse voltammetry clearly demonstrate the reversible oxidation/reduction of surface-bound ferrocenes by ion pairing with alkyl sulfates and sulfonates.

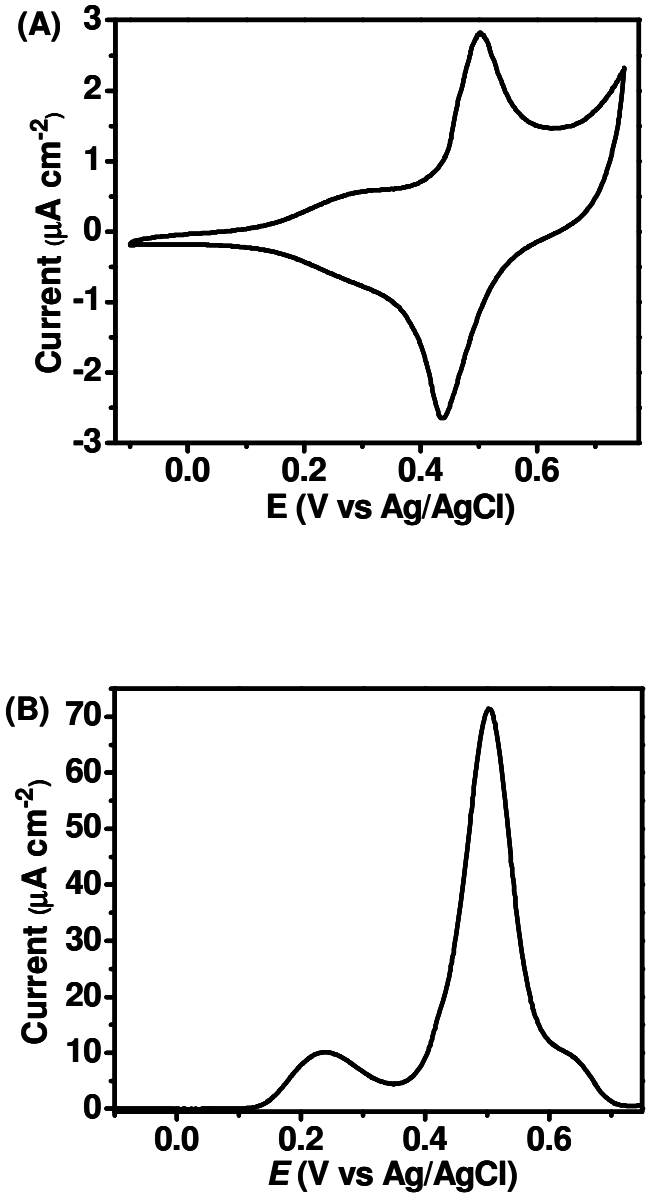

Figure 4.6 $FcC_{11}SAu$ SAM in 50 mM SHS solution: **(A)** CV scan (scan rate = 10 $mV \cdot s^{-1}$) and **(B)** DPV scan (scan rate = 5 $mV \cdot s^{-1}$).

4.4.3 Determination of Redox-Induced $FcC_{11}SAu$ Thickness Change

For the layer thicknesses and molecular coverages of the adsorbed dodecyl sulfate and hydroxyundecyl sulfonate to be accurately quantified by SPR, any redox-induced orientational changes in the $FcC_{11}SAu$ monolayer must be accounted for in the Fresnel modeling. Previous ellipsometry[60,107,108] and SPR[97] investigations using perchlorate electrolyte have reported an increase in film thickness of the order of 0.1–0.3 nm upon oxidation of the ferrocene to ferrocenium. There is no real consensus among the *in-situ* spectroelectrochemical investigations, each carried out on monolayers prepared from different ferrocenylalkanethiols ($FcC_{11}SH$, $FcCOOC_{11}SH$, $FcCOC_{2-9}SH$, and $Fc(COC_5SH)_2$), of redox-induced structural transformations giving rise to the change in film thickness.[88,96,98,99,107] Both an untilting of the alkyl chains[98,99] and a rotation of the ferrocene cyclopentadiene rings around the terminal ferrocene–carbon bond[96,107] have been proposed. We carried out initial ESPR experiments in perchlorate to (i) quantify the electrochemically induced film thickness change and (ii) verify the sensitivity of our commercial instrument, which uses a focused beam of single-wavelength incident light to probe a finite angular spread. Typical current and SPR responses, with respect to time, obtained for multiple cyclic voltammetric scans of the $FcC_{11}SAu$ SAM between –0.1 V to 0.75 V in 0.01 M $HClO_4$/0.1 M $NaClO_4$ solution are shown in Figure 4.7. Ferrocene oxidation results in a maximum SPR resonance angle shift ($\Delta\Theta_m$) of 0.0193 ± 0.0003º. The reproducibility of the multiple SPR scans suggests that the molecular adsorption/desorption events and any film structural changes accompanying the ferrocene oxidation/ferrocenium reduction cycles are reversible. However, there is a small decrease (~3%) in the current between the first and the fourth CV scan due to the well-known susceptibility of the ferrocenium cation to undergo nucleophilic substitution.[88,109] A

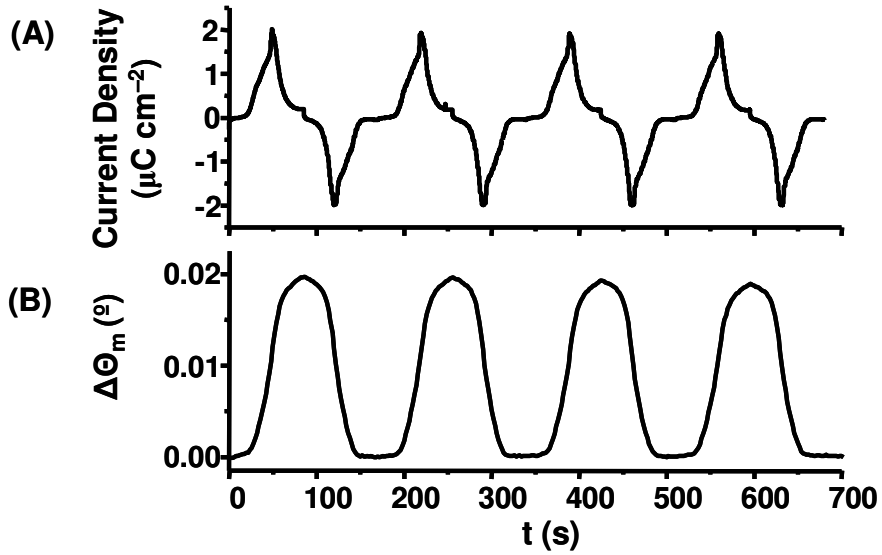

Figure 4.7 (A) Current vs. time profile obtained during potential cycling between –0.10 V and +0.75 V of a $FcC_{11}SAu$ SAM at a rate of 10 $mV \cdot s^{-1}$ in 0.01 M $HClO_4$/0.1 M $NaClO_4$ solution. **(B)** Corresponding SPR profiles. Maximum $\Delta\Theta_m = 0.0193 \pm 0.0003°$.

comparison of the variation, with the applied potential, of the percent change in SPR response with the fractional surface coverage of ferrocenium is given in Figure 4.8. The SPR response directly tracts the conversion of the ferrocene to ferrocenium.

Ferrocene and ferrocenium exhibit absorption maxima at 442 nm and 617 nm, respectively (Figure 4.1). Hence, the absorption of either species at the incident light wavelength (780 nm) used to excite the surface plasmons does not contribute to the observed resonance angle shifts. It is unlikely that the measured shift is due to a change in the refractive index, n, of the $FcC_{11}SAu$ SAM because Uosaki et al. found by ellipsometry that $n_{FcC_{11}S-}$ (reduced form) is the same as $n_{Fc^+C_{11}S-}$ (oxidized form).[60]

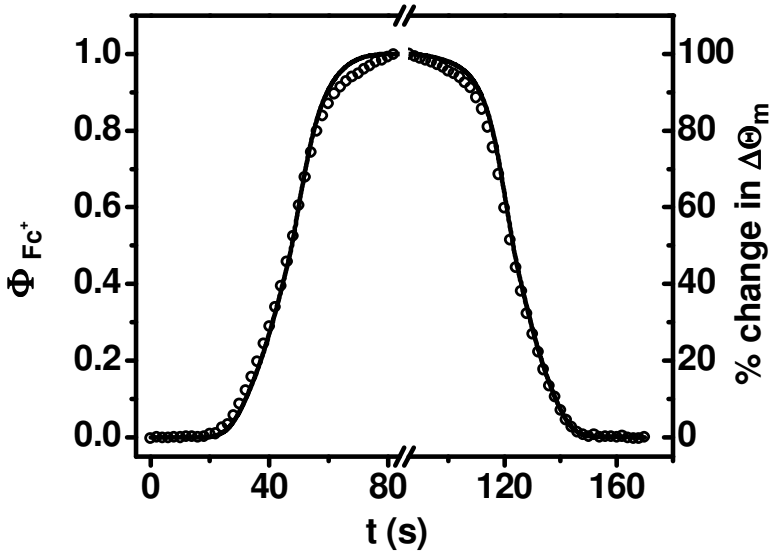

Figure 4.8 Plot of fractional coverage (Φ) of ferrocenium (—) and % change in SPR response (○) vs. the time for a complete voltammetric cycle.

Furthermore, it has been previously shown that the presence of an inert SAM dielectric suppresses potential-induced changes in the gold reflectivity in aqueous solution.[110,111] Consistent with this previous observation, no SPR angle shift is observed prior to ferrocene oxidation (Figure 4.8), indicating that the measured resonance angle shifts are not due to potential-induced changes in the gold reflectivity.[110,111]

We have interpreted the measured shift in the SPR resonance angle as resulting from both $Fc^{+}-ClO_4^{-}$ ion-pair formation and a change in orientation of the $Fc^{+}C_{11}S$– chains (with respect to neutral ferrocene). The multilayer Fresnel models given in columns 1 and 2 of Table 4.1 were used to calculate the angle shift. It has been

demonstrated by the electrochemical quartz crystal microbalance (EQCM) that for a compact $FcC_{11}SAu$ SAM, such as the one used here, there is no water uptake upon ferrocene oxidation and perchlorate ion association.[112] Furthermore, for a well-packed SAM, the 1:1 contact ion pairing between the oxidized ferrocene and the ClO_4^- at the monolayer/solution interface is so strong, that the monolayer, including the associated anions, behaves as a rigid layer.[112] Considering these results, we incorporated a solid monolayer of perchlorate anions of 0.472 nm[97] in thickness and index of refraction of 1.38[67] on top of the $Fc^+C_{11}SAu$ SAM to calculate the expected resonance angle shift. Our calculations also assume that the alkyl chains untilt by 30°, as suggested by the spectroelectrochemical measurements carried out by Ye et al. on $FcC_{11}SAu$ SAMs. This chain untilting yields a change in the monolayer thickness of ~0.29 nm. Our calculated value of 0.021° agrees well with our measured value of 0.019 ± 0.001°. We expect that the oxidation of the ferrocene in the $SN_{12}S$ and SHS electrolyte also induces a thickening of the $FcC_{11}SAu$ SAM by 0.29 nm, and have thus used a $Fc^+C_{11}SAu$ SAM thickness of 2.13 nm (vs. 1.84 nm for $FcC_{11}SAu$) to determine the adsorbed dodecyl sulfate and hydroxyundecyl sulfonate layer thicknesses from the measured $\Delta\Theta_m$ (Table 4.1, column 3). However, we would like to point out that the $\partial\Theta_m/\partial d$ calculated value does not change if the $Fc^+C_{11}SAu$ SAM thickness is assumed to be the same as that of the $FcC_{11}SAu$ SAM. Because the thicknesses of $HOC_{11}SAu$ and $FcC_{11}SAu$ SAMs are comparable and the assumed potential-induced thickness change for a 100% $FcC_{11}SAu$ SAM (maximum change) is small (~16% increase), the same layer model was simply used for both the $FcC_{11}SAu$ and mixed $FcC_{11}SAu/HOC_{11}SAu$ surfaces.

The $FcC_{11}SAu$ SAM/perchlorate results establish that our commercial SPR instrument is capable of tracking a monolayer-confined redox reaction as a function of the applied potential as well as readily detecting conformational or film thickness changes as small as 0.3 nm. We were thus able to employ this instrument to quantify the surfactant anions adsorbed at an electroactive interface under different conditions.

4.4.4 Assembly of Dodecyl Sulfate and Hydroxyundecyl Sulfonate to $FcC_{11}SAu$ SAMs

Because amphiphilic alkyl sulfates can adsorb non-specifically to hydrophobic surfaces,[8,15,17-19,23,45,48,113] it was initially necessary to check for adsorption of the dodecyl sulfate to the $FcC_{11}SAu$ SAM at open circuit (no applied potential) to ascertain whether the resonance angle shift measured upon oxidation of the $FcC_{11}SAu$ is only due to ion pairing of the surfactant anion to the ferrocenium or to the redox-induced re-organization of already adsorbed dodecyl sulfate and/or additional dodecyl sulfate adsorption. This was readily achieved by comparing the $\Delta\Theta_m$ measured for the adsorption of dodecyl sulfate from a 100 mM solution (12.5 × cmc) to the $FcC_{11}SAu$ monolayer to that of a $HO(EO)_3C_{11}SAu$ SAM known to resist surfactant adsorption. The same shift in the resonance angle, whose magnitude could be entirely accounted for by the increase in bulk refractive index on going from pure water to 100 mM $SN_{12}S$, was experimentally observed for the $FcC_{11}SAu$ SAM compared to the $HO(EO)_3C_{11}SAu$ SAM, demonstrating that little or no non-specific adsorption occurs prior to ferrocene oxidation (Figure 4.9). Adsorption of the alkyl sulfate anions to the $FcC_{11}SAu$ is therefore governed by ion-pair formation between the alkyl sulfate anions and the ferrocenium cations.

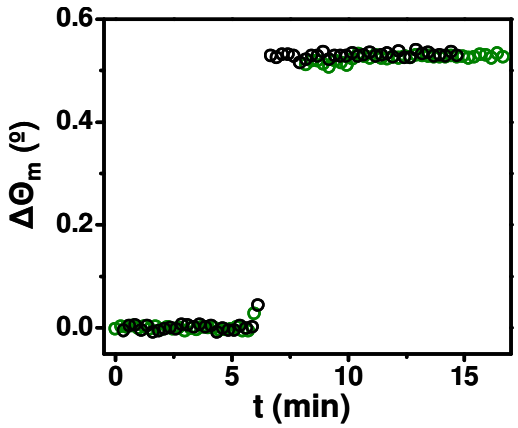

Figure 4.9 Comparison of the adsorption of SN_{12}S (100 mM) to a FcC_{11}SAu SAM (○) and to a HO$(EO)_3C_{11}$SAu SAM (○) using a scanning angle SPR spectrometer (λ = 633 nm, Resonant Probes GmbH).

Ion pairing to the electrochemically generated ferrocenium and the resulting molecular coverage were monitored by SPR. Scheme 1A illustrates the molecular characteristics of dodecyl sulfate. We first investigated the adsorption of the amphiphilic dodecyl sulfate to a 100% FcC_{11}SAu monolayer from aqueous solutions of different surfactant concentrations (Figure 4.10). Typical current and SPR responses with respect to time obtained for the FcC_{11}SAu monolayer during multiple cyclic voltammetric scans between –0.1 V and 0.75 V (vs. Ag/AgCl) in 100 mM SN_{12}S solution (12.5 × cmc) are shown in Figure 4.10A. An increase in the resonance angle occurs with the oxidation of ferrocene to ferrocenium (anodic segment), and a decrease of the same magnitude in resonance angle is observed upon reduction (cathodic segment). This shift in resonance angle is primarily attributed to the adsorption and desorption of surfactant. Similar to the perchlorate experiments, the stability and reproducibility of the multiple SPR angle scans

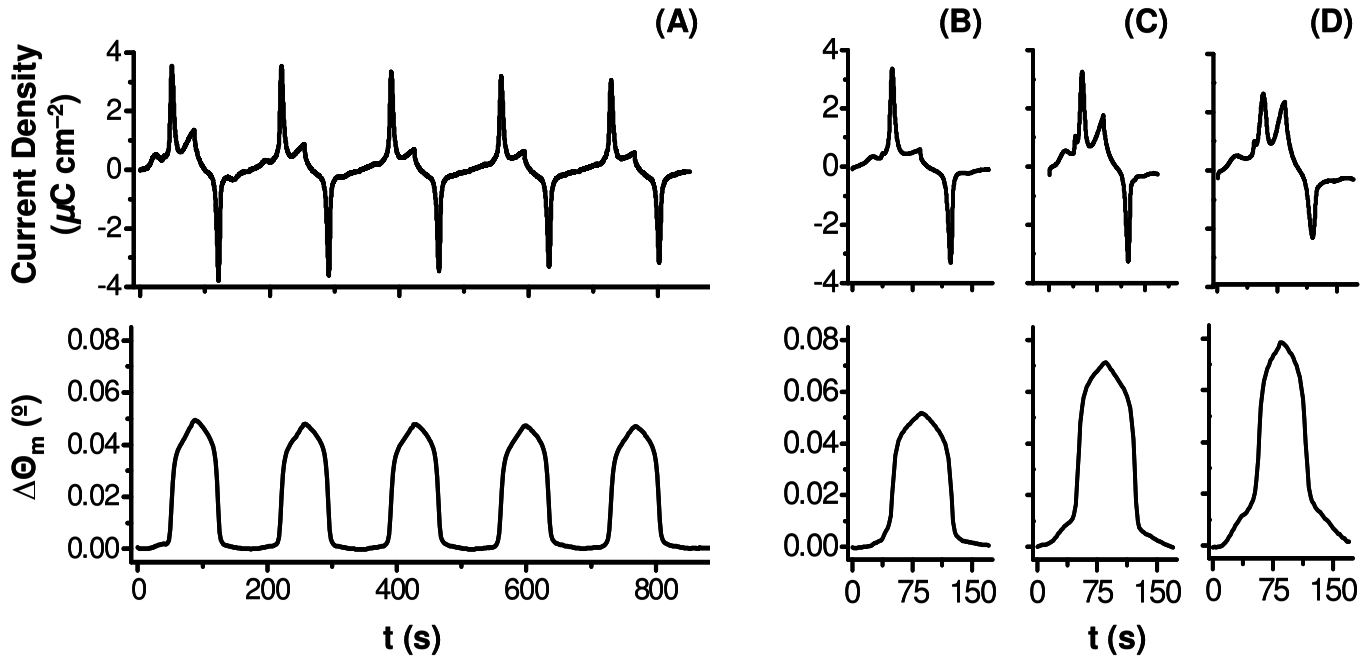

Figure 4.10 Current vs. time profiles obtained during potential cycling between -0.10 V and +0.75 V of a $FcC_{11}SAu$ SAM at a rate of 10 mV s^{-1} and the corresponding SPR profiles in **(A)** 100 mM (12.5 x cmc), **(B)** 32 mM (4 x cmc), **(C)** 8 mM (cmc) and **(D)** 2 mM (0.25 x cmc) $SN_{12}S$ solution.

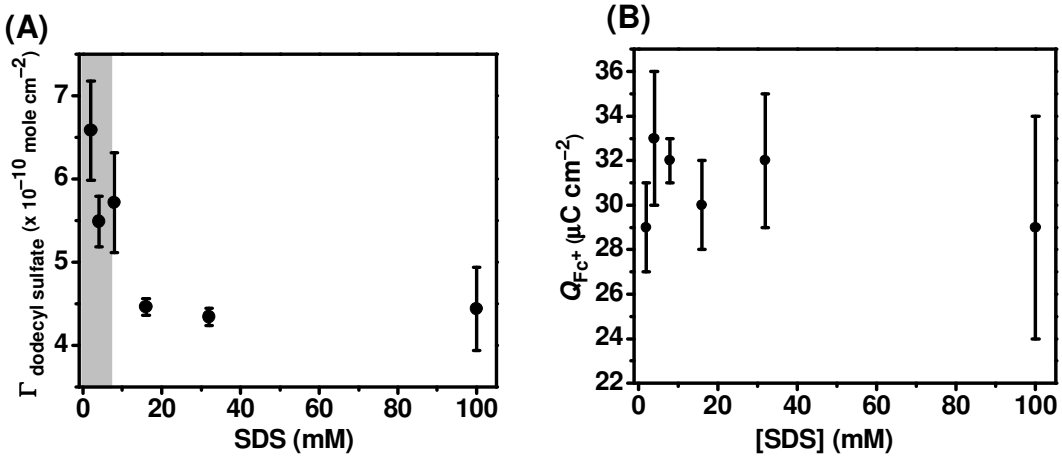

Figure 4.11 **(A)** A plot of the surface coverage (Γ) of dodecyl sulfate vs. the bulk concentration of SN_{12}S for a 100% FcC_{11}SAu SAM. The shaded region indicates data acquired below the cmc in water (8 mM). A surface concentration of ~3.6 x 10^{-10} mole·cm^{-2} corresponds to an effective layer thickness of 1 nm. **(B)** A plot of Q_{Fc^+} versus the [SN_{12}S] for a 100 % FcC_{11}SAu SAM. The error bars represent the standard deviation for at least 4 different experiments.

suggest that the redox-induced adsorption/desorption of dodecyl sulfate to/from the FcC_{11}SAu surface and any accompanying SAM orientational changes are reversible. From the maximum $\Delta\Theta_m$ recorded, the adsorbed surfactant layer surface coverage can readily be calculated, as previously outlined, from the parameters listed in Table 4.1. The effective surface coverage of the adsorbed dodecyl sulfate as a function of the bulk SN_{12}S concentration is shown in Figure 4.11A. Our study was limited in the lower concentration region to 2 mM, given the concentration of SN_{12}S electrolyte required for electrochemistry. The average layer thickness measured by SPR for the purified SN_{12}S above the cmc of 8.1 mM[34] is 1.2 ± 0.1 nm ($\Delta\Theta_m$ = 0.050 ± 0.005°). This layer thickness corresponds to a dodecyl sulfate surface coverage of 2.6 ± 0.1 molecules·nm^{-2} (Γ = 4.4 (±

0.4) x 10^{-10} mole·cm^{-2}) and an area per molecule of 0.38 ± 0.04 nm^2. We and others[23] have measured a similar layer thickness and coverage by SPR for the adsorption of dodecyl sulfate onto a hydrophobic undecanethiolate (C_{11}SAu) SAM above the cmc (i.e., in our case, d = 1.3 ± 0.2 nm at 100 mM SN_{12}S). As already mentioned in the introduction, AFM images have revealed that the dodecyl sulfate adsorbs to the C_{11}SAu SAM as cylindrical hemimicelles at [SN_{12}S] > cmc (Scheme 4.1B). Although the effective layer thickness and surface coverage are similar to that of the C_{11}SAu SAM, it is unlikely that dodecyl sulfate is adsorbed to the oxidized FcC_{11}SAu as hemicylindrical micelles, as discussed below.

As the bulk SN_{12}S concentration decreases below the cmc (i.e., [SN_{12}S] < 8 mM), there is an increase in the adsorbed layer thickness (Figures 4.10B–D and 4.11A), which reaches a maximum of 1.8 ± 0.2 nm or 4.0 ± 0.3 molecules·nm^{-2} (i.e., Γ = 6.6 (±0.6) x 10^{-10} mole·cm^{-2} or 0.25 ± 0.02 nm^2 per dodecyl sulfate). The measured thickness is too low for a bilayer film, even a disordered one. The surface coverage and molecular area instead correspond nicely with a condensed interdigitated monolayer of adsorbed dodecyl sulfate, where half of the surfactant molecules are oriented with their sulfate headgroups to the SAM (i.e., presumably ion-paired to the ferroceniums) and half have their headgroups exposed to the aqueous interface (Scheme 4.1C).[3,4] The surface coverage of adsorbed dodecyl sulfate obtained below the cmc on the FcC_{11}SAu SAM falls within the range of maximum values, 6.3 x 10^{-10} – 7 x 10^{-10} mol·cm^{-2}, attained on positively-charged $^{+}(CH_3)_3NC_{11}$SAu and $^{+}H_3NC_2$SAu SAMs.[24,49]

The charge density associated with the oxidation of 100% FcC_{11}SAu SAMs (Q_{Fc^+}) in aqueous SN_{12}S solutions ranging from 2 to 100 mM in concentration is given in

Figure 4.11B. Although there is some variability in the Q_{Fc^+} value measured for each SN_{12}S concentration, the charge remains essentially constant at an average value of 31 ± 2 μC·cm^{-2}. Our SPR results instead reveal that there is a 50% increase in the *total* surface coverage of dodecyl sulfate as the [SN_{12}S] is decreased below 8 mM. We have attempted to reconcile the SPR results with the electrochemistry data by considering how the number of surfactant molecules that would be ion paired to the ferrocenium, the only ones detected electrochemically, compare for the cylindrical hemimicelle and interdigitated monolayer configurations, assuming a 1:1 stoichiometric pairing as for ClO_4^-. There are five dodecyl sulfate monomers in the unit cell of the 2D lattice of hemicylindrical dodecyl sulfate aggregates (Scheme 4.1B).[4] Only two of these five monomers are lying flat down with their sulfate headgroups to the monolayer surface in a unit cell area of 4.4 nm × 0.50 nm.[4] Such a configuration would yield an effective electrochemical coverage of 0.9 dodecyl sulfate nm^{-2} or a theoretical Q_{Fc^+} of ~14 μC·cm^{-2}. In the close-packed, interdigitated monolayer configuration (Scheme 4.1C), half of the total dodecyl sulfates are ion paired to surface ferroceniums, corresponding to an electrochemical surface coverage of 2 dodecyl sulfates·nm^{-2} or $Q_{Fc^+} \approx 33$ μC·cm^{-2}. On the basis of the more than 2-fold difference in charge density, we should in practice be able to discriminate between these two different adsorption states via integration of the anodic peaks at ~0.16 V and ~0.40 V in the cyclic voltammograms (Figure 4.5A). The average Q_{Fc^+} (~31 μC·cm^{-2}) measured as a function of the bulk SN_{12}S concentration is comparable to the value predicted for an interdigitated monomolecular film in which ~70 % of the available ferrocenes are ion paired, as already alluded to in the electrochemistry part of the discussion. The lower thickness and coverage measured by SPR above the cmc may

therefore reflect a less densely packed interdigitated monolayer or disorganized surfactant aggregates that are dispersed across the ferrocenium surface rather than well-defined hemicylindrical micelle morphology. Moreover, although the dodecyl sulfate molecular area (~0.38 nm^2) measured by SPR above the cmc is compatible with the cross-sectional area of $FcC_{11}SAu$ (0.34 nm^2), a monolayer configuration in which all of the dodecyl sulfates are ion paired to ferrocenium and have their hydrophobic alkyl tails exposed to the aqueous solution would be thermodynamically unfavourable. Taking the surface coverage measured by SPR at [SN_{12}S] > 8 mM, Γ = 4.4 (±0.4) x 10^{-10} mole·cm^{-2}, and assuming an interdigitated monomolecular adsorption state, we calculate Q_{Fc^+} = 21 ± 2 μC·cm^{-2}, which is comparable (within our reported error) to the lower charge density values measured experimentally (Figure 4.11B).

To validate our conclusion that the dodecyl sulfate is ion paired to the ferrocenium as a close-packed interdigitated monolayer at [SN_{12}S] < cmc, we investigated the potential-induced adsorption/desorption of hydroxyundecyl sulfonate. By replacing the terminal methyl group with a hydrophilic OH group, the adsorption of the hydroxyundecyl sulfonate should be limited to a monolayer film in which *all* of the sulfonate headgroups are ion paired to the surface and the hydroxyl-terminated alkyl tails extend toward the aqueous solution. Isothermal titration calorimetry (results not shown) confirmed that SHS does not aggregate in deionized water at the solution concentration (20 mM) used for the ESPR measurements. In this case, a $\Delta\Theta_m$ = 0.053 ± 0.003° was observed,[114] which corresponds to an effective monolayer thickness of 1.3 ± 0.1 nm and a coverage of 3.9 (± 0.3) x 10^{-10} mole·cm^{-2}. The corresponding molecular area, 0.42 ± 0.03 nm^2 ·$molecule^{-1}$, is similar to that measured for a monolayer of SN_{12}S at the air/water

interface (i.e., 0.38 nm^2 (excess added salt) and 0.52 nm^2 (pure water)).[115,116] More importantly, the hydroxyundecyl sulfonate coverage determined by SPR is close to the coverage of 3.5 (±0.4) x 10^{-10} mole·cm^{-2} obtained from Q_{Fc^+}. In this case, the surface concentrations reported by CV and SPR should be the same.

We also investigated the adsorption of dodecyl sulfate onto mixed $FcC_{11}SAu/HOC_{11}SAu$ monolayers at bulk concentrations above and below the cmc. We used $HOC_{11}SH$ to prepare the mixed monolayers because it has been demonstrated that there is little nonspecific adsorption of dodecyl sulfate to hydroxyl-terminated SAMs.[19,24] $FcC_{11}SAu/HOC_{11}SAu$ monolayers, in which the ferrocene is homogeneously distributed throughout the surface at all $\chi_{Fc}^{surf} < 1$, were sought out here for an investigation of the effect of the ferrocenium charge density on surfactant adsorption. The surface distribution/microenvironment of the ferrocene in the mixed monolayers can be qualitatively ascertained from the shape of the voltammograms. The same general features reported in previous studies of SAMs formed from binary mixtures of ferrocenylalkanethiols and alkanethiols were observed for the $FcC_{11}SAu/HOC_{11}SAu$ monolayers used in the ESPR studies (Figure 4.12).[85,95,105,117] The multiple redox peaks present in the cyclic voltammograms recorded for mixed monolayers in which the mole fraction of ferrocene in solution (χ_{Fc}^{soln}) is >0.25 point to the presence of phase separation; the composition and size of the domains cannot be assessed with the available data.[94,105] Only at $\chi_{Fc}^{soln} \leq 0.25$ are single peaks observed at lower potential (~0.20 V). The mole fraction of $FcC_{11}S-$ contained in the mixed monolayers, χ_{Fc}^{surf}, dictates the resultant Q_{Fc^+}. The presence of phase separation in $FcC_{11}SAu/HOC_{11}SAu$ SAMs for which $\chi_{Fc}^{surf} \gtrsim 0.2$

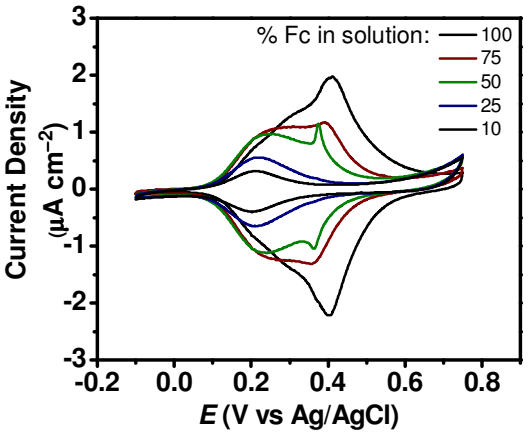

Figure 4.12 CV scans of $FcC_{11}SAu$ and $FcC_{11}S/HOC_{11}SAu$ SAMs in perchlorate solution (scan rate 10 $mV \cdot s^{-1}$).

precludes a meaningful analysis of the adsorption state of the dodecyl sulfate as a function of the surface ferrocene concentration. We focus instead on a comparison of the amount of adsorbed surfactant with χ_{Fc}^{surf} for two extreme concentrations: 2 mM $SN_{12}S$ (0.25cmc) and 100 mM $SN_{12}S$ (12.5cmc). Figure 4.13A shows the SPR-derived surface coverage of dodecyl sulfate as a function of the mole fraction of ferrocene contained at the interface and Figure 4.13B presents the ferrocenium charge density obtained from the anodic voltammetric curves. The Q_{Fc^+} values (Figure 4.13B) level off at a maximum of ~25 to 29 $\mu C \cdot cm^{-2}$ as χ_{Fc}^{surf} approaches unity for both $SN_{12}S$ concentrations, indicating that the number of ion paired dodecyl sulfates is similar in each case (i.e. 2.6–3.0 x 10^{-10} $mole \cdot cm^{-2}$). SPR (Figure 4.13A) demonstrates that the total dodecyl sulfate surface coverage plateaus at Γ is ~ 4.5 x 10^{-10} $mole \cdot cm^{-2}$ for the 100 mM $SN_{12}S$. Interestingly,

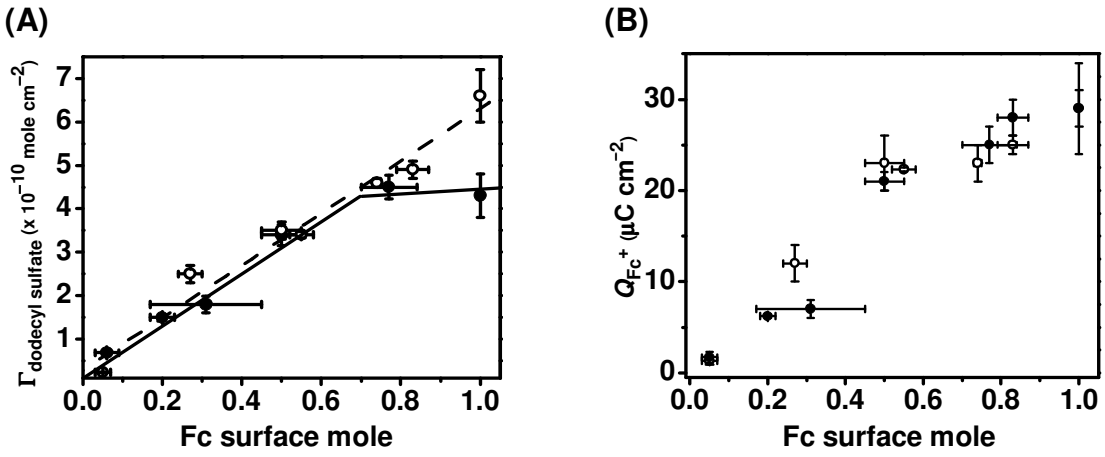

Figure 4.13 **(A)** A plot of $\Gamma_{\text{dodecyl sulfate}}$ vs. the mole fraction of ferrocene in $FcC_{11}SAu/HOC_{11}SAu$ SAMs: 100 mM (●) and 2 mM (○) SN_{12}S. The solid (100 mM) and dotted (2 mM) lines are guides for the eye. The mole fraction of ferrocene in the mixed SAMs was determined from the anodic voltammetric scans in perchlorate solution. **(B)** A plot of Q_{Fc^+} vs. the mole fraction of ferrocene in mixed SAMs: 100 mM (●) and 2 mM (○) SN_{12}S. The error bars represent the standard deviation for at least 4 different experiments.

both the Q_{Fc^+} and the SPR-measured dodecyl sulfate coverage plateau out at $\chi_{Fc}^{surf} \geq 0.7$, where the corresponding maximum Q_{Fc^+} that can be generated (i.e., ~32 to 46 $\mu C \cdot cm^{-2}$) is equal to or greater than the charge required to support an interdigitated dodecyl sulfate monolayer, according to the work of Lipkowski et al.[3,4] In contrast to the 100 mM SN_{12}S concentration, the total dodecyl sulfate coverage increases quasi-linearly to that of a compact interdigitated monolayer (theoretical $\Gamma \approx 6.6 \times 10^{-10}$ mole$\cdot cm^{-2}$) when the concentration of SN_{12}S in solution is 2 mM (Figure 4.13A). The different adsorption

behavior of dodecyl sulfate observed by SPR on $FcC_{11}SAu/HOC_{11}SAu$ monolayers at $SN_{12}S$ concentrations of 12.5 × cmc and 0.25 × cmc concurs with the variation of the layer thickness and molecular coverage observed above and below the cmc on pure $FcC_{11}SAu$ SAMs.

In the case of the 100% $FcC_{11}SAu$ SAM and the mixed $FcC_{11}SAu/HOC_{11}SAu$ monolayers where $\chi_{Fc}^{surf} \geq 0.7$, Γ_{Fc} yields maximum ferrocenium charge densities (~32 to 46 $\mu C \cdot cm^{-2}$) that are more than sufficient to support a condensed, interdigitated monomolecular film of dodecyl sulfate.[3,4] Our results, however, indicate that, in addition to the surface charge, the aggregation state of the $SN_{12}S$ in solution is also a critical determinant of the coverage of surfactant obtained by ion pairing to the electrochemically generated surface ferroceniums. This behaviour is in marked contrast to that reported for dodecyl sulfate adsorption to bare gold surfaces as the applied potential is cycled in the double-layer charging region[3,4] and to alkylthiolate–Au SAMs.[18,19,23,24,49] For dodecyl sulfate adsorption to a charged electrode, the amount and layer thickness of adsorbate was found to depend only on the applied potential and not on the aggregation state of the $SN_{12}S$ in solution. However, for neutral hydrophobic surfaces (methyl-terminated SAMs and polystyrene)[18,23,48] and cationic SAM surfaces (fixed-positive charge $^{+}(CH_3)_3NC_{11}SAu$ and charge-regulated $^{+}H_3NC_2SAu$ SAMs),[24,49] the amount of adsorbed dodecyl sulfate increases with the bulk $SN_{12}S$ concentration and plateaus at concentrations above the cmc. The redox-induced ion pairing of dodecyl sulfate investigated here exhibits the opposite behaviour, even though similar maximum coverages are attained in the $FcC_{11}SAu$ SAM with respect to the positively charged $^{+}(CH_3)_3NC_{11}SAu$ and $^{+}H_3NC_2SAu$ SAMs. The different surfactant adsorption

behaviour observed for the redox-active SAM system (Figure 4.11A) can be explained by the nature of the dodecyl sulfate–ferrocenium interaction (i.e., ion pairing versus Coulombic attraction[118] in the case of the charged electrode and SAM surfaces) as well as the fact that the concentration of surface ferroceniums and their average spacing are continuously changing during the course of the anodic voltammetric scan. The progressively increasing ferrocenium concentration has an obvious effect on the nucleation and growth of the dodecyl sulfate layer. The free dodecyl sulfate unimers that exist in solution below the cmc can more readily adapt to the changing ferrocenium concentration, since these interact independently with the surface to screen the positive charge of the electrochemically generated ferrocenium. This direct interaction should facilitate the formation of a more densely-packed interdigitated monolayer within the time frame of the anodic scan (85 s). As the SN_{12}S concentration is increased above the cmc, the monomer surfactant concentration remains approximately constant ([monomer] = cmc) and the concentration of SN_{12}S micelles increases with the bulk concentration.[34] Therefore, at [SN_{12}S] > cmc, SN_{12}S micelles adsorb to the surface, spread, and reorganize themselves to form a monolayer film, in a process analogous to the fusion of small unilamellar lipid vesicles onto solid supports[119] or the monomers present in the solution in proportionally lower concentration can adsorb directly to the surface. The deposition of dodecyl sulfate from micelles can be expected to be kinetically slower than the direct ion pairing of free unimers, giving rise to a less compact adsorbate structure as suggested by our results. With regards to the adsorption of SN_{12}S micelles, our SPR results show that dodecyl sulfate does not initially adsorb onto the neutral ferrocene surface (Figure 4.9). However, it is known from contact angle studies and AFM force measurements that the oxidation of the ferrocene to ferrocenium renders the SAM surface more

hydrophilic.[109,120,121] It is therefore conceivable that the negatively-charged and hydrophilic SN_{12}S micelles adsorb to the ferrocenium monolayer and rearrange themselves on the surface during the potential scan. To gain a better understanding of the adsorption mechanism below and above the cmc, electrochemical AFM imaging and AFM force measurements will be used in future experiments to follow the dodecyl sulfate adsorption process and visualize the adsorbed surfactant structure.

4.5 Conclusions

The study reported herein presents the first evidence that the assembly of an anionic surfactant, dodecyl sulfate, on a monolayer surface by specific ion pairing interactions with cationic moieties formed by potential-induced oxidation is governed by different factors than the electrostatic adsorption of the same surfactant to fixed-charge surfaces. We have demonstrated that SPR spectroscopy is a sensitive surface technique for investigating the redox-driven assembly of ionic surfactants at SAM-modified Au surfaces. Both alkyl sulfates and alkyl sulfonates ion-pair with a ferrocenium alkanethiolate surface to form a monolayer film. In the case of the amphiphilic dodecyl sulfate, the molecules in the adsorbed monolayer alternate between a head up and head down orientation with respect to the surface. The surface coverage of dodecyl sulfate depends on both the ferrocenium surface concentration and the surfactant aggregation state. The maximum coverage of dodecyl sulfate on the ferrocenium surface is obtained below the cmc, in contrast to dodecyl sulfate adsorption to a static cationic SAM. This marked difference in adsorption behaviour is attributed to the dynamic generation of the ferrocenium and the specific nature of the ion pairing interactions versus pure

electrostatic ones. Hydroxyl-terminated undecyl sulfonate anions are all adsorbed to the ferrocenium monolayer with their headgroups to the surface and the hydrophilic endgroup exposed to the aqueous solution.

The interfacial assembly of molecules via ion pairing interactions between the adsorbate and a surface-confined redox species is not limited to ionic surfactants that form micelles in solution. This work, therefore, opens the way for the controlled assembly of other materials (block copolymers, surfacto-mesogens, metal nanoparticles, etc.) at electroactive ultrathin film interfaces using either ion-pair recognition or electron donor–acceptor-type charge-transfer complexation with redox moieties in the film. Both molecular structure/property variation and electrochemical modulation should provide for exquisite control over the extent of the pairing or complexation interactions and thus the organization of the adsorbed materials.

4.6 Acknowledgments

This work was supported by NSERC (Canada), CFI (Canada), FQRNT (Québec), Canada Research Chairs program, and the Université de Montréal. L.N. gratefully acknowledges fellowship support from the Groupe de recherche en technologie des couches minces. We thank Ms. Patricia Moraille (Laboratoire de caractérisation des matériaux, Université de Montréal) for AFM imaging and Mr. Martin Lambert (Chemistry Mechanics Shop, Université de Montréal) for the design and construction of the ESPR cell.

4.7 References

(1) Myers, D. *Surfaces, Interfaces and Colloids: Principles and Applications*; 2 nd ed.; Wiley-CH: New York, 1999.

(2) Atkin, R.; Craig, V. S. J.; Wanless, E. J.; Biggs, S. *Adv. Colloid Interface Sci* **2003**, *103*, 219–304 and references therein.

(3) Burgess, I.; Jeffrey, C. A.; Cai, X.; Szymanski, G.; Galus, Z.; Lipkowski, J. *Langmuir* **1999**, *15*, 2607–2616.

(4) Burgess, I.; Zamlynny, V.; Szymanski, G.; Lipkowski, J.; Majewski, J.; Smith, G.; Satija, S.; Ivkov, R. *Langmuir* **2001**, *17*, 3355–3367.

(5) Jaschke, M.; Butt, H.-J.; Gaub, H. E.; Manne, S. *Langmuir* **1997**, *13*, 1381–1384.

(6) Lachlan, M. G.; Tiberg, F.; Ducker, W. A. *J. Phys. Chem. B* **1998**, *102*, 4288–4294.

(7) Petri, M.; Kolb, D. M. *Phys. Chem. Chem. Phys.* **2002**, *4*, 1211–1216.

(8) Wirth, M. J.; Piasecki-Coleman, D. A.; Montgomery, M. E. J. *Langmuir* **1995**, *11*, 990–995.

(9) Schulz, J. C.; Warr, G. G. *Langmuir* **2002**, *18*, 3191–3197.

(10) Böhmer, M. R.; Koopal, L. K. *Langmuir* **1992**, *8*, 2660–2665.

(11) Wanless, E. J.; Davey, T. W.; Ducker, W. A. *Langmuir* **1997**, *13*, 4223–4228.

(12) Atkin, R.; Craig, V. S. J.; Wanless, E. J.; Biggs, S. *J. Colloid Interface Sci.* **2003**, *266*, 236–244.

(13) Fan, A.; Somasundaran, P.; Turro, N. J. *Langmuir* **1997**, *13*, 506–510.

(14) Király, Z.; Findenegg, G. H.; Klumpp, E.; Schlimper, H.; Dékány, I. *Langmuir* **2001**, *17*, 2420–2425.

(15) Montgomery, M. E. J.; Wirth, M. J. *Langmuir* **1994**, *10*, 861–869.

(16) Hu, C.; Hu, S. *J. Solid State Electrochem.* **2004**, *8*, 947–956.

(17) Hu, K.; Bard, A. J. *Langmuir* **1997**, *13*, 5418–5425.

(18) Sigal, G. B.; Mrksich, M.; Whitesides, G. M. *Langmuir* **1997**, *13*, 2749–2755.

(19) Sigal, G. B.; Mrksich, M.; Whitesides, G. M. *J. Am. Chem. Soc.* **1998**, *120*, 3464–3473.

(20) Bolze, J.; Hörner, K. D.; Ballauff, M. *Colloid Polym. Sci.* **1996**, *274*, 1099–1108.

(21) Galisteo González, F.; Cabrerizo Vilchez, M. A.; Hidalgo-Alvarez, R. *Colloid Polym. Sci.* **1991**, *269*, 406–411.

(22) Griskey, R. G.; Woodward, C. E. *J. Appl. Polym. Sci.* **1966**, *10*, 1027–1032.

(23) Levchenko, A. A.; Argo, B. P.; Vidu, R.; Talroze, R. V.; Stroeve, P. *Langmuir* **2002**, *18*, 8464–8471.

(24) Tulpar, A.; Ducker, W. A. *J. Phys. Chem. B* **2004**, *108*, 1667–1676.

(25) Tiberg, F.; Brinck, J.; Grant, L. *Curr. Opin. Colliod Interface Sci.* **1999**, *4*, 411–419.

(26) Manne, S.; Cleveland, J. P.; Gaub, H. E.; Stucky, G. D.; Hansma, P. K. *Langmuir* **1994**, *10*, 4409–4413.

(27) Manne, S.; Gaub, H. E. *Science* **1995**, *270*, 1480–1482.

(28) Retter, U.; Tchachnikova, M. *J. Electroanal. Chem.* **2003**, *550–551*, 201–208.

(29) Tiberg, F. *J. Chem. Soc. Faraday Trans.* **1996**, *92*, 531–538.

(30) Tiberg, F.; Landgren, M. *Langmuir* **1993**, *9*, 927–932.

(31) Wandlowski, T.; Hromadova, M.; de Levie, R. *Langmuir* **1997**, *13*, 2766–2772.

(32) Hamley, I. W. *Introduction to Soft Matter: Polymers, Colloids, Amphiphiles and Liquid Crystals*; Wiley-VCH: New York, 2000.

(33) Aniansson, E. A. G.; Wall, S. N.; Almgren, M.; Hoffmann, H.; Kielmann, H.; Ulbricht, W.; Zana, R.; Lang, J.; Tondre, C. *J. Phys. Chem.* **1976**, *80*, 905–922.

(34) Israelachvili, J. N. In *Intermolecular and Surface Forces*; 2nd ed. ed.; Academic Press: London, 1992, p 341–385.

(35) Lianos, P.; Zana, R. *J. Colloid Interface Sci.* **1981**, *84*, 100–107.

(36) The given surface coverage is the average of the values obtained by Burgess et al. by electrochemistry and neutron reflectivity.

(37) Retter, U. *Langmuir* **2000**, *16*, 7752–7756.

(38) Ulman, A. *Chem. Rev.* **1996**, *96*, 1533–1554.

(39) Dubois, L. H.; Nuzzo, R. G. *Annu. Rev. Phys. Chem.* **1992**, *43*, 437–463.

(40) Goloub, T. P.; Koopal, L. K.; Bijsterbosch, B. H. *Langmuir* **1996**, 3188–3194.

(41) Lee, E. M.; Koopal, L. K. *J. Colloid Interface Sci.* **1996**, *177*, 478–489.

(42) Leimbach, J.; Sigg, J.; Rupprecht, H. *Colloids Surf., A* **1995**, *94*, 1–11.

(43) Schulz, J. C.; Warr, G. G.; Hamilton, W. A.; Butler, P. D. *Phys. Rev. E* **2001**, *63*, 1604–1608.

(44) Velegol, S. B.; Fleming, B. D.; Biggs, S.; Wanless, E. J.; Tilton, R. D. *Langmuir* **2000**, *16*, 2548–2556.

(45) Wanless, E. J.; Ducker, W. A. *J. Phys. Chem.* **1996**, *100*, 3207–3214.

(46) Wanless, E. J.; Ducker, W. A. *Langmuir* **1997**, *13*, 1463–1474.

(47) Somasundaran, P.; Fuerstenau, D. W. *J. Phys. Chem. B* **1966**, *70*, 90–96.

(48) Turner, S. F.; Clarke, S. M.; Rennie, A. R.; Thirtle, P. N.; Cooke, D. J.; Li, Z. X.; Thomas, J. K. *Langmuir* **1999**, *15*, 1017–1023.

(49) Artyukhin, A. B.; Burnham, K. J.; Levchenko, A. A.; Talroze, R. V.; Stroeve, P. *Langmuir* **2003**, *19*, 2243–2248.

(50) Abbott, N. L.; Whitesides, G. M. *Langmuir* **1994**, *10*, 1493–1497.

(51) Luk, Y.-Y.; Abbott, N. L. *Science* **2003**, *301*, 623–626.

(52) Ivanisevic, A.; Im, J.-H.; Lee, K.-B.; Park, S.-J.; Demers, L. M.; Watson, K. J.; Mirkin, C. A. *J. Am. Chem. Soc.* **2001**, *123*, 12424–12425.

(53) This work differs from published investigations of the effect of preassembled layers of surfactants (Peng, Z.; Qu, X.; Dong, S. J. Electroanal. Chem. 2004, 563, 291–298) and Twardowski, M.; Nuzzo, R. G. Langmuir 2004, 20, 175–180) on the electrochemical behaviour of ferrocene-terminated alkanethiolate monolayers in aqueous solutions containing added electrolyte and/or redox probes.

(54) Sumner, J. J.; Creager, S. E. *J. Phys. Chem. B* **2001**, *105*, 8739–8745.

(55) Valincius, G.; Niaura, G.; kazakevičienė, B.; Talaikytė, Z.; Kažemėkaitė, M.; Butkus, E.; Razumas, V. *Langmuir* **2004**, *20*, 6631–6638.

(56) Kazakevičienė, B.; Valincius, G.; Niaura, G.; Talaikytė, Z.; Kažemėkaitė, M.; Razumas, V. *J. Phys. Chem. B* **2003**, *107*, 6661–6663.

(57) Ju, H.; Leech, D. *Phys. Chem. Chem. Phys.* **1999**, *1*, 1549–1554.

(58) Creager, S. E.; Rowe, G. K. *J. Electroanal. Chem.* **1994**, *370*, 203–211.

(59) *Handbook of Optical Constants of Solids III*; Palik, E. D., Ed.; Academic Press, Inc.: New York, 1985.

(60) Ohtsuka, T.; Sato, K.; Uosaki, K. *Langmuir* **1994**, *10*, 3658–3662.

(61) Bard, A. J.; Faulkner, L. R. *Electrochemical Methods Fundamentals and Applications*; 2nd ed. ed.; J. Wiley & Sons: New York, 2001.

(62) Mukhopadhyay, R. *Anal. Chem.* **2005**, *17*, 313A–317A.

(63) Aust, E. F.; Ito, S.; Sawodny, M.; Knoll, W. *TRIP* **1994**, *2*, 313–323.

(64) Davies, J.; Faulkner, I. In *Surface Analytical Techniques for Probing Biomaterial Processes* Davies, J. ed.; CRC Press: Boca Raton, Fl, 1996, p 67–87 and references therein.

(65) Knoll, W. *Ann. Rev. Phys. Chem.* **1998**, *49*, 569–638.

(66) Johansen, K.; Stålberg, R.; Lundström, I.; Liedberg, B. *Meas. Sci. Technol.* **2000**, *11*, 1630–1638.

(67) *CRC Handbook of Chemistry and Physics*; 85 th. ed.; Lide, D. R., Ed.; CRC Press LLC: Boca Raton, Fl, 2004.

(68) Marra, J.; Israelachvili, J. N. *Biochemistry* **1985**, *24*, 4608–4618.

(69) Peterlinz, K. A.; Georgiadis, R. *Opt. Commun.* **1996**, *130*, 260–266.

(70) Peterlinz, K. A.; Georgiadis, R. *Langmuir* **1996**, *12*, 4731–4740.

(71) Jung, L. S.; Campbell, C. T.; Chinowsky, T. M.; Mar, M. N.; Yee, S. S. *Langmuir* **1998**, *14*, 5636–5648.

(72) *American Institute of Physics Handbook*; 3 rd. ed.; Gray, D. E., Ed.; McGraw-Hill, Inc: New York, 1972.

(73) Camin, D. L.; Rossini, F. D. *J. Phys. Chem.* **1955**, *59*, 1173–1179.

(74) For example, for polyethylene, $n_{633\ nm} - n_{780\ nm}$.[60] For *n*-$C_{11}H_{24}$ to *n*-$C_{15}H_{32}$, $n_{589\ nm} - n_{780\ nm} = -0.0020 - 0.0025$ (25 °C).

(75) Defeijter, J. A.; Benjamins, J.; Veer, F. A. *Biopolymers* **1978**, *17*, 1759–1772

(76) Kavanagh, R. J.; lu, K. K.; Thomas, J. K. *Langmuir* **1992**, *8*, 3008–3013.

(77) Tiberg, F.; Ederth, T. *J. Phys. Chem. B* **2000**, *104*, 9689–9695.

(78) Harvey, A. H.; Gallagher, J. S.; Sengers, J. M. H. L. *J. Phys. Chem. Ref. Data* **1998**, *27*, 761–774.

(79) Tumolo, T.; Angnes, L.; Baptista, M. S. *Anal. Biochem.* **2004**, *333*, 273–279.

(80) Bain, C. D.; Troughton, E. B.; Tao, Y.-T.; Evall, J.; Whitesides, G. M.; Nuzzo, R. G. *J. Am. Chem. Soc.* **1989**, *111*, 321–335.

(81) Biebuyk, H. A.; Bain, C. D.; Whitesides, G. M. *Langmuir* **1994**, *10*, 1825–1831.

(82) Porter, M. D.; Bright, T. B.; Allara, D. L.; Chidsey, C. E. D. *J. Am. Chem. Soc.* **1987**, *109*, 3559–3568.

(83) Chidsey, C. E. D.; Bertozzi, C. R.; Putvinski, T. M.; Mujsce, A. M. *J. Am. Chem. Soc.* **1990**, *112*, 4301–4306.

(84) Chidsey, C. E. D. *Science* **1991**, *251*, 919–922.

(85) Creager, S. E.; Rowe, G. K. *J. Electroanal. Chem.* **1997**, *420*, 291–299.

(86) De Long, H. C. D.; Buttry, D. A. *Langmuir* **1992**, *8*, 2491–2496.

(87) De Long, H. C. D.; Donohue, J. J.; Buttry, D. A. *Langmuir* **1991**, *7*, 2196–2202.

(88) Popenoe, D. D.; Deinhammer, R. S.; Porter, M. D. *Langmuir* **1992**, *8*, 2521–2530.

(89) Uosaki, K.; Sato, Y.; Kita, H. *Langmuir* **1991**, *7*, 1510–1514.

(90) Walczak, M. M.; Popenoe, D. D.; Deinhammer, R. S.; Lamp, B. D.; Chung, C.; Porter, M. D. *Langmuir* **1991**, *7*, 2687–2693.

(91) Collard, D. M.; Fox, M. A. *Langmuir* **1991**, *7*, 1192–1197.

(92) Creager, S. E.; Rowe, G. K. *Anal. Chim. Acta* **1991**, *246*, 233–239.

(93) Kondo, T.; Okamura, M.; Uosaki, K. *J. Organomet. Chem.* **2001**, *637–639*, 841–844.

(94) Lee, L. Y. S.; Sutherland, T. C.; Rucareanu, S.; Lennox, R. B. *Langmuir* **2006**, *22*, 4438–4444.

(95) Rowe, G. K.; Creager, S. E. *Langmuir* **1991**, *7*, 2307–2312.

(96) Viana, A. S.; Jones, A. H.; Abrantes, L. M.; Kalaji, M. *J. Electroanal. Chem.* **2001**, *500*, 290–298.

(97) Yao, X.; Wang, J.; Zhou, F.; Wang, J.; Tao, N. *J. Phys. Chem. B* **2004**, *108*, 7206–7212.

(98) Ye, S.; Haba, T.; Sato, Y.; Shimuza, K.; Uosaki, K. *Phys. Chem. Chem. Phys.* **1999**, *1*, 3653–3659.

(99) Ye, S.; Sato, Y.; Uosaki, K. *Langmuir* **1997**, *13*, 3157–3161.

(100) Quist, F.; Tabard-Cossa, V.; Badia, A. *J. Phys. Chem. B* **2003**, *107*, 10691–10695.

(101) Sato, Y.; Mizutani, F.; Shimuza, K.; Ye, S.; Uosaki, K. *J. Electroanal. Chem.* **1999**, *474*, 94–99.

(102) Shimuza, K.; Yagi, I.; Sato, Y.; Uosaki, K. *Langmuir* **1992**, *8*, 1385–1387.

(103) Calvente, J. J.; Andreu, R.; Molero, M.; López-Pérez, G.; Domínguez, M. *J. Phys. Chem. B* **2001**, *105*, 9557–9568.

(104) Surface concentrations of the electroactive moieties cannot be directly quantified by DPV.

(105) Auletta, T.; van Veggel, F. C. J. M.; Reinhoudt, D. N. *Langmuir* **2002**, *18*, 1288–1293.

(106) The use of chronocoulometry may have allowed us to more accurately determine the charge density associated with ferrocene oxidation in $SN_{12}S$ and SHS solution because the double-layer charging contribution can be directly quantified by chronocoulometry as compared to CV.

(107) Abrantes, L. M.; Kalaji, M.; Viana, A. S. *Russ. J. Electrochem.* **2002**, *38*, 39–43.

(108) Viana, A. S.; Abrantes, L. M.; Jin, G.; Floate, S.; Nichols, R. J.; Kalaji, M. *Phys. Chem. Chem. Phys.* **2001**, *3*, 3411–3419.

(109) Green, J.-B. D.; McDermott, M. T.; Porter, M. D. *J. Phys. Chem.* **1996**, *100*, 13342–13345.

(110) Badia, A.; Arnold, S.; Scheumann, V.; Zizlsperger, M.; Mack, J.; Jung, G.; Knoll, W. *Sens. Actuators B* **1999**, *54*, 145–165.

(111) Heaton, R. J.; Peterson, A. W.; Georgiadis, R. M. *PNAS* **2001**, *98*, 3701–3704.

(112) Shimuza, K.; Yagi, I.; Sato, Y.; Uosaki, K. *J. Electroanal. Chem.* **1994**, *372*, 117–124.

(113) Ducker, W. A.; Grant, L. M. *J. Phys. Chem.* **1996**, *100*, 11507–11511.

(114) The same resonance angle shift was measured at 10 and 50 mM SHS.

(115) Tajima, K.; Muramatsu, M.; Sasaki, T. *Bull. Chem. Soc. Jpn.* **1970**, *43*, 1991–1998.

(116) Sasaki, T.; Hattori, M.; Sasaki, J.; Nukina, K. *Bull. Chem. Soc. Jpn.* **1975**, *48*, 1397–1403.

(117) Kawaguchi, T.; Tada, K.; Shimuza, K. *J. Electroanal. Chem.* **2003**, *543*, 41–49.

(118) The term "ion pair" refers to a pair of oppositely charged ions held together by coulomb attraction without the formation of a covalent bond, whereas a coulomb interaction is the electrostatic force of attraction exerted by one charged particle on another charged particle of opposite sign.

(119) Richter, R. P.; Bérat, R.; Brisson, A. R. *Langmuir* **2006**, *22*, 3497–3505 and references therein.

(120) Sondag-Huethorst, J. A. M.; Fokkink, L. G. J. *Langmuir* **1994**, *10*, 4380–4387.

(121) Sondag-Huethorst, J. A. M.; Fokkink, L. G. J. *Langmuir* **1992**, *8*, 2560–2566.

Chapter 5

Electrochemical Surface Plasmon Resonance Investigation of the Directed Interfacial Assembly of Sodium *n*-Alkyl Sulfates to a Redox-Active Self-Assembled Monolayer via Ion-Pairing Interactions

5.1 Introduction

The electrochemically-induced assembly of molecules and nanoparticles via the formation of ion pairs or charge-transfer complexes with surface-immobilized redox moieties is a potentially attractive means of organizing materials on modified electrodes.[1-3] This chapter reports on the potential-induced aggregation of amphiphilic sodium *n*-alkyl sulfates ($C_nH_{2n+1}OSO_3Na$, where n = 0, 1, 6, 8, 10, 12 or 14) at the surface of SAMs of $FcC_{11}SH$ on gold. Our CV and ESPR spectroscopy results show that the longer chain alkyl sulfates form a condensed monolayer at the SAM/solution interface via ion-pairing interactions between the anionic sulfate headgroups and the electrogenerated ferrocenium cations. By varying the chain length of the alkyl tail, and hence the hydrophobicity of the anion, the relative ion-pairing ability of the alkyl sulfate can be varied by a factor of ~100. The longer chain dodecyl and tetradecyl sulfates exhibit ion pairing abilities that are comparable to or greater than that of perchlorate, an anion commonly used in electrochemical investigations of ferrocene-terminated SAMs, and which forms 1:1

contact (tight) ion pairs that stabilize the oxidized ferrocenium cations. In a more general context, this work demonstrates that molecular structure/physical property variation and electrochemical modulation can provide for exquisite control over the organization of ionic amphiphiles at modified electrodes by redox-induced ion-pairing interactions. Such a finding is of potential value to manufacturing technologies that operate by assembling or orienting molecules via electrical stimuli.

The work described herein extends previous investigations of electrolyte anion effects on the oxidation of ferrocenylalkylthiolate SAMs from simple inorganic anions (i.e., $PF_6^- > ClO_4^- > BF_4^- > NO_3^- > Cl^- > SO_4^{2-} > NH_2SO_4^{2-} > F^-$) to anionic surfactants. Anions carrying a substantial hydrocarbon residue must be thought of in a different way than simple approximately spherically symmetrical ions. When hydrophobic and hydrophilic groups are present in the same system, their effect on the solvation or hydration of the molecule depends on a variety of factors, such as the relative number and hydrophobic/hydrophilic strength of the groups, their mutual position, the structure of the amphiphilic aggregates, and the solution concentration.[4-6] For instance, studies on amino acids and oligopeptides have shown that up to the six methylenes closest to the amino and carboxylate groups exhibit a lower apparent hydrophobicity because these are situated within the hydrophilic hydration spheres of the polar groups.[4] Here, alkyl sulfates were chosen as prototypes because these are commonly used surfactants in consumer and industrial applications, and we[7] and others[8,9] have shown the reversible oxidation and reduction of ferrocenylalkanethiolate SAMs in aqueous solutions of alkyl sulfates and aryl sulfonates. Sodium *n*-alkyl sulfates spontaneously aggregate in water to form nearly-spherical micelles at room temperature above the cmc.[10-12] The process of surfactant

clustering or micellization is primarily an entropy-driven process, where the growth of the micelles is limited by the Coulomb interaction between the headgroup ions.[11] The number of carbon atoms in the hydrocarbon chain plays a dominant role in the behaviour of the system in solution.[13] The cmc decreases with increasing chain length from ~500 mM for n = 6 to 2 mM for n = 14 and the aggregation number increases from 17 for n = 6 to ~80 for n = 14 at room temperature.[11] While there exist numerous studies on the solution aggregation behavior of n-alkyl sulfates,[12-17] surprisingly there have only been a few systematic investigations of the interdependence between the molecular structure and the interfacial properties.[18-20] The adsorption of surfactants at interfaces, particularly at the solid/liquid and liquid/liquid interfaces, is important in many industrial and biological applications. Moreover, because most particles in aqueous solutions carry a net surface-charge, which is also the case with many biological molecules, the study of surfactant adsorption at charged interfaces should provide insight about their role in physico-chemical[21,22] and biological[22,23] processes.

In the previous chapter, we found that the anionic surfactant, dodecyl sulfate ($N_{12}S^-$), readily forms an ion pair with the oxidized ferrocenium. We combined electrochemistry with the surface sensitive technique of SPR spectroscopy to monitor the real-time adsorption/desorption of $N_{12}S^-$ during the oxidation/reduction of the surface-confined ferrocene/ferrocenium moieties. For a single-component $FcC_{11}SAu$ SAM, we found that the amount of adsorbed $N_{12}S^-$ was dependent on the bulk surfactant solution concentration. Well below the cmc (<0.25 × cmc) there was a tendency to form more tightly compact interdigitated monolayers, whereas an increase in the surfactant concentration to where both monomers and micelles are found in solution resulted in a

decrease in the Γ_{SPR} observed by ESPR. In this chapter, we continue our investigation of the ion pair complexation of a homologous series of anionic *n*-alkyl sulfates to a 100% $FcC_{11}SAu$ SAM.

5.2 Materials and Methods

5.2.1 Materials

Sodium 1-tetradecyl sulfate ($SN_{14}S$, 99%), sodium octyl sulfate (SN_8S, 99%), and sodium *n*-hexyl sulfate (SN_6S, 99%) were purchased from Alfa Asear (Ward Hill, MA). Sodium decyl sulfate ($SN_{10}S$, 99+%) and perchloric acid (70% in water, 99.999) were obtained from Fluka Canada. Sodium sulfate (SN_0S, $\geq 99\%$), sodium methyl sulfate (SN_1S) and sodium perchlorate (98%) where all obtained from Sigma-Aldrich Canada. The above compounds were used as received. Sodium dodecyl sulfate ($SN_{12}S$, 99+%, Sigma-Aldrich) was recrystallized three times from absolute ethanol before use. The absence of hydrolyzed product (i.e., dodecanol) was verified by ^1H NMR spectroscopy (400 MHz, d_6-DMSO).

Deionized-distilled water obtained by further purification of distilled water with a Milli-Q Gradient system (Millipore, Bedford, MA) was used to prepare all the aqueous solutions. The purified water has a resistivity of 18.2 MΩ·cm and a surface tension of 72 $mN \cdot m^{-1}$ measured at 24 °C. The aqueous surfactant electrolyte solutions, which contained no added salt, were purged with nitrogen for at least 20 minutes prior to the electrochemical measurements.

5.2.2 $FcC_{11}SH$, Electrode, and Monolayer Preparation

$FcC_{11}SH$ was synthesized as outlined in Chapter 4 (section 4.3.1) prior to proceeding with the preparation of the $FcC_{11}SAu$ slides which is also outlined in the same chapter.

5.2.3 Instrumentation and Electrochemical Measurements

Electrochemical Measurements. All CV experiments were carried out using an Epsilon potentiostat (Bioanalytical Systems, Inc., West Lafayette, IN). A custom-built, one-compartment three-electrode cell was employed, where the $FcC_{11}SAu$ substrate served as the working electrode, the counter electrode was a platinum wire (99.9%, Alfa Aesar), and all potentials are reported with respect to an aqueous Ag/AgCl reference electrode (3 M NaCl, Bioanalytical Systems). The CVs were acquired from –0.10 V to 0.75 V at a potential scan rate of 10 $mV \cdot s^{-1}$. The Γ_{Fc^+} was determined using equation 4.3.[24]

In-situ SPR Measurements. To carry out ESPR measurements, the custom-built electrochemical cell was mounted on a computer-controlled SR7000 surface plasmon resonance instrument (Reichert, Inc., Depew, NY) enabling simultaneously monitoring of the optical/electrochemical processes occurring at the gold substrate. The details of this setup have been previously described elsewhere in proceeding chapters.

Adsorbed Layer Thickness Calculations. Adsorbed layer thicknesses were determined from the $\Delta\Theta_m$ values using Fresnel multilayer modeling (Winspall software version 2.20, MPI-P, Mainz, Germany) as outlined in Chapter 4. $\partial\Theta_m/\partial d$ values are listed in Table 5.1 (column 2) and vary slightly with the bulk SN_cS concentration (Table 5.1,

Table 5.1 Parameters for Determining the Effective Thickness and Surface Coverage of the Potential-Induced Surfactant Adsorption.

	Surfactant concentration (mM)	$\partial\Theta/\partial d$ ($^\circ\cdot nm^{-1}$)	$\partial n/\partial C$ ($\times 10^{-5}$ mM^{-1})
SN_6S	28	0.0411	2.57
SN_8S	33	0.0411	2.59
	100	0.0407	
	130	0.0405	
	390	0.0391	
SN_{10}S	8	0.0411	3.12
	32	0.0402	
	100	0.0404	

column 1). The refractive indices of 1.46 and 1.45 were used in the Fresnel calculations for the self-assembled $FcC_{11}S$– monolayer[25] and the adsorbed layers of N_cS^- ,[26,27] respectively. The effective thickness of the adsorbed layer can be determined using the reciprocal of the concentration specific $\partial\Theta_m/\partial d$ by equation 4.2.[26-28] The amount of N_cS^- adsorbed to the surface ($\Gamma_{N_cS^-}$), which unlike d and $n_{adsorbate}$, does not depend on the assumption of layer uniformity, can then be obtained by equation 4.3 as outlined in section 4.3.5.[29] The incremental change of refractive index with increase in the SN_cS concentration, $\partial n/\partial C$, was measured by refractometry (λ = 589 nm) and the values are listed in Table 5.1 (column 3).

5.3 Results and Discussion

5.3.1 Electrochemical Characterization of $FcC_{11}SAu$ SAMs in Sodium *n*-Alkyl Sulfate ($C_nH_{2n+1}OSO_3Na$) Electrolytes

Shown in Figure 5.1 are typical CVs recorded for $FcC_{11}SAu$ SAMs in a series of sodium *n*-alkyl sulfate solutions (SN_cS). The *n*-alkyl sulfate anions are denoted N_cS^-, where N_c is the total number of carbon atoms in the alkyl chain (N_c = 0, 1, 6, 8, 10, 12 or 14). The concentration of SN_cS in solution was kept constant, and the oxidation and reduction of the $FcC_{11}SAu$ SAM was investigated as a function of increasing N_cS^- hydrophobicity. Several interesting trends were observed with increasing alkyl chain length. These are described below.

The (nearly) spherical more hydrophilic anions N_0S^- (SO_4^{2-}) and N_1S^- ($CH_3OSO_3^-$) exhibit a low propensity for ion pairing. The CVs exhibit markedly asymmetric broad peaks with a ΔE_p > 100 mV and ΔE_{fwhm} that are difficult to accurately measure (Figure 5.1). N_0S^- and N_1S^- show more positive half-wave potentials ($E_{1/2}$) (Figure 5.2A). A more positive $E_{1/2}$ is indicative of a less favourable energetic process and can be considered an indirect measure of the difficulty of solvent reorganization in order to form an ion pair between the anion and the oxidized $Fc^+C_{11}SAu$ SAM.[30-32] Furthermore, hydrophilic anions are transported with a large amount of water, inhibiting the extent of anion interaction with the ferrocenium cation.[30-33] Consequently, the ferrocene cation is subject to nucleophilic attack, resulting in the degradation of the electroactive SAM.[34] For the N_0S^- and N_1S^- species, this degradation is evidenced by

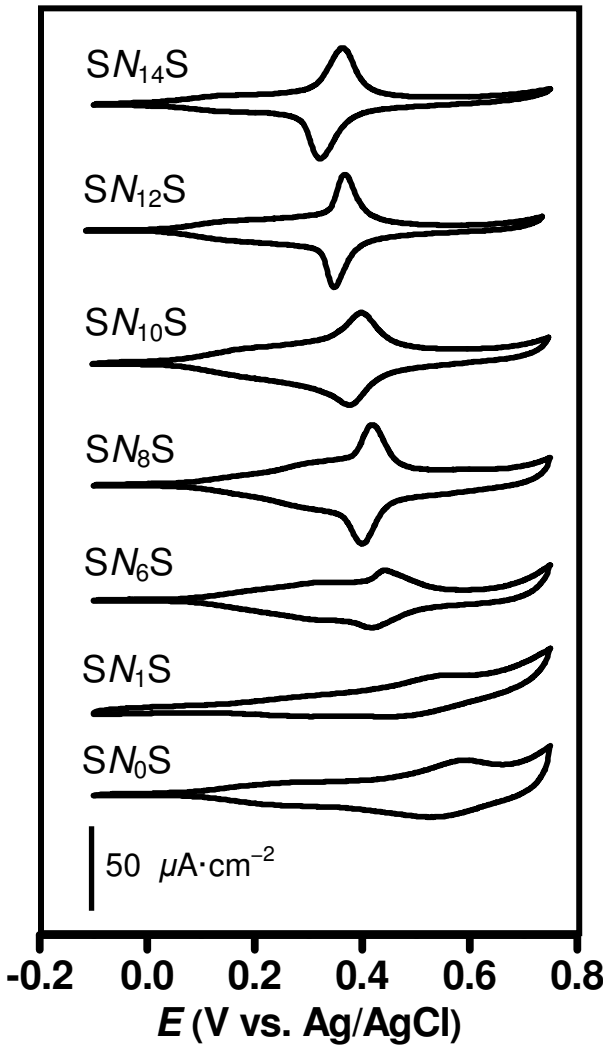

Figure 5.1 CVs of the $FcC_{11}SAu$ SAM in different sodium *n*-alkyl sulfate solutions. The potential was scanned between –0.10 V to +0.75 V at a constant rate of 10 $mV \cdot s^{-1}$ for all electrolyte solutions. The electrolyte concentration was 100 mM for all the SN_cS solutions, except for $SN_{14}S$ where the concentration was 25 mM.

an irreversible decrease in the peak current with successive potential cycling of the $FcC_{11}SAu$ SAM (not shown here).

Well-defined and reversible redox waves are observed for the N_cS^- anions where $N_c \geq 6$ (Figure 5.1). The average ΔE_p of the main redox peaks of the $FcC_{11}SAu$ SAM in N_6S^-, N_8S^-, $N_{10}S^-$, and $N_{12}S^-$ is 24 (±3) mV and increases to 50 (±10) mV for the $N_{14}S^-$. Shoulder peaks are present on the negative potential side of the main redox peaks for all the N_cS^- species investigated (Figure 5.1). Multiple voltammetric waves are also observed in the perchlorate electrolyte commonly used in electrochemical investigations of ferrocene-terminated SAMs,[25,33,35-40] and are attributable to different physical microenvironments.[35-37,41-43] In single-component monolayers, ferrocene alkyl chains found at grain or domain boundaries as well as defect sites are postulated to be less constrained than the surrounding matrix which gives rise to greater conformational mobility and an increased accessibility to the electrolyte solution promoting a favourable redox process at lower voltage potentials.[44-46] As discussed in previous chapters, positively-shifted voltammetric peaks are a consequence of clustered $FcC_{11}S–$ domains because electrostatic repulsion and steric constraints from ferrocenium cations renders the oxidation of neighbouring ferrocene molecules less favorable.[37,41] The actual size and shape of the domains formed by the aggregated $FcC_{11}S–$ are unknown parameters, however a loose hexagonal lattice structure has been observed by scanning tunneling microscopy for the $FcC_{11}SAu$ SAM.[47] A fitting procedure[37] involving both a Gaussian and a Lorentzian distribution is used for deconvolution of the voltammetric anodic peaks observed in the anionic surfactant solutions. This method helps to characterize the degree of SAM homogeneity revealed by ion pairing of the surfactant anion to the oxidized

$Fc^+C_{11}SAu$ monolayer. It was found that the lower-potential peaks (peak I and/or peak II) are fitted to a Gaussian distribution and the higher-potential peak (peak III) is fitted to either a Gaussian or Lorentzian distribution. Three fitting parameters, peak position, peak width, and peak area, were used to fit all of the assigned peaks. Shown in Figure 5.2B are the anodic peak potentials (E_a) obtained by deconvolution. The E_a for the higher-potential peak III, shows a linear negative shift with increasing hydrocarbon chain length. Individual peak area percentages provide a relative measure of the ferroceniums found in each state ($\Gamma^{I}_{Fc^+}$, $\Gamma^{II}_{Fc^+}$, $\Gamma^{III}_{Fc^+}$). As indicated in Table 5.2 (column 6), peak III contributes the most to the total Γ_{Fc^+}, and its contribution increases only slightly with chain-length. This finding confirms that higher-potential peak III is the main anodic peak, originating

Table 5.2 Relative Ion Pairing Affinity, Surface Coverages, and Peak Widths, After Deconvolution of the Cyclic Voltammograms for $FcC_{11}SAu$ in the Sodium *n*-Alkyl Sulfate Electrolyte Solutions.

		peak I		peak II		peak III	
	$\frac{K_{N_cS^-}}{K_{ClO_4^-}}$ [a]	$\Gamma^{I}_{Fc^+}$ [b] ($\times 10^{-10}$ mol·cm^{-2})	ΔE_{fwhm} (V)	$\Gamma^{II}_{Fc^+}$ [b] ($\times 10^{-10}$ mol·cm^{-2})	ΔE_{fwhm} (V)	$\Gamma^{III}_{Fc^+}$ [b] ($\times 10^{-10}$ mol·cm^{-2})	ΔE_{fwhm} (V)
SN_6S	0.2	0.35 ± 0.02	0.12 ± 0.01	1.0 ± 0.2	0.17 ± 0.02	1.9 ± 0.4	0.08 ± 0.02
SN_8S	0.4	0.41 ± 0.02	0.13 ± 0.02	1.41 ± 0.07	0.15 ± 0.01	1.9 ± 0.1	0.050 ± 0.001
$SN_{10}S$	0.7	0.47 ± 0.02	0.13 ± 0.02	0.72 ± 0.04	0.15 ± 0.02	2.4 ± 0.1	0.078 ± 0.003
$SN_{12}S$	1.9	1.18 ± 0.08	0.22 ± 0.03			2.3 ± 0.2	0.060 ± 0.009
$SN_{14}S$	22.6	0.67 ± 0.01	0.19 ± 0.02			2.9 ± 0.1	0.07 ± 0.01

[a]The calculated relative ion pairing ability of the electrolyte anions with respect to the reference electrolyte solution 0.10 M $NaClO_4$/0.01 M $HClO_4$. [b]Calculated from the measured total Γ_{Fc^+} and the individual peak area percentages obtained from peak deconvolution.

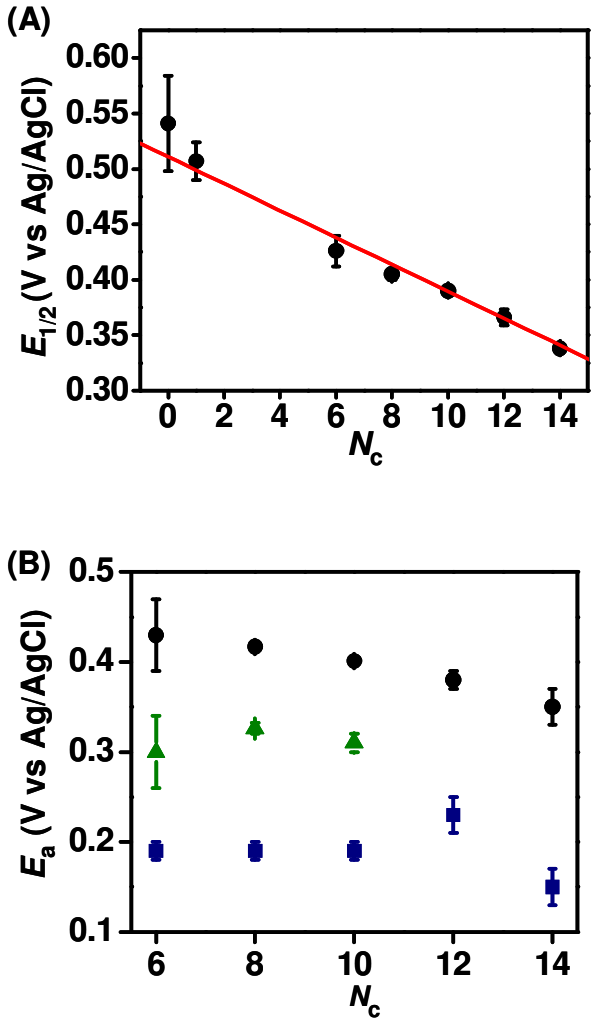

Figure 5.2 Plots of the **(A)** midpoint half-wave potential ($E_{1/2}$) and **(B)** the anodic peak potentials (E_a) of peaks I (■), II (▲), and III (●) for the $FcC_{11}SAu$ SAM as function of the increasing *n*-alkyl chain (N_c) length of the anionic sulfate (N_cS^-). The solid red line is a linear regression of the plotted data having a slope of –0.0123 V per methylene unit. The error bars represent the standard deviation of at least four different experiments.

from ferrocenes/ferroceniums clustered inside domains. SN_6S, SN_8S, and SN_{10}S show two additional voltammetric peaks at similar potentials: peak I, E_a = 0.19 (±0.01) V, and peak II, E_a = 0.31 (±0.01) V. Only one additional peak was observed for $N_{12}S^-$ (peak I, E_a = 0.23 (±0.02) V) and $N_{14}S^-$ (peak I, E_a = 0.15 (±0.02) V). In all cases, the ΔE_{fwhm}'s of peaks I and II are larger than the theoretical 90.6 mV, whereas peak III generally shows a narrower ΔE_{fwhm}, suggesting interactions between the redox centers (Table 5.2).[30,32,33,48,49]

The $E_{1/2}$ of the main redox peaks (i.e., higher potential waves) shifts linearly to more negative potentials with increasing hydrocarbon chain length (Figure 5.2A). A shift in $E_{1/2}$ towards more negative potentials indicates that the oxidation of the ferrocene is thermodynamically more favourable.[30,32,33,35,50,51] A quantitative comparison of the ion pairing affinity of various anions with the $Fc^+C_{11}SAu$ SAM is not possible since the standard formal potential of the surface-confined species ($E^{0'}_{SAM}$) is unknown. However, ion pairing tendencies of individual anions can be qualitatively compared with that of a reference anion by using the following relation derived from the Nernst equation[30,33]

$$\frac{K^{N_cS^-}}{K^{ClO_4^-}} = \frac{C^{ClO_4^-}}{C^{N_cS^-}} \exp\left[\frac{F(E_{1/2}^{ClO_4^-} - E_{1/2}^{N_cS^-})}{RT}\right] \qquad (5.1)$$

where K is the formation constant, C is the corresponding electrolyte concentration, F is Faraday's constant, R is the gas constant, and T is the temperature (298 K). We compare the relative ion pairing of the individual alkyl sulfate anions to that of perchlorate. The relatively hydrophobic perchlorate was selected as the reference because ClO_4^- is known to complex strongly with the SAM-bound ferroceniums, forming 1:1 ion pairs. Listed in

Table 5.2 (column 2) are the $K_{N_cS^-}/K_{ClO_4^-}$ ratios calculated for Fc^+-N_cS^- ion pairs. The magnitude of the ratios suggests that the ion pairing of the $N_{12}S^-$ and $N_{14}S^-$ anions is considerably more thermodynamically favourable than that of ClO_4^-. The results confirm that the increased hydrophobicity of the longer chain alkyl sulfate anions stabilizes the non-polar microenvironment preferred by the $Fc/Fc^+C_{11}SAu$ SAM.[30,32,33,52] The ion pairing tendencies of the *n*-alkyl sulfates qualitatively agree with the trends reported for spherically symmetric anions.[8,30-33,35,50]

The total area of the anodic peaks (peaks I, II, and III) gives Q_{Fc^+} from which the Γ_{Fc^+} can be calculated (Figure 5.3), as already mentioned above. N_0S^- and N_1S^- exhibit the lowest Γ_{Fc^+} values: 1.8 (±0.6) and 2.7 (±0.1) × 10^{-10} moles·cm^{-2} (Figure 5.3A), respectively. For $N_c \geq 6$, Q_{Fc^+}, and the corresponding Γ_{Fc^+}, were found to be independent of the alkyl chainlength (Figure 5.3A) and solution concentration of the amphiphilic anion (for SN_8S $SN_{10}S$, and $SN_{12}S$; see Figure 5.3B). A mean Γ_{Fc^+} of 3.5 (±0.2) × 10^{-10} moles·cm^{-2} (Q_{Fc^+} = 34 ± 2 μC·cm^{-2}) was determined from the anodic segment of the CVs acquired in $N_{c\geq6}S^-$ solutions. The value of Γ_{Fc^+} indicates that only ~75% of the available surface-confined ferrocenes (i.e., theoretical maximum of 4.5 × 10^{-10} moles·cm^{-2})[34-36,48,53-56] are ion paired with the $N_{c\geq6}S^-$ anions. Although the size of the sulfate headgroup (cross-sectional area of ~0.28 nm^2)[26,27] vs. that of the ferrocene (~0.34 nm^2)[33,48] should allow the anion to complex with each of the SAM-bound ferroceniums, its hydrocarbon tail imposes an interfacial packing constraint on the ion-pairing reaction.

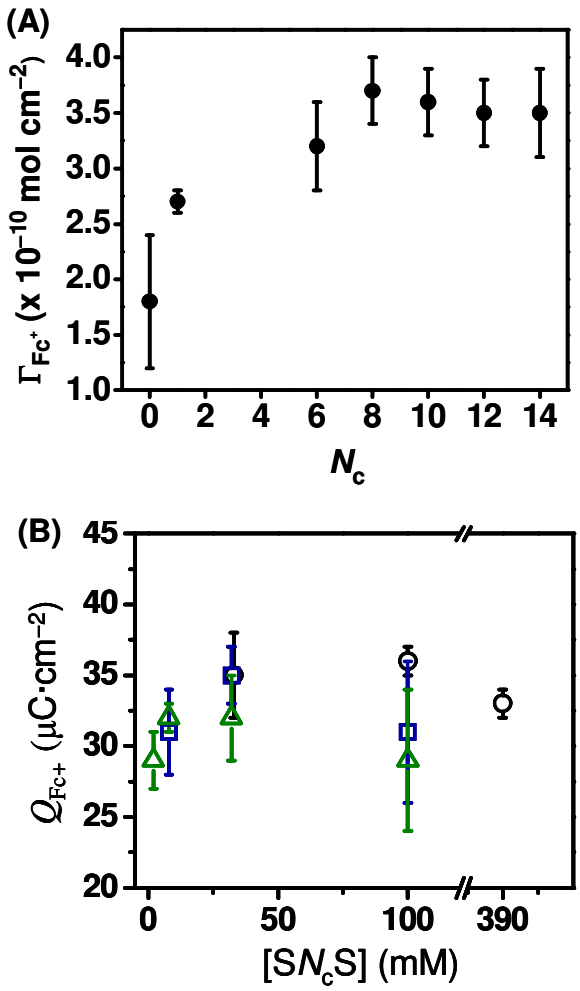

Figure 5.3 **(A)** Plot of the electrogenerated ferrocenium concentration (Γ_{Fc^+}) for the $FcC_{11}SAu$ SAM as a function of the increasing *n*-alkyl chain (N_c) length of the sulfate anions (N_cS^-). **(B)** Plot of the charge density (Q_{Fc^+}) vs. the solution concentration of SN_8S (○), SN_{10}S (□), and SN_{12}S (Δ). The error bars represent the standard deviation of at least four different experiments.

It is postulated that this packing constraint affects the quantity of electrogenerated ferroceniums.

In summary, cyclic voltammetry clearly demonstrates the reversible oxidation/reduction of the SAM-bound ferrocenes by ion pairing with *n*-alkyl sulfates. The results indicate that these amphiphilic electrolytes have a strong effect on the thermodynamics of the interfacial redox reaction. Increasing the hydrophobicity of the anionic amphiphile *via* a longer alkyl chain shifts the redox potential to more negative values. A corresponding trend was also observed with the relative anion pairing ability, with SN_{14}S yielding the largest value. The number of electron transfer events provides a direct measure of the number of SAM-bound ferroceniums ion paired to alkyl sulfates. Deconvolution of the anodic waves suggests the presence of different ferrocene microenvironments (i.e., sites of different packing density/order) in the SAM. However, electrochemistry provides limited details in terms of the structure of the alkyl sulfate aggregates formed at the charged SAM interface. To gain further insight into the interfacial organization of the N_cS^- molecules, the surfactant coverage was measured by SPR.

5.3.2 Assembly of *n*-Alkyl Sulfates onto $Fc^+C_{11}SAu$ SAMs

In this chapter, the previous SPR study of $N_{12}S^-$ is extended by investigating the potential-controlled adsorption/desorption of the shorter chains $N_{10}S^-$, N_8S^-, and N_6S^-. This study is limited to these three surfactants due to constraints imposed by the electrolyte concentration required for electrochemistry and the surfactant solubility at room temperature. Typical current and SPR responses with respect to time obtained for

the $FcC_{11}SAu$ monolayer during multiple CV scans between –0.10 and 0.75 V (vs. Ag/AgCl) in $SN_{10}S$, SN_8S and SN_6S are shown in Figure 5.4. The $\Delta\Theta_m$ is attributable to the adsorption/desorption of surfactant. The redox-induced adsorption/desorption of the alkyl sulfates to/from the $Fc^+/FcC_{11}SAu$ interface and accompanying molecular orientational changes in the SAM are reversible, as suggested by the stability and reproducibility of both the CV and SPR data. In the next section, an investigation of the redox-induced adsorption of the alkyl sulfates to the $Fc^+C_{11}SAu$ SAM as a function of the physical state of the surfactant in solution (i.e., monomer vs. micelle) is undertaken.

Figure 5.5 shows the maximum $\Delta\Theta_m$ observed for ion pairing of the N_cS^- with the oxidized $Fc^+C_{11}SAu$ SAM as a function of the *n*-alkyl chain length. We investigated the adsorption/desorption of $N_{10}S^-$ and N_8S^- anions at bulk solution concentrations = 0.25 × cmc, = cmc, and >> cmc. The cmc's reported at 25 ˚C for $SN_{10}S$ and SN_8S in water are 3.2×10^{-2} M and 1.3×10^{-1} M, respectively.[57] Ion pair formation with N_6S^- was monitored at 2.8×10^{-2} M only, which is ~20 times lower than the cmc (5.2×10^{-1} M[57]). Not surprisingly, the $\Delta\Theta_m$ values for $N_cS^- - Fc^+C_{11}SAu$ increase with increasing *n*-alkyl sulfate chain length for all the bulk solution concentrations considered. When the bulk SN_cS concentration is below the cmc where the amphiphile molecules are found as *solvated* monomers in solution, a linear relationship is observed between $\Delta\Theta_m$ and the chain length (i.e., $\Delta\Theta_m$ per methylene = 0.0061˚), indicating an additive effect with elongation of the hydrocarbon chain. Using Fresnel multilayer modeling (Winspall software version 2.20, MPI-P, Mainz, Germany), a $\partial\Theta/\partial d$ of 0.041° nm^{-1} for an adsorbed surfactant layer was calculated. Using this value of $\partial\Theta/\partial d$, a film thickness change of ~0.15 nm per methylene is derived from the experimentally measured variation in $\Delta\Theta_m$.

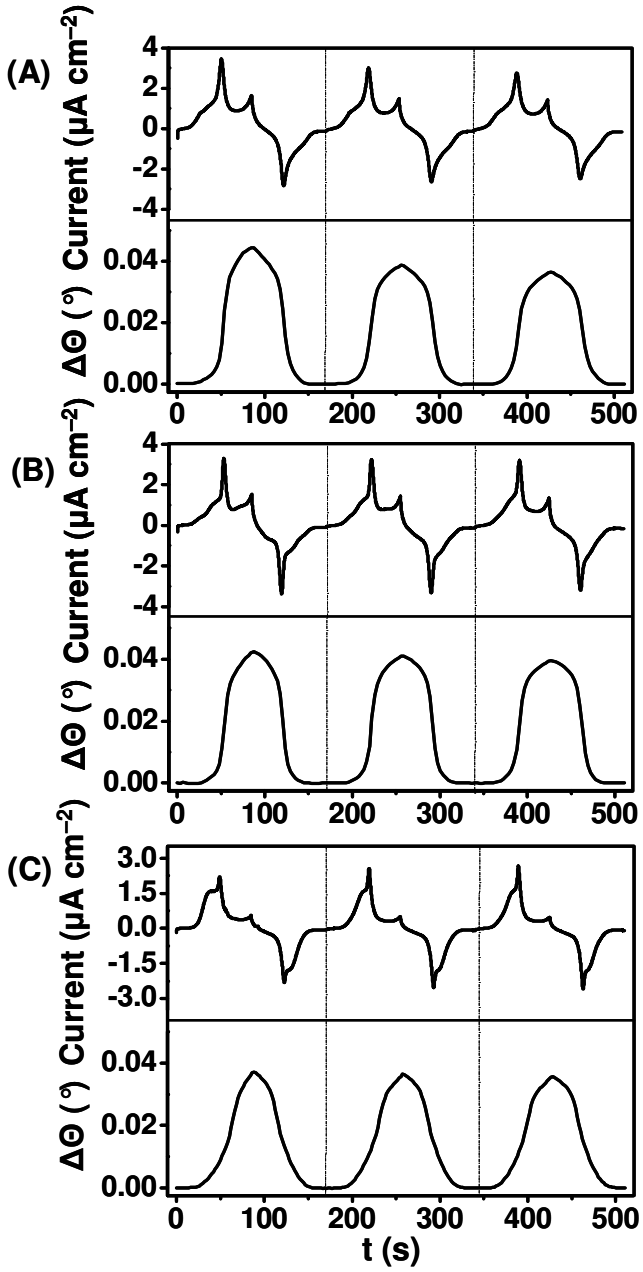

Figure 5.4 Current (top panel) vs. time profile obtained during potential cycling between –0.10 V and +0.75 V of the $FcC_{11}SAu$ SAM at a rate of 10 mV s^{-1} and the corresponding SPR profiles (bottom panel) in **(A)** 0.10 M SN_{10}S, **(B)** 0.10 M SN_8S and **(C)** 0.03 M SN_6S solutions.

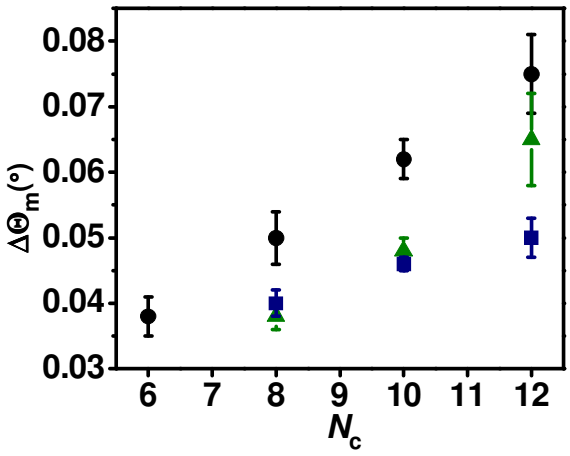

Figure 5.5 Plot of maximum $\Delta\Theta_m$ for the oxidation of the $FcC_{11}SAu$ SAM vs. the *n*-alkyl chain (N_c) length of the investigated anionic sulfates (N_cS^-) below the cmc (●), at the (▲) and above the cmc (■). The error bars represent the standard deviation of at least four different experiments.

This film thickness change is comparable to the carbon-to-carbon distance of 0.1265 nm in a hydrocarbon chain in its most stable *trans* configuration,[58] suggesting that the alkyl sulfate chains, on average, are in a solid-like condensed state. Chidsey *et* al. [59] also observed an incremental change of 0.15 nm per $-CH_2-$ for the ellipsometric thicknesses of *n*-alkylthiolate SAMs between 9 and 21 methylene units. An increase in $\Delta\Theta_m$ with chain length is also observed at the cmc for $N_{12}S^-$, $N_{10}S^-$, and N_8S^-, whereas for the same homologous series $\Delta\Theta_m$ tends to plateau for concentrations above the cmc.

Below the cmc, sodium *n*-alkyl sulfates behave as non-associated electrolytes in solution and their solvation properties are not only influenced by the polar headgroup but also by the hydrocarbon chain length. The observed effective thickness of the adsorbed N_6S^- layer, calculated from the maximum $\Delta\Theta_m$ as previously described, is 0.92 ± 0.07 nm which corresponds to a $\Gamma_{N_6S^-}$ of 4.4 (±0.3) × 10^{-10} mole·cm^{-2} or a surfactant

molecular area of 0.38 ± 0.3 nm^2 per N_6S^-. This value is close to the cross-sectional area occupied by a ferrocene molecule (~0.34 nm^2)[48]. A Γ_{Fc^+} of 3.8 (±0.4) × 10^{-10} mole·cm^{-2} (i.e., Q_{Fc^+} = 37 ± 4 $\mu C \cdot cm^{-2}$) was found for the oxidation of $FcC_{11}SAu$ SAMs in aqueous SN_6S solution. This indicates the probability of 1:1 ion pair complexation of the shorter chain N_6S^- anions with the oxidized $Fc^+C_{11}SAu$ SAM, where the negatively charged sulfate anions are specifically adsorbed at the positively charged interface and the tail groups extend away from the monolayer interface. As already mentioned, the anion solvation properties largely dictate the favorability of the electrochemical redox reaction, where poorly-solvated hydrophobic molecules will ion pair more effectively with the electrogenerated ferrocenium than well-solvated hydrophilic molecules. The overall hydrophobicity of amphiphilic *n*-alkyl sulfates is affected by the sulfate group in such a way that it decreases the availability of the methylene moieties for hydrophobic interactions up to 6 methylene units.[60] At this chain length, it is anticipated that the interchain van der Waals forces are not maximized, leading to a degree of disorder as well as probable ion and water penetration into the adsorbed surfactant layer.

Maximum effective thicknesses of 1.6 ± 0.1 nm and 1.2 ± 0.1 nm are observed at 0.25 × cmc for $N_{10}S^-$ and N_8S^-, respectively. The observed thicknesses correspond to $\Gamma_{N_nS^-}$ of 6.1 (±0.3) × 10^{-10} mole·cm^{-2} (i.e., 0.27 ± 0.01 nm^2 per $N_{10}S^-$) and 5.7 (±0.4) × 10^{-10} mole·cm^{-2} (i.e., 0.29 ± 0.02 nm^2 per N_8S^-). The Q_{Fc^+} associated with the oxidation of the $FcC_{11}SAu$ in aqueous $SN_{10}S$ and SN_8S solutions (0.25 × cmc) are 31 ± 3 $\mu C \cdot cm^{-2}$ (3.2 (±0.3) × 10^{-10} mole·cm^{-2}) and 35 ± 3 $\mu C \cdot cm^{-2}$ (3.6 (±0.3) × 10^{-10} mole·cm^{-2}), respectively. These results indicate that ~69% for $N_{10}S^-$ and ~78% for N_8S^- of the

available ferrocene molecules are ion paired with the corresponding surfactant anion, assuming a 1:1 stoichiometric pairing. A $\Gamma_{N_{12}S^-}$ of 6.6 (±0.6) × 10^{-10} mole·cm^{-2} (0.25 ± 0.02 nm^2 per $N_{12}S^-$) and layer thickness of 1.8 ± 0.1 nm at 0.25 × cmc by SPR and a surface concentration of ion-paired $N_{12}S^-$ of 3.0 (±0.2) × 10^{-10} mole·cm^{-2} from Q_{Fc^+} = 29 ± 2 μC·cm^{-2} was previously obtained.[7] To summarize, SPR yields an alkyl sulfate surface coverage that is *ca.* twice that obtained electrochemically and film thicknesses that are consistent with a monolayer rather than a bilayer (even a disordered bilayer) for the longer chain N_8S^-, $N_{10}S^-$, and $N_{12}S^-$. These results point to the presence of a condensed interdigitated monolayer of N_cS^- molecules at the monolayer/solution interface. In the close-packed interdigitated monolayer configuration, half of the total sulfate headgroups are ion-paired to the surface ferroceniums, while half of the headgroups are exposed to the aqueous interface (Scheme 1.1C). Our experimental results concur reasonably well with the theoretical charge density of 33 μC·cm^{-2} and average molecular area of 0.25 nm^2 calculated for the two-dimensional spatial distribution of sulfate headgroups (cross-sectional area ≈ 0.28 nm^2)[26,27] and alkyl chains (cross-sectional area ≈ 0.21 nm^2)[26,27] in an interdigitated monomolecular assembly.[7]

As previously reported for $N_{12}S^-$,[7] a decrease in the amount of adsorbed $N_{10}S^-$ and N_8S^- is observed at the onset of solution micellization (Figure 5.6). As the bulk solution concentrations of SN_{10}S (cmc = 3.2 × 10^{-2} M) and SN_8S (cmc = 1.3 × 10^{-1} M) are increased to their respective cmcs, our SPR results indicate a ~25% decrease in the total surface coverage; $\Gamma_{N_{10}S^-}$ = 4.7 (±0.2) × 10^{-10} mole·cm^{-2} and $\Gamma_{N_8S^-}$ = 4.4 (±0.2) × 10^{-10} mole·cm^{-2}. At the cmc, the effective layer thicknesses are 1.19 ± 0.04 nm ($N_{10}S^-$)

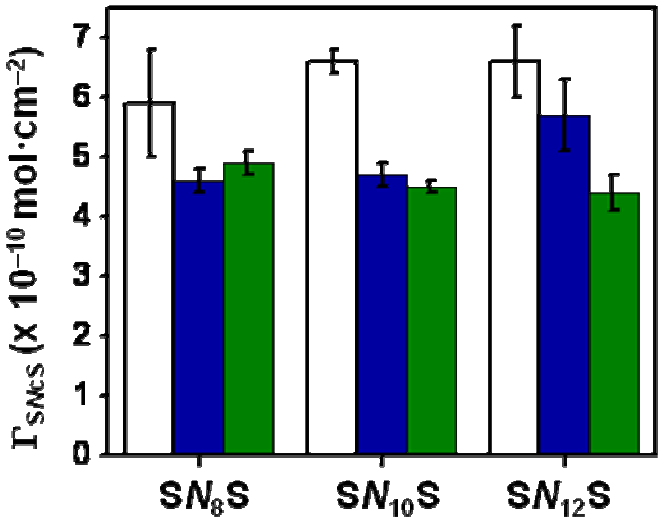

Figure 5.6 Plot of the surface coverage (Γ_{SPR}) of N_8S^-, $N_{10}S^-$, and $N_{12}S^-$; where □ < cmc, ■ = cmc, and ■ > cmc for all investigated surfactants. The error bars represent the standard deviation of at least four different experiments.

and 0.94 ± 0.05 nm (N_8S^-). Further increasing the solution concentration above the cmc results in an additional ~20% decrease in $\Gamma_{N_cS^-}$ for $SN_{10}S$ (4.5 (±0.1) × 10^{-10} mol·cm^{-2}) and a ~10% increase for SN_8S (4.8 (±0.2) × 10^{-10} mol·cm^{-2}). Interestingly, there is a ~10% decrease in $\Gamma_{N_cS^-}$ obtained at solution concentrations well above the cmc as the hydrocarbon chain length increases from 8 to 12 carbons (Figure 5.6). It has already been shown for $SN_{12}S$ that at bulk solution concentrations ranging from 2 × cmc to 12.5 × cmc, the surface concentration of the aggregated surfactant is constant.[7] By contrast, the Q_{Fc^+} values remain generally constant at an average value of 33 ± 2 μC·cm^{-2} over the

entire concentration range for all anionic surfactants (Figure 5.4). While the values of the N_cS^- molecular area measured by SPR at and above the cmc, i.e. 0.35–0.38 nm^2, are compatible with the cross-sectional area of $FcC_{11}SAu$ (0.34 nm^2), a monolayer configuration in which the N_cS^- are all ion paired to the ferrocenium with their hydrocarbon alkyl tails exposed to the aqueous solution would be thermodynamically unfavourable. The surface coverages of alkyl sulfate obtained by electrochemistry and SPR instead suggest the formation of a disordered interdigitated monolayer configuration above the cmc.

In order to explain the decrease in total surface concentration with bulk solution concentration and increasing hydrocarbon chain length it is helpful to consider the surfactant solution properties. Increasing the solution concentration of the surface-active amphiphiles amounts to the formation of micellar structures where the alkyl hydrocarbon chains form the compact inner core and the polar headgroups are directed outwards into the bulk water, ultimately increasing the overall molecular hydrophilicity.[17,61-63] The hydrated micellar interface contains the anionic head groups, a small part of the hydrocarbon tails and charge compensating counterions which are generally separated by a layer of water molecules. The micellar structures can be considered as charged particles and their properties vary depending on the hydrocarbon chain length. For example, micelles composed of short-chain surfactants are more loosely packed structures due to weaker van der Waals attractive forces and less hydrophobic effect.[5,11] Furthermore, the micelle is not a static particle but a dynamic entity where the monomers are in equilibrium with the micellar structure, and the micelles themselves are continuously disintegrating and reassembling.[11,64] In fact, the solvation dynamics of micellar sodium

n-alkyl sulfate solutions exhibit two relaxation processes involved.[17] A fast relaxation is associated with the quick exchange of monomers between micelles and the surrounding bulk phase, whereas a slower relaxation is attributed to the formation and dissolution process reflecting micellar stability. Tamoto et al. showed nearly equivalent rates of monomer exchange for the micellar series SN_8S, $SN_{10}S$ and $SN_{12}S$, whereas for the same surfactants, the second relaxation time increased by nearly a factor of 2 in the same order.[17] Their study showed that increasing the chain length amounts to more stable micelles (i.e., tightly packed micelles) in aqueous solution. A strong correlation between micellar kinetics and dynamic processes at the liquid/liquid and liquid/solid interfaces has been identified by several researchers.[65] In our system, the applied potential results in a charge-regulated surface that is stabilized by ion pair complexation of N_cS^- surfactant anions with the surface-confined $Fc^+C_{11}SAu$ SAM. As the surfactant concentration is increased above the cmc, the monomer concentration is usually assumed constant and in dynamic equilibrium with the micelles.[64] The equilibrium condition between monomers and micelles is disturbed when existing micelles are forced to break up in order to provide additional monomers to the surface for ion pair formation. If the micelles in solution are very stable, monomers cannot be provided fast enough for ion complexation and the dynamically generated surface coverage will decrease. However, if micelles in solution are relatively unstable, their disintegration supplies the depleted monomers and a minimal change is expected to be observed for the $\Gamma_{N_cS^-}$, which seems plausible for the investigated SN_8S.

To gain a better understanding of the adsorption process below and above the cmc, electrochemical AFM imaging and AFM force measurements will be used in future

experiments to follow the redox-induced ion-pairing of *n*-alkyl sulfates to the ferrocenium-terminated SAM surface and visualize the adsorbed surfactant structure.

5.4 Conclusion

n-Alkyl sulfates with chain lengths of 6, 8, 10 and 12 carbons ion pair with monolayer-bound ferroceniums generated by potential-induced oxidation. The relative ion pairing affinities increase with chain length, consistent with the chemical preference of ferrocene for a hydrophobically-shielded microenvironment. $N_{12}S^-$ and $N_{14}S^-$ exhibit relative ion pairing affinities, with respect to perchlorate, > 1. Our results point to the interfacial assembly of alkyl sulfates being governed by factors other than the electrostatic interaction of the surfactant anions with the cationic ferroceniums, such as the monomer solution concentration and the micellar stability. Consistent with specific ion effects,[61,66,67] electrostatic repulsion between the ionic groups becomes progressively screened as the formation of the $N_cS^- - Fc^+$ complex becomes more favorable with increasing *n*-alkyl chain length, leading to larger packing densities. With increasing hydrocarbon chain length, the negatively charged sulfate ions are specifically adsorbed by the discrete ferrocenium cations at the monolayer/solution interface, where stabilization of the adsorbed surfactant layer can proceed by van der Waals forces between the intercalated alkyl chains. The surfactant surface coverages indicate that well below the cmc, monomers can more readily adapt to the changing ferrocenium concentration because they interact independently with the surface to screen the positive charge of the electrochemically generated ferrocenium. This direct interaction facilitates the formation

of a densely packed interdigitated monolayer within the time frame of the anodic scan (~85 s). As the bulk solution concentration is increased in excess of the cmc, an adsorption plateau is observed for the SN_8S and more notably for SN_{10}S. This study shows how mutual interactions between constituent ionic and hydrocarbon groups in the alkyl sulfate determine the overall adsorption and surface aggregation.

5.5 References

(1) Ivanisevic, A.; Im, J.-H.; Lee, K.-B.; Park, S.-J.; Demers, L. M.; Watson, K. J.; Mirkin, C. A. *J. Am. Chem. Soc.* **2001**, *123*, 12424–12425.

(2) Luk, Y.-Y.; Abbott, N. L. *Science* **2003**, *301*, 623–626.

(3) Skulason, H.; Frisbie, C. D. *Langmuir* **1998**, *14*, 5834–5840.

(4) Schulz, J. C. In *Encyclopedia of Surface and Colloid Science*; Somasundaran, P., Ed.; CRC Press Inc.: 2006; Vol. 8, p 6562–6577.

(5) Tanford, C. *The Hydrophobic Effect*; 1 st. ed.; Wiley: New York, 1973.

(6) Marcus, Y. *J. Chem. Soc. Faraday Trans.* **1993**, *89*, 713–718.

(7) Norman, L. L.; Badia, A. *Langmuir* **2007**, *23*, 10198–10208.

(8) Sumner, J. J.; Creager, S. E. *J. Phys. Chem. B* **2001**, *105*, 8739–8745.

(9) Uematsu, T.; Kuwabata, S. *Anal. Sci.* **2008**, *24*, 307–312.

(10) Evans, D. F.; Wennerström, H.; 2 ed. ed.; Wiley-VCH: New York, 1999.

(11) Israelachvili, J. N. In *Intermolecular and Surface Forces*; 2nd ed. ed.; Academic Press: London, 1992, p 341–385.

(12) Vass, S. *Struct. Chem.* **1991**, *2*, (167)375–(189)397 and references therein.

(13) Lebedeva, N. V.; Shabine, A.; Bales, B. L. *J. Phys. Chem. B* **2005**, 19806–19816.

(14) Brun, T.; Høiland, H.; Vikingstad, E. *J. Colloid Interface Sci.* **1978**, *63*, 89–96.

(15) Bloor, D. M.; Gormally, J.; Wyn-Jones, E. *J. Chem. Soc. Faraday Trans. 1* **1984**, *80*, 1915–1923.

(16) Varga, I.; Mészáros, R.; Gilányi, T. *J. Phys. Chem. B* **2007**, *111*, 7160–7168.

(17) Tamoto, Y.; Segawa, H.; Shirota, H. *Langmuir* **2005**, *21*, 3757–3764.

(18) Lunkenheimer, K.; Czichocki, G.; Hirte, R.; Barzyk, W. *Colloids Surf., A* **1995**, *101*, 187–197.

(19) Li, B.; Ruckenstein, E. *Langmuir* **1996**, *12*, 5052–5063.

(20) Lu, J. R.; Marroco, A.; Su, T. J.; Thomas, J. K.; Penfold, J. *J. Colloid Interface Sci.* **1993**, *158*, 303–316.

(21) Brown, G. E. J.; Henrich, V. E.; Casey, W. H.; Clark, D. L.; Eggleston, C.; Felmy, A.; Goodman, D. W.; Grätzel, M.; Maciel, G.; McCarthy, M. I.; Nealson, K. H.; Sverjensky, D. A.; Toney, M. F.; Zachara, J. M. *Chem. Rev.* **1999**, *99*, 77–174.

(22) Koelsch, P.; Viswanath, P.; Motschmann, H.; Shapovalov, V. L.; Brezesinski, G.; Möhwald, H.; Horinek, D.; Netz, R. R.; Giewekemeyer, K.; Salditt, T.; Schollmeyer, H.; von Klitzing, R.; Daillant, J.; P., G. *Colloids Surf., A* **2007**, *303*, 110–136.

(23) Kunz, W.; Nostro, P. L.; Ninham, B. W. *Curr. Opin. Colloid Interface Sci.* **2004**, *9*, 1–18.

(24) Bard, A. J.; Faulkner, L. R. *Electrochemical Methods Fundamentals and Applications*; 2nd ed. ed.; J. Wiley & Sons: New York, 2001.

(25) Ohtsuka, T.; Sato, K.; Uosaki, K. *Langmuir* **1994**, *10*, 3658–3662.

(26) Sigal, G. B.; Mrksich, M.; Whitesides, G. M. *Langmuir* **1997**, *13*, 2749–2755.

(27) Sigal, G. B.; Mrksich, M.; Whitesides, G. M. *J. Am. Chem. Soc.* **1998**, *120*, 3464–3473.

(28) Tulpar, A.; Ducker, W. A. *J. Phys. Chem. B* **2004**, *108*, 1667–1676.

(29) Defeijter, J. A.; Benjamins, J.; Veer, F. A. *Biopolymers* **1978**, *17*, 1759–1772.

(30) Ju, H.; Leech, D. *Phys. Chem. Chem. Phys.* **1999**, *1*, 1549–1554.

(31) Rowe, G. K.; Creager, S. E. *J. Phys. Chem.* **1994**, *98*, 5500–5507.

(32) Valincius, G.; Niaura, G.; kazakevičienė, B.; Talaikytė, Z.; Kažemėkaitė, M.; Butkus, E.; Razumas, V. *Langmuir* **2004**, *20*, 6631–6638.

(33) Rowe, G. K.; Creager, S. E. *Langmuir* **1991**, *7*, 2307–2312.

(34) Popenoe, D. D.; Deinhammer, R. S.; Porter, M. D. *Langmuir* **1992**, *8*, 2521–2530.

(35) Uosaki, K.; Sato, Y.; Kita, H. *Langmuir* **1991**, *7*, 1510–1514.

(36) Walczak, M. M.; Popenoe, D. D.; Deinhammer, R. S.; Lamp, B. D.; Chung, C.; Porter, M. D. *Langmuir* **1991**, *7*, 2687–2693.

(37) Lee, L. Y. S.; Sutherland, T. C.; Rucareanu, S.; Lennox, R. B. *Langmuir* **2006**, *22*, 4438–4444.

(38) Quist, F.; Tabard-Cossa, V.; Badia, A. *J. Phys. Chem. B* **2003**, *107*, 10691–10695.

(39) Ye, S.; Sato, Y.; Uosaki, K. *Langmuir* **1997**, *13*, 3157–3161.

(40) Fujii, S.; Kurokawa, S.; Murase, K.; Lee, K.-H.; Sakai, A.; Sugimura, H. *Electrochim. Acta* **2007**, *52*, 4443–4448.

(41) Auletta, T.; van Veggel, F. C. J. M.; Reinhoudt, D. N. *Langmuir* **2002**, *18*, 1288–1293.

(42) Calvente, J. J.; Andreu, R.; Molero, M.; Lopez-Perez, G.; Domínguez, M. *J. Phys. Chem. B* **2001**, *105*, 9557–9568.

(43) Smith, C. P.; White, H. S. *Anal. Chem.* **1992**, *64*, 2398–2405.

(44) Poirier, G. E. *Chem. Rev.* **1997**, *97*, 1117–1127.

(45) Lee, L. Y. S.; Lennox, R. B. *Langmuir* **2007**, *23*, 292–296.

(46) Collard, D. M.; Fox, M. A. *Langmuir* **1991**, *7*, 1192–1197.

(47) Müller-Meskamp, L.; Lüssem, B.; Karthäuser, S.; Prikhodovski, S.; Homberger, M. *Phys. Stat. Sol.* **2006**, *203*, 1448–1452.

(48) Chidsey, C. E. D.; Bertozzi, C. R.; Putvinski, T. M.; Mujsce, A. M. *J. Am. Chem. Soc.* **1990**, *112*, 4301–4306.

(49) Creager, S. E.; Rowe, G. K. *Anal. Chim. Acta* **1991**, *246*, 233–239.

(50) Kondo, T.; Okamura, M.; Uosaki, K. *J. Organomet. Chem.* **2001**, *637–639*, 841–844.

(51) Vos, J. G.; Forster, R. J.; Keyes, T. E. *Interfacial Supramolecular Assemblies*; John Wiley & Sons Ltd: West Sussex, 2003.

(52) Cruañes, M. T.; Drickamer, H. G.; Faulkner, L. R. *Langmuir* **1995**, *11*, 4089–4097.

(53) Chidsey, C. E. D. *Science* **1991**, *251*, 919–922.

(54) De Long, H. C. D.; Buttry, D. A. *Langmuir* **1992**, *8*, 2491–2496.

(55) De Long, H. C. D.; Donohue, J. J.; Buttry, D. A. *Langmuir* **1991**, *7*, 2196–2202.

(56) Creager, S. E.; Rowe, G. K. *J. Electroanal. Chem.* **1997**, *420*, 291–299.

(57) Suárez, M. J.; López-Fontán, J. L.; Sarmiento, F.; Mosquera, V. *Langmuir* **1999**, *15*, 5265–5270.

(58) Israelachvili, J. N. *Intermolecular and Surface Forces*; 2nd. ed.; Academic Press: London, 1992.

(59) Porter, M. D.; Bright, R. M.; Allara, D. L.; Chidsey, C. D. E. *J. Am. Chem. Soc.* **1987**, *109*, 3559–3568.

(60) Noordman, W. H.; Blokzijl, W.; Engberts, J. B. F. N. *J. Org. Chem.* **1993**, *58*, 7111–7114.

(61) Ropers, M. H.; Czichocki, G.; Berzesinski, G. *J. Phys. Chem. B* **2003**, *107*, 5281–5288.

(62) Seimiya, T. *J. Colloid Interface Sci.* **2003**, *266*, 422–429.

(63) Romsted, L. S. *Langmuir* **2007**, *23*, 414–424.

(64) Zana, R. In *Encyclopedia of Surface and Colloid Science*; 1st ed.; Hubbard, A. T., Ed.; CRC Press: Boca Raton, 2002, p 1515–1528.

(65) Patist, A.; Kanicky, J. R.; Sukla, P. K.; Shah, D. O. *J. Colloid Interface Sci.* **2002**, *245*, 1–15 and references therein.

(66) Rakitin, A. R.; Pack, G. R. *J. Phys. Chem. B* **2004**, *108*, 2712–2716.

(67) Gilányi, T.; Varga, I.; Mészáros, R. *Phys. Chem. Chem. Phys.* **2004**, *6*, 4338–4346.

Chapter 6

General Conclusions, Contributions to Original Knowledge, and Suggestions for Future Work

6.1 General Conclusions and Contributions to Original Knowledge

The electrochemical switching capabilities of ferrocenylalkylthiolates chemisorbed to gold surfaces have been harnessed to effect macroscopic changes in interfacial properties via two main categories: (i) conformational changes and/or the motion of one molecule with respect to another within a two-dimensional assembly and (ii) the directed adsorption/desorption of self-organizing anionic surfactants at the electrolyte/solid surface.

Microcantilevers functionalized with molecules consisting of components that undergo conformational changes in response to an external stimulus have been the subject of a number of investigations. One of the first and ground breaking examples was the translation of DNA hybridization into nanomechanical motion by Fritz et al.[1] The intrinsic information processing of DNA hybridization has received a lot of attention as a model system to investigate the chemomechanical transduction mechanism when oligonucleotides in solution bind to single stranded DNA tethered to one face of the microcantilever. However, while biomolecular interactions such as DNA hybridization are highly specific and evolve under mild aqueous conditions, their inherent complexity

renders the exact origin of the measured surface stress difficult to ascertain. For this reason, a chemical system where the extent or degree of actuation could be dynamically controlled using a single external parameter, such as an applied potential, would enable a more straightforward analysis of the observed surface stress. This led to the motivation behind the first part of the dissertation where gold-coated microcantilevers functionalized with a model $FcC_{11}SAu$ SAM were used to effect a micromechanical motion and elucidate the origin of the corresponding surface stress. Here, the redox reaction of the surface-confined ferrocene elicited conformational transitions that typically result in submicron scale deflections. Having established that redox transformations occurring in a monomolecular film could in fact deflect the cantilever, a number of systematic investigations were undertaken to reveal the origin of the surface stress responsible for the measured micromechanical motion (Chapter 2). It was initially recognized that while the magnitude of the deflection response was dependent on the microcantilever spring constant, the corresponding change in surface stress was not. The dynamic response of the FcRSAu cantilevers did not correlate with a static bending of the free end of the cantilever as a result of 1:1 anion-pairing with the ferrocenium, which was concurrently measured by the implementation of a complementary electrochemical technique where individual ion-pairing events were recorded and readily translated to anion accumulation. In other words, a certain number of redox and anion-pairing events are required to trigger the cantilever bending. As a result, it was obvious that individual ion pairing events can not elicit a microcantilever response regardless of experimental parameters (i.e., potential scan rate or step changes), which firmly established that single molecule detection for microcantilever systems employing molecular SAMs with chemical or biological specificity operating in the static modes is presently not possible.

A significant achievement of this work was a molecular-level understanding of the origin of the surface stress. By independently measuring the electrochemical interactions and combining published spectroscopic and variable pressure electrochemistry data about the model ferrocenylalkanethiolate surface-confined system, it was possible to elucidate that the differential surface stress is predominantly a result of a volume expansion of the monomolecular film required to enable ion pairing under an applied potential. Having established the physical origin of the measured surface stress for electroactive SAM modified gold-coated microcantilevers, this spurred an investigation of the ability to control the directional motion and amplitude of the microcantilever response, which was carried out in Chapter 3. Here, the effects of the alkyl chain structure and anion type on the microcantilever response were investigated. Not surprisingly, these variables lead to different microcantilever stress profiles and were found to play an important role in the magnitude and reversibility of the redox-induced cantilever bending. First, the effect of anion-pairing affinity for the surface-confined ferrocenium substantiated the hypothesis that the magnitude of the observed microcantilever surface stress reflects the extent of the redox-induced perturbation of the monolayer film. Second, a proportional decrease was observed in the microcantilever response when the hydrocarbon spacer chain length was decreased. By contrast, an *in-situ* electrochemical surface plasmon resonance (SPR) spectroscopy study did not reveal significant differences in the SPR shifts associated with the structural transitions and anion pairing as a function of the chain length. Similarly, *ex-situ* infrared studies also reveal similar structural characteristics for all the investigated monolayers. These findings suggest that the microcantilever bending is sensitive to molecular interactions which are not detectable by SPR.

To conclude, compelling evidence has been provided that chemically well-defined redox-active SAMs provide a relatively simple and versatile system with tailorable interfacial chemistry enabling one to probe specific molecular events. Moreover, the electromechanical bending of a microcantilever coated with FcRSAu SAMs that undergo potential-induced molecular transformations that can be applied to device structures generate charge normalized surface stress changes that are 10- to 100-fold greater in magnitude than that of conducting polymer-based actuators. From these findings, it appears possible that microcantilevers modified with FcRSAu SAMs could readily act as actuating materials or even artificial muscles in some carefully chosen applications.

In Chapters 4 and 5 an investigation of the potential (or charge) controlled adsorption and aggregation of a prototypical series of *n*-alkyl sulphates to the redox-active ferrocene-terminated SAM was undertaken. The anionic surfactants were chosen to have a similar headgroup but different hydrocarbon chain lengths. A common feature that was found for all the surfactants used herein was their propensity to form an ion-pair with the surface-confined ferrocenium. The combination of electrochemical measurements with *in-situ* SPR spectroscopy enabled a qualitative description of the adsorbed surfactant configuration. Electrochemistry measures single charge transfer events, and in this case, allows the accurate determination of the number of surfactant anions paired with the ferrocenium-terminated interface. On the other hand, SPR measures changes in the refractive index at the electrode/solution interface and reports the total surface concentration of the adsorbed molecules.

Presently, there are no universal models that can adequately represent the adsorption of surfactants on different solid substrates. What is known is that the adsorption will depend on the nature of the functional group as well as on the properties

of the solid and the solvent. In the system investigated herein, the adsorption appears to be dependent on surface charge density, surfactant structure, and electrolyte concentration. It was initially established that the driving force for adsorption was the specific interactions between the anionic headgroup and the cationic surface ferrocenium groups. However, the features of the interfacial adsorption are strongly affected by the concentration of the *n*-alkyl sulfates (SN_cS, where $N_c \geq 8$) in the bulk solution. At low concentrations, where the surfactant molecules are present as solvated monomers, the surfactant moieties pack perpendicular to the electrode surface in the form of an interdigitated condensed film. In this formation, the surfactant molecules are organised in a compact monolayer where half the sulfate headgroups are ion-paired to the surface ferroceniums ("heads down") and half of the polar sulfate heads are exposed to the aqueous environment ("heads up"). This intercalation is stabilized by van der Waals interactions between the lateral hydrocarbon chains. The surface coverages of alkyl sulfate indicate that at concentrations below the cmc, the surfactant monomers in solution can readily adapt to the changing ferrocenium concentration at the surface because they interact independently with the surface to screen the positive charge of the electrochemically generated ferrocenium.

A different behaviour was recorded at bulk concentrations above the cmc. At and above the cmc, the alkyl sulfates aggregate in water to form colloidal micelles with a hydrophobic interior and a hydrophilic peripheral. This is largely driven by the *hydrophobic* effect where the minimization of the hydrocarbon-water contact increases not only with increasing bulk concentration, but also with increasing hydrocarbon chain length. Increasing the hydrocarbon chain length of the amphiphile also increases the micellar stability. At this time, we speculate that the increasing micellar stability for the

series $SN_8S \rightarrow SN_{10}S \rightarrow SN_{12}S$ results in lower surfactant packing densities because of the inability to effectively respond to the dynamically changing surface concentration of ferroceniums.

It should also be noted that the adsorption isotherm for the ion-paired alkyl sulfates to the ferrocenium surface is different than that of alkyl sulfates that are electrostatically bound to static positive charged SAM surfaces. A maximum coverage of alkyl sulfate on the ferrocenium surface is obtained well below the cmc, in contrast to alkyl sulfate adsorption to static cationic SAM surfaces where the surface coverages of alkyl sulfate increases with the bulk solution concentration and attains a maximum value at the cmc. The noticeable difference in adsorption behaviour is attributed to the dynamic generation of ferroceniums by potential cycling and the specific nature of the ion-pairing interactions versus pure electrostatic ones.

The results of this body of work demonstrate the tremendous ability of redox reactions to influence mechanical actuation and the surface adsorption and aggregation of surfactants. Electrochemistry, when coupled with additional surface sensitive techniques, provides unique opportunities to study different molecular assemblies with potential applications in areas including templating, microelectronic and microfluidic devices, industrial and environment catalysis, bio(chemical)-sensors, and biocompatible implants.

6.2 Suggestions for Future Work

This Thesis provides a detailed description of the molecular-level origin of the micromechanical motion and surface stress of microcantilevers functionalized with electroactive self-assembled monolayers. While the development of microcantilever-

based sensing and actuating technologies is still in its infancy, the field has matured to the point where reports of new applications of this technology should include performance testing under relevant conditions. To this end, the author suggests a comprehensive study of actuation performance and stability of the FcRSAu microcantilevers investigated herein.

While some control over the magnitude of the micromechanical motion was demonstrated by employing cantilevers with different spring constants (Chapter 2) or manipulating the redox behaviour of the FcRSAu SAM (Chapter 3), it would be advantageous to try a redox-active polymer such as poly(vinyl)ferrocene. Presumably this should enable further amplification of the redox elicited actuation provided enough redox groups are incorporated into the thin polymeric film.

As mentioned in the Introduction, single cantilever experiments are susceptible to parasitic deflections. In the system used here, it was possible to deconvolute the microcantilever signal from such deflections because of the nature of the electrochemically elicited response, however it would be valuable to carry out double cantilever experiments where a reference SAM is employed. However, careful consideration as to what monolayer would be an appropriate reference for the electroactive ferrocene-terminated SAM is required. The author suggests the cationic $(CH_3)_3^+N(CH_2)_{11}SAu$ SAM system as a possibility. This SAM is redox-inactive, has a packing density which is comparable to that of the FcRSAu, and a fixed positive charge.

Finally, the author suggests the combination of electrochemistry with other surface sensitive techniques, such as AFM or STM, to visualize in real-time with molecular-level resolution the surfactant adsorption and aggregation processes occurring

at the ferrocene/ferrocenium surface. Such investigations should provide valuable information on the growth and structural organization of the surfactant aggregate adlayer on the solid electrode surface.

(1) Fritz, J.; Baller, M. K.; Lang, H. P.; Rothuizen, H.; Vettiger, P.; Meyer, E.; Güntherodt, H.-J.; Gerber, C.; Gimzewski, J. K. *Science* **2000**, *288*, 316–318.

Appendix A

Figure 2.10 shows a schematic representation of the redox-induced deflection of $FcC_{11}SAu$ microcantilevers in perchlorate solution. The ferrocenes are oxidized to ferroceniums so that Coulomb repulsion between adjacent ferrocenium moieties could contribute to the magnitude of the deflection. The average electrostatic force on a charge (z_1) due to the presence of a second charge (z_2) is given by[1]

$$\overrightarrow{F_{12}} = \frac{z_1 z_2 e^2}{4\pi\varepsilon_0\varepsilon_r r^2}\hat{r}_{21} \qquad \text{(A.1)}$$

Here e is the elementary charge (1.602×10^{-19} C), ε_0 is the permittivity of free space ($\approx 8.854 \times 10^{-12}\ C^2J^{-1}m^{-1}$), ε_r is the relative permittivity of the medium (for water $\varepsilon_r = 78$), r is the distance between the charges and $\hat{r}_{21}$ is the unit vector between charges z_2 and z_1. The spacing between adjacent ferrocenium anions is readily calculated from the experimentally determined ferrocene surface coverage of 4.7 ($\pm$0.3) $\times 10^{-10}$ mol·cm^{-2} (Q_{Fc^+} = 45 ($\pm$3) μC·cm^{-2}) which is close to theoretical value of a ferrocene–ferrocenium separation expected from the close packing of ferrocene spheres of 6.6 Å diameter.[2] From equation A.1, the average Coulombic force contribution of each individual ferrocenium–ferrocenium interaction (for unpaired ferroceniums) to the deflection of the cantilever is only ~3 pN (for an x-vector along the length of the cantilever).

(1) Israelachvili, J. N. *Intermolecular and Surface Forces*; 2nd. ed.; Academic Press: London, 1992; p 450.

(2) Chidsey, C. E. D.; Bertozzi, C. R.; Putvinski, T. M.; Mujsce, A. M. *J. Am. Chem. Soc.* **1990**, *112*, 4301–4306.